Additive Manufacturing of 3D Functional Materials: From Surface Chemistry to Combustion-Derived Materials

Thesis by
Daryl W. Yee

In Partial Fulfillment of the Requirements for the
Degree of
Doctor of Philosophy

CALIFORNIA INSTITUTE OF TECHNOLOGY
Pasadena, California

2020
Defended May 29th, 2020

Daryl W. Yee
ORCID: 0000-0002-4114-6167

ACKNOWLEDGEMENTS

Caltech has been one of the most special communities I have ever had the privilege of being a part of, and I know that my time here will hold a special place in my heart for the rest of my life. It has been an absolutely incredible journey, full of wonder and difficulty, but exceedingly fulfilling at the same time. No man is an island, and I have only come this far because of the support and love from everyone around me.

None of this could have been possible without my advisor, Professor Julia R. Greer. Julia, thank you for everything. The freedom you gave me to explore my own direction in the lab, and more importantly, the trust you had in me, has made me the scientist I am today. I am grateful for your unwavering support and the opportunities you have given me. Your infinite energy and enthusiasm for science has made my time at Caltech that much more enjoyable.

I have also been extremely fortunate to have had an unofficial advisor in Professor Robert H. Grubbs. Bob, thank you for taking this non-chemist in and showing me the ropes on how to be a chemist. It meant a lot to me that someone of your stature was willing to take a chance on me to work on chemistry-related projects. My time with you has given me a completely new perspective on materials science, and I will always be grateful for that.

I would also like to thank my committee members, Professors Katherine T. Faber and William L. Johnson. Kathy, I have always appreciated our chats about science and life, thank you. Professor Johnson, your curiosity about science has always inspired me.

I am also thankful for the mentorship from some very brilliant chemists who took their time to take me under their wing. Michael Schulz, Sankarganesh Krishnamoorthy, Carl Blumenfeld, and Jeong Hoon Ko — all members from the Grubbs group who I worked with at some point. Michael and Sankar in particular were instrumental in setting me on this track. Thank you for being so patient.

My time with the Greer group has been fantastic. To the 215 crew, Carlos Portela and Bryce Edwards, you two have been the best office mates and friends I could ask for. Michael Citrin and Max Lifson, thank you for your friendship over the years and I am glad we got a chance to work together. Ryan Ng, Andrey Vyatskikh, Rebecca Gallivan, Jane Zhang, Max Saccone, and all the other Greer group members have been fantastic friends and colleagues. Ottman Tertuliano, Xiaoxing Xia, Stephane

Delalande, Dylan Tozier, Victoria Chernow and Lucas Meza, thank you for your mentorship and guidance over the years. The days are long, but the years are short. I have treasured all the time we have had together.

I would also like to acknowledge Zane Taylor and Victoria Tovmasyan, two fantastic undergraduates that I got to work with over the years. You two will be fantastic scientists in the future. Zane, it has been an absolute pleasure, thank you for indulging my crazy science.

I have been a part of so many different communities at Caltech: Aftermath, thank you for those five years of ultimate frisbee — Zachary Sternberger, Sundar Pandian, Erika Ye, Bryce Edwards, Peishi Cheng, Paul Kempler, Evan Yeh, Helena Wu, Kevin Yang, Axl LeVan, Craig Cahillane, and so many more — thank you for your friendship. To the ORE team, thank you. Being an RA has been one of the best parts of the Caltech experience. Lloyd, I will look back fondly on my graduate student years because of you all. Thank you for letting me be your RA, it has been an honor, and I cannot wait to see what you do next. The APhMS staff: Christy Jenstad, Jennifer Blankenship, Angie Riley, Elizabeth Rodriguez, Cecilia Gamboa, and Jennifer Palmer. Thank you for everything you do behind the scenes.

To my support system, Bryce Edwards, Carlos Portela, Jennifer Norris, Beka Ivanova, Namita Sarraf, Michael Citrin, Max Lifson, Neal Brodnik, Ryan Ng, Ottman Tertuliano, and everyone else that I have missed, you have made this journey special and I could not have done this without you. Thank you.

Jenny and Beka, your friendship over the years have been invaluable, thank you. Bryce, from teammates to housemates to office mates, I look forward to more mischief in the future. Carlos, we have been together from the very beginning. To many more years.

To my girlfriend, Radka Dančíková, your love and support has carried me through this journey. Thank you for always listening and encouraging me. You have been a constant light in even the darkest times. Thank you for everything. Here is to adventures always.

Finally, to my family, Melissa, Jessica, and especially my parents, George Yee and Michelle Yee, thank you for your unconditional love and support. Mum and Dad, it has been almost a decade since I left Singapore, thank you for everything you have done for me. This is as much yours as it is mine.

Daryl W. Yee, 14th May 2020

ABSTRACT

Over the past decade, additive manufacturing has emerged as one of the most powerful manufacturing tools available today. Vat photopolymerization techniques, in particular, are especially promising as they are capable of achieving high resolutions and throughputs. However, the vast majority of materials that are compatible with them only have structural functionality. The fabrication of functional materials still remains a challenge in the field: functional polymers often require a complex multi-step synthesis. Ceramics-based photoresins are limited in composition and are challenging to use or synthesize. Metals have also been hardly explored with vat photopolymerization techniques.

This thesis explores methods of fabricating functional materials with vat photopolymerization. We develop accessible techniques for the fabrication of functional polymers, ceramics, metals, and multimaterials at a variety of length scales, from sub-micron to centimeter scales. On the polymer front, we first explore how surface coatings can be an accessible method of introducing chemical functionality to a material. In particular, we demonstrate the surface coating of genomic DNA on an architected polymeric structure and show how it can be used as a drug capture device to reduce off-target toxicity in chemotherapy. We also explore the use of click chemistry, the thiol-Michael reaction in particular, in the facile synthesis of acrylate monomers with a variety of functional groups. We demonstrate the compatibility of these functionalized monomers with two-photon lithography and highlight some potential applications of these functional polymers structures.

In the fabrication of ceramics and metals, we present a novel technique called photopolymer complex synthesis that combines solution combustion synthesis with vat photopolymerization to enable their fabrication. We illustrate the use of this technique by first fabricating piezoelectric zinc oxide architected structures with sub-micron features using two-photon lithography. Following that, we fabricate lithium cobalt oxide structures using digital light processing printing and highlight their use as architected lithium-ion battery cathodes. Lastly, we show how photopolymer complex synthesis can be expanded to fabricate metal and multimaterial architected structures. Our work highlights the use of polymer chemistry and materials science in expanding the range of materials that are compatible with vat photopolymerization, with the vision of democratizing the fabrication of advanced functional materials and enabling the production of previously impossible 3D devices.

PUBLISHED CONTENT AND CONTRIBUTIONS

Chapter 2 has been adapted from:

1. Yee, D. W., Hetts, S. W., Grubbs, R. H. & Greer, J. R. "3D Printed Drug Capture Materials Based on Genomic DNA Coatings". *Submitted*. (2020).
   Contributions: participated in the conception of the project, developed the coating chemistry, designed and conducted the experiments, and wrote the manuscript.

2. Schulz, M. D., Blumenfeld, C. M., Grubbs, R. H., Greer, J. R. & Yee, D. W. "DNA-Functionalized Scaffolds for Drug Capture Applications". *U.S. Patent No. 10,646,505*. (May 12, 2020).
   Contributions: participated in the design of the project, fabricated samples, performed drug binding tests, characterized the samples, and partially wrote the application.

Chapter 3 has been adapted from:

3. Yee*, D. W., Schulz*, M. D., Grubbs, R. H. & Greer, J. R. "Functionalized 3D Architected Materials via Thiol-Michael Addition and Two-Photon Lithography". *Advanced Materials* **29**, 1605293. (2017).
   DOI: https://doi.org/10.1002/adma.201605293
   Contributions: participated in the conception of the project, fabricated and characterized the structures, conducted the Orange II assay, prepared the data, and wrote the manuscript.

Chapter 4 has been adapted from:

4. Yee*, D. W., Lifson*, M. L., Edwards, B. W. & Greer, J. R. "Additive Manufacturing of 3D-Architected Multifunctional Metal Oxides". *Advanced Materials* **31**, 1901345. (2019). DOI: https://doi.org/10.1002/adma.201901345
   Contributions: participated in the conception of the project, developed the polymer chemistry, fabricated the structures, performed some of the material characterizations, and wrote the manuscript.

Chapter 5 has been adapted from:

5. Yee*, D. W., Citrin*, M. A., Taylor, Z. W., Saccone, M. A., Tovmasyan, V. & Greer, J. R. "Aqueous Salt Solutions As a Platform for Additive Manufacturing of Architected Complex Metal Oxides". *Submitted*. (2020).
Contributions: participated in the conception of the project, developed the polymer chemistry, fabricated the structures, performed the material characterizations, and wrote the manuscript.

Chapter 6 has been adapted from:

6. Yee, D. W., Saccone, M. A., & Greer, J. R. "Additive Manufacturing of Metals via Photopolymer Complex Synthesis". *In Preparation*. (2020).
Contributions: participated in the conception of the project, developed polymer chemistry, fabricated and characterized the samples.

7. Yee, D. W., Lifson, M. L., Citrin, M. A. & Greer, J. R. "3D Printing of Metal Containing Structures". *U.S. Patent Application No. 16/577,253*. (September 20, 2019).
Contributions: participated in the conception of the project, developed polymer chemistry, fabricated and characterized the samples, and wrote the application.

Not directly adapted in this thesis:

8. Portela, C. M., Ananthan, V. Krodel, S., Weissenbach, T., Yee, D. W., Greer, J. R. & Kochmann, D. M. "Extreme Mechanical Resilience of Self-Assembled Nanolabyrinthine Materials". *Proceedings of the National Academy of Sciences* **117**, 5686. (2020). DOI: https://doi.org/10.1073/pnas.1916817117
Contributions: synthesized the phase-separating polymer.

TABLE OF CONTENTS

LIST OF ILLUSTRATIONS

LIST OF TABLES

Chapter 1

INTRODUCTION

1.1 The Age of Designer Materials

The history and evolution of humanity have always been deeply intertwined with our use of materials — so much so that entire periods of our collective history have been named after the engineering materials that defined that era. The discovery of each progressively sophisticated material spurred the growth of numerous new technologies, resulting in increasingly advanced civilizations. Yet, even up to the first Industrial Revolution in the 19^{th} century, most of these material advances came about from a painstakingly slow iterative empirical process. The turning point really only came in the 20^{th} century, as progress in the fields of physics and chemistry provided a framework in which all materials could be understood. Physicists showed that every material had an underlying atomic/molecular structure, while chemists could determine the elemental composition behind it. More importantly, the interrelationship between both of them was finally recognized, providing a more unified understanding of materials[1] [1]. Since then, there have been rapid advances in materials development, culminating in a complete paradigm shift in how we approach materials design and selection. Rather than being limited to the properties of the materials that are available to us, our knowledge of materials science now allows us to design materials to have the specific properties that we want. From single layer graphene sheets for nanoelectronics [2], to high temperature ceramics for space flight [3], our ability to manipulate materials at a microstructural, and even atomic level, has ushered in a new age of designer materials, where we are now only limited by the laws of science.

Today, materials innovation has the potential to address some of the key challenges of our generation, such as climate change [4–6], energy storage [7], healthcare [8, 9], and even poverty [10, 11]. However, the complexity of these issues requires materials with increasingly demanding properties — properties that are challenging to meet through optimization of composition and microstructure alone. And while computational efforts such as The Materials Project [12] and the use of artificial

[1] I encourage the reader to refer to [1] for a fantastic read on the history of Materials Science.

intelligence [13] have been phenomenal in accelerating this optimization process, innovations in other aspects of materials science are necessary if we are to push the envelope further.

1.2 Architected Materials

In recent decades, the introduction of architecture into materials design has emerged as a new approach to obtaining materials with unprecedented properties. Rather than just optimizing for composition or microstructure, architected materials realize a particular function or property via the optimization of the geometric arrangement of the material as well [14, 15] — providing another degree of freedom in the design of a material. This architecture can manifest itself in a variety of different ways, sometimes involving multiple phases [15] and/or length scales [16].

We can illustrate this by looking at some man-made architected *structures*, the classic example of which is the Eiffel Tower, with its hierarchical truss structure [17]. The Eiffel Tower stands at 324m tall, with a base of 125m on each side. But if you were to melt down all the iron in the tower into a ball, the ball would only have a diameter[2] of $\approx$ 12m. The Eiffel Tower is incredibly light for a structure of that size, and this can be attributed to its efficient use of architecture to maintain its structural integrity, while minimizing the amount of material used.

This is the fundamental concept behind architected materials — the introduction of an internal structure to obtain some previously unattainable property. While the idea still stands, it is important to emphasize that the Eiffel Tower is an architected *structure*, and not an architected *material*. The distinction lies in the relative scale between the characteristic length of the internal structure and the length scale of interest, i.e. architected materials need to appear homogeneous at the length scales of interest [14, 18].

1.2.1 Natural Architected Materials

Some of the best examples of architected materials can be found in nature — in fact, almost every biological material studied today has been found to utilize some form of three-dimensional (3D) architecture and/or hierarchy in its microstructure, allowing them to achieve some property that would have been difficult to reach through the sole use of homogeneous bulk materials [19]. For example, diatoms are able to achieve high specific fracture toughness through the use of architecture to arrest

[2] Using a mass of 7.3 x 10^6 kilograms, and the density of iron as 7874 kg/m^3.

crack growth, despite being comprised of a relatively amorphous biosilica that has no intrinsic toughening mechanism [20]. Nacre's "brick-and-mortar" like structure, where hard mineral tablets are tiled together with soft organic materials, allows it to exhibit fracture toughness values approximately three to nine times that of its constituent mineral phase [21]. Perhaps some of the best examples that highlight the complexities of natural architected materials are bone and bamboo, as illustrated in Fig. 1.1 below.

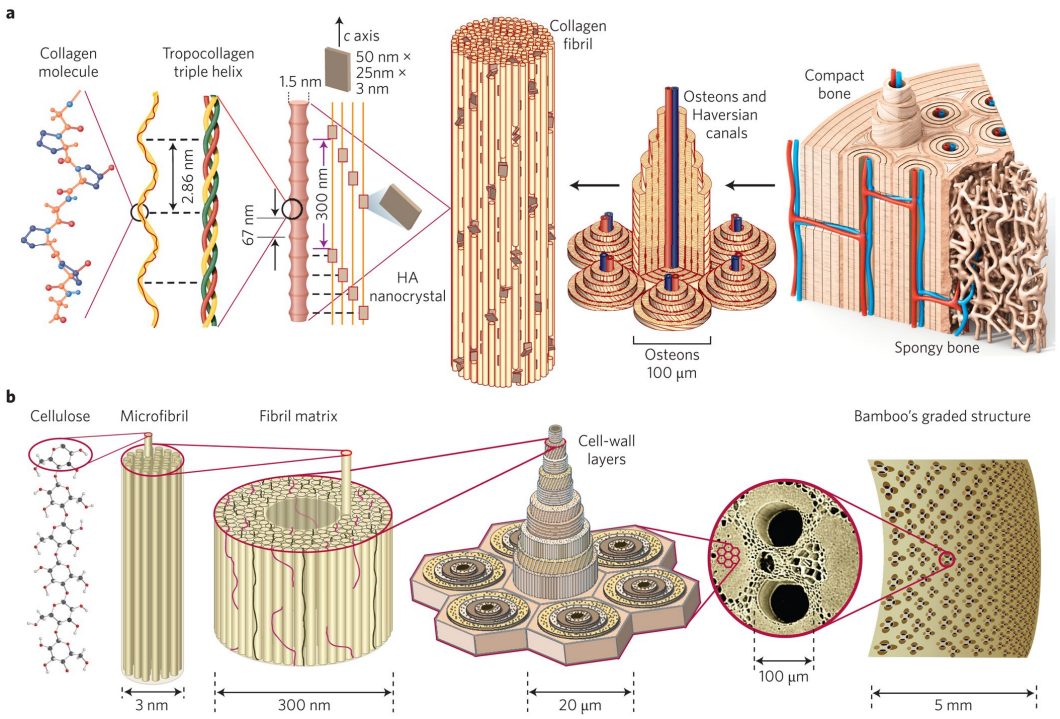

Figure 1.1: Hierarchical architecture of **a)** bone, and **b)** bamboo. Reprinted by permission from Springer Nature: Nature Materials, Reference [22] ©(2015).

Both these materials exhibit hierarchies that span over multiple orders of magnitude, and exhibit exceptional specific strengths and toughnesses despite being fundamentally comprised of weak biopolymer fibrils [22].

Architecture has also enabled unique properties that go beyond mechanics. For instance, the dry adhesion ability of geckos stems from the van der Waals forces between the surface and the millions of sub-micron hair-like structures on the gecko's feet [23, 24]. Sharks are able to swim really quickly due to the presence of tiny aligned denticles, approximately 150μm in size, on their skin that reduce the drag experienced as they swim [25]. A lot of the brilliant iridescent colors found in birds and insects actually arise from periodic nanostructured features on their bodies [26, 27].

The variety of properties that can arise from architecture is remarkable, even more so when you consider the limited number of building blocks that nature has to work with [28]. The organic phase is typically one of eight different structural biopolymers[3], and the inorganic phase is generally either a carbonate, phosphate, or silica [19]. Yet, nature has been able to combine these building blocks into highly diversified structures to adapt to different environmental pressures faced by each biological species.

1.2.2 Synthetic Architected Materials

Synthetic architected materials have existed for thousands of years, although it has only been in the past few decades that they have been referred to as such. Some of the earliest known examples take the form of composite materials, going as far back as 3400 B.C. with the use of plywood by the ancient Mesopotamians [29]. Although composite materials are rarely referred to as architected materials today, some of them do fulfill the main criteria of exploiting material configuration to achieve a desired property [15]. For example, fiber-reinforced composites can be designed to have anisotropic mechanical properties by dictating the orientations of the fibers within the matrix or stack [30].

Over the past few decades, as we have started to develop a more comprehensive understanding of how natural materials utilize complex architecture to enhance material properties, there has been a growing interest in fabricating synthetic architected materials that could surpass them. This is emboldened by the fact that we have access to a significantly larger pool of material building blocks, which should allow us to enter property spaces that are impossible even for natural materials, and surpass even the best materials that we have today.

Modern synthetic architected materials have largely revolved around cellular solids. As their name implies, these materials are fundamentally comprised of cells — an interconnected network of solid struts or plates. These unit cells are then packed in two or three dimensions to form the overall material [31]. Foams are one of the most commonly used synthetic cellular solids today as they are easy to manufacture and can be utilized in a variety of different applications. By simply varying the size and shape of the cell, and the materials of which the cell walls are made, these foams can exhibit a wide range of mechanical, electrical, and thermal properties [31, 32]. Our control over materials processing has allowed us to make these foams out of

[3]Collagen, keratin, elastin, resilin, abductin, fibroin, chitin, and cellulose.

almost any material: polymers [33], metals [34], ceramics [35], glasses [36, 37], and even composites [38, 39] can be made into foams. However, despite the amount of control that we have over the constituent material of the foam, current fabrication techniques are unable to precisely control the geometries of the unit cells, often resulting in stochastic irregular foams, as seen in Fig. 1.2. This irregularity is a far cry from the well-ordered architected natural materials that we have discussed prior, and actually limits the performance of these materials.

For example, let us briefly discuss how this impacts the mechanical properties of the foam. In general, the effective stiffness of a cellular material, E^* scales as:

$$E^* \propto E_s \overline{\rho}^n \tag{1.1}$$

where E_s is the Young's modulus of the fully dense constituent material, $\overline{\rho}$ is the relative density ($\overline{\rho} \leq 1$), and n is a scaling coefficient defined by the cell geometry.

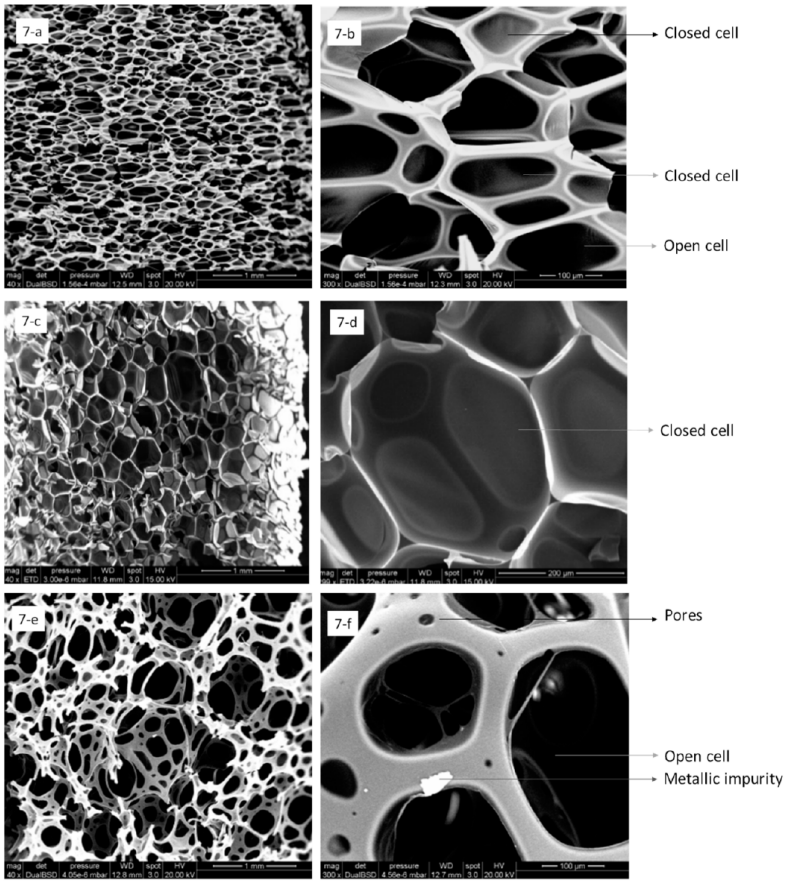

Figure 1.2: Microstructures of stochastic polyurethane foams. Reproduced from [40] - Published by the Multidisciplinary Digital Publishing Institute, under the Creative Commons Attribution 4.0 International License.

According to classical formulation, for stochastic open-cell foams, n has a theoretical value of 2 [41], although experimentally, it has been shown to range between 2-3 [42–44]. In contrast, periodic topologically defined architected materials (Fig. 1.3) are able to access lower n values, with n now theoretically able to have a value of 1 [32, 41]. Experimental studies of these materials have showed that they can exhibit n values between 1-2 instead [45, 46], which means that at the same relative density, these materials can be many times stiffer than their stochastic foam counterparts.

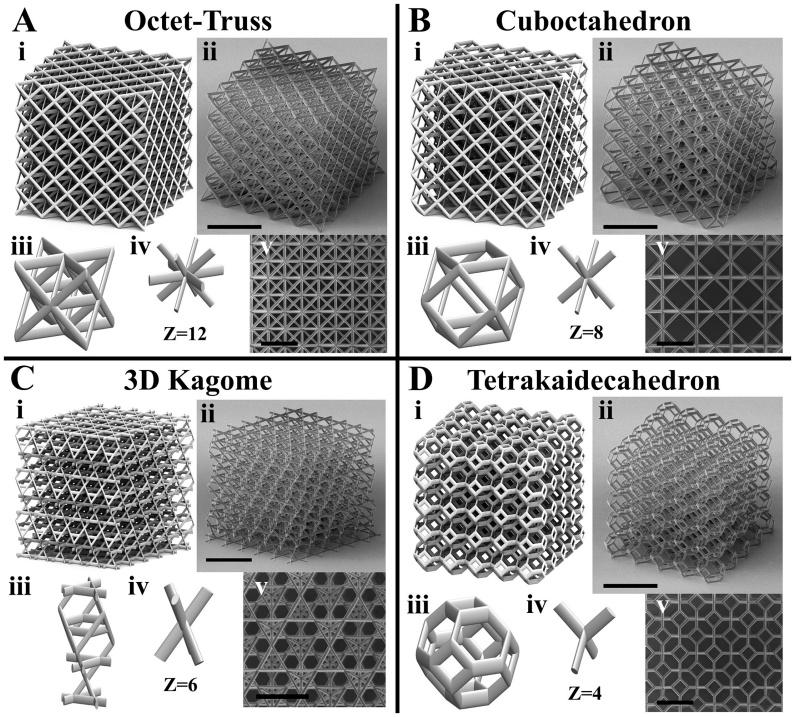

Figure 1.3: Examples of topologically defined architected materials — octet-truss, cubooctahedron, 3D kagome, and tetrakaidecahedron. Reprinted by permission from Elsevier: Acta Materialia, Reference [45] ©(2017).

The implication of this is that to fully leverage the capabilities of architected materials, we need to have topologically defined architectures that are optimized for a particular function. In order to realize this, more advanced fabrication methodologies have been developed to try and fabricate more topologically defined architected materials. Methods such as templating [47, 48], dealloying [49, 50], phase separation [51], and self-assembly [52] have been successful at making more regular architectures, but they are all limited in the architectures that they can achieve.

1.3 Additive Manufacturing

Additive manufacturing (AM) has recently emerged as one of the most promising technologies for fabricating architected materials. Broadly speaking, AM encompasses a set of techniques that are based on the computer-guided layer-by-layer fabrication of a 3D structure [53]. This layer-by-layer manufacturing enables an unprecedented level of freedom in design, allowing for the fabrication of arbitrarily complex geometries that would be impossible with traditional manufacturing processes [54].

Since the first demonstration of AM in 1981 by Hideo Kodama[4] with the use of photopolymers [56], the field has expanded significantly. On the technological front, there are now over fifteen different AM techniques that collectively span almost every material class [57–59], at scales less than 10 nanometers [60] to over 10 meters [61]. And the pace of progress has been phenomenal, with an increasing number of articles on the topic being published every year (Fig. 1.4).

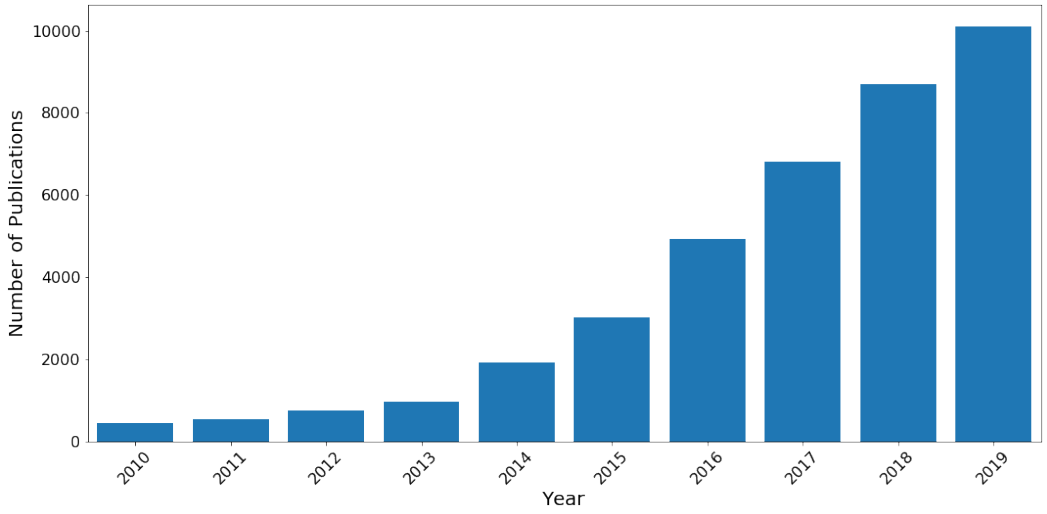

Figure 1.4: Number of publications pertaining to additive manufacturing over the past ten years. Data obtained from Web of Science using the key words *Additive Manufacturing* and *3D Printing*. Date of access: 16th April 2020.

AM has also had a broader impact on industry and society. The ability to fabricate structures with any arbitrary geometry has completely revolutionized the engineering and manufacturing industry. Complex architected parts can now be made faster with less processing and waste, allowing engineers to design more efficient and lightweight structures [18, 62]. This revolution in manufacturing has also permeated

[4]Not to be confused with the first *commercial* demonstration by Charles Hull in 1988 [55].

into other industries. For example, in the field of education, AM has been used as an outreach tool to develop interest in STEM[5] subjects [63]. From an industrial and economic standpoint, this growth and uptake of AM has given rise to a multi-billion dollar ecosystem [64] that includes material suppliers, hardware manufacturers, software vendors, and even quality assurance companies. At a societal level, AM is one of the few cutting-edge technologies that have been normalized by society — having entered the general lexicon[6], and even being a regular feature in science-fiction media. More importantly, it has helped to democratize manufacturing — anyone is able to purchase their own AM machine and start making anything that they want or need. This maker culture has led to the fabrication of cheap prostheses in developing countries [65], and even ventilator parts and personal protective equipment for healthcare workers during a global pandemic[7] [66] .

1.3.1 Additive Manufacturing Processes

In general, all AM processes can be classified into seven broad categories, based on how they deposit and bond the layers [67]. In this section, we will briefly survey each of the different processes to provide a foundation for the work that will be discussed in this thesis.

1.3.1.1 Binder Jetting

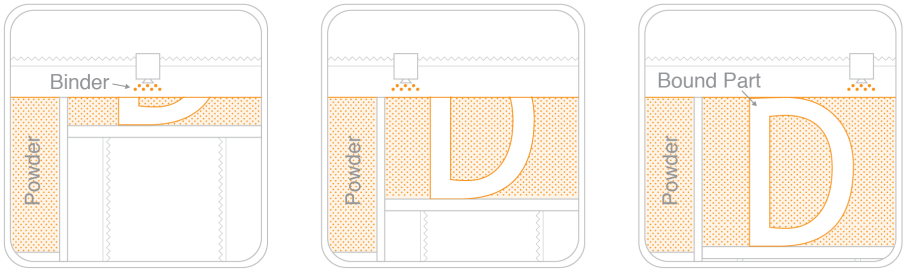

Figure 1.5: Schematic of Binder Jetting. A liquid binder is selectively deposited onto a layer of powder. The build platform is then lowered, the powder re-coated, and the process repeated until the structure is complete. The powder bed acts as its own support structure.

Binder jetting is a powder-based process where a liquid bonding agent is spatially deposited onto a thin layer of powder (Fig. 1.5). After the layer is complete, the build platform on which the powder is sitting is lowered, and a thin layer of powder

[5]Science, Technology, Engineering, and Mathematics.
[6]Albeit as "3D Printing", instead of "Additive Manufacturing", although the concept still stands.
[7]This thesis was written during the COVID19 global pandemic.

is reapplied over the previous. The process is then repeated until the structure is formed. The resolution achievable with this process is largely dependent on the size of the powders used and the binder drop size. After fabrication, the part is typically subjected to a post-processing step to remove the binder and/or improve its mechanical properties. One of the advantages of this process is that all types of powder materials can be used, making this a highly versatile technique for printing polymers, metals, and ceramics. Furthermore, as the bonding process occurs at room temperature, there is little to no heat-induced warping in the as-printed part. There is also no need for support structures since the surrounding powder provides all the necessary support, allowing for designs with almost no geometric limitations. However, one of its main drawbacks is that incomplete coalescence of the powders during the post-processing step(s) leads to internal porosities that are detrimental to the properties of the structure [54, 68].

1.3.1.2 Material Jetting

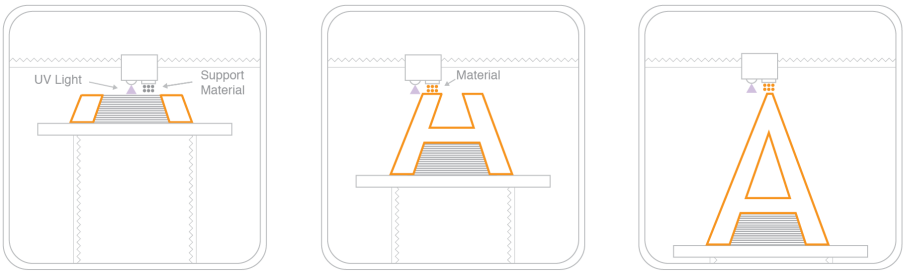

Figure 1.6: Schematic of Material Jetting. Droplets of material are selectively deposited onto a substrate. The build platform is lowered and the process repeated until the structure is complete. Supports are needed for overhangs.

Material jetting (MJ) is a process that operates similarly to a standard inkjet printer. Droplets of material are selectively deposited onto a substrate. Once all the material in the layer has solidified, the build platform is moved, and the process repeated until the layer is formed (Fig. 1.6). The resolution achievable is dependent on the size of the drop and its wetting properties. MJ is typically used with photopolymers, although ceramics [57], metals [69], and composites [70] have also been demonstrated. Solidification can be achieved in a few different ways: UV curing of a photopolymer, evaporation of a solvent [69], or solidification from a melt [71]. Additional post-processing steps are also sometimes necessary to make fully dense materials. The main advantage of MJ is that multiple nozzles can be easily incorporated into the print head, allowing for multi-material AM [72].

Some of the drawbacks include the need for supports during fabrication and MJ's relatively expensive cost [54].

1.3.1.3 Material Extrusion

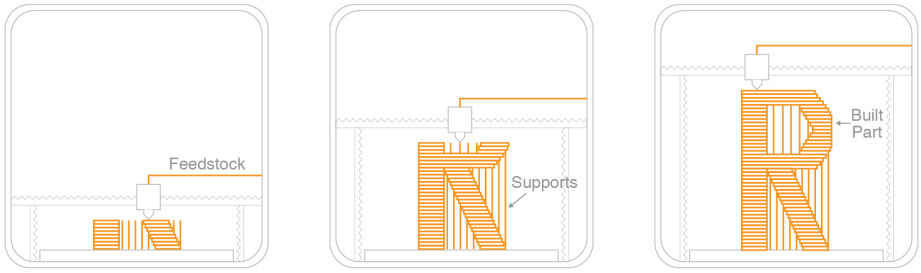

Figure 1.7: Schematic of Material Extrusion. Material is selectively deposited through a nozzle onto a substrate. The extrusion head is moved up, and the process repeats till the structure is complete. Supports are needed for any overhangs.

Material extrusion processes are where a material is selectively deposited through a nozzle onto a substrate (Fig. 1.7). Heat and/or pressure is typically applied to allow the material to flow smoothly and continuously through the nozzle in a semi-solid state. The material then solidifies after deposition while retaining its shape. The part is then built up by depositing over previously extruded layers. The resolution achievable is primarily determined by the diameter of the nozzle, and the solidification rate of the material. In most cases, the material is a polymer, a polymer-based composite material, or a paste. Metals or ceramics can be printed by incorporating the appropriate precursors into the feedstock, but require some additional post-processing treatments to remove the binder and consolidate the material [73, 74]. Material extrusion is one of the most commonly used AM processes due to its simplicity and accessibility of the inexpensive parts needed. Multi-material structures can also be easily fabricated via the installation of additional nozzles [75]. However, some of the main limitations include: Warping due to the change in dimensions that occurs during the transition between the semi-solid and solid state. Supports are often needed for more complex geometries since the material is not rigid enough in the semi-solid state to support itself in free space. The properties of the structures are also highly anisotropic due to the differences in bonding within and between the layers [54].

1.3.1.4 Powder Bed Fusion

Powder bed fusion (PBF) processes use a focused thermal source to selectively fuse regions of a powder bed together (Fig. 1.8).

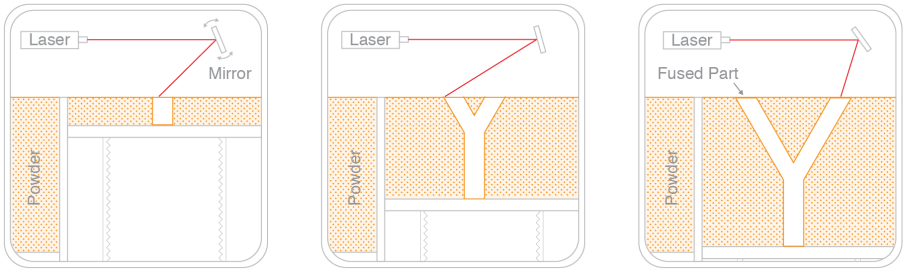

Figure 1.8: Schematic of Powder Bed Fusion. A focused thermal source is used to selectively fuse regions of a powder bed together. When the layer is complete, the platform is lowered, the powder reapplied, and the process repeated until the structure is complete. No supports are needed as the powder bed acts as its own support.

Similar to binder jetting, after a layer is completed, the build platform is lowered, and a thin layer of powder reapplied for the process to continue. The resolution achievable is determined by the size of the powder and the fusion zone [76]. All types of powders can be used, allowing for the fabrication of polymers, metals, ceramics, and composites. A controlled atmosphere is often used to prevent any high-temperature reactions that can occur between the powder and the air. Fusion can occur through one of four different mechanisms: solid-state sintering, chemically-induced binding, liquid-phase sintering, and full melting. The mechanism employed is determined by the type of powder used and the temperature at the focus point, and will result in structures with different degrees of porosity. Post-processing steps like infiltration or high-temperature sintering can then be used to obtain higher densities. Structures made with PBF are susceptible to warping due to residual thermal stresses. Although the powder bed can act as its own support, support structures are often needed to mitigate warping of the structure. PBF processes are relatively expensive due to the need of a high-power thermal source and a controlled atmosphere [54].

1.3.1.5 Directed Energy Deposition

In directed energy deposition (DED) processes, patterned layers are fabricated via the simultaneous local melting and deposition of material from a powder or wire feedstock. This is commonly achieved via the focusing of an energy beam onto a

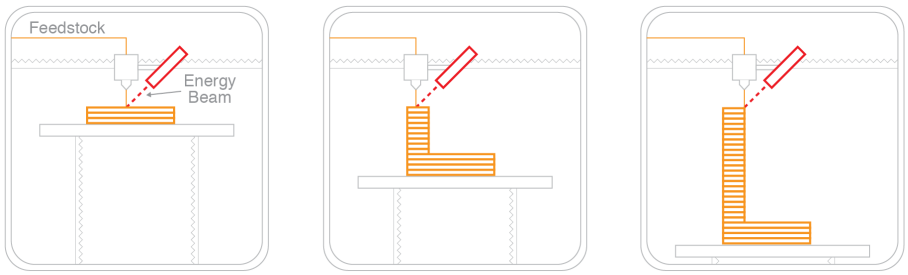

Figure 1.9: Schematic of Directed Energy Deposition. Patterned layers are fabricated via the simultaneous local melting and deposition of material from a wire feedstock. When the layer is complete, the platform is lowered, and the process repeated until the structure is complete.

continuous stream of feedstock that is being deposited onto a substrate. After each layer is completed, the build platform is lowered, and the process repeated until the structure is made (Fig. 1.9). The resolution achievable is largely dictated by the size of the melt pool. DED has hallmarks of powder bed fusion processes, but is similar to extrusion in that the material is only deposited where it is needed. Although the technique is theoretically compatible with polymers and ceramics, it is primarily used with metal feedstocks. Structures made with DED are highly dense due to their formation from a traveling melt pool. Unfortunately, the rapid cooling from the melt often leads to residual thermal stresses, and the complex thermal history can also lead to an inhomogeneous microstructure within the structure. Supports are also needed for more complex geometries, and a controlled atmosphere is necessary to prevent oxidation of the metal [54, 77].

1.3.1.6 Sheet Lamination

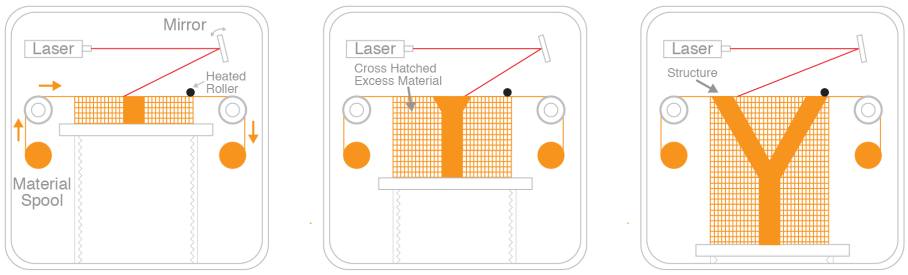

Figure 1.10: Schematic of Sheet Lamination. In this schematic, a heated roller is used to adhere each layer to the previous stack. A laser is then used to cut out the desired contour. The unwanted areas of the sheet are then sliced using a crosshatching method for easy removal after. The platform is lowered and a new sheet rolled over. The process then repeats until the structure is complete.

In sheet lamination (SL) processes, sheets of material are bonded to form an object. The desired shape is cut into the material via a laser or a mechanical blade, and then stacked over the previous layer (Fig. 1.10). Bonding is achieved by one of the following ways: adhesive bonding, thermal bonding, clamping, or ultrasonic welding. Depending on the process used, the unwanted parts of the sheet are either completely removed or sliced into small cubes of material. For the latter-type of processes, the small cubes act as supports, and need to be removed after fabrication. The resolution achievable is largely determined by the precision of the cutting tool. SL is compatible with polymers, metals, ceramics, and composites. Although, much like the other techniques discussed so far, for non-polymeric materials, post-processing steps are needed to debind and consolidate the part. SL is a relatively quick process since only the contours of the layer need to be cut, rather than the entire cross-sectional area. Furthermore, depending on the bonding type used, the structures can exhibit little shrinkage or residual thermal stresses. However, removal of supports can be time-consuming and also challenging. The properties of the structures are also anisotropic due to the differences in bonding within and between the sheets [54].

1.4 Additive Manufacturing — Vat Photopolymerization

The last category of AM is vat photopolymerization (VP). As it is the foundation of all the work in this thesis, a more in-depth description is warranted. VP is a family of AM processes in which a liquid photopolymer in a vat is selectively cured via photopolymerization. For most VP systems, this entails the use of either ultraviolet (UV) or visible light to initiate the photopolymerization process. Before we go into more details about the different type of VP processes, it is worth briefly going over some of the general principles behind photopolymerization.

1.4.1 Overview of Photopolymerization

In general, most *conventional* VP occurs via free-radical chain polymerization. This is a rapid process which consists of the characteristic steps of initiation, propagation, and termination[8], ultimately resulting in the formation of a polymer.

Initiation

The initiation step is considered to involve two reactions. First, free radicals are produced from some reaction process. In the context of photopolymerization, this

[8]This section has been largely adapted from George Odian's classic text "Principles of Polymerization" [78]. I encourage the reader to refer to it for a more in-depth discussion.

occurs via the absorption of light, with an appropriate wavelength, by a photoinitiator. Generally speaking, radical photoinitiators can be designated as either Norrish Type I or Type II (Fig. 1.11). Norrish Type I photoinitiators are single molecules that cleave into radical fragments on absorption of light with the appropriate energy. In contrast, Norrish Type II photoinitiators require a co-initiator for the generation of the free-radicals. Upon irradiation, the Type II photoinitiator reaches an excited state, and then proceeds to abstract a hydrogen from the co-initiator, leading to the formation of free-radicals. In some cases, Type II photoinitiators are able to generate radicals via direct hydrogen abstraction from monomers or solvents [59].

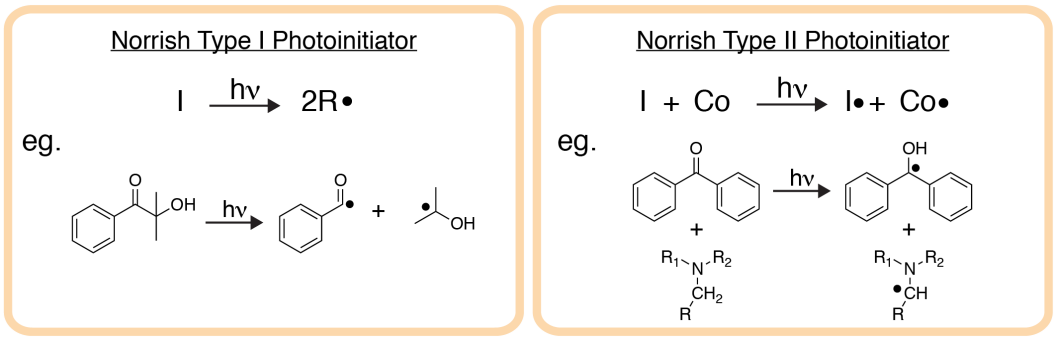

Figure 1.11: Examples of Norrish Type I (2-hydroxy-2-methylpropiophenone) and Type II (benzophenone and a tertiary amine co-initiator) photoinitiators.

For simplicity, we will depict the formation of a radical species via the homolytic cleavage of an initiator species **I** to generate a pair of radials **R•**.

$$\mathrm{I} \xrightarrow{h\nu} 2\mathrm{R}\bullet$$

The second reaction involves the addition of an initiator radical, **R•**, to a monomer molecule, **M**, to produce the chain-initiating radical $\mathbf{RM}^{\bullet}_{1}$. These monomers typically feature an unsaturated double bond for the radical to add to.

$$\mathrm{R}\bullet + \mathrm{M} \longrightarrow \mathrm{RM}^{\bullet}_{1}$$

Propagation

During the propagation step, the chain-initiating radical grows via the successive addition of monomer molecules. For simplicity, we will illustrate these in the growth of a linear homopolymer (i.e. one type of monofunctional monomer) (Fig.1.12).

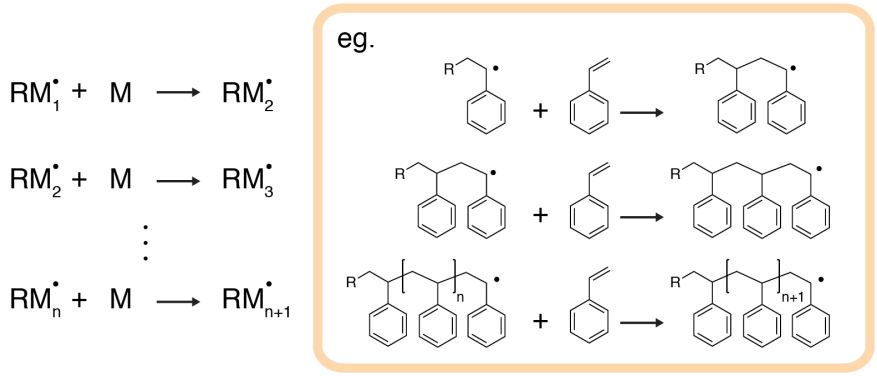

Figure 1.12: Generalization of propagation steps and a representative example illustrated with the linear growth of polystyrene. n denotes the number of monomers in the chain.

For VP processes, the most commonly used type of monomer is acrylates, due to their high reactivities that arise from their activated double bonds. Multifunctional acrylates are used to obtain a highly crosslinked network, while monofunctional acrylates are often employed as reactive diluents [79].

Termination

In general, the propagating chain will stop growing and terminate at some point. The termination reaction usually occurs by a bimolecular reaction involving radical chains. Two growing radical chains can react with each other via coupling or disproportionation (Fig. 1.13). Coupling involves the combination of two radical chains to form a single chain. In contrast, in disproportionation, a hydrogen atom from one chain end is abstracted to the other, producing two polymers, one of which is unsaturated. While not a termination reaction, the growing radical chains can also react with oxygen to form peroxy radicals at the chain ends. These peroxy radicals inhibit the growth of the polymer chains and slow down the polymerization significantly [80].

Figure 1.13: Generalization of termination steps and representative examples illustrated with the termination of polystyrene. n and m denote the number of monomers in the chain.

Termination reactions in VP processes are significantly more complicated. The use of multifunctional monomers leads to an increasingly crosslinked network as the reaction proceeds. At some point after the gel point[9], autoacceleration occurs, where the termination reaction becomes diffusion controlled since the chains have reduced mobilities. The concentration of active chains increases and polymerization increases significantly since the small monomers are still able to travel relatively freely. As the crosslink density increases further, polymer propagation becomes diffusion controlled as the mobility of all the reactive molecule decreases [82]. The trapped radicals remain in the polymer but are effectively "terminated" since they are isolated from unreacted monomers [83].

Taken together, we can see that light is used to initiate the formation of a chain-initiating radical, which then grows rapidly via the addition of monomer molecules. After a period of time, this propagating chain stops growing to give the final polymer.

Post-curing

The use of multifuntional monomers implies that gelation occurs at very low conversions [84]. Thus, a post-cure in often necessary to increase the degree of double bond conversion. This is typically achieved via additional UV exposure or thermal treatment [59, 85].

1.4.2 Vat Photopolymerization Processes

Now that we have covered the basics of photopolymerization, let us discuss how VP is achieved. There are multiple ways to achieve spatial patterning, namely: vector scanning, mask projection, two-photon absorption, and volumetric absorption.

1.4.2.1 Vector Scanning

In vector scanning processes such as stereolithography (SLA), a laser is used to initiate photopolymerization at its focal point. The laser is then selectively rastered across the build platform to fabricate the desired 2D pattern [54]. Vector scanning is conducted using either a top-down or bottom-up configuration (Fig. 1.14).

In a top-down configuration, the build platform is submerged just beneath the surface of a large vat filled with photoresin. The laser is then focused onto the surface of the photoresin to begin the patterning process. When the layer is complete, the build platform descends into the photoresin by a distance equal to the layer thickness, and

[9]Not to be confused with the gel effect [81].

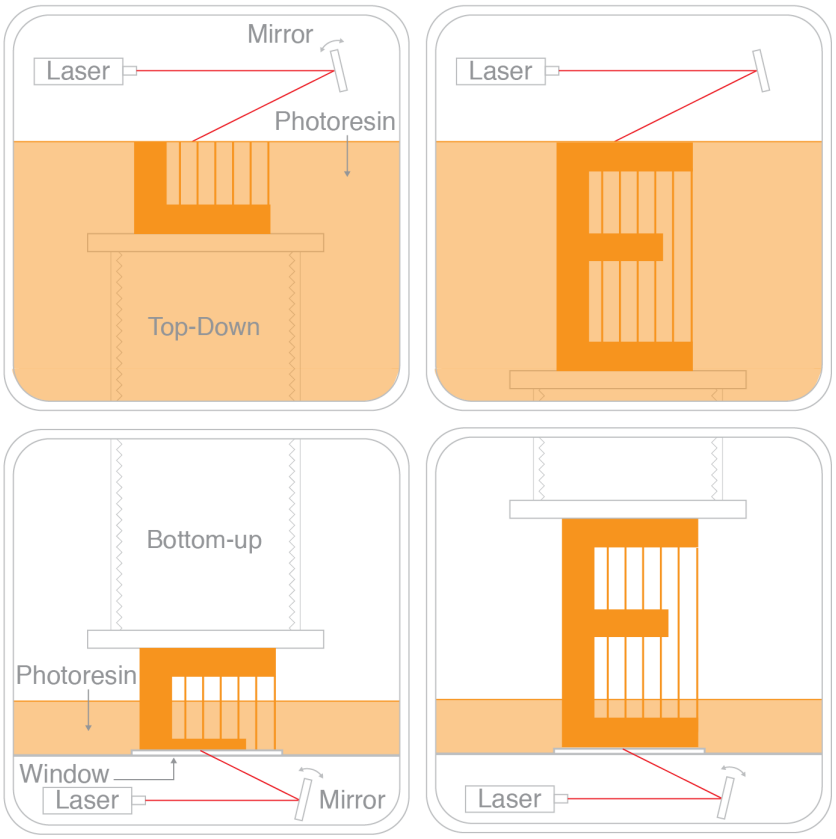

Figure 1.14: Top-down (top row) and bottom-up (bottom row) configurations for vector scanning VP processes.

a blade sweeps across the vat to circulate and flatten the photoresin. The process then repeats itself until the structure is complete. One of the main advantages of the top-down configuration is the large build volume possible — the size of the structure is only constrained by the size of the vat. There are also very low forces on the part during the fabrication process, resulting in good dimensional accuracy. The main disadvantage is that for a given structure, the entire vat must be filled to a point where it can fully enclose that structure. This requires a large amount of photoresin, most of which will remain unused during the entire process. Because of this, it is also time consuming to handle, filter, and swap photoresins. Furthermore, as photopolymerization occurs at the surface of the resin exposed to the atmosphere, curing speeds are slow due to oxygen-inhibition [86, 87].

In contrast, in bottom-up configurations, a small vat with a transparent window at the bottom is used instead. The build platform is lowered all the way into the filled vat, leaving a space equivalent to the desired layer thickness. The UV laser is then focused onto the build platform from the bottom of the vat, curing the polymer

between the build platform and the window. The cured layer is then separated from the window either through tilting, rotation, sliding, pulling, or a combination thereof [88]. The build platform then rises away from the window by a distance equal to the layer thickness, and the process then repeats itself until the structure is complete. The main advantage of using the bottom-up configuration is that the size of the structure is independent of the volume of the vat. Thus, a shallow vat can be used for fabrication, making the process more cost-effective and also easier to handle. During the curing process, the photoresin is also isolated from the environment, reducing the effect of oxygen inhibition. However, the separation of the cured layer from the window is challenging, often causing the structure to break or deform during the process [89]. To address this, coatings can be applied onto the transparent window to reduce the attachment force of the cured layer [90]. Polydimethylsiloxane (PDMS), in particular, is widely used as a coating material as molecular oxygen diffusing through it results in a thin oxygen inhibition layer at its interface, preventing the cured layer from attaching to it [91].

In both the top-down or bottom-up configurations, the resolution achievable is dependent on the laser spot size. Supports are required for more complex geometries, and the fabricated structures also exhibit some degree of anisotropy [92, 93].

1.4.2.2 Mask Projection

In mask projection processes, such as projection micro-stereolithography (PμSL) and digital light processing (DLP) printing, the entire pattern of the layer is projected onto the photoresin, resulting in the simultaneous curing of the entire cross-section. Once the layer is complete, the build platform moves by a distance equivalent to the layer thickness, and the process repeats itself. Mask projection can be realized in both top-down and bottom-up configurations, and share the same setups, advantages, and disadvantages as its respective vector scanning counterparts [54, 90].

The projection of the pattern onto the photoresin is achieved through a dynamic digital photomask that only allows light to shine through in a defined pattern. This is identical to the use of a photolithography mask in standard 2D photolithography. However, here, the photomask is able to rapidly reconfigure itself to display the next pattern in the series [54] (Fig. 1.15). The dynamic photomask is generated using one of two systems: a light-emitting diode (LED) array used with a liquid-crystal display (LCD) screen or a lamp with a digital micromirror device (DMD).

With the LED system, a UV or visible light LED array backlights an LCD screen.

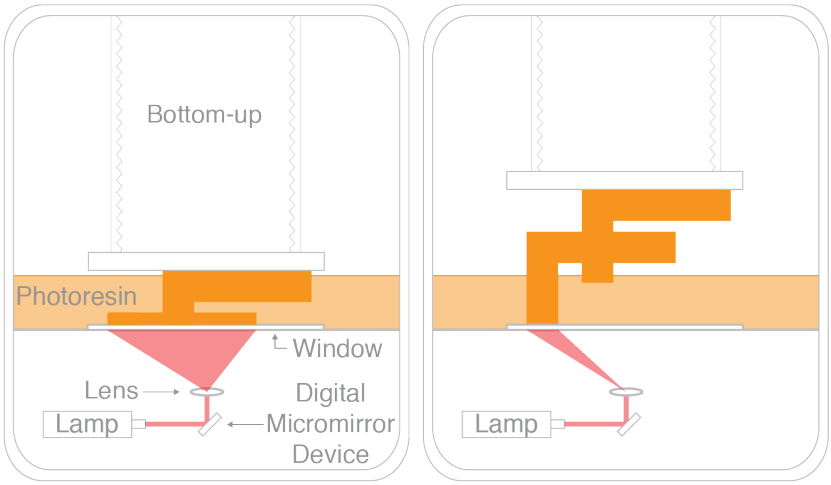

Figure 1.15: Bottom-up configuration for a mask projection VP system using a DMD system.

The pixels on the LCD screen act as the dynamic photomask by selectively transmitting the light in the desired pattern to initiate the photopolymerization process [94]. On the other hand, the DMD system uses a rectangular array of micromirrors that correspond to the pixels in the pattern to be displayed. These micromirrors can individually rotate $\approx \pm 10^{\circ}$ to reach an "on" and "off" state. In the "on" state, the light from the lamp is reflected off the micromirror and into the lens, turning that pixel bright. In the "off" state, the light is directed elsewhere and the pixel remains dark. The desired pattern is then generated by modulating which micromirrors are "on" or "off" [95].

In both systems, the resolution achievable is dependent on the size of the pixel. DMD systems typically offer higher resolutions but are generally more expensive. Although the entire layer is cured simultaneously, the use of supports is sometimes still necessary, especially for large overhangs. Similar to vector scanning processes, structures fabricated with mask projection typically exhibit some degree of anisotropy [96].

In recent years, there have been significant advances in mask projection VP technology towards industrial-scale fabrication. Of the processes discussed so far, bottom-up mask projection VP has all the makings of an industrial process — fast fabrication speeds, high resolution and accuracy, and minimum waste. However, the process is still too slow for mass production. This is largely due to the time needed for the separation step and subsequent repositioning for the next layer to be fabricated. In 2015, Joseph DeSimone and his colleagues demonstrated a new

mask projection process called Continuous Liquid Interface Production (CLIP) that used a continuous printing approach to achieve ≈100x faster fabrication speeds [97]. CLIP uses an oxygen-permeable transparent window to exploit the oxygen inhibition effect — generating a persistent liquid interface between the window and the fabricated part. The rate at which the build platform is raised can then be timed with the projected image to continuously fabricate a structure. As a result of this, these structures also exhibit little to zero anisotropy [98]. At the time of this writing, Carbon, the company behind CLIP, is worth an estimated $2.4 billion, and is best known for its partnership with Adidas to make additively manufactured shoes [99].

More recently, in late 2019, Chad Mirkin and his team at Northwestern University unveiled a new mask projection process called High-Area Rapid Printing (HARP). Similar to CLIP, HARP utilizes a persistent liquid interface to enable continual fabrication of the structure. In HARP, the photoresin floats on a bed of flowing immiscible fluorinated oils instead. This oil layer prevents sticking to the transparent window and also helps to dissipate the heat generated from polymerization. Structure fabricated with HARP exhibited litte warping, and could be made at speeds comparable to CLIP [100].

1.4.2.3 Two-Photon Absorption

Spatial patterning can also occur via a two-photon absorption (TPA) process[10], in a technique called two-photon lithography (TPL). In the VP processes described earlier, polymerization was initiated via a one-photon absorption, i.e. for an energy gap, $\mathbf{E_{gap}}$, between the ground state and the lowest excited state, a photon of energy $\mathbf{E_{1P}}$ that is larger than or equal to $\mathbf{E_{gap}}$ is absorbed to start the process of radical generation for polymerization (Fig. 1.16). In TPL, two photons, *each* of energy $\mathbf{E_{2P}}$ that is less than $\mathbf{E_{gap}}$ is absorbed to reach the lowest excited state and start the process of radical generation for polymerization [102].

Since there is no allowed state on absorption of $\mathbf{E_{2P}}$, the lifetime of this virtual state is on the order of femtoseconds. Within this time, the molecule has to absorb a second photon to reach the excited state. As you can imagine, this is extremely difficult to achieve with a classical incoherent light source. Thus, for TPA to occur, a femtosecond pulsed laser is necessary to provide sufficient photon density. As the

[10]Multiphoton absorption can also happen, although it is not in the scope of this work. I encourage the reader to refer to [101] for more details.

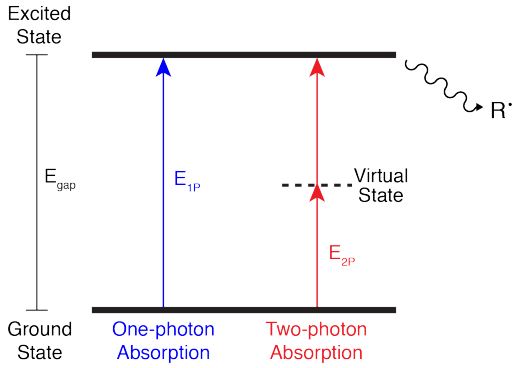

Figure 1.16: Simplified Jablonski diagram showing one-photon absorption and degenerate two-photon absorption, leading ultimately to radical generation.

probability of TPA is proportional to the square of light intensity, TPA only occurs within a small volume at the focal point of the laser [101].

To fabricate structures with TPL, the laser focus is moved around the photoresin in the desired pattern. Because one-photon absorption is insufficient to cause radical generation, cross-linking only occurs at the focal point, allowing for structures to be fabricated anywhere *within* the photoresin. As a result of this, TPL is not always a layer by layer technique since the laser focus can be moved in any direction within the resin (Fig. 1.17). TPL can occur in a few different configurations: the conventional way is to drop-cast the photoresin onto a transparent substrate, and then focus the laser into the photoresin through the transparent substrate. This method requires the use of an immersion liquid that has the same index of refraction as the objective, but is especially useful if the photoresin is corrosive or could leave some residue on the lens since the photoresin is never in contact with the objective (Fig. 1.17a). The major disadvantage here is that the substrate can limit the movement of the objective, restricting the height of the structures that can be fabricated.

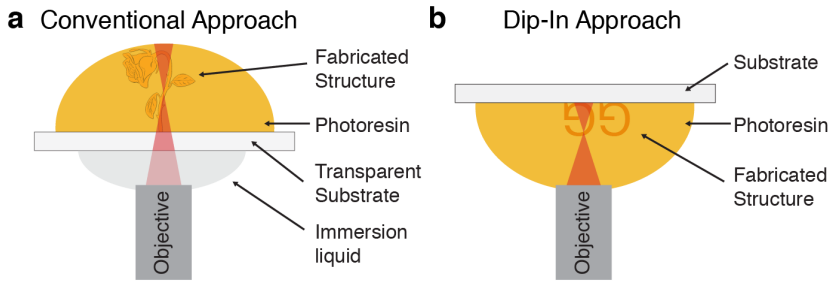

Figure 1.17: Schematics of the **a**. conventional and **b**. dip-in (right) configurations for two-photon lithography.

Another approach is to drop cast a photoresin onto a substrate before immersing

the objective into the photoresin directly. The laser is then focused through the photoresin without passing through any other medium. This is often referred to as the "Dip-In" method (Fig. 1.17b). The benefit of this approach is the increase in height of the structures that can be fabricated. The height is now dictated by the cohesive forces of the liquid photoresin, i.e. how much the objective can move away from the substrate before either the objective leaves the photoresin completely, or the photoresin splits into separate drops. Another advantage to this approach is the ability to use almost any substrate. However, the photoresin must be index-matched with the objective, which can be challenging. Furthermore, the photoresin should also be benign to the objective, and must leave little to no residue behind.

Regardless of experimental configuration, one of the main advantages of TPL is that it is able to achieve extremely high resolutions of ≈100 nm [59]. However, because of that, it is not feasible to fabricate large structures due to the serial nature of the process; although, recent work in the field has suggested that this could change in the next few years [103].

1.4.2.4 Volumetric Absorption

Recently, a new class of VP techniques based on volumetric absorption has been developed [104–106]. In brief, structures fabricated with these techniques are generally formed in a single step by the irradiation of a photoresin from multiple angles. The desired geometry is converted into a set of 2D images and then projected into the photoresin at different angles. The superposition of energy from the different angles results in a total volumetric energy dose that is sufficient to cross-link the photoresin in the desired shape (Fig. 1.18).

As a volumetric printing technique, no supports are needed since the entire structure is fabricated simultaneously. Photoresins with high viscosities can also now be used since there is no need to reflow the photoresin in between layers. This is an exciting new area of research in VP, and has the potential to significantly improve the fabrication speeds of VP.

1.4.3 Materials Compatible with Vat Photopolymerization

The majority of the materials compatible with VP are polymer based by definition. Any monomer and/or macromonomer that has photopolymerizable groups can, in theory, be used with VP to fabricate polymer structures. VP is also capable of fabricating ceramics and, to some extent, metals. In brief, this involves the use of a

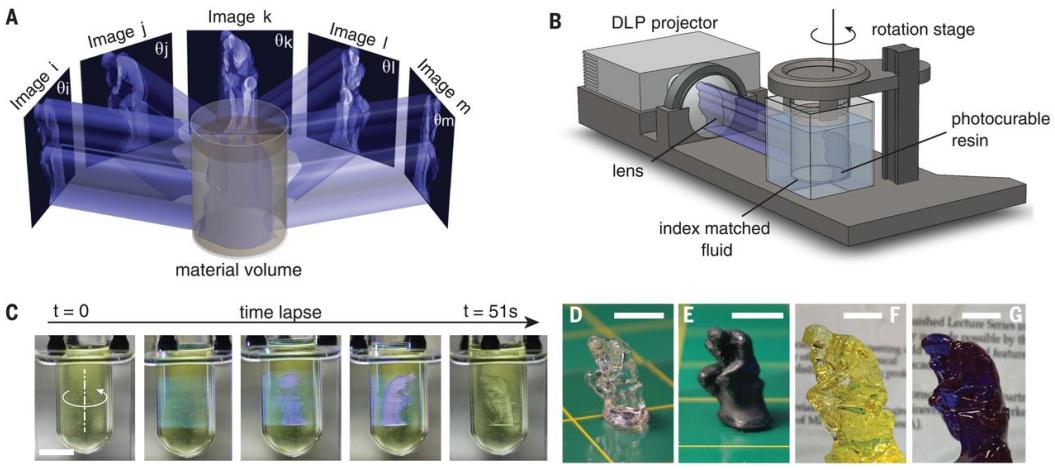

Figure 1.18: Concept behind volumetric absorption. Irradiation of the photoresin from different angles results in the concurrent formation of the structure. From [104]. Reprinted with permission from AAAS.

hybrid polymer or polymer system that contains inorganic precursors [57]. Structures fabricated with these hybrid polymers are then treated at high temperatures to remove the organic polymer binder, leaving the inorganic components behind. As such, VP is a versatile technique that is compatible with every class of materials.

1.5 Vat Photopolymerized Architected Structures and Materials

The ability to produce arbitrarily complex geometries with additive manufacturing makes VP ideal for fabricating topologically defined architected structures and materials. Vat photopolymerization techniques, in particular, are well suited to this purpose, as they are able to achieve both high resolutions and fabrication speeds. Over the past decade, the use of VP has led to the development of numerous materials and devices with exotic and unprecedented properties, especially for mechanical, optical, and biomedical applications. We will highlight just a few examples in the literature, as there has been so much work in the field that it would be impossible to cover it all in this section.

Mechanical Behavior

As alluded to earlier in this chapter, the use of architecture has tremendous benefits for the mechanical properties of a material. As a result, it has been heavily investigated by the mechanics community — materials that are ultra-strong but have very low relative densities have been achieved through the fabrication of topologically defined architected materials [45, 46, 107]. There have also been

numerous examples in the literature of how architecture can be used to imbue ductility to a material despite being made from an underlying brittle material [16, 108, 109] (Fig. 1.19).

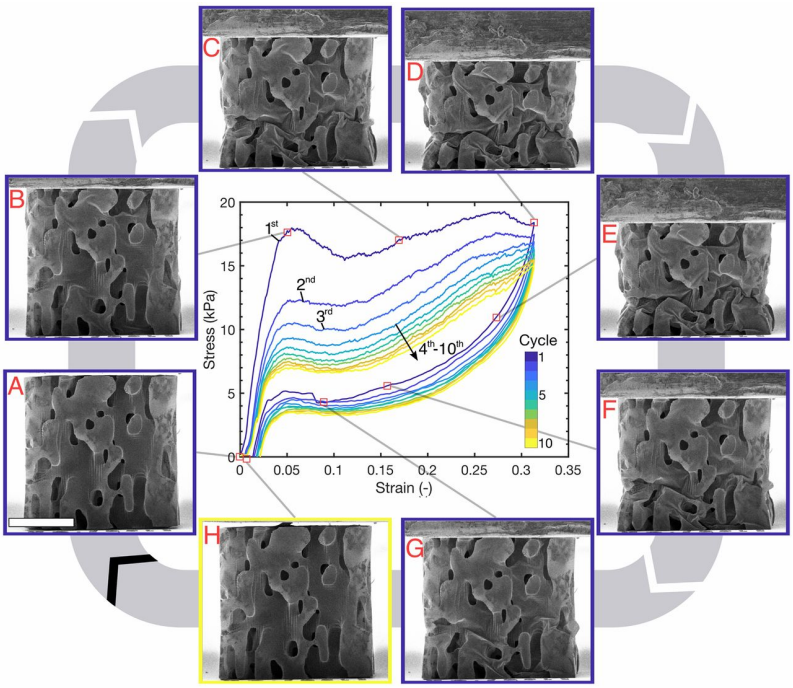

Figure 1.19: Example of a resilient architected material made from an underlying brittle material. Cyclic deformation of a hollow alumina structure with bicontinuous geometries shows strains up to 0.3. Bulk alumina typically fails at strains of ≈ 0.0002. No visible permanent deformation or microcracks can be seen after 10 cycles. All micrographs correspond to the first cycle except for H, which corresponds to the end of the 10th cycle [108].

Architecture has also been demonstrated to be able to dictate the fracture behavior of a material or structure [110]. For example, Brodnik et al. fabricated "fracture diodes", which used triangular voids in a structure to create directionally-dependent toughness behaviors [111]. Materials and structures with unusual mechanical responses, including twisting on compression [112, 113], negative Poisson's ratio [114], and bistability [115] have also been achieved through precise tailoring of topology. Recently, composite materials with interpenetrating architected phases have also been explored, and have led to materials with exceptional mechanical properties [116, 117].

Optical Properties

The ability to fabricate materials with periodic defined features, that are on the order of the wavelength of light, has also allowed for the precise control and manipulation

of light-matter interactions. VP is particularly suited for these applications because it is the only process that is able to reach the sub-micron features necessary for visible light interactions. As a result of this, VP has been able to fabricate photonic crystals [118, 119], materials with structural color [120] (Fig. 1.20), and even materials that can exhibit negative refractive indexes [121].

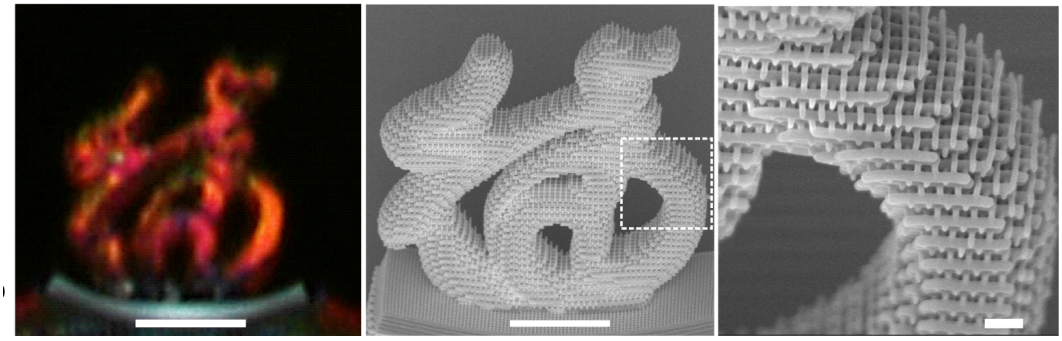

Figure 1.20: Optical micrograph (left) and SEM image (middle) of a architected material that exhibits sturctural color. (Right) A close-up image of the highlighted box in the middle panel shows that the material is comprised of woodpiles. Scale bars: (left-middle) 10 μm, (right) 1 μm. Adapted from [120] - Published by Springer Nature, and is under the Creative Commons Attribution 4.0 International License. The original image was cropped to only highlight these panels.

Biomedical Engineering

Architected materials have also found applications in biomedical engineering as architecture has been shown to influence migration and growth of cells through the material [122]. This has led to significant efforts in the field to try and understand how to exploit architecture to guide tissue formation by creating scaffolds with rationally designed geometries [123]. Although not strictly architected, it is worth highlighting that numerous biomedical devices have also been fabricated using VP, from microneedles for drug delivery [124] to magnetically guided microswimmers [125].

1.5.1 Structural Materials

Up until recently, most materials that were used with VP only had structural functionalities. This was a deliberate choice as it made it clear that any emergent and/or enhanced material properties observed were solely due to the architecture, without any contribution from the inert constituent material. This has been incredibly useful in developing a more comprehensive understanding of how architecture impacts material properties. However, as the field has matured, and we now have established design rules on how to utilize architecture in materials

design, there has been a surge of interest in utilizing functional materials with VP. There is immense untapped potential in combining structural-derived properties with chemical functionality — architecture could drive new applications of these functional materials, or new synergistic properties could arise from these combinations.

1.5.2 Functional Materials

There have been significant efforts in the development of functional materials for VP. This has largely been driven by the polymer chemistry community as their organic synthesis knowledge and expertise are well suited towards developing the polymeric materials that are used in VP. As a result of this, it is now commonplace to fabricate functional polymeric structures that can exhibit properties such as self-healing, stimuli-responsiveness, biodegradability, etc [126–128].

Innovations in polymeric materials has even driven the development of ceramic, and to some extent, metal fabrication with VP. Advances in preceramic polymers and inorganic-organic photoresins have been instrumental in expanding the library of functional inorganic materials that can be fabricated with VP [57, 129].

However, there are still significant challenges in the development of these functional materials. On the polymer front, the synthesis of these functional polymers can be complex and inaccessible to the general scientific community. While ceramic fabrication with VP is gaining popularity, it often requires using reagents that are challenging to work with or difficult to synthesize. There has also been very little in the way of metal fabrication using VP — most metal AM is still achieved via expensive powder bed fusion processes.

1.6 Thesis Outline

This thesis presents an exploration on the fabrication of functional materials with vat photopolymerization, from polymers to ceramics to metals. It seeks to explore the following three main questions: How can we synthesize functional polymers in an accessible way? How can we fabricate advanced ceramics with simple reagents? And can we use vat photopolymerization as an inexpensive alternative for metal additive manufacturing? The overall goal of this work is to develop new methodologies for the democratization of the fabrication of advanced functional materials.

Chapter 2 seeks to explore how surface chemistries and coatings can be used to

introduce functionality onto otherwise inert structural polymeric materials. We demonstrate the coating of commercially available photopolymers with genomic DNA and discuss how these functionalized structures can be used as drug-capture materials to reduce off-target toxicities in chemotherapy. More generally, we show that surface chemistry is a powerful approach to fabricating functional architected materials.

Chapter 3 focuses on the use of click-chemistry, namely the thiol-Michael addition, in the facile synthesis of functionalized acrylate monomers for use in vat photopolymerization. We demonstrate the versatility of the technique by synthesizing monomers with a wide variety of functional groups and highlight some potential applications of these functional polymers structures.

In Chapter 4, we move away from functional polymers and explore the fabrication of ceramics instead. We introduce the concept of architected chemical reactors for the *in situ* generation of materials. To illustrate this, we present a novel technique called photopolymer complex synthesis that combines solution combustion synthesis, an established materials chemistry technique for the synthesis of inorganic nanoparticles, with vat photopolymerization to enable the fabrication of multifunctional metal oxide structures. We demonstrate this with the facile fabrication of zinc oxide structures with sub-micron features using two-photon lithography, and highlight its electromechanical capabilities.

Chapter 5 highlights the capability of photopolymer complex synthesis in fabricating complex metal oxides. We explore the use of this technique in the fabrication of lithium cobalt oxide at the centimeter scale and demonstrate its use as a lithium-ion battery cathode.

Chapter 6 further explores the potential of photopolymer complex synthesis in fabricating metals and multimaterial structures. We discuss how the technique can be expanded to accommodate the synthesis of these materials, and illustrate the fabrication of structures made out of copper, a cupronickel alloy, and a multimaterial combination of iron oxide and lithium cobalt oxide.

Finally, in the last chapter, we will summarize the work presented in this thesis, discuss some possible future research directions, and provide an outlook of the field moving forward.

Chapter 2

SURFACE FUNCTIONALIZED ARCHITECTED DEVICES FOR CHEMOTHERAPY

Chapter Abstract

Functional polymer materials for vat photopolymerization have gained significant interest over the past decade. There is immense untapped potential in combining architecture with chemical functionality to design new novel devices. Organic synthesis of functional monomers or the use of nanoparticle composite systems have proven effective in producing functional polymers, but run into the issues of accessibility and printability.

In this chapter, we discuss how surface functionalization of commercially available structural photopolymers can provide an alternative accessible approach instead. We demonstrate this in the surface functionalization and coating of genomic DNA on a commercial photopolymer, and highlight how these functional architected structures are ideal as drug capture devices to reduce the problem with systemic toxicity in chemotherapy.

This chapter has been adapted from:

1. Yee, D. W., Hetts, S. W., Grubbs, R. H. & Greer, J. R. 3D Printed Drug Capture Materials Based on Genomic DNA Coatings. *Submitted* (2020).

Contributions: participated in the conception of the project, developed the coating chemistry, designed and conducted the experiments, and wrote the manuscript.

1. Schulz, M. D., Blumenfeld, C. M., Grubbs, R. H., Greer, J. R. & Yee, D. W. DNA-Functionalized Scaffolds for Drug Capture Applications. *U.S. Patent No. 10,646,505* (May 12, 2020).

Contributions: participated in the design of the project, fabricated samples, performed drug binding tests, characterized the samples, and partially wrote the application.

2.1 Functional Polymers for Vat Photopolymerization

Most commercially available photoresins for vat photopolymerization (VP) have been designed with mechanical properties in mind. There has been so much research and development on this front that there are now entire catalogs of photoresins with different mechanical properties. This has been a boon for the manufacturing industry which in turn has led to significant investments in the field. However, the structural nature of these materials preclude them from certain applications — applications that requires a response from an external non-mechanical stimuli, or perform a function of interest without any external stimuli.

To address this, there has been a surge in the development of functional polymer systems that are compatible with VP. Broadly speaking, functional polymers are polymers that have specified physical, chemical, biological, pharmacological, or other uses which depend on specific chemical functional groups [130]. The incorporation of nanoparticles with functional properties with a polymer to form a composite system also falls under this category [131]. This surge of interest from the polymer chemistry community in VP has led to some very interesting applications. There have been demonstrations of: conductive [132–135], and magnetic [136, 137] structures. Biocompatible scaffolds that are biodegradable [138–140], able to facilitate cell-growth [122, 141, 142], and deliver drugs [125, 143–145]. Sensors that can respond to heat [146], force [147], pH [148], electric field [149], oxygen [150], etc [151].

The extensive organic synthesis toolbox available to polymer chemists has allowed them to precisely synthesize any polymer imaginable. However, what is often understated is the printability of these functional polymer photoresins. For example, the use of nanoparticle fillers in a composite photoresin might imbue new functional properties, but at an increase in viscosity, making it more challenging to use. Agglomeration of these fillers will also decrease the shelf life of these photoresins [152]. Long exposure times needed might also make the fabrication of large structures difficult [138]. The use of certain reagents might also preclude certain processes from being used effectively. For example, thiol-ene based resins boast lower shrinkage stress and more homogenous polymer networks [126], but cannot be used with bottom-up VP processes that rely on oxygen-inhibition due to their insensitivity to it [100]. Furthermore, the mechanical properties and resolutions achievable might not be suitable for the desired application, despite having the appropriate chemical functionality. Thus, a balance often needs to be

struck between printability and functionality.

Another aspect of polymer synthesis that is often not considered is the accessibility of the methodology to the general scientific community. For a novel functional polymer to gain traction, it is critical that researchers from other fields are able to access it and adapt it for their own purposes. And while synthesis of polymers might be trivial to a polymer chemist, and only slightly challenging to someone with a background in organic chemistry, it might be a serious barrier to a mechanical engineer or a materials scientist. This is especially so if large volumes of polymer are needed, for example in top-down VP processes.

2.2 Introducing Functionality via Surface Chemistry

Another approach to making functional structures is to introduce the desired functionality via surface chemistry. The main advantage of this is that we are now able to utilize all the commercially available photoresins that have been highly engineered for printability, resolution, and mechanical properties. The use of surface chemistry thus allows us to retain the desired bulk properties of the material while introducing new functionalities. There have been numerous examples of this in the literature, albeit mostly on extruded poly(lactic acid) or polycaprolactone structures — For example, surface modifications have been used to tailor the surface wetting properties [153, 154] and to promote cell adhesion [155–157].

Surface functionalization of commercial photoresins in VP is much less explored. Most of the work in the field has largely revolved around the post-polymerization surface functionalization of *non-commercial* photoresins instead. This is typically achieved via the synthesis or inclusion of monomers and/or macromonomers that have functional groups that can be reacted with after the polymerization reaction [158–161]. While an effective methodology for achieving functional materials, the issues with printability and accessibility still remain. It is thus of interest to explore the surface modification of commercial photopolymers and demonstrate how they can be used to vastly expand their applications.

In this chapter, we introduce the concept of drug capture devices for the reduction of systemic toxicity in chemotherapy, and highlight that additive manufacturing is key to realizing it *in vivo*. We explore the surface functionalization and coating of vat photopolymerized commercial photopolymers with genomic deoxyribonucleic acid (DNA), and show that it is a facile, scalable method of realizing this device. Finally,

we investigate the stability of these coatings and their use as drug capture materials *in vitro*. Let us first start by giving some background on cancer and chemotherapy.

2.3 Systemic Toxicity in Chemotherapy

Cancer is a global public health challenge that affects people in every world region, regardless of demographic and socioeconomic background. It is one of the leading causes of death, contributing to about one in every six deaths worldwide. It is estimated that by 2040, cancer-related deaths will grow to approximately sixteen million each year, placing a significant burden on healthcare systems around the world [162]. Chemotherapy is one of the most powerful tools that we have to treat cancer today, but is limited by its systemic toxicity: chemotherapeutic agents that are not taken up by cancer cells can kill healthy cells instead, which causes debilitating side effects, irreversible organ damage [163], and affects patient survival [164]. Many common chemotherapy drugs have greater efficacy at higher dosages [165], which requires the clinicians to often make the choice between maximizing tumor suppression and avoiding irreversible off-target toxicity. This limits the anti-cancer efficacy of the existing drugs.

Over the past decades, enormous efforts have been made to develop new therapeutic agents that can target cancer cells more precisely while simultaneously minimizing the damage to healthy cells [166]. These drug development cycles are extremely lengthy, lasting many years, and prohibitively expensive, with translates into increasingly more costly drugs [167, 168]. The associated financial burden on the patients is significant and often causes nonadherence to treatment schedules, and a reduction in overall quality of life [169]. It is thus imperative to go beyond the small-molecule approach and develop new technologies and devices to reduce and/or to eliminate off-target toxicity of well-established traditional drugs.

2.4 ChemoFilter Background

2.4.1 Concept of Drug Capture

One such approach is transarterial chemoembolization (TACE) for the treatment of hepatocellular carcinoma (HCC) in the liver. In TACE, chemotherapeutic agents are directly administered to the tumor in conjunction with embolic agents, allowing the drug to be in contact with the tumor for a longer period of time [170]. TACE has been shown to improve the survival of patients, likely due to its improved drug dose profile [171]. However, despite the targeted delivery and increased retention time of the chemotherapeutic agents, previous studies have shown that between 50-70%

of the drugs still end up entering systemic circulation [172].

To reduce the systemic toxicity during TACE, in 2014, Patel and coworkers proposed chemotherapy filtration devices ("ChemoFilters") that could sequester excess chemotherapeutic agents from the bloodstream prior to them entering systemic circulation. Conceptually, these devices would be deployed in the vein draining the organ undergoing intra-arterial chemotherapy, forming a closed system where the drug would be prevented from leaving the organ and causing systemic toxicity. It was envisioned that that the ChemoFilter could be used in the treatment of HCC, as depicted schematically in Fig. 2.1.

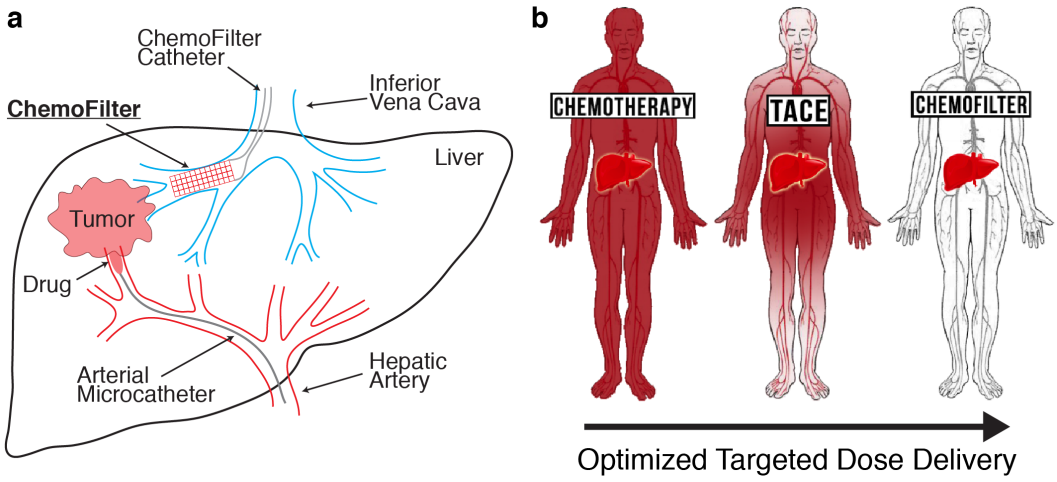

Figure 2.1: ChemoFilter concept: **a**. The deployment of the ChemoFilter in the inferior vena cava captures any excess chemotherapeutic agent, that is not taken up by the tumour, from entering systemic circulation. **b**. Envisioned goal of the ChemoFilter. The red areas denote areas where the chemotherapeutic agents are present. Subfigure **b** adapted from ChemoFilter Inc.

The liver was a model organ to test this device as established procedures like TACE already allowed the localized delivery of high dose chemotherapy directly to the tumor. More importantly, the hepatic veins and inferior vena cava (IVC) provided direct downstream locations to deploy the ChemoFilter.

2.4.2 Drug-binding Materials

The first generation of devices featured a simple Nitinol frame attached to a sulfonated ion-exchange membrane that could bind via electrostatic interactions to doxorubicin, a commonly used chemotherapy drug. In a simulated TACE treatment of HCC in swine, the deployment of these devices in the IVC resulted in an 85% reduction in the concentration of doxorubicin in the blood postfilter,

demonstrating *in vivo* proof-of-concept of chemotherapy filtration (Fig. 2.2) [173].

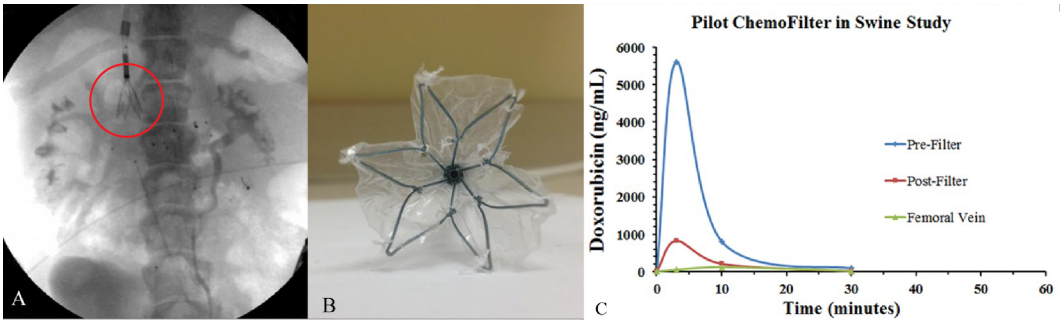

Figure 2.2: First demonstration of ChemoFilter: **a**. ChemoFilter (circled) deployed in a simulated TACE treatment in swine **b**. First generation ChemoFilter - ion-exchange membrane attached to Nitinol frame. **c**. Concentration of doxorubicin pre- and post-filter over time. Figure adapted from [173].

Successive generations of ChemoFilter devices in subsequent years have explored different drug binding materials based either on ion-exchange [174–176] or DNA interaction [177–179]. Compared to the electrostatic interactions used in the ion-exchange materials, DNA-based materials exploit the intrinsic DNA-targeting mechanism of action of many common chemotherapy drugs to capture them. The idea is to introduce external DNA into the body for it to be deliberately attacked by the chemotherapy drugs instead of healthy cell DNA. The benefit of this approach is that the drugs do not need to be charged under physiological conditions for capture to happen, as evidenced by the capture of cisplatin (neutral in solution) from DNA-based materials [179], and not from the ion-exchange ones [177].

2.4.3 Device Design — The Need for Additive Manufacturing

The specific design of the ChemoFilter is critical to its *in vivo* performance because it has to maximize surface area and interaction time for drug binding, while minimizing hemodynamic disturbances, such as flow obstruction and induction of thrombosis. As such, there have been significant ongoing efforts to model the hemodynamic performances of these devices *in vivo* to determine their optimal geometry [180]. However, what has limited the progress on this front are the form factors of the drug binding materials that have been developed so far. The membranes, micro/nanoparticles, or meshes used can only be implemented in certain configurations, limiting the designs that can be achieved (Fig. 2.3).

Additive manufacturing (AM) offers a potential solution to this problem because it enables the fabrication of materials with arbitrarily complex geometries in a single processing step. Computational fluid dynamics models of ChemoFilter devices

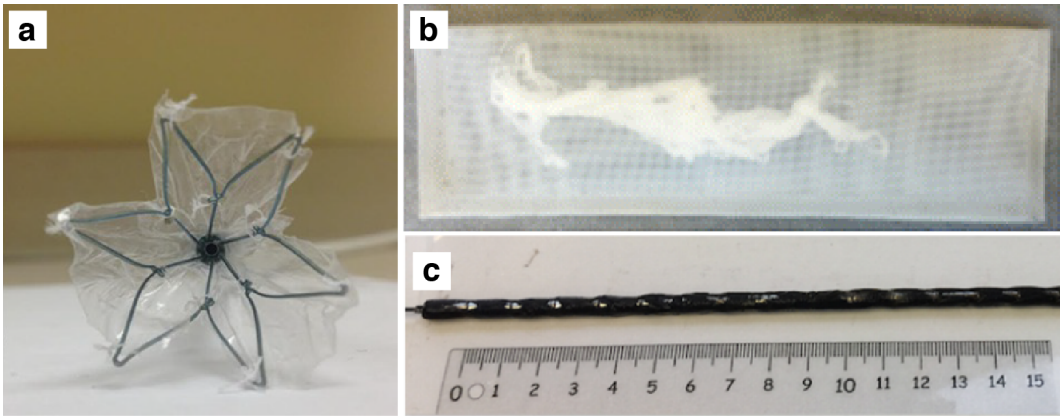

Figure 2.3: ChemoFilters made with traditional materials: **a**. Membranes attached to a frame. Frame is 22mm across. Adapted from [173]. **b**. Mesh bag to contain microbeads or DNA strands. Reprinted by permission from Springer Nature: Biomedical Microdevices, Reference [178] ©(2016). **c**. Magnetic nanoparticles attached to magnets threaded on a wire. Image reproduced from [179] - Published by Springer Nature, and is under the Creative Commons Attribution 4.0 International License. The original image was cropped to only highlight this panel.

with different geometries have also suggested that 3D-printed architectures are ideal for this application because they can be easily optimized to have the desired hemodynamic performances [181, 182] (Fig. 2.4). However, a substantial challenge with AM is that the existing materials compatible with it do not have drug binding capabilities, so there is a need to develop new chemistries and materials for this purpose.

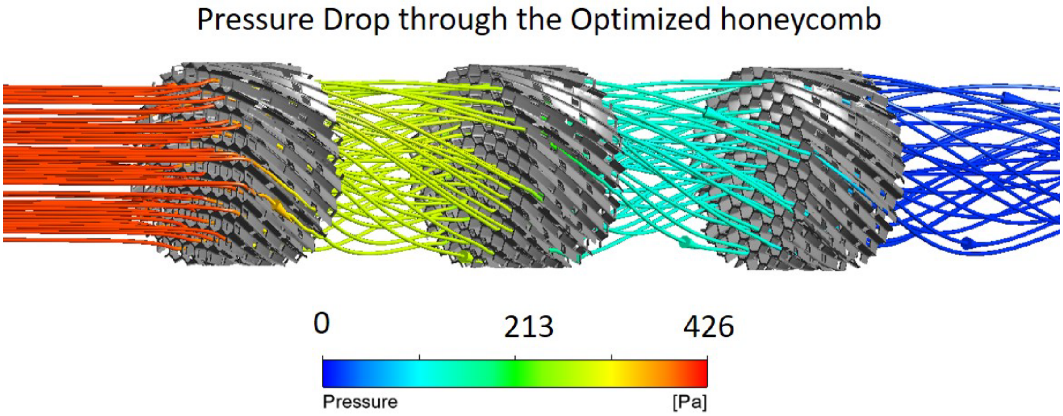

Figure 2.4: Computational fluid dynamics model of a staged twisted honeycomb ChemoFilter device. Pressure drop across this device design is calculated to be 3mmHg, which is less than the threshold value of 5-7mmHg. Figure courtesy of Nazanin Maani, Ph.D.

2.5 ChemoFilter Design Consideration

The target drug in this work is doxorubicin, one of the most commonly used drugs used to treat HCC. Doxorubicin is known to have improved tumor suppression effects at higher dosages, but off-target accumulation of the drug in the heart can increase the risk of congestive heart failure [183]. Thus, there are tangible benefits from reducing the off-target toxicity of it. Doxorubicin causes cytotoxicity by intercalating between the cell DNA's base pairs, preventing them from replication [184]. The use of DNA as a drug-binding material exploits doxorubicin's natural mechanism of action against itself to sequester it from solution.

The dimension of the inferior vena cava, where the device will be deployed, is between 12-17mm in diameter [185]. The small size of the device coupled with the fact that the amount of drug binding is correlated to the surface area of the device, means that a high-resolution additive manufacturing technique would be ideal. Thus, in this work, a digital light process (DLP) printer, the Autodesk Ember, was used for fabrication, since it can achieve up to $\approx 50\mu$m resolutions

Surface functionalization of DNA is an ideal approach for a few different reasons:

1. The venous hepatic blood flow velocity is $\approx$100 cm/s [182], thus in the absence of additional occlusion, there would likely be insufficient time for the blood to diffuse into the bulk of the material and interact with any DNA there. Any interactions would likely only be confined to the surface.

2. DNA is very sensitive to its environment. It would denature rapidly in organic photoresins. The use of an aqueous photoresin might mitigate that, but the free-radicals generated during the polymerization process would also damage the DNA [186].

3. As alluded to earlier, the use of surface functionalization allows us to utilize commercially available materials that have already been optimized for additive manufacturing (Autodesk's PR48, Formlabs's Elastic Resin, etc.), without the need for a lengthy customized photoresin optimization process — simplifying the fabrication process. The broad range of commercially available materials also provides access to a huge library of materials with varying mechanical and chemical properties.

4. Methods for functionalizing surfaces with DNA are well established in literature; they rely on specially designed synthetic DNA sequences whose

functional groups can bind to a complementary moiety on the substrate [187].

However, the main drawback to using synthetic DNA is its relatively high cost, which renders the fabrication of DNA-based ChemoFilters (DNA-ChemoFilters) prohibitively expensive and impractical. An alternative approach is to functionalize the surface with genomic DNA, which is inexpensive and easily obtainable, but does not possess reactive end-groups or functional groups that can be used to anchor it to a surface [188]. Up until recently, the surface functionalization of genomic DNA remained a challenge until Blumenfeld et al. developed magnetic iron nanoparticles (IONP) with surface-bound alkylating agents that could covalently bind to genomic DNA [179]. Although the stability of these surface-DNA adducts were not part of the study, it is known that alkylation of DNA can lead to depurination at the alkylation site, effectively severing the bond between the DNA and the substrate [189] (Fig. 2.5).

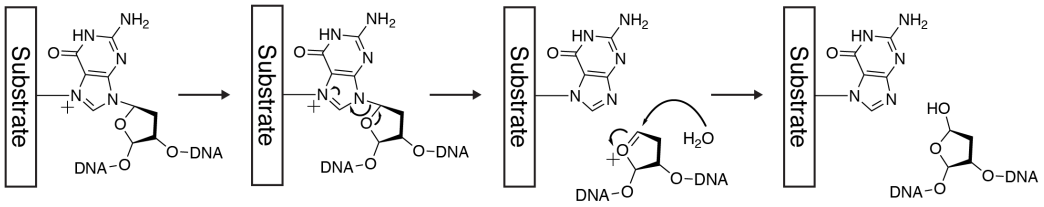

Figure 2.5: Schematic of depurination of alkylated DNA. Depurination leads to the loss of the surface bound DNA.

The stability of these surface-DNA adducts is critical for the safe *in vivo* operation of these devices. The long-term impact of free-floating genomic DNA in the bloodstream is unclear: some studies indicate that the presence of foreign DNA in the bloodstream is not unusual [190, 191], others indicate that it could lead to autoimmune diseases such as lupus [192]. Thus, the possibility of depurination prompted us to consider alternative chemistries for genomic DNA functionalization.

2.6 DNA Coatings

Initial attempts to covalently bind genomic DNA (DNA) to the surface were centered around small-molecule approaches, from cycloaddition with intercalated psoralen to amine formation from imine reduction, all with varying degrees of success. But inspired by the coatings of sulfonated block copolymers on 3D-printed devices by Oh et al. [174], we decided to tackle this from a coatings approach instead. Of

particular interest in the literature was the work by Yamada et al. who showed that UVC (254 nm) irradiation of dried DNA films resulted in the formation of insoluble films that were stable in water for over 24 hours at room temperature [193].

2.6.1 Fabrication of Architected Structures

3D square lattices were fabricated using the Autodesk Ember, a commercially available DLP printer, out of PR48, an open source acrylate-based photoresin (Table 2.1). After fabrication, the samples were soaked in methanol for 5 hours, blow-dried with compressed air, and then followed by a UV post-cure (350–380 nm, 36W)(MelodySusie DR 301C) for 3 hours. The samples were then soaked in methanol for 2 x 360 minutes to leach out as much unreacted small molecules as possible. Finally, the lattices were dried under vacuum (National Appliance Company) at room temperature for 10 hours to give the untreated lattices.

Function	**Reagent**	**Weight% (wt/wt)**
Oligomer	Allnex Ebecryl 8210	39.776
Oligomer	Sartomer SR 494	39.776
Reactive Diluent	Rahn Genomer 1122	19.888
Photoinitiator	Esstech TPO+	0.400
UV Blocker	Mayzo OB+	0.160

Table 2.1: Composition of Autodesk PR48 resin.

We chose square lattices as they exemplified a geometry that was easily fabricated with additive manufacturing but was challenging to produce using traditional manufacturing processes. Each lattice was about 12 mm wide, 2.5 mm tall, and contained 16 x 16 x 3 cubic unit cells, with a unit cell length ≈750 μm and ≈250 μm wide beams, as shown in Fig. 2.6. The surface area of each lattice was ≈1200 mm^2.

We explored two different methods of coating with DNA, as described below.

2.6.2 DNA-UVC Coating Methodology

In the first approach, DNA coatings were deposited by immersing the lattices in an acidic DNA solution, followed by drying under vacuum. The DNA coated lattices were then exposed to UVC irradiation to crosslink the DNA. This is depicted schematically in Fig. 2.7.

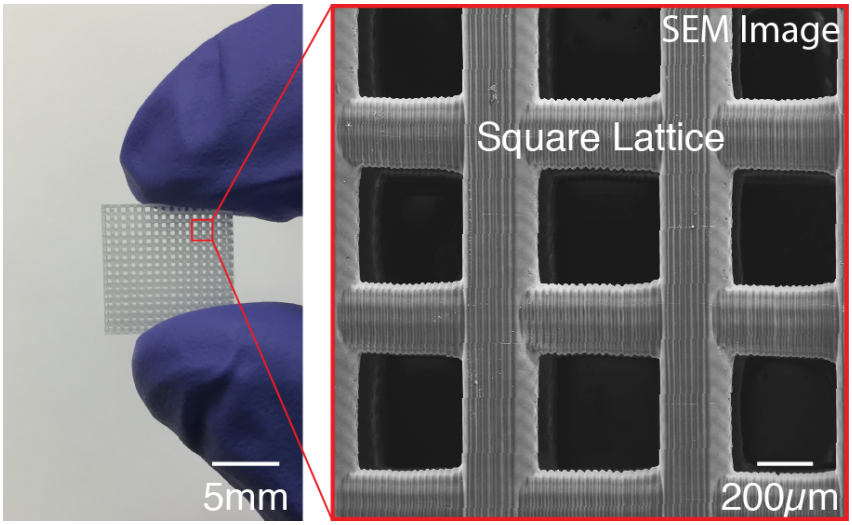

Figure 2.6: 3D square lattices fabricated via DLP printing. A representative scanning electron microscope (SEM) image of the square lattice.

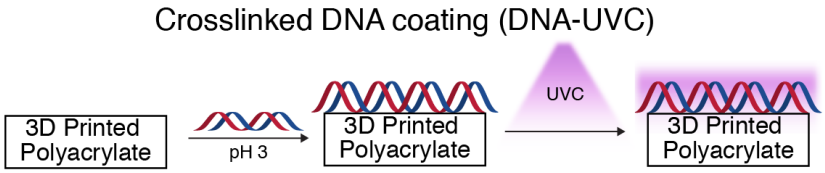

Figure 2.7: Schematic of DNA-UVC coating. DNA coating is achieved by immersing the substrate in an acidic solution of DNA, followed by vacuum drying. The DNA coated substrate is then subjected to UVC irradiation to induce DNA crosslinking.

Acidic solutions of DNA were first prepared by dissolving DNA (DNA sodium salt from salmon testes (Sigma-Aldrich)) in pH 3 water (deionized water adjusted to pH 3 with 37% hydrochloric acid (Sigma-Aldrich)) to give an acidic DNA solution of concentration 2.5 mg/mL. Each lattice was then immersed separately in 3 mL of the acidic DNA solution for 60 minutes at room temperature, without any external agitation. The lattices were then carefully removed from the solution and placed on a PTFE mesh (0.045" x 0.025" Opening Size, McMaster-carr) on a glass petri dish, and dried under vacuum at room temperature for 180 minutes to give the DNA coated samples.

The use of an acidic solution of DNA is key to this approach. At low pHs, the hydrophobic core of DNA is exposed and can interact with the hydrophobic polyacrylate surface, anchoring itself at random points along the strands to the substrate surface. Drying of the DNA solution results in a receding air-water interface, extending and fixing the DNA as the interface passes over it [194, 195].

There was no visual difference in the lattices before and after this coating process (Fig. 2.8a). In contrast, applying this coating procedure using a neutral solution of DNA resulted in a lower percentage of successful coats, with DNA strands often precipitating in fibrous masses within the lattice (Fig. 2.8b).

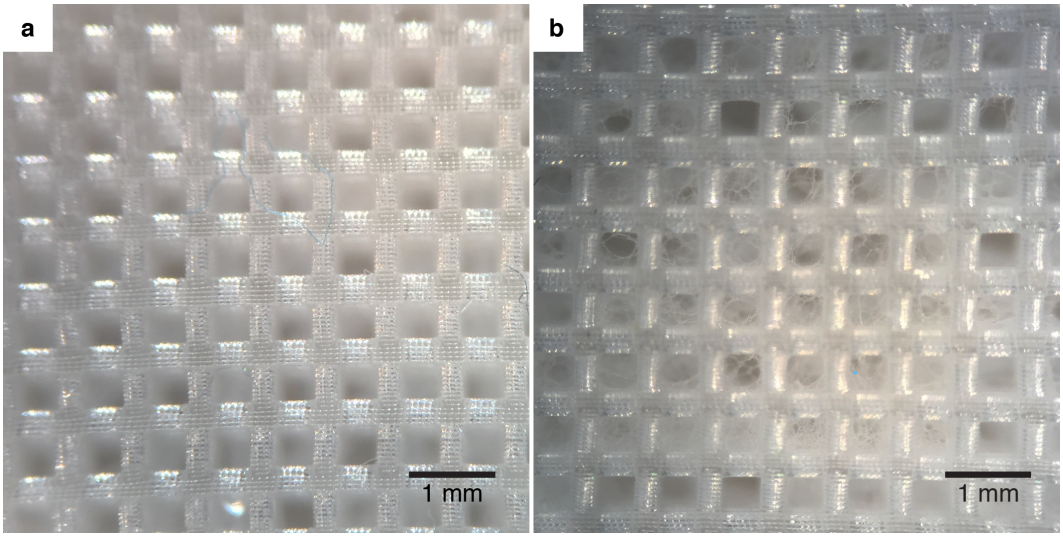

Figure 2.8: 3D square lattices coated with an **a**. acidic and **b**. neutral solution of DNA. Fibrous masses of DNA could be seen precipitating within the one treated with the neutral solution.

The DNA coated samples were then irradiated with UVC light to initiate the DNA crosslinking process. Three DNA coated lattices were placed on a PTFE mesh on a glass petri dish. Three lattices were used due to the small size of the UVC device (Analytik Jena UVGL-25). The lattices were irradiated with 254 nm UVC light, at a distance of 8mm from the lattices, for 60 minutes on the major face of the lattice (16 x 16 unit cells). Following that, they were flipped onto the other major face and irradiated for another 60 minutes. To remove any uncrosslinked DNA, all three lattices were added to 6 mL of 1X phosphate buffered saline (PBS) (Corning) and gently shaken for 30 minutes at room temperature. The lattices were then briefly rinsed in deionized water and then blow-dried with compressed air. After drying, the UVC irradiation was then repeated for another 60 minutes on each major face, for a total irradiation time of 240 minutes, to produce the "DNA-UVC" lattices.

2.6.3 eDNA-UVC Coating Methodology

The second approach utilizes electrostatic interactions to facilitate the DNA coating process described in the previous section (Fig. 2.9). DNA possesses negatively charged phosphate groups along its backbone, which can bind to positively charged

substrates [196]. One of the most commonly used cationic moieties is protonated amines, which have been used extensively in the literature to reversibly bind to DNA [197, 198].

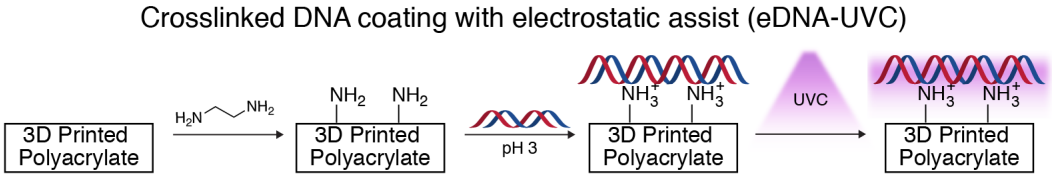

Figure 2.9: Schematic of eDNA-UVC coating. Surface amines were first installed by treating the 3D printed lattices with ethylenediamine. DNA coating is achieved by immersing the substrate in an acidic solution of DNA, followed by vacuum drying. The DNA coated substrate is then subjected to UVC irradiation to induce DNA crosslinking.

Amines were installed on the surfaces of the 3D printed lattices by treating them with neat ethylenediamine [199] (≥99%, Sigma Aldrich) at room temperature for 1 hour with gentle stirring. To ensure that all the ethylenediamine swollen in the polymer lattice is removed, the aminated lattices were soaked in methanol extensively after the treatment. This involved 4 x 30 minute soaks in methanol, followed by another 2 x 360 minute soaks in methanol. After each soak, the methanol was decanted and fresh methanol added. After all the soaks, the samples were dried under vacuum at room temperature for 10 hours to give the aminated lattices.

The aminated lattices were then coated with DNA in the exact same way as the first approach — soaked in an acidic DNA solution (pH 3, 2.5mg/mL) for 60 minutes, dried under vacuum for 180 minutes, and then subjected to the same UVC treatment of 240 minutes — to produce the "eDNA-UVC" lattices. It is important to note that the acidic DNA solution used here had a secondary function of protonating the surface amines.

2.7 Characterization of DNA Coatings

To evaluate the impact of amination on the coating process, we characterized both the untreated and aminated lattices *after* they were coated in DNA, but *prior* to UVC treatment using energy dispersive X-ray spectroscopy (EDS). The DNA coated lattices were first coated in 10 nm of carbon (Leica EM ACE600) and then imaged in an SEM (Zeiss 1550VP FESEM) equipped with an Oxford X-Max SDD EDS system. A low voltage of 5 kV was used to improve the surface sensitivity of the elemental maps.

2.7.1 DNA Coated Lattices

Fig. 2.10 shows the SEM images from untreated lattices coated with DNA and their corresponding phosphorous elemental maps.

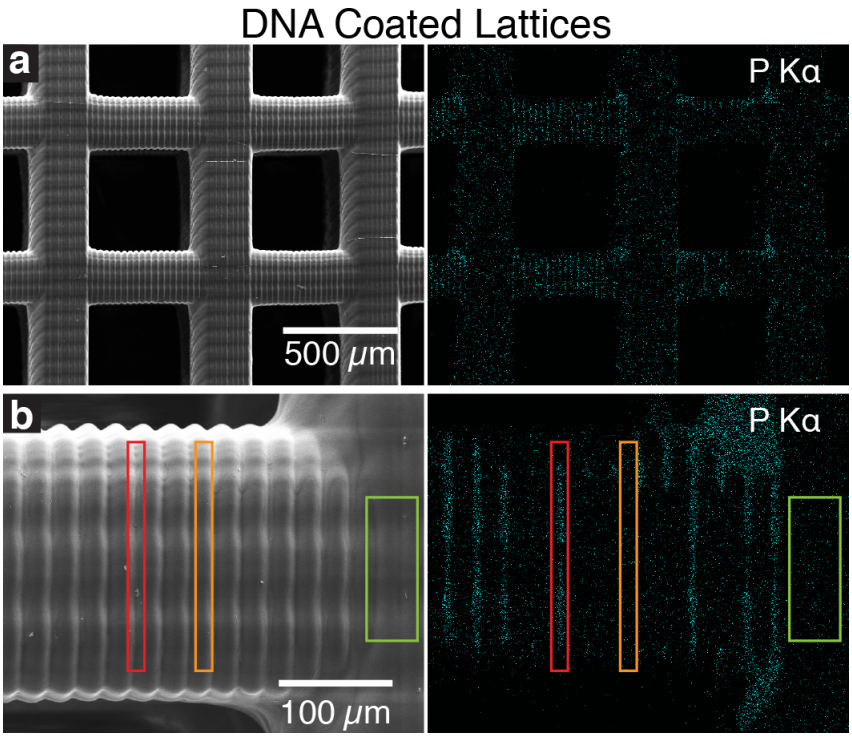

Figure 2.10: SEM images and their corresponding phosphorous elemental maps of untreated lattices coated with DNA. Outlined rectangles in red represent grooves on the beam, ones in orange correspond to the ridges on the beam, and green marks a node that contains a vertical beam.

The presence of phosphorous is indicative of DNA, as it is the only possible source of phosphorous at this point in the coating process. It is clear from the EDS analysis that that the DNA coating was inhomogeneous on the untreated lattices. Analysis of the different morphological features, highlighted by the red, orange, and green rectangles in Fig. 2.10b, indicates that DNA mostly accumulated in the grooves (red box) on the horizontal beams. These grooves were introduced by the 3D printing process, and are inevitable due to the layer-by-layer nature of the fabrication. No DNA was detected on the vertical beams (green rectangle) or on the ridges (orange rectangle) of the horizontal beams. The amount of phosphorous in the highlighted red region was approximately 8.8 at% (Fig. 2.11). The lattices were orientated in this particular direction to avoid any shadowing effects that would arise due to the presence of these grooves. Relative to the images in Fig. 2.10, the EDS detector was positioned directly north of them. It is currently unclear why the DNA only

segregates to the grooves. One possibility is that during the drying process, as the liquid interface recedes from the outside-in, its contact line is pinned on the grooves, resulting in deposition of DNA only in those regions.

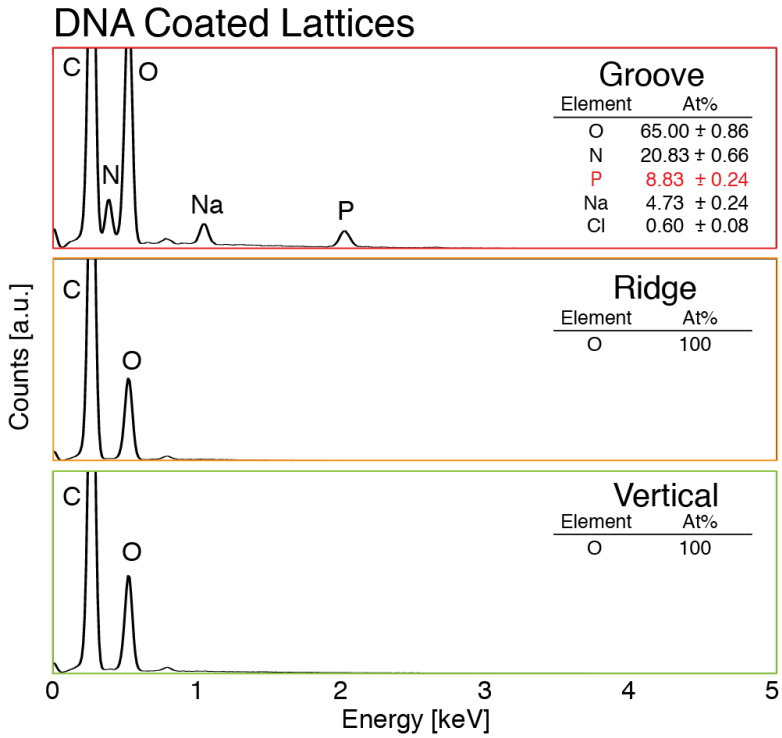

Figure 2.11: Elemental map spectra analysis of the different morphological features of the DNA coated lattices.

2.7.2 eDNA Coated Lattices

In contrast, the eDNA coated lattice had phosphorous distributed homogeneously throughout the structure (Fig. 2.12). The horizontal grooves (red rectangle) showed a similar amount of phosphorous as the DNA coated sample, at approximately 7.7 at%, with the ridges (orange rectangle) and the vertical beams (green rectangle) having 3.5 at% and 4.8 at% of phosphorous, respectively (Fig. 2.13). The increased amount of nitrogen detected is due to the presence of the primary amines on the surface and the amides formed during the amination reaction.

The chemical composition determined by EDS depends on the interaction volume, which implies that a lower amount of detected phosphorous corresponds to a thinner layer of DNA at these areas. That said, it is important to emphasize that the compositions determined should be treated as an approximation due to the inaccuracies associated with measuring light elements using EDS.

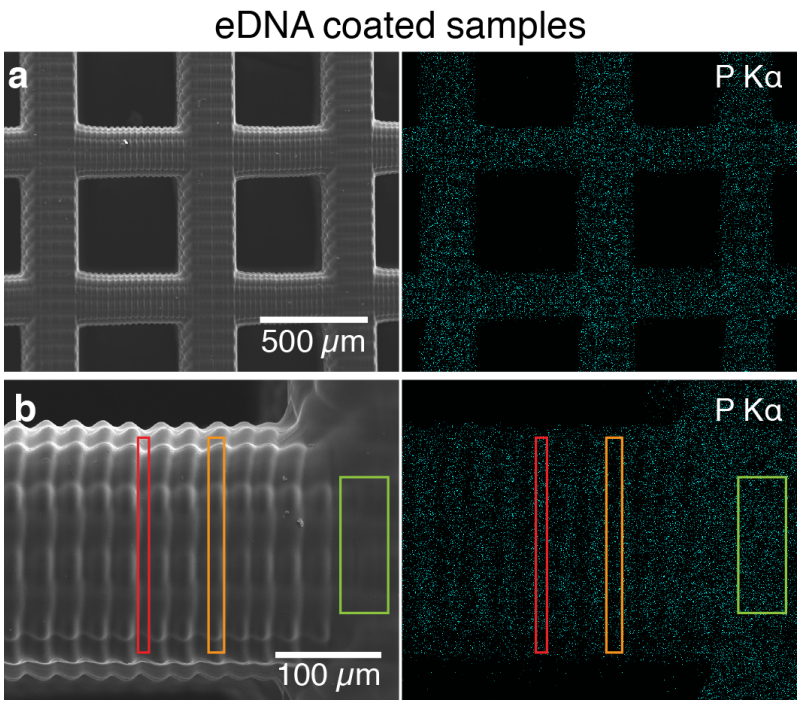

Figure 2.12: SEM images and their corresponding phosphorous elemental maps of aminated lattices coated with DNA. Outlined rectangles in red represent grooves on the beam, ones in orange correspond to the ridges on the beam, and green marks a node that contains a vertical beam.

However, the presence of phosphorous in both DNA and eDNA coated lattices indicates that both approaches successfully coated the 3D printed lattices with DNA, with the amination approach showing markedly more uniform DNA coverage.

2.8 Stability of DNA Coatings

The stability of the DNA coating is critical to the operation of the DNA-ChemoFilter. As such, we invested significant efforts to systematically investigate the amount of DNA leaching into solution.

2.8.1 Leaching Study Methodology

Lattices were first soaked in PBS at 37°C for 30 minutes while being vigorously shaken, then removed from solution and blow-dried with air, and soaked again in a fresh solution of PBS under the same conditions. This procedure was repeated two more times, for a total of 4 x 30-minute soaks. The PBS solutions were then stored for further measurements (DNA-PBS solutions). Following the last soak, the lattices were briefly rinsed with deionized water and then blow-dried with compressed air. Ultraviolet-visible (UV-Vis) spectroscopy (Agilent Cary 60) was used to determine

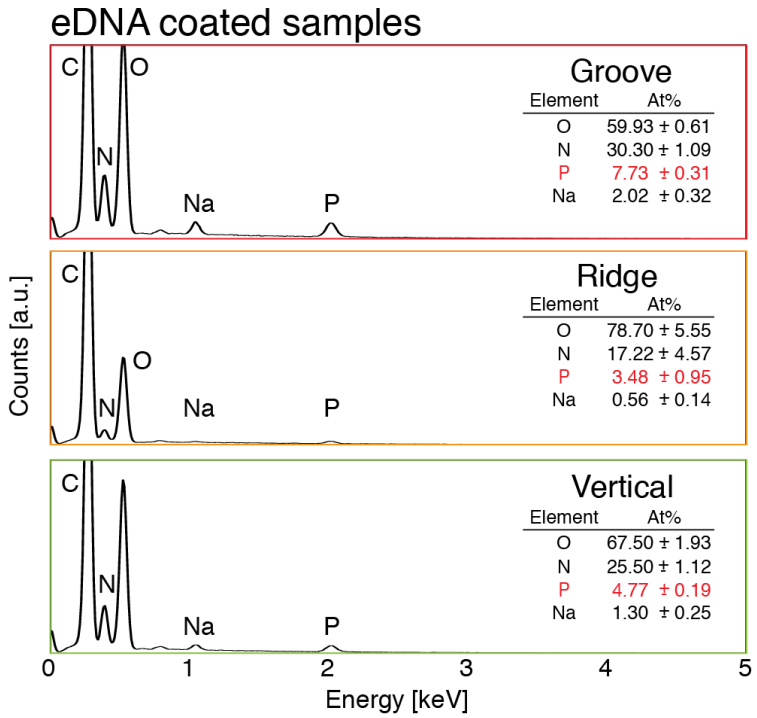

Figure 2.13: Elemental map spectra analysis of the different morphological features of the eDNA coated lattices.

the amount of DNA leached into the DNA-PBS solutions. Baseline measurements using PBS were first established and then used to obtain the spectra from the DNA-PBS solutions.

To determine the impact of UVC irradiation on the stability of these DNA coatings, we conducted the leaching studies on four different categories of samples: DNA (Control), eDNA (Control), DNA-UVC, and eDNA-UVC coated samples. The DNA (Control) and eDNA (Control) lattices were prepared using the exact same methodologies as their UVC-treated counterparts except they were exposed to ambient light in lieu of the two UVC irradiation steps. Three lattices were used each time, and soaked in 6 mL of PBS. Each treatment condition was tested three times (n=3). That is, in the case of the eDNA-UVC treatment, three separate *sets* of eDNA-UVC lattices were evaluated for their leaching parameters, with each *set* of lattices comprising 3 eDNA-UVC lattices.

2.8.2 Quantification Methodology of DNA Leached

Representative UV-Vis absorption spectra of the DNA-PBS solutions from the four different DNA treatment conditions are shown in Fig. 2.14 below. It is clear that there is a marked difference in the absorption spectra between the control lattices

(Fig. 2.14a, b) and the UVC irradiated ones (Fig. 2.14d, e), so much so that the y-axes have to be re-scaled significantly to even visualize it (Fig. 2.14e, f).

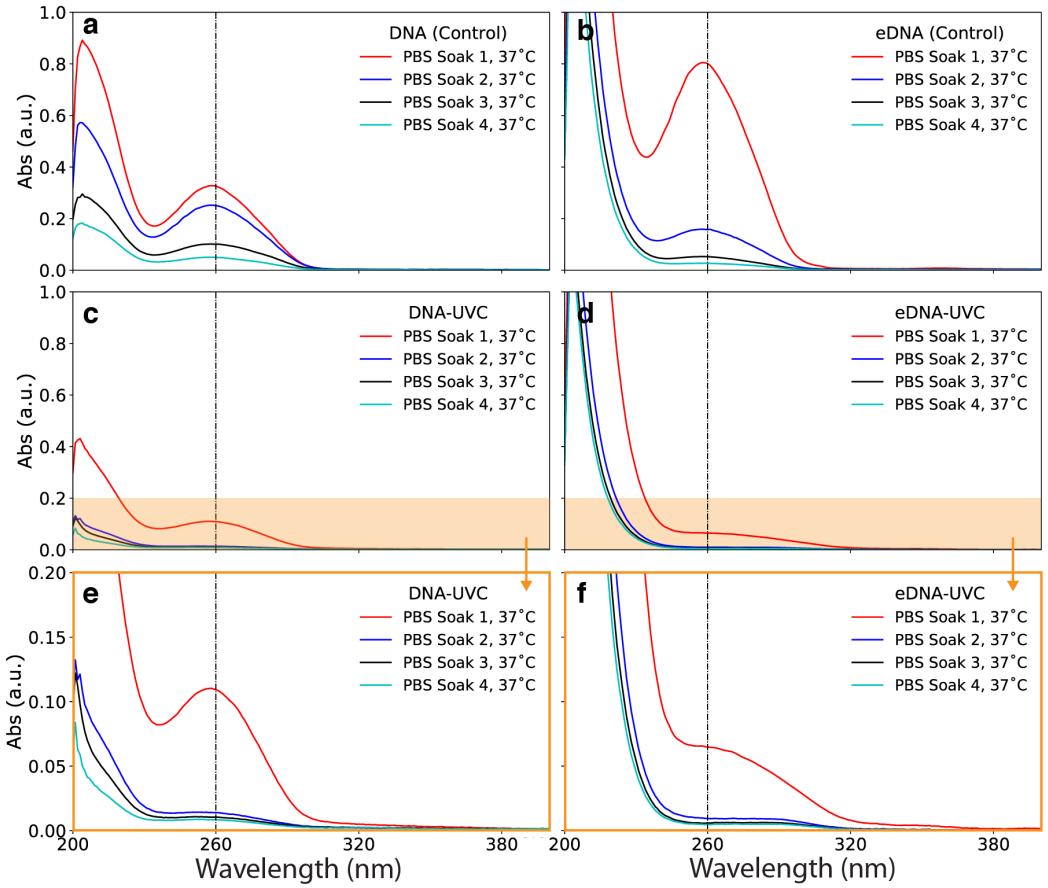

Figure 2.14: Representative UV-Vis absorption spectra of the DNA-PBS solutions from each treatment condition: **a**. DNA (Control), **b**. eDNA (Control), **c, e**. DNA-UVC, **d, f**. eDNA-UVC. Subfigures **e** and **f** are the zoomed in orange sections from **c** and **d** respectively.

The dotted lines at 260 nm are a guide to the eye as to what the measured absorbances at 260 nm (A_{260}) are. Interestingly, unlike the other spectra, the 260 nm points for the eDNA-UVC spectra are not at a local maxima, which would be expected for DNA. Despite this, it was still assumed that the absorptions at 260 nm were still due to DNA. This would give us an upper bound as to the DNA leached.

The amount of DNA in the DNA-PBS solutions was quantified by correlating the A_{260} to the concentration of DNA using a calibration curve (Fig. 2.15). The calibration curve was constructed by determining the A_{260} of PBS solutions with known concentrations of DNA.

To ensure that the measurements accurately reflected just the concentration of DNA in solution, we have to correct for any contributions to absorbance from the untreated

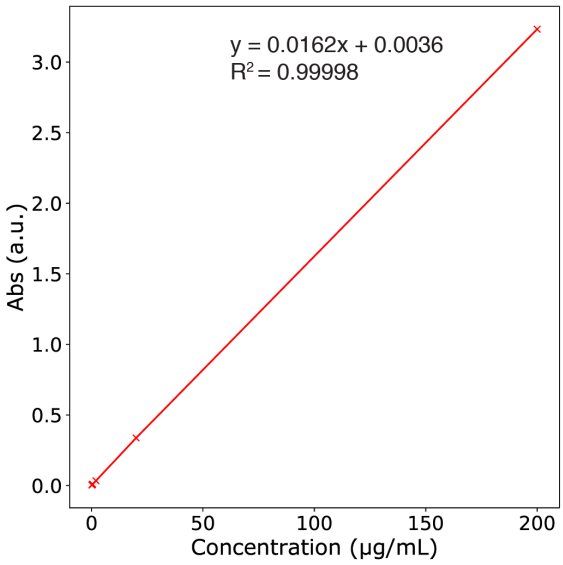

Figure 2.15: DNA quantification calibration curve. Concentrations of 200, 20, 2, 0.5, 0.4 μg/mL were used to construct this curve.

and aminated lattices themselves. Thus, the leaching study was also conducted on UVC-only and amine-UVC lattices. The UVC-only samples were untreated lattices (no exposure to DNA) that were treated with the same UVC irradiation treatment. And the amine-UVC samples were aminated samples (no exposure to DNA) that were also treated with the same UVC irradiation treatment.

Representative absorption spectra from the UVC-only and the amine-UVC lattices are shown in Fig. 2.16. For the UVC-only lattices, virtually no signal can be seen, even after rescaling the y-axis to 0.2. For the amine-UVC lattices, a small signal can be seen after rescaling the y-axis. It is interesting to note that the amine-UVC spectra look similar to that of the eDNA-UVC spectra.

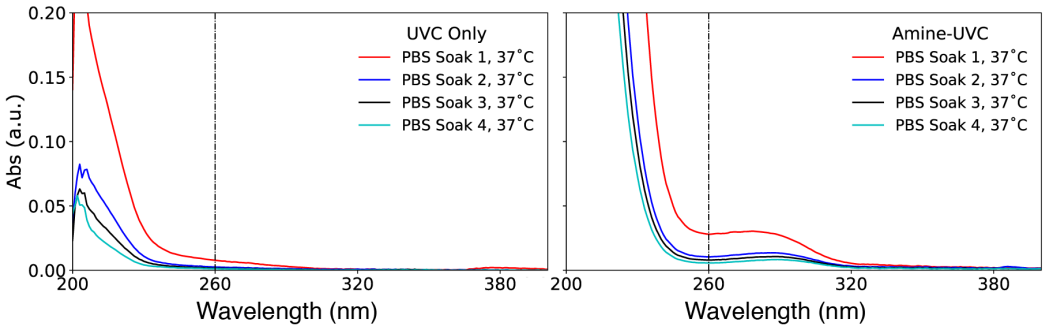

Figure 2.16: Representative UV-Vis absorption spectra of the PBS solutions from the UVC-only (left) and amine-UVC lattices (right). Note that the y-axes have been set to 0.2.

The A_{260} values for the UVC-only and amine-UVC spectra were determined and then converted to background "DNA" via the calibration curve in Fig. 2.15. These background "DNA" values were then used to correct for the actual amount of DNA leached. For example, the average A_{260} from the amine-UVC lattices were converted to background "DNA" and then subtracted from the average DNA values from the eDNA (Control) and eDNA-UVC lattices. The error-propagated standard deviation was determined from the standard deviations in the DNA leached from the treated samples and its associated background “DNA” baseline.

2.8.3 Analysis of DNA Coating Stability

Fig. 2.17 shows the corrected amount of DNA leached per mm^2 of 3D printed lattice (ng of DNA/mm^2) over the multiple PBS soaks.

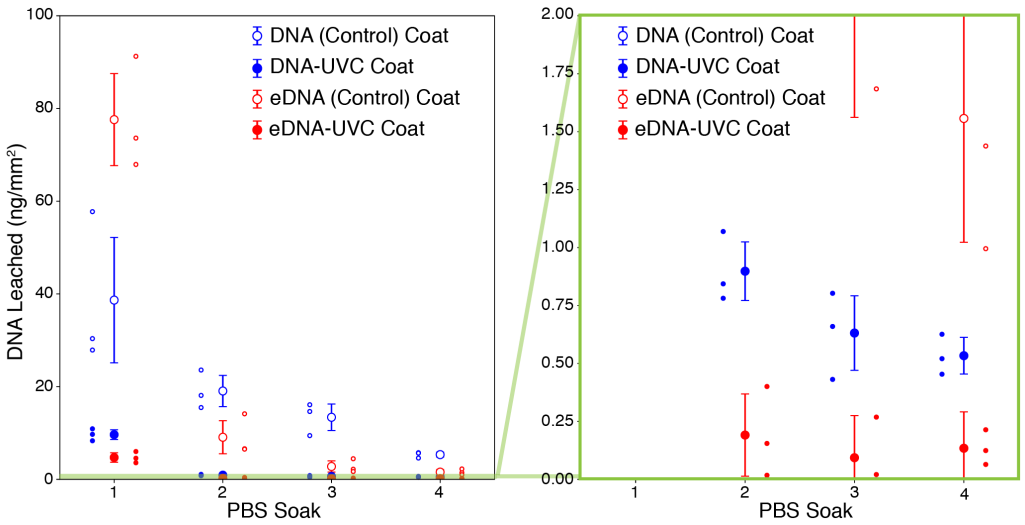

Figure 2.17: Amount of DNA leached normalized by surface area of lattice over multiple PBS soaks, as determined by UV-Vis spectroscopy. Data points (shown) and error bars correspond to the mean and error-propagated standard deviations of the set (n = 3). Plot on the right contains a zoomed-in section of the original plot, outlined by the green rectangle, which shows that all UVC treated samples show a considerable decrease in the amount of leached DNA (< 1 ng/mm^2).

As would be expected, without the UVC-induced crosslinking, both types of control lattices leached a considerable amount of DNA over the four soaks, with the eDNA (Control) lattices leaching a total of 91.0 ± 10.6 ng of DNA/mm^2 and the DNA (Control) lattices - 76.4 ± 14.2 ng of DNA/mm^2 (all values are mean ± error-propagated standard deviation, and refer to the mass of DNA leached per mm^2 of 3D printed lattice).

The greater amount of leaching from the eDNA (Control) lattices is consistent with its more extensive DNA coverage (Fig. 2.10, 2.12). The eDNA (Control) lattices leached DNA at a much faster rate than the DNA (Control) ones, losing 85% of the total leached amount in the first soak, compared with 51% for the latter. This may be a result of competitive binding of the phosphate anions present in PBS with the surface functionalized amines [200], driving DNA desorption. By the fourth soak, the eDNA (Control) lattices leached 1.6 ± 0.5 ng of DNA/mm^2, more than 4x less than 5.3 ± 0.5 ng of DNA/mm^2 for the DNA (Control) ones.

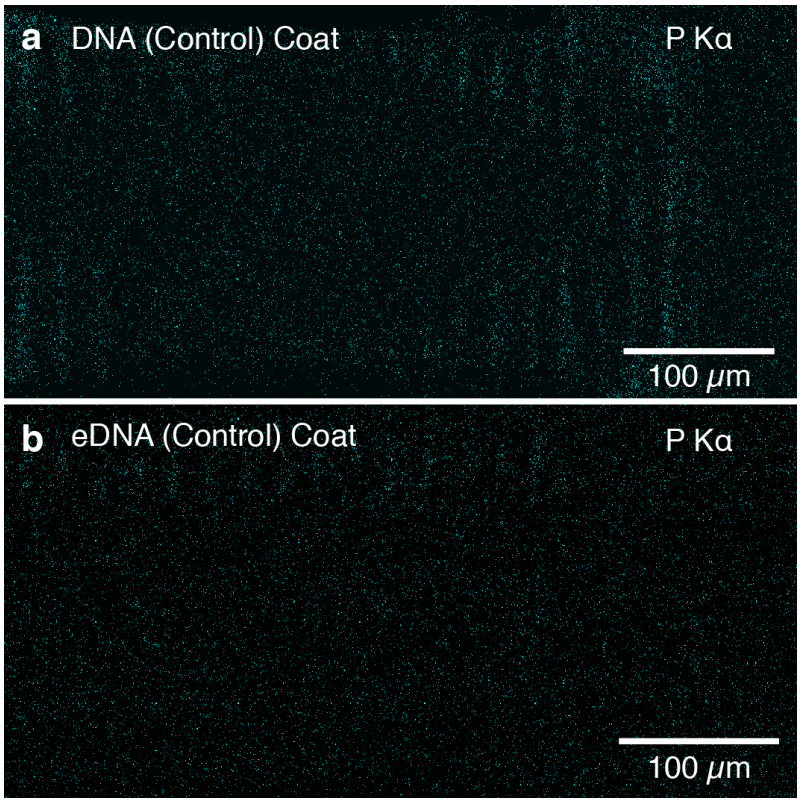

Figure 2.18: Phosphorous elemental map of **a**. DNA (Control) and **b**. eDNA (Control) lattices after the leaching study.

EDS elemental mapping conducted on both types of control lattices after the leaching experiments (Fig. 2.18) indicated that this was due to the difference in the DNA coatings left on the surface. Phosphorous could only be found sporadically on the edges of some horizontal beams of the eDNA (Control) lattices, whereas it could still be clearly seen in some grooves of the horizontal beams in the DNA (Control) lattices — implying the persistence of some DNA on the DNA (Control) lattices, but not on the eDNA (Control) ones.

In contrast, the UVC irradiated lattices leached considerably less DNA than their

unirradiated controls (Fig. 2.17). The eDNA-UVC and DNA-UVC lattices leached a total of 5.1 ± 1.1 and 11.7 ± 1.1 ng of DNA/mm^2 respectively over the four soaks. This implies that the UVC treatment was successful in producing insoluble crosslinked DNA coatings. The eDNA-UVC coated lattices leached about half that of the DNA-UVC lattices, possibly implying that the additional electrostatic interactions helped to further improve the stability of these crosslinked films.

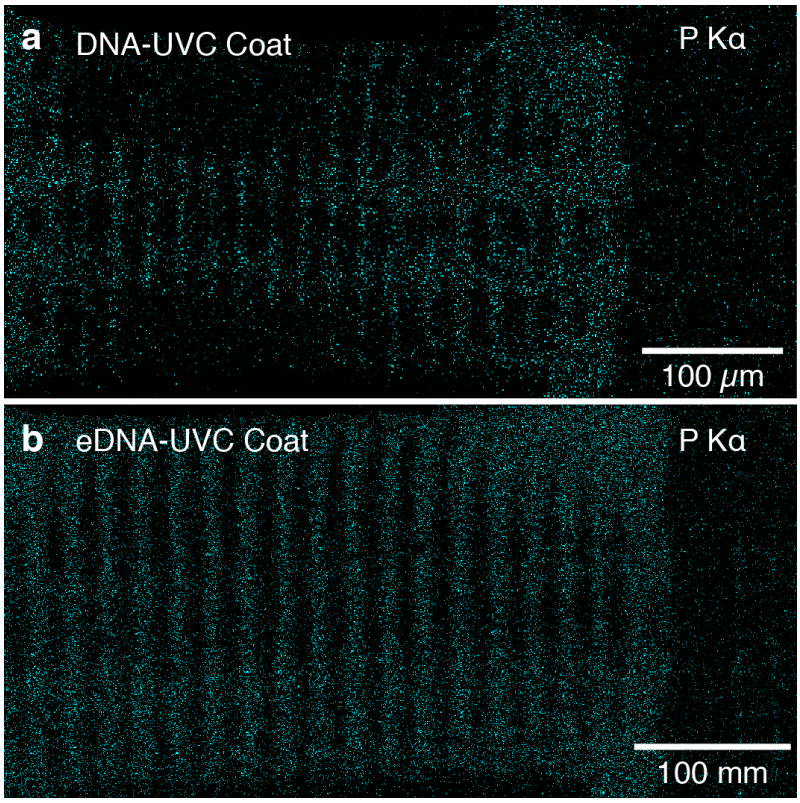

Figure 2.19: Phosphorous elemental map of **a**. DNA-UVC and **b**. eDNA-UVC lattices after the leaching study.

EDS elemental mapping of the irradiated lattices post-leach shows clear evidence of phosphorous remaining on the lattices (Fig. 2.19). The DNA-UVC phosphorous map post-leach (Fig. 2.19a) resembled that of the as-coated samples (Fig. 2.10). However, the eDNA-UVC phosphorous map showed that phosphorous was now *only* present on the grooves of the horizontal beams and at the junctions between the horizontal and vertical beams (Fig. 2.19b). There was no phosphorous on the ridges of the horizontal beams and on the lattice nodes, implying that the coatings at those regions were likely not sufficiently crosslinked to prevent leaching into solution. It is interesting to note that despite the differences in the initial coating coverage for the eDNA and DNA coated samples, the eDNA-UVC and DNA-UVC samples

looked relatively similar after the leaching studies — Only the DNA on the grooves of the horizontal beams were left after the extensive soaking process. It is currently unclear why this is the case, and is a subject of ongoing investigation.

That notwithstanding, despite the larger amount of DNA present, the eDNA-UVC and DNA-UVC samples only leached 0.1 ± 0.2 and 0.5 ± 0.1 ng of DNA/mm^2 respectively at the end of the leaching experiments. This further highlights the stability of these UVC crosslinked DNA coatings. From the decreasing amount of DNA leached with each soak, it would be expected that subsequent soaks in PBS would also give approximately the same low values of DNA leached. The non-physical values obtained from the leaching studies for the eDNA-UVC samples were due to error propagation in the standard deviation (cf. Section 2.8.2).

As described earlier, the amount of DNA leached is an important metric of success since the long-term impact of cell-free foreign DNA in the body is still relatively unknown. The evaluation and reduction of DNA leaching is thus crucial in the translation of these DNA-based ChemoFilters from bench top to clinical application. While a finite amount of DNA was leached from our materials, it is worth noting that cell-free DNA is already present in our bodies, with cancer patients having anywhere between 0-5 and > 1000 ng/mL of blood [201]. In the future, this might provide us with some bounds as to what is acceptable in the human vascular system.

2.9 *In Vitro* Evaluation of Drug Capture

The doxorubicin binding capacity of the functionalized lattices were tested in PBS at 37°C. Prior to these tests, the lattices were all subjected to 4 x 30 minutes PBS soaks at 37°C, as described in the previous section, to minimize the amount of DNA that would leach into solution during the drug-binding process.

2.9.1 Doxorubicin Binding Methodology

The doxorubicin solution was prepared as follows: a 1 mg/mL stock solution of doxorubicin (doxorubicin hydrochloride salt (>99%, LC Laboratories)) in water was first prepared and vortexed to ensure complete dissolution. 1 mL of this stock solution was then added to 19 mL of PBS to give the doxorubicin testing solution of concentration 0.05 mg/mL. 7.7 mL of solution was used as the testing volume. A 0.7 mL aliquot of solution was drawn as the initial 0 minute time point. The remaining doxorubicin solution (7 mL) was then warmed up to 37°C before three samples were added in, and then shaken at 200 RPM. Aliquots of 0.7 mL were then drawn at the 10 and 20 minute mark. From each 0.7 mL aliquot, 3 x 0.1 mL were drawn and

placed in a 96-well microplate. The concentrations of doxorubicin in each well were then measured by way of fluorescence on a microplate reader (Molecular Devices Flexstation 3). The measurement parameters were as follows: λ_{ex} = 480 nm, λ_{em} = 550 - 590 nm, $\lambda_{cut-off}$ = 530 nm, sensitivity = 100. Each treatment condition was tested three times (n = 3). That is, in the case for the eDNA-UVC treatment, three separate *sets* of eDNA-UVC lattices were evaluated for their doxorubicin binding capacities, with each *set* of lattices comprising 3 eDNA-UVC lattices.

2.9.2 Quantification Methodology of Doxorubicin Bound

The measured fluorescence intensity at 590 nm was correlated to the concentration of doxorubicin in PBS via the use of a calibration curve (2.20).

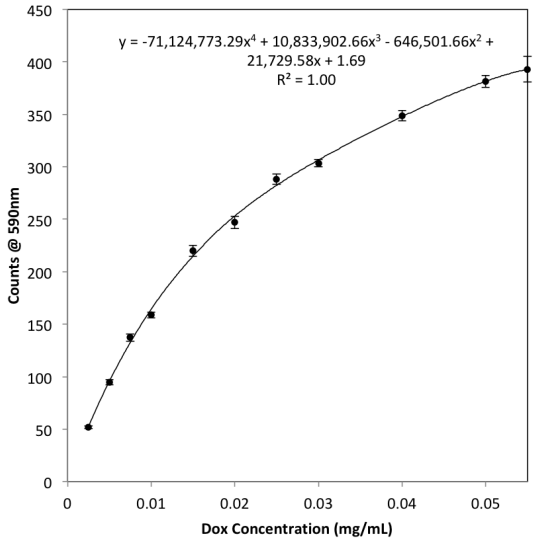

Figure 2.20: Doxorubicin calibration curve. Points represent the mean of the three measurements. Error bars here represent the standard error of measurement (n = 3).

The calibration curve was constructed by determining the fluorescence intensity at 590 nm of PBS solutions with known concentrations of doxorubicin. 3 x 100 μL of each of these solutions were placed in a 96-well microplate. The fluorescence of each well was then measured in the same way. The average of the three measurements was calculated and the standard deviation determined. Note: the standard deviation here represents the standard deviation of the measurement. A 4th order polynomial fit was used to construct the calibration curve. To determine the concentration of doxorubicin from a known count value, the polynomial was solved using Python (numpy.roots function).

2.9.3 Analysis of Doxorubicin Binding Capacities

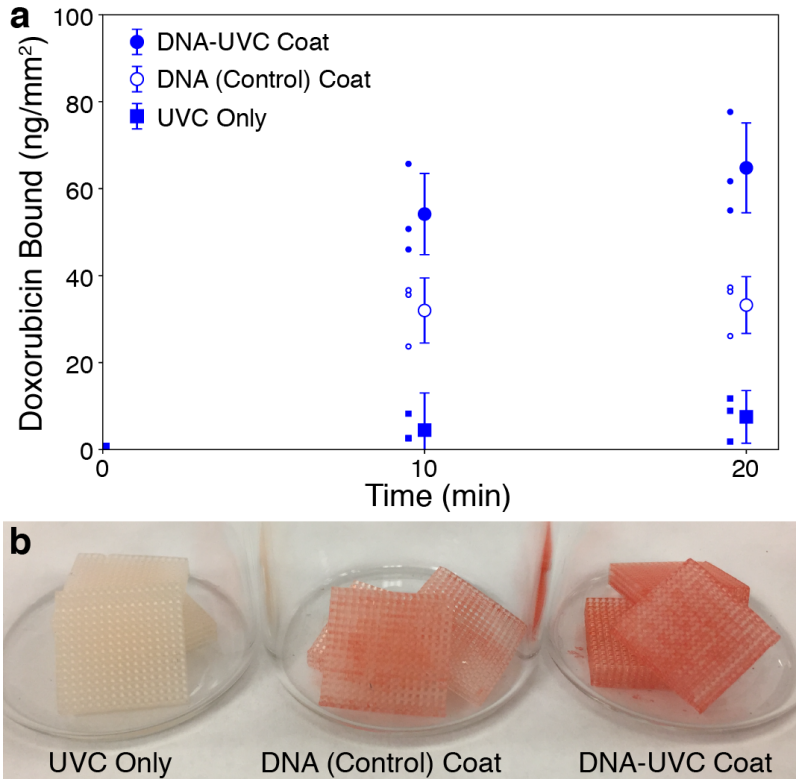

Figure 2.21: Doxorubicin capture in PBS. **a**. The cumulative amount of doxorubicin bound over 20 minutes, as determined by fluorescence, normalized by surface area for the DNA-UVC lattices and its associated controls. All points and error bars show the mean and error-propagated standard deviations of the set (n = 3). Each individual data point in the set is also shown. **b**. Resulting lattices from the doxorubicin binding experiments for the DNA-UVC lattices and its controls.

Figure 2.21a shows that the DNA-UVC lattices bound a total of 64.8 ± 10.3 (mean ± error-propagated standard deviation) ng of doxorubicin/mm^2 of 3D printed lattice (ng of doxorubicin/mm^2) in 20 minutes from a 0.05 mg/mL solution of doxorubicin in PBS at 37°C. This is almost double that of the DNA (Control) lattices, which bound 33.2 ± 6.5 ng of doxorubicin/mm^2. These results are consistent with the greater amount of DNA left on the DNA-UVC lattices compared to the DNA (Control) ones after the PBS soaks (Fig. 2.18, 2.19). As an additional control, we also tested lattices that were UVC-treated but not coated in DNA. These UVC-only lattices exhibited very low binding capacities of 7.5 ± 6.1 ng/mm^2, likely due to nonspecific physical adsorption. The extent of drug capture is easily visible: doxorubicin is a bright red drug, and the DNA coated lattices are slightly off-white. Fig. 2.21b clearly demonstrates the increasing extent of red staining: DNA-UVC > DNA (Control) > UVC only, which is consistent with the binding capacities observed. For the DNA

treated lattices, the underlying white substrate can still be seen amongst the red regions, which is due to the inhomogeneous DNA coatings observed without the amination treatment.

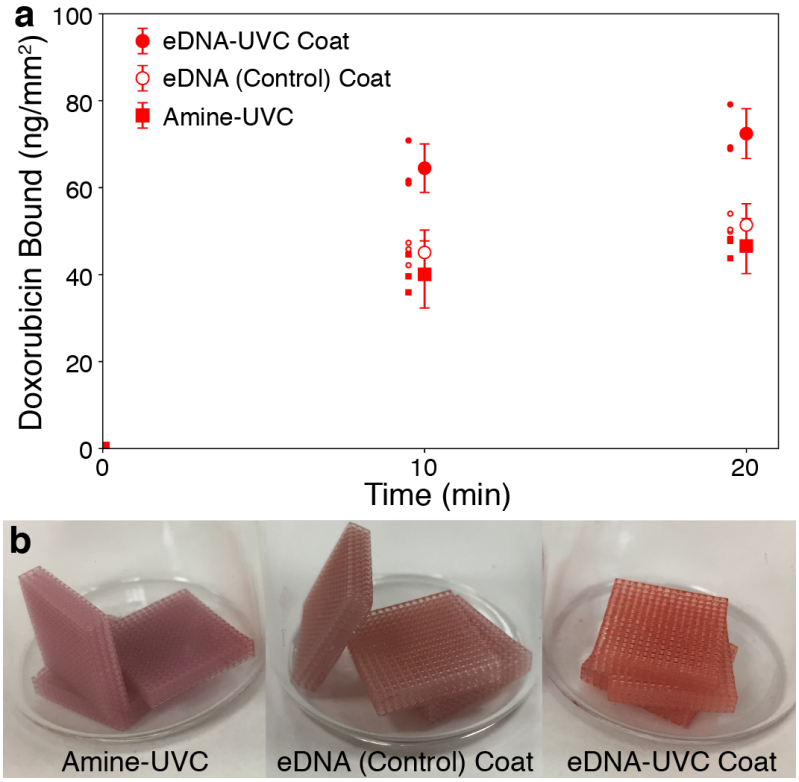

Figure 2.22: Doxorubicin capture in PBS. **a**. The cumulative amount of doxorubicin bound over 20 minutes, as determined by fluorescence, normalized by surface area for the eDNA-UVC lattices and its associated controls. All points and error bars show the mean and error-propagated standard deviations of the set (n = 3). Each individual data point in the set is also shown. **b**. Resulting lattices from the doxorubicin binding experiments for the eDNA-UVC lattices and its controls.

The aminated set of lattices showed a different trend (2.22a): the eDNA-UVC lattices bound 72.4 ± 5.7 ng of doxorubicin/mm^2, compared with 51.4 ± 4.9 ng of doxorubicin/mm^2 for the eDNA (Control) lattices. The considerable amount of doxorubicin bound by the eDNA (Control) lattices, despite the lack of DNA on the surface (2.18), can be explained by looking at the results of the amine-UVC controls.: amine-UVC lattices bound 46.6 ± 6.3 ng of doxorubicin/mm^2. Visual observations of the three different treatment conditions, as shown in Fig. 2.22b, indicated that the amine-UVC and eDNA (Control) coat lattices both turned a pale purple after the doxorubicin binding experiments. These results indicated that the binding of doxorubicin in the eDNA (Control) lattices were due to the surface amines. In

contrast, the eDNA-UVC lattices still turned red, albeit a darker shade of red than their DNA-UVC counterparts.

Doxorubicin is known to turn purple either under basic conditions [202] or when complexed with transition metal cations [203]. Since the doxorubicin tests were conducted in PBS, and the lattices had already been soaked in PBS for an extensive amount of time prior, it is reasonable to assume that the primary amines on the surface were completely protonated. It is thus unlikely that the observed purple color was due to pH changes. Furthermore, doxorubicin degrades rapidly in basic conditions, turning colorless over time [204]. However, the purple colors of these lattices persisted for months. All of these results strongly suggest that the purple color is likely due to the formation of a complex between the protonated surface amines on the lattices and doxorubicin. The darker red color seen in the eDNA-UVC lattices can then be attributed to a combination of red and purple from the regions with and without DNA respectively (Fig. 2.19), suggesting a mixed-mode binding.

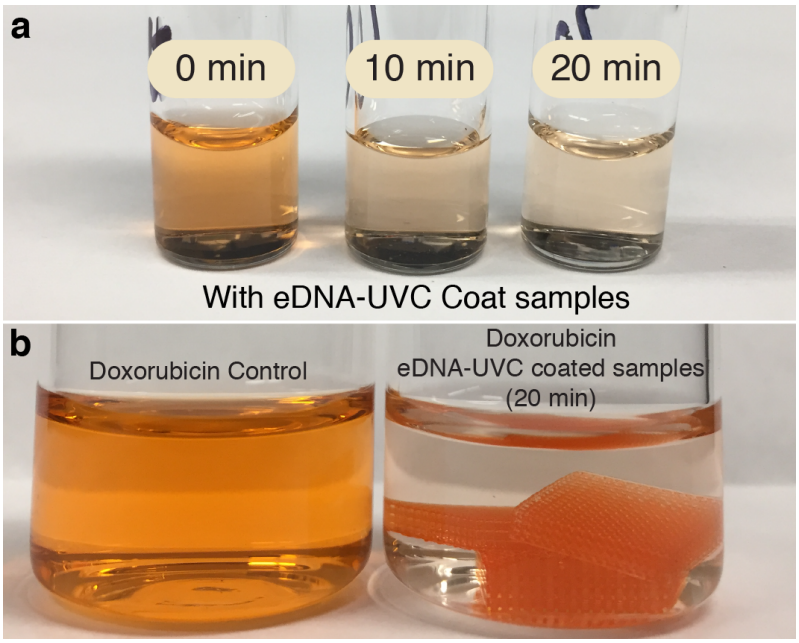

Figure 2.23: **a**. Color of the doxorubicin solution at various time points of the doxorubicin binding experiments. **b**. Comparison of color between the initial doxorubicin solution and the solution 20 minutes after the eDNA-UVC lattices have been introduced. The lattices also turned from white to red.

The results across both the DNA and eDNA sets of lattices indicated that the combination of DNA coating and UVC treatment was the most effective in fabricating stable coatings capable of capturing doxorubicin from PBS. Visual tracking of the doxorubicin solution after the introduction of the lattices further

confirmed this, with the red intensity of doxorubicin decreasing over time (Fig. 2.23a), and a concurrent red staining of the off-white samples (Fig. 2.23b).

From the DNA leaching studies and the doxorubicin binding experiments, it is clear that both approaches resulted in DNA coated structures that could bind to doxorubicin *in vitro* while barely releasing any DNA (<1 ng of doxorubicin/mm^2) into solution. However, the role that amination plays in this process is still relatively unknown. It is not immediately clear how amination reduces the amount of DNA leached (Fig. 2.17). And despite the increased coverage of DNA on the eDNA-UVC lattices as compared to the DNA-UVC lattices (Fig. 2.19) and the amine complex effect, the eDNA-UVC lattices still bound a comparable amount of doxorubicin as the DNA-UVC lattices. While this likely implies that the quality of the DNA in the eDNA-UVC lattices were lower than that of the DNA-UVC lattices, it still needs to be experimentally validated. A more in-depth characterization of the DNA coatings is currently underway.

2.10 Summary and Outlook

We demonstrate two viable approaches to fabricating stable genomic DNA coated 3D printed polymeric square lattices that are capable of capturing doxorubicin from solution. The coatings were achieved via the simple immersion of untreated or aminated 3D square lattices into an acidic DNA solution, followed by vacuum drying and UVC irradiation. UVC irradiation was critical in creating stable crosslinked DNA coatings that were resistant to leaching while still capturing doxorubicin from solution. The DNA-UVC samples leached 0.5 ± 0.1 ng of DNA/mm^2 and captured 64.8 ± 10.3 of doxorubicin/mm^2 of 3D printed material. In comparison, the eDNA-UVC samples leached 0.1 ± 0.2 ng of DNA/mm^2 and captured 72.4 ± 5.7 of doxorubicin/mm^2 of 3D printed material.

There are a few approaches to improving the performance of these materials. The intensity of UVC irradiation could be increased to enhance crosslinking. Multiple coats of DNA could be used to increase the amount of DNA on the structures. Understanding how the DNA coats the surface could also provide some insight on how we can tune the design of the structure to improve the coating coverage on them. Once these have been investigated and optimized to ensure minimal DNA leaching, the surface area can be increased to further improve total binding capacity.

While we have demonstrated the ability of these structures to bind to doxorubicin in PBS in this preliminary study, there is still a long way to go before these devices

can be used outside of a laboratory setting. For one, more still needs to be done to determine the true efficacy of these devices. PBS is the simplest physiologically relevant solution — the binding capacity of these coated structures still needs to be determined in more complex solutions like human serum and human blood. Furthermore, the performance of these structures under dynamic flow conditions also needs to be studied to determine the true binding kinetics of these devices. *In vivo* animal studies are also needed to determine the safety and viability of these DNA-ChemoFilters as a chemotherapy procedure. In particular, these animal studies will help elucidate the impact of deoxyribonuclease on the operation of these DNA-based ChemoFilters.

There is also lot of potential in utilizing the genomic DNA coating methodologies developed here on other substrates. For example, flexible substrates such as Nitinol or elastomers open up the possibility of deployable ChemoFilter devices, minimizing the invasiveness of the insertion procedure. While further development is needed, we believe that this work will provide a platform for DNA-based 3D printed materials for chemotherapy applications that are inexpensive and simple to fabricate. The reduction of off-target toxicity in chemotherapy from a device approach has immense implications, and has the potential to improve how we manage cancer. This concept of drug capture can also be extended to tackle other problems in medicine that have to contend with off-target toxicities.

More generally, this work demonstrates the utility of surface chemistry in fabricating architected functional materials. It allows us to exploit the printability and accessibility of commercially available materials, while still imbuing chemical functionality for more advanced applications. This partially simplifies the process for fabricating functional polymer structures, making it more accessible to the greater scientific community.

Chapter 3

FUNCTIONAL MONOMER SYNTHESIS VIA THIOL-MICHAEL ADDITION FOR TWO-PHOTON LITHOGRAPHY

Chapter Abstract

The previous chapter demonstrated the utility of surface functionalization to imbue functionality onto commercially available structural polymers. Surface chemistry is a powerful synthesis tool, but has its limitations — often, it is necessary to have control over the chemical functionality in the volume of the polymer as well. In this chapter, we discuss how the use of thiol-Michael addition can be a facile and accessible method for the synthesis of functionalized acrylates, which can then be used with two-photon lithography to fabricate functional micro-architected materials. We demonstrate the compatibility of this technique with a wide variety of functional groups and highlight some potential applications of these materials.

This chapter has been adapted with permission from:

1. Yee*, D. W., Schulz*, M. D., Grubbs, R. H. & Greer, J. R. Functionalized 3D Architected Materials via Thiol-Michael Addition and Two-Photon Lithography. *Advanced Materials* **29,** 1605293. doi:https://doi.org/10.1002/adma.201605293 (2017).

Contributions: participated in the conception of the project, fabricated and characterized the structures, conducted the Orange II assay, prepared the data, and wrote the manuscript.

3.1 Functional Polymers for Two-Photon Lithography

Two-photon lithograpy (TPL) is one of the most powerful tools available today for creating complex, small-scale architected materials [101, 205]. By focusing a femtosecond pulsed laser into a photoresist, reactions such as polymerization can be locally induced within the focal region of the beam. Moving the laser focus in three dimensions then enables the creation of polymer structures with virtually any geometry.

The high resolutions acheivable by TPL make it one of the best AM techniques to explore and probe phenomena that only happen at the micron to sub-micron length scales. For example, in photonics, the ability to fabricate materials with periodic and topologically defined nano-sized features has allowed for the precise control and manipulation of light-matter interactions in materials [118, 120]. In tissue engineering, the use of architected 3D cell culture scaffolds, with characteristic dimensions on the order of that of the cells, has been incredibly useful in instructing cell behavior, and also answering fundamental question on how cells behave [206, 207]. The precise control of topology in architected materials has also enabled the fabrication of lightweight materials with unprecedented mechanical properties [45, 107, 108].

Up until recently, the TPL field has largely relied on commercially available photopolymers, that only have structural functionality, in the fabrication of these architected materials. This was a deliberate choice as it made it clear that any emergent/enhanced material property observed was solely due to the architecture, without any contribution from the inert constituent polymer. However, as the field has matured and a greater understanding of architecture has emerged, there has been a surge of interest in architecting *functional* materials instead [208, 209]— if we can already achieve so much with inert materials, imagine the potential with functional materials.

As discussed in the previous chapter, surface functionalization is a powerful tool for fabricating functional architected materials. However, for certain applications, it is necessary to have control over the functionality within the volume of the 3D structures as well. One approach that is commonly taken is the addition of functional nanoparticles into the photoresin, which then get incorporated into the structure during the photopolymerization process. Structures with magnetic [210], luminescence [211], and electrical [212] properties have been fabricated in this fashion. While simple, the drawback with this method is that agglomeration of

these particles interferes with the ability of the laser to penetrate into the resin, limiting the doping concentration of these nanoparticles [213]. The scattering of light from these nanoparticles also limits the resolutions and sizes of the structures that can be fabricated.

In recent years, with influence from the polymer chemistry community, the field has started to pivot towards directly synthesizing monomers with the functional groups of interest instead. This is significantly more efficient and also allows for a much broader range of functionalities — structures with unique properties such as photoreactive surfaces [214], stimuli-responsiveness [215], intrinsic chemical sensing [216], and actuation [217] can now be fabricated. However, these functional monomers are often challenging to synthesize, requiring a controlled atmosphere, and/or a complex, multistep synthesis.

In this chapter, we show how click chemistry, the thiol-Michael addition reaction in particular, can provide a facile method for the synthesis of a wide variety of functionalized acrylates. We demonstrate the compatibility of these functionalized acrylates with two-photon lithography and highlight some of their potential applications.

3.2 Click Chemistry

Click chemistry provides an alternative facile route to the synthesis of functional monomers. Coined by K. Barry Sharpless in 2001, click chemistry encompasses a class of reactions that are: a) modular, b) give high yields, c) generate only inoffensive byproducts that can be removed by nonchromatographic methods, d) stereospecific, and e) orthogonal to many other common organic synthesis reactions. The process should also: a) be insensitive to oxygen and water, b) use readily available starting materials and reagents, c) use no solvent or a solvent that is benign or easily removed, and d) have simple product isolation [218]. The strict criteria outlined mean that only a handful of reactions have been identified as click reactions, such as the copper(I)-catalyzed azide-alkyne cycloaddition [219], strain-promoted azide alkyne cycloaddition [220], sulfur(VI) fluoride exchange [221], thiol-ene, and thiol-Michael addition [222][1].

The simplicity of these click reactions has made synthesis and chemical modification significantly more accessible to the general scientific community, and has allowed

[1] I strongly encourage the reader to refer to [223] for an excellent discussion on the application of click chemistry in materials science.

for the rapid discovery of new functional materials [223].

3.3 Thiol-Michael Addition

The thiol-Michael addition, in particular, is well suited for use in synthesizing functional monomers for vat photopolymerization. Broadly speaking, the Michael addition reaction is the reaction of a nucleophile, in the presence of a catalyst, to an α,β-unsaturated carbonyl. As the name implies, in the thiol-Michael addition, the nucleophiles used are thiols or thiolate anions [224]. But what makes the reaction particularly appealing is that acrylates, one of the most commonly used monomers in vat photopolymerization, are by definition, α,β-unsaturated carbonyls — making this reaction applicable to reagents that are immediately compatible with vat photopolymerization, and by extension, two-photon lithography. The reaction pathway for the base- and nucleophile-catalyzed thiol-Michael addition for acrylates is shown in Fig. 3.1 below.

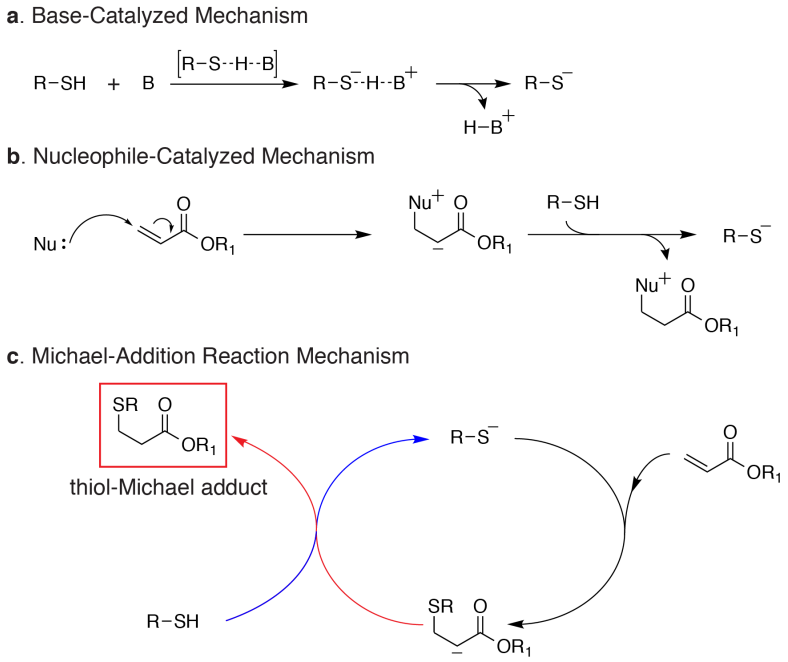

Figure 3.1: Thiol-Michael addition reaction mechanism. **a**. Base- and **b**. nucleophile-catalyzed reaction pathway for the generation of the thiolate anion. **c**. Thiol-Michael addition of the thiolate anion to the acrylate.

3.4 Functionalized Acrylates Synthesis

To demonstrate the versatility of this method, we used a variety of thiols to produce acrylates with different functionalities. As our substrate, we chose pentaerythritol tetraacrylate (PETTA) as it is one of the most widely used monomers in TPL. Nine

different thiols that encompassed a wide range of chemical functionalities were used: 2,3,4,5,6-pentafluorothiophenol (97%), 2-(Boc-amino)ethanethiol (97%), 1-octanethiol (>98.5%), (3-mercaptopropyl) trimethoxysilane (95%), 3,3,4,4,5,5,6,6,7,7,8,8,8-tridecafluoro-1-octanethiol (97%), benzyl mercaptan (99%), N-(tert-butoxycarbonyl)-l-cysteine methyl ester (97%), 2-mercaptoethanol (>99%), and 2,2,2-trifluoroethanethiol (95%).

The general procedure for the synthesis is as follows:

3.4.1 General Procedure

Pentaerythritol tetraacrylate (1.0 equiv., 3 g, 8.51 mmol), thiol (1.0 equiv., 8.51 mmol), and hexylamine (0.1 equiv., 0.112 mL, 0.85 mmol) were added to a 20 mL scintillation vial. The reaction mixture became warm and homogeneous within 2 min, and was stirred at 40 °C for 14 h. ^{1}H and ^{13}C nuclear magnetic resonance (NMR) was used to verify the completion of the reaction. The product was used without any further purification.

All the chemicals used in the reaction were acquired from Sigma-Aldrich, and were used as received without further purification.

3.4.2 Product Analysis

Fig. 3.2 shows the chemical structure of the functional acrylates synthesized. The thiol-Michael addition reaction of a thiol with PETTA enabled the attachment of the desired functionality directly onto the monomer while maintaining an average degree of acrylate functionality equivalent to pentaerythritol triacrylate. The stoichiometry of thiol to acrylate in the reaction is critical because the polymerization/crosslinking during TPL is dictated by the average acrylate functionality of the monomer. While the thiol-Michael reaction in this context produces a statistically determined distribution of products depending on the reaction stoichiometry, it is the average functionality of the monomer mixture that determines the extent of crosslinking during TPL. By using a 1:1 molar ratio, we ensured that the final monomer mixture had an average of three acrylates per monomer molecule, which is sufficient for effective crosslinking [78].

^{1}H and ^{13}C NMR conducted on the products indicated that the thiol-Michael reaction was quantitative within the limit of detection for NMR. This can be attributed to the following: a) the thiol-Michael reaction is inherently efficient [224]; b) although the molar ratio of PETTA to thiol was 1:1, the ratio of acrylate functional group to thiol

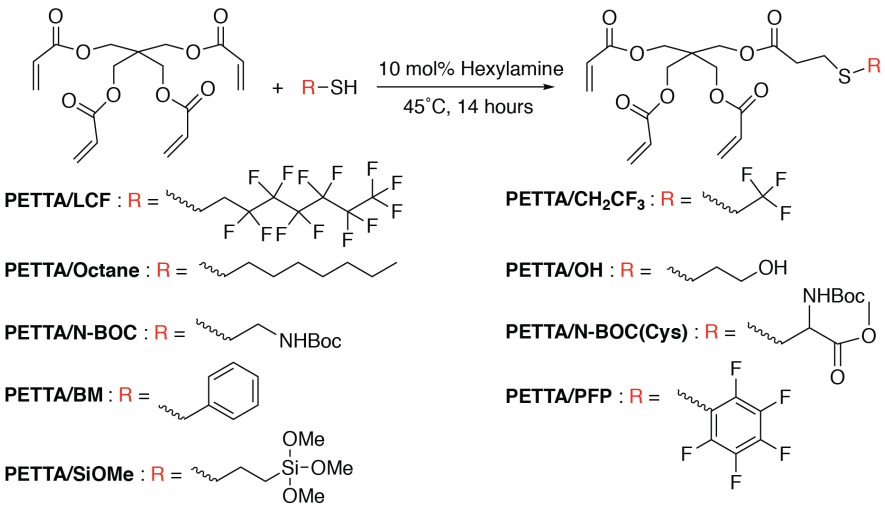

Figure 3.2: Chemical structures of the functionalized acrylates synthesized by reacting PETTA with a thiol via the thiol-Michael reaction. The names of the synthesized monomers are also displayed.

was 4:1. This excess acrylate biases the reaction toward complete consumption of the thiol; c) the reactions were run without solvent, thus maximizing the concentration of the reactants, which further enhances the reaction conversion.

Purification of the crude product would be necessary if one wanted to isolate a particular product, for example the diadduct. But for the purpose of TPL, no further purification is needed for the following reasons: At the end of the reaction, virtually all the thiols are consumed and every acrylate monomer, functionalized or not, necessarily contributes to the statistical average functionality and can participate in the TPL process. During TPL, any residual unreacted thiols would also be incorporated into the material via thiol–ene chemistry and thus would not adversely affect the polymerization process. The amine catalyst, in addition to being a very minor component of the reaction mixture, is volatile and would have no effect at these concentrations on subsequent TPL or the structures produced as it is not a photoactive molecule.

The fact that these monomers can be used without purification is a key advantage of this approach as it makes this technique broadly accessible to scientists and engineers from a variety of backgrounds.

3.5 Two-Photon Lithography of Functionalized Acrylates

Photoresins comprising these functionalized acrylates were then prepared and used with TPL to fabricate a range of structures with different unit cell geometries.

3.5.1 Functional Photoresin Preparation

The functional photoresins were prepared by mixing the functionalized acrylates with a two-photon photoinitiator (7-diethylamino-3-thenoylcoumarin (DETC, Exciton)) in a small amount of solvent. The general procedure is as follows: DETC (5.6 mg) was first mixed in dichloromethane (20 μL) (DCM, >99%, Alfa Aesar) in a 2.5 mL Eppendorf tube. Once the DETC was completely dissolved, the thiol-Michael adduct (300 mg) was added to the solution. The photoresist was then vortexed for 10 s and stored overnight in yellow light conditions. There were no observable changes in the TPL performance of the functional photoresins over a period of three months.

3.5.2 Two-Photon Lithography Fabrication Methodology

TPL was performed using a commercially available system (Photonic Professional GT, Nanoscribe GmbH) using a Zeiss Plan-Apochromat 63×/1.4 Oil DIC objective. Rastering of the laser was achieved via a set of galvo mirrors and piezoelectric actuators. The TPL setup is as follows: The photoresin is first drop cast onto a glass substrate 30 mm in diameter and 0.17 mm thick. A silicon chip 1 cm (L) x 1 cm (W) is placed over the drop, using Kapton tape of ≈100 μm in thickness as a spacer (Fig. 3.3). The structures were then written on the silicon chip via TPL. For all the structures fabricated, the distance between the rastered laser scans in the x–y plane and the slicing distance of the layers in the z-direction were set at a constant 200 nm, the laser power was set at 20 mW, and the writing speed was set at 2 cm/s. Once the TPL was complete, the finished sample was developed in propylene glycol monomethyl ether acetate (⩾99.5%, Sigma-Aldrich) for 30 min followed by an immersion in isopropanol (99.7%, Sigma-Aldrich) for 5 min.

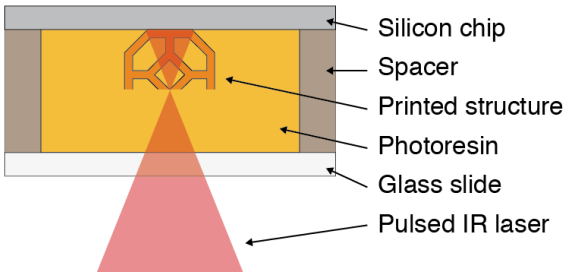

Figure 3.3: Schematic of the TPL setup. The photoresin is sandwiched between a glass slide and a silicon chip, using Kapton tape as a spacer. The structures are written on the silicon chip using TPL.

3.5.3 Functionalized Architected Structures

We fabricated a range of structures with different unit cell geometries to highlight the compatibility and versatility of these functional photoresins with the TPL process (Table 3.1). For each photoresin, two different structures were made: a lattice comprising multiple small unit cells each ≈20 μm in size and a single large unit cell ≈70 μm tall. The structures were then imaged in an FEI Versa 3D Dual Beam scanning electron microscope (SEM). A low accelerating voltage of 2kV was used to minimize charging.

Fig. 3.4 shows the SEM images of the structures fabricated with the functional photoresins. The functional group that was installed onto the monomer is displayed in the insert of each panel.

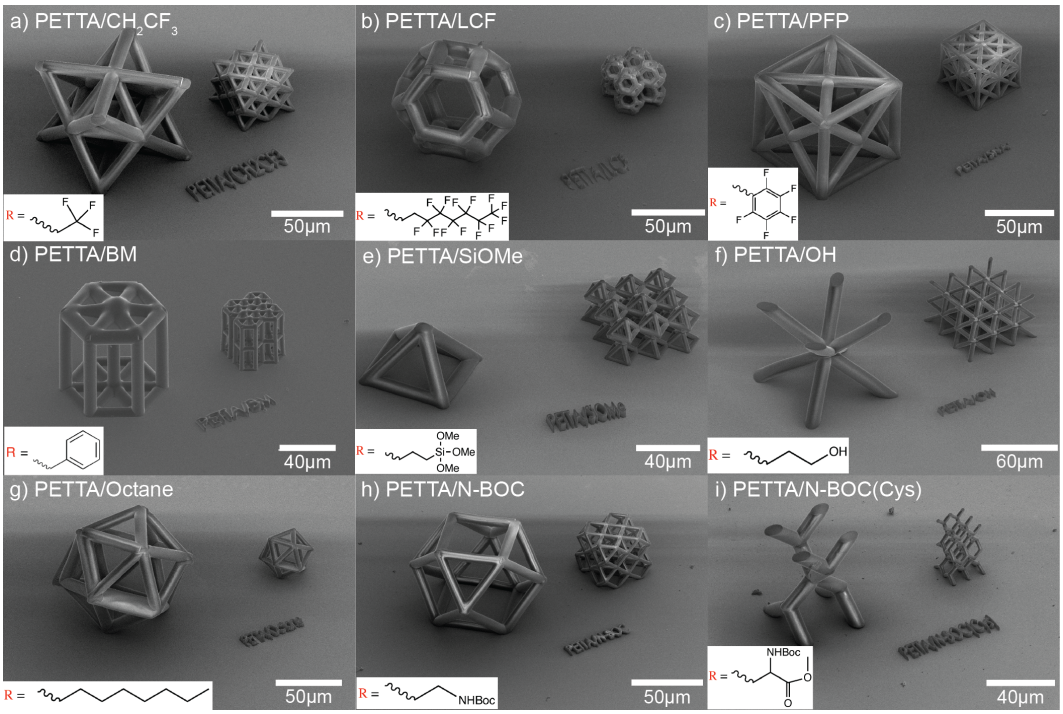

Figure 3.4: SEM images of the architected structures written with **a**. PETTA/CH_2CF_3, **b**. PETTA/LCF, **c**. PETTA/PFP, **d**. PETTA/BM, **e**. PETTA/SiOMe, **f**. PETTA/OH, **g**. PETTA/octane, **h**. PETTA/N-BOC, and **i**. PETTA/N-BOC(Cys). The functional group attached can be seen in the inset of each panel.

All the structures fabricated were fully resolved and had smooth surfaces. They were also slightly smaller than designed, with shrinkages ranging from 5 - 13% depending on the photoresin used (Table 3.1). This reduction in size can be attributed to the following: a) shrinkage associated from the polymerization of acrylates [225], b) solvent evaporation during and after fabrication, and c) inaccuracies in

the positioning of the laser focus due the index of refraction mismatch between the immersion oil, photoresin, and the cross-linked polymer [226].

Photoresin	Geometry	Linear Shrinkage (%)
PETTA/CH_2CF_3	Octet	8.5
PETTA/LCF	Tetrakaidecahedron	11.7
PETTA/PFP	Reinforced Cube	5.3
PETTA/SiOMe	Octahedron	5.0
PETTA/OH	Body Centered Cubic	5.6
PETTA/Octane	Icosahedron	5.6
PETTA/N-BOC	Shifted Octahedron	13.6
PETTA/N-BOC(Cys)	Diamond	12.9
PETTA/BM	Hexagon	5.5

Table 3.1: Details of the geometries used for each photoresin used in the two-photon lithography experiments. The linear shrinkage exhibited by each photoresin is also indicated.

3.6 Characterization of Fabricated Structures

Although the NMR results provided evidence that the synthesis was complete, we wanted to further characterize the structures to verify that they also had the desired functionality.

3.6.1 Energy-dispersive X-ray Spectroscopy

Energy dispersive X-ray spectroscopy (EDS) was conducted on the structures to determine their material composition. EDS maps were generated using a Zeiss 1550VP FESEM equipped with an Oxford X-Max SDD X-ray energy-dispersive spectrometer (EDS) system. The applied voltage was 15 kV and the structures were coated with a 10 nm carbon layer before characterization.

EDS analysis would allow us to detect the sulfur atoms present in the thioether bond, and the elements other than carbon and oxygen on the installed functional groups, i.e. all the monomers described in Fig. 3.2 with the exception of PETTA/OH, PETTA/Octane, and PETTA/BM. Fig.3.5 depicts the EDS maps of all the structures made, with the elemental maps highlighting the presence of sulfur and the other distinguishable elements found in the attached functional groups throughout the structure. This provided strong evidence that the fabricated

structures exhibited the desired functionality, and also indicated that the functional groups were homogeneously distributed throughout the structures and were not preferentially localized.

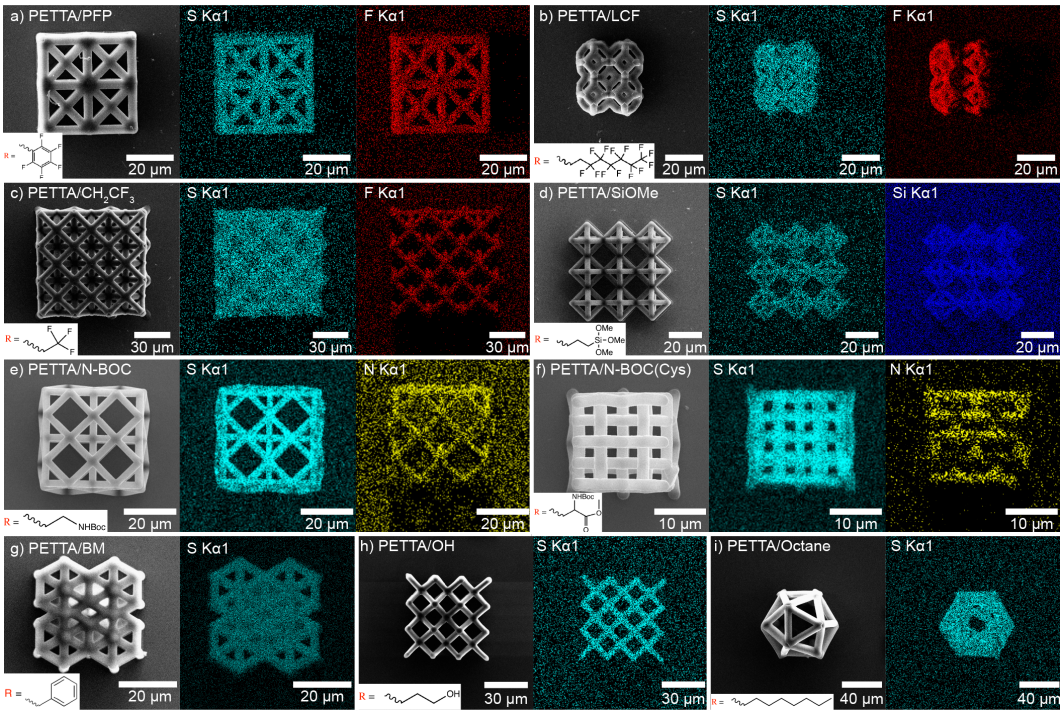

Figure 3.5: Energy-dispersive X-ray spectroscopy elemental maps for **a**. PETTA/PFP, **b**. PETTA/LCF, **c**. PETTA/CH_2CF_3, **d**. PETTA/SiOMe, **e**. PETTA/N-BOC, **f**. PETTA/N-BOC(Cys), **g**. PETTA/BM, **h**. PETTA/OH, and **i**. PETTA/Octane. For each set of images, the first image is the SEM image; the second image is the sulfur Kα1 map, and the third image (if applicable) is the distinguishable element map. Insets show the functional group attached.

3.6.2 X-ray Photoelectron Spectroscopy

Since a significant amount of chemical reactions occurs on interfaces, it was also important to determine if the functional groups of interest were also on the surface. This information could not be obtained from the EDS maps because of the large interaction volume of the electron beam within the polymer. Furthermore, surfaces of polymers can reconstruct during development, so it was important to know if any of these functional groups got buried. To more precisely characterize the surface, we conducted X-ray photoelectron spectroscopy (XPS) measurements on 3 mm (L) × 3 mm (W) × 300 nm (H) polymer 2D plates fabricated via TPL.

XPS was performed under 10^{-9} Torr with a Surface Science Instruments M-Probe ESCA controlled by Hawk Data Collection software. The X-ray source was a

monochromatic Al Kα line at 1486.6 eV. All spectra were collected using a spot size of 800 μm. A low-energy electron flood gun was used to minimize charging effects. Survey scans from 0 to 1000 eV using a pass energy of 150 eV and a step size of 1 eV were performed to identify the elements that were present on the surface.

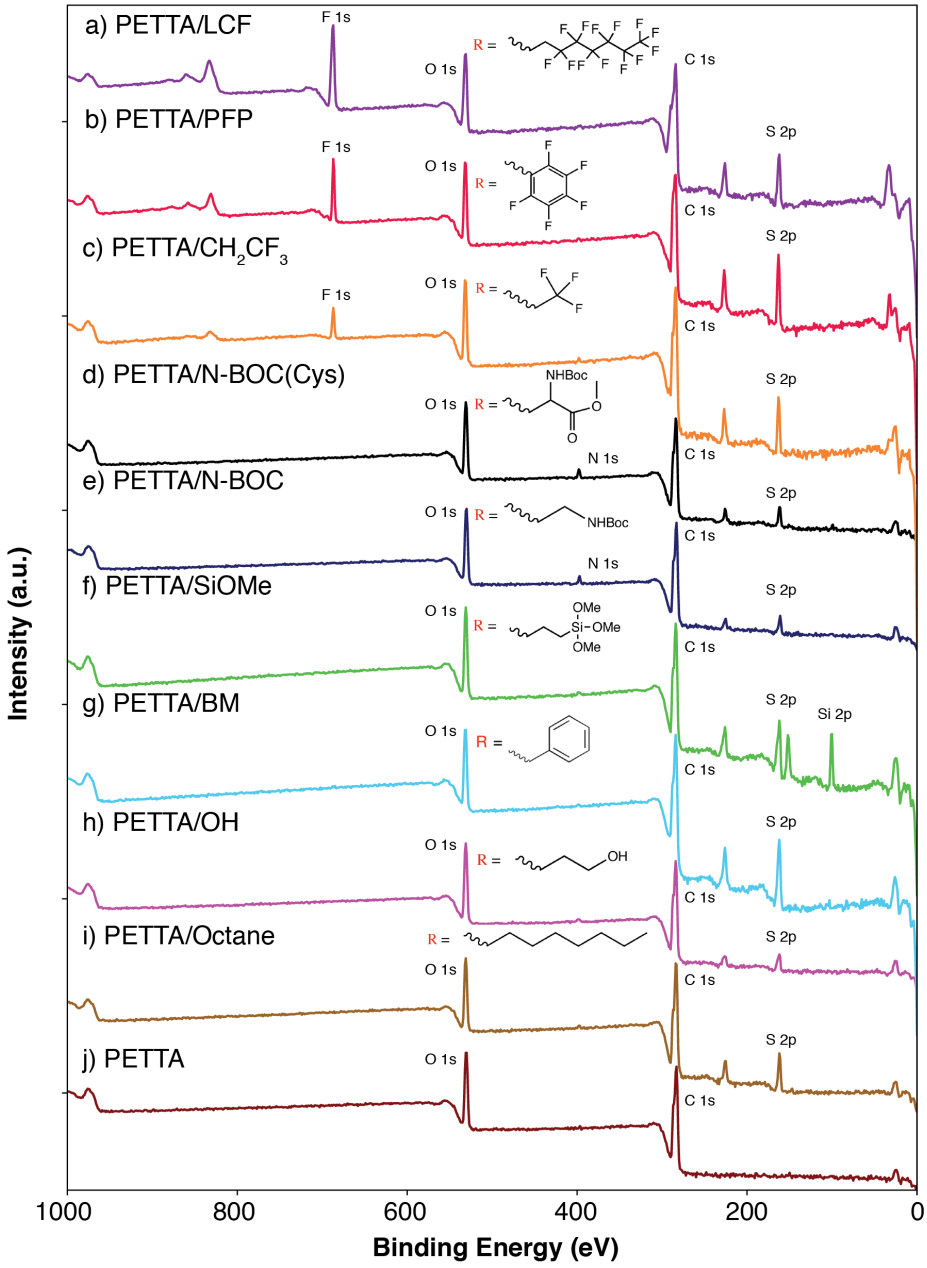

Figure 3.6: XPS survey spectra of **a**. PETTA/LCF, **b**. PETTA/PFP, **c**. PETTA/CH_2CF_3, **d**. PETTA/N-BOC(Cys), **e**. PETTA/N-BOC, **f**. PETTA/SiOMe, **g**. PETTA/BM, **h**. PETTA/OH, **i**. PETTA/Octane and **j**. PETTA. Intensity was plotted on a log scale to better show all detected peaks, regardless of the intensity differences between them.

Fig. 3.6 shows the survey spectra of all the plates. The presence of the S 2p peak

(≈165 eV) in all the samples is indicative of the thioether bond, which confirms the presence of the functional groups on the surface. This is further supported by the F 1s peak (≈688 eV) in the spectra of PETTA/LCF, PETTA/PFP and PETTA/CH_2CF_3, the N 1s peak (≈400 eV) in PETTA/N-BOC and PETTA/N-BOC(Cys), and the Si 2p peak (≈100 eV) in PETTA/SiOMe. A control plate fabricated from PETTA also did not show any other peak aside from the C 1s and O 1s peaks. Based on these results, it is reasonable to conclude that the 3D structures also exhibit functionality on the surface because they were identically fabricated via TPL.

3.7 Contact Angle Measurements

Surface functionalization leads to a modification in surface energy. To demonstrate this, we performed contact angle measurements on TPL fabricated plates of PETTA/OH, PETTA/octane, and PETTA/LCF, with PETTA as the control. These particular resists were chosen because they theoretically exhibit the widest range of hydrophobicity. The contact angle data were obtained using a contact angle goniometer equipped with an AmScope Microscope Camera model MU300. A syringe was used to place a water droplet on the surface of the polymer plates. The image was captured 10 s after the drop was placed and then analyzed using ImageJ and DropSnake (software developed at Ecole Polytechnique Federale De Lausanne). Each reported contact angle was the average of four different measurements.

Contact angle measurements (Fig. 3.7) demonstrate that compared to the control PETTA plate, the PETTA/OH photoresin is more hydrophilic and the PETTA/octane and PETTA/LCF photoresins are more hydrophobic. This observation is expected based on the chemistry of the functional groups: the hydroxyl groups present on the surface of the PETTA/OH plates allow for the formation of hydrogen bonds with water, which makes the surface more hydrophilic. For the PETTA/octane and PETTA/LCF photoresists, the long chain alkanes and fluoroalkanes are nonpolar and do not interact favorably with water, which results in a hydrophobic surface. These results indicate that chemical functionalization provides tunability in surface properties. Considering that nanostructuring of the surface has also been shown to modify its contact angle [227], the potential combination of nanostructuring and surface chemistry functionalization of the constituent polymer described in this work could be an interesting direction in the future.

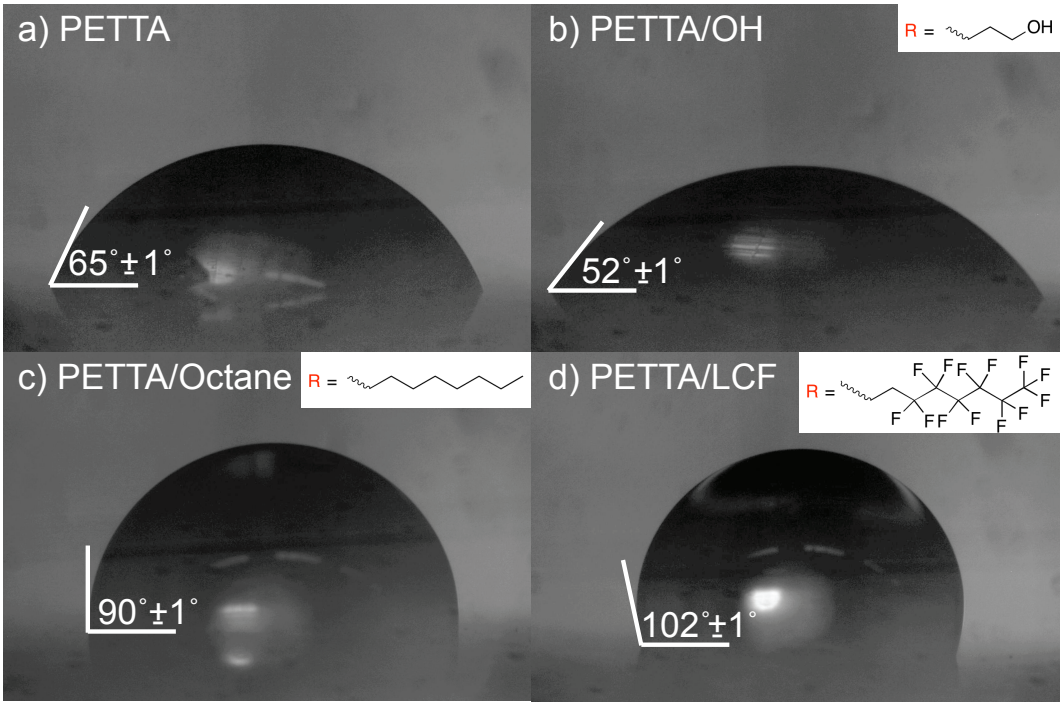

Figure 3.7: Measurements of the static contact angle of a water droplet on a plate of **a**. PETTA (control) (65°), **b**. PETTA/OH (52°), **c**. PETTA/Octane (90°), and **d**. PETTA/LCF (102°). All functionalized plates had markedly different contact angles from that of the control, highlighting the effect of functionalization on surface properties. Insets show the functional groups attached.

3.8 Post-Polymerization Modification

The introduction of reactive functional groups throughout the structures also makes them amendable to post-polymerization modifications. To illustrate this point, we fabricated PETTA/N-BOC and PETTA/N-BOC(Cys) structures which contained Boc-protected amine groups. We deprotected the amines and demonstrate the use of these primary amines for post-polymerization modifications.

We found that the deprotection step often resulted in the structures peeling away from the substrate, so we treated the glass substrate with 3-(trimethoxysilyl)propyl methacrylate to promote adhesion of the polymer to the glass substrate.

3.8.1 Preparation of Functionalized Glass Slides

Glass slides were ultrasonicated in isopropanol for 15 min and then dried with argon. A 95% ethanol (95%, Koptec) /5% water solution was adjusted to pH 4.5–5.5 with acetic acid (>99.7%, J. T. Baker). 3-(Trimethoxysilyl)propyl methacrylate (98%, Sigma-Aldrich) was then added to the solution with stirring to yield a 2% final concentration. The cleaned glass slides were then immersed into the silane solution

with gentle stirring for 2 min. The slides were then dipped briefly in ethanol to rinse away the excess silane. The silane layer was then baked at 110 °C for 15 min.

3.8.2 Quantification of Accessible Amines

We fabricated 2D plates of known dimensions with TPL using PETTA/N-BOC on the functionalized glass substrates. The Boc-protected amines in the functional polymer plates were then deprotected in a solution of 50/50 vol% of trifluoroacetic acid (TFA, >99%, TCI) and DCM for 60 minutes, to give primary amines. Using a procedure adapted from Noel et al., we quantified the number of accessible amines using a colorimetric method based on the azo dye Orange II: in acidic solutions of Orange II, the positively charged protonated amines are reversibly bound to the negatively charged sulfonated Orange II dye via electrostatic interactions. On subsequent immersion in basic media, the amines become deprotonated and release the Orange II molecules into solution (Fig. 3.8). The quantity of desorbed dye can then be determined by measuring the absorbance of the solution and comparing it to solutions of known Orange II concentrations. Assuming each Orange II molecule binds to only one amine, the number of accessible amines can then be determined [228].

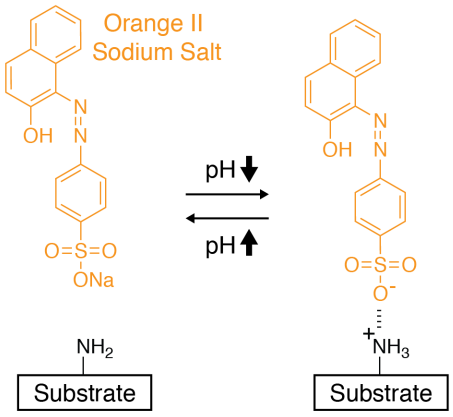

Figure 3.8: Orange II amine assay mechanism. Changes in pH allow for the reversible electrostatic interaction between the Orange II sodium salt and the surface amines.

The general procedure of the Orange II amine assay is as follows. A 14 mg/mL Orange II dye solution was prepared by dissolving Orange II sodium salt (>85%, Sigma-Aldrich) in Milli-Q water adjusted to pH 3 using hydrochloric acid (36.5–38%, J. T. Baker.) The deprotected plates were then immersed in 7 mL of the Orange II acidic solution for 30 min at 40 °C. The plates were then rinsed five times using the pH 3 solution to remove excess dye and then dried with argon. The

colored plates were then immersed in a known volume of alkaline solution at 40 °C (Milli-Q water adjusted to pH 12 with a 1M NaOH solution (>98%, Macron Chemicals)). After 12 hours, the plates were removed from solution. As expected, after the soak, the plates were no longer colored and the solution was orange. The pH of the solution was then adjusted to pH 3 by adding concentrated hydrochloric acid. The measured absorbances of the Orange II solutions at 480 nm (Molecular Devices Flexstation 3) were then correlated to its concentration in solution via the use of a calibration curve (Fig. 3.9).

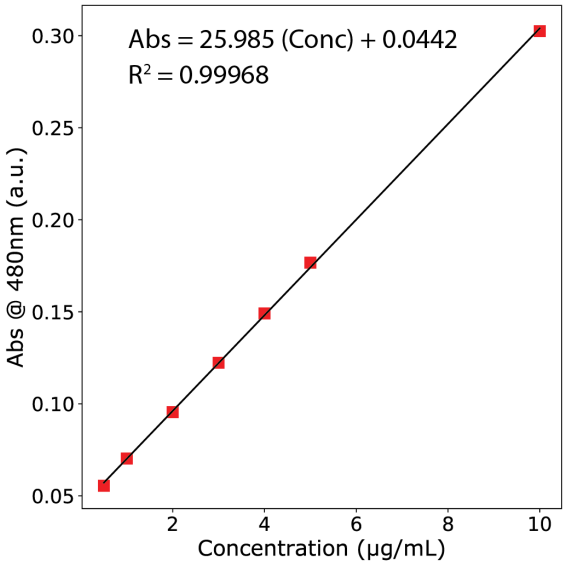

Figure 3.9: Calibration curve constructed using the absorbance of Orange II solutions of concentrations from 10 μg/mL to 0.5 μg/mL.

The Orange II dye test is a simple assay that can visually determine (Fig. 3.10) and quantify the presence of amines in a material. Using this method, the surface density of *accessible* amines was determined to be $3.9 \pm 0.7 \times 10^8$ molecules/μm^2.

It is important to emphasize that this value is not the surface density of amines, but the surface density of *accessible* amines. The distinction here lies in the fact that the Orange II dye can swell into the polymer and react with the amines there. Since it was unclear as to what this penetration depth was, we decided to use the term "surface *accessible* amines" to account for the volumetric contribution. To be precise, the value reported is technically the number of amines per unit area of the structure surface accessible by the Orange II dye.

The implication of this is that the Orange II test likely gives a lower bound for the number of accessible amines. The steric hindrance from bound Orange II molecules

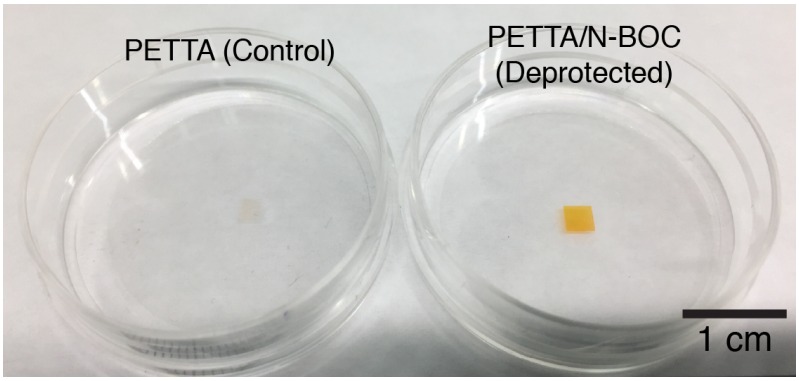

Figure 3.10: PETTA plate (left) and deprotected PETTA/N-BOC plate (right) after immersing in the Orange II acidic solution and washing. The lack of color in the PETTA control plate and the orange PETTA/NBOC plate indicates that the Orange II molecules were successfully bound to the amines on the PETTA/N-BOC polymer.

potentially limits the accessibility of neighboring amine groups to free Orange II molecules, which would consequently reduce the measured amount of accessible amines. The bulky size of the molecule would also limit its diffusion into the bulk of the polymer. The number of accessible amines would likely be higher for a smaller molecule.

3.8.3 Fluorescent Labeling

To visually demonstrate the use of these surface amines for post-polymerization modification reactions, we attached a fluorescent molecule via an N-hydroxysuccinimide (NHS) ester (Fig. 3.11).

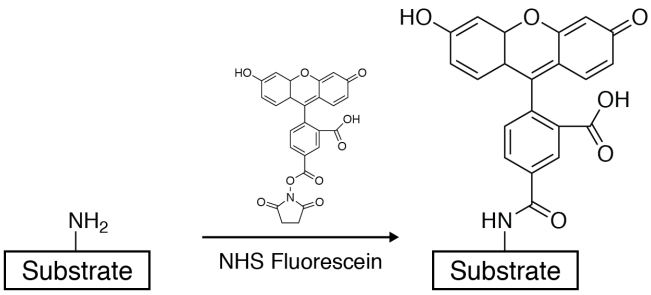

Figure 3.11: Fluorescent labelling of surface amines via the attachment of NHS-fluorescein.

The procedure for the fluorescent labelling is detailed below:

PETTA, PETTA/N-BOC, and PETTA/N-BOC(Cys) structures were first fabricated on the functionalized glass slides using TPL. They were then soaked in a 50/50 vol% solution of TFA and DCM for 15 minutes to deprotect the amines. Following

that, the structures were soaked in a saturated sodium bicarbonate solution, and then deionized water to remove any residual TFA. As it is possible for the deprotected primary amines to react with any unreacted acrylates on the surface, the structures were immediately immersed in a 3 mg/mL solution of 5(6)-carboxyfluorescein N-hydroxysuccinimide ester (NHS fluorescein, >99%, Fisher Scientific) in N,N-dimethylformamide (DMF, >99%, Sigma-Aldrich) for 60 minutes. The reaction was conducted in the dark to reduce any photobleaching of the fluorophore. To remove the unreacted NHS fluorescein at the end of the reaction, the structures were soaked in DMF for 15 minutes, and then in deionized water for another 15 minutes.

Fluorescence microscopy was then used to determine the success of the reaction. The fluorescence images were obtained using a Nikon Eclipse Ti-E and the software Micro-Manager (developed by the University of California, San Francisco). The objective lens used was a 40× air objective. Bright field images were imaged in transmission mode. Fluorescence images were imaged using a broad-spectrum mercury lamp with an excitation filter between 457 and 487 nm and a fluorescence emission filter between 502 and 538 nm. All the samples were excited for 5 ms each.

Fig. 3.12 shows the fluorescence images of the reacted structures. The strong emission in the detection region of ≈525 nm indicates that the fluorescein functional group was successfully attached to the surface of the PETTA/N-BOC and PETTA/N-BOC(Cys) structures. A slight amount of fluorescence was detected in the PETTA control sample because of the auto fluorescence of DETC [226]. To isolate the emission from the fluorescein molecule, we determined the intensity from DETC based on the control sample and subtracted it from that of the PETTA/N-BOC and PETTA/N-BOC(Cys) structures. To more accurately reflect the relative intensity of fluorescence emission, the intensities of all the structures in Fig. 3.12 were normalized to the maximum intensity detected, i.e. that of PETTA/N-BOC.

Normalized fluorescence results show that the emission from the PETTA/N-BOC structure was greater than that of the PETTA/N-BOC(Cys) structure, while virtually no detectable fluorescence emanated from the PETTA control. The reduced relative fluorescence emission from the PETTA/N-BOC(Cys) structures was likely due to a lower reactivity of the amine with the NHS-fluorescein arising from steric hindrance around the PETTA/N-BOC(Cys) primary amine compared with that from PETTA/N-BOC.

The nonuniform intensities in the 3D fluorescence images (Fig. 3.12d, e, f) arise

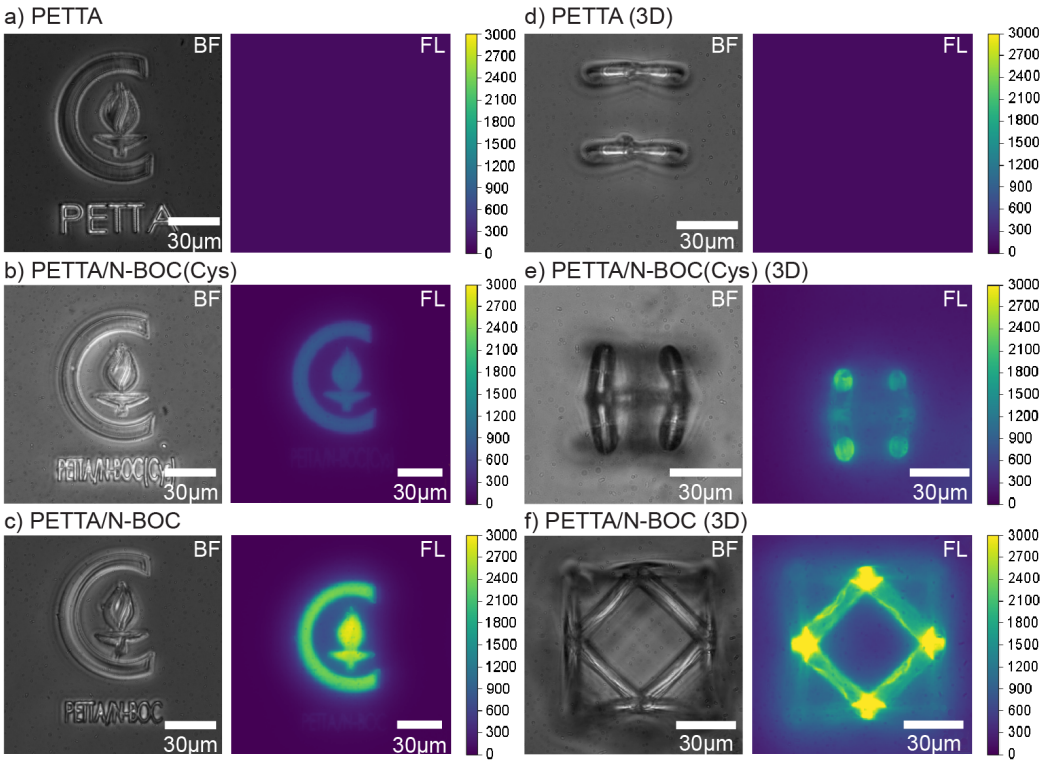

Figure 3.12: Fluorescence images of 2D structures of **a**. PETTA, **b**. PETTA/N-BOC(Cys), and **c**. PETTA/N-BOC. Fluorescence images of 3D architected structures of **d**. PETTA, **e**. PETTA/N-BOC(Cys), and **f**. PETTA/N-BOC. Each set of images has a bright-field (BF) image and a corresponding fluorescence image (FL). The fluorescence intensities were all normalized to that of PETTA/N-BOC.

from capturing all of the emitted light, including that from the unfocused background. To circumvent this, we used confocal fluorescence microscopy to image the 3D structures. A confocal laser scanning microscope Zeiss model LSM 800 equipped with a 20× water immersion objective (Achroplan, NA = 0.5) was used. The structures were directly mounted in the objective immersion water. A 488 nm laser line was used for excitation, and the emission was measured between 500 and 550 nm. We acquired z-stacks with 1 μm spacing between successive slices. Imaris (developed by Bitplane) was used to generate 3D visualization and movies of our structures.

Fig. 3.13 shows the z-image stacks acquired by confocal fluorescence microscopy. The nonuniform fluorescence intensities observed in the PETTA/N-BOC structures were due to a self-shadowing effect that arose due to the design of the structures — emitted light from the bottom half of the sample was blocked by the top half of the sample. Where there was no overlap of structure, i.e. the top half of the

PETTA/N-BOC structure and the entire PETTA/N-BOC(Cys) structure, a uniform intensity was observed, indicating that the fluorescein was uniformly attached to the structures. (See videos attached in the Supplementary Information for different observation angles).

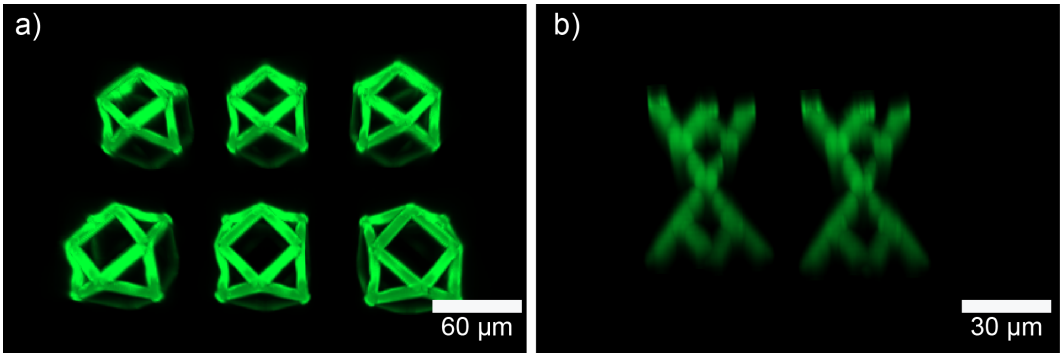

Figure 3.13: Confocal fluorescence images of 3D structures of **a**. PETTA/N-BOC and **b**. PETTA/N-BOC(Cys).

It is worth mentioning that the post-polymerization modification methodology described above currently does not allow for spatial control of the reaction. To achieve spatial resolution on the surface of the structures as demonstrated in other works in the literature [157, 229], it is necessary to have photoactive functional groups, which cannot be achieved by using amines alone. However, the approach taken here does not necessarily preclude spatial resolution as photoactive groups could potentially be installed via the amines, which could be subsequently modified on the surface in a spatially controlled manner.

3.9 Summary and Outlook

In conclusion, we fabricated functionalized 3D architected structures by first synthesizing functional acrylates via the thiol-Michael addition reaction, and then polymerizing these functionalized monomers using TPL. The advantages of this approach are the simplicity of the thiol-Michael reaction and the variety of functional groups that are compatible with the reaction. The functionalized structures were characterized using EDS and XPS, both of which confirmed the presence of the functional groups in the structures. We also highlight how functionalization can be used to tune the hydrophobicity of the structures, and also allow for post-polymerization modification reactions such as fluorescent labeling.

These functional 3D structures provide an effective pathway for a variety of applications. For example, attaching biologically relevant molecules such as

peptides, poly(ethylene glycol) (PEG) chains, or antibodies to the amines could allow for drug delivery or biosensing. The modulation of hydrophobicity based on the functionalization of the monomer could enable the fabrication of materials with antifouling properties. The inclusion of the trimethoxysilane group introduces the possibility of performing sol–gel chemistry on these structures. In addition, multifunctional structures can also be easily made by using a combination of different functional acrylates. The diversity of chemical functionality that we can now incorporate into these photoresins really points to the versatility of this approach.

In the context of TPL, this work provides an effective approach to controlling the geometry, dimensions, *and* chemical functionality of the structures fabricated. But more importantly, this work conveys the utility of click chemistry in materials science — it is an accessible way for material scientists to venture into the organic synthesis arena and start performing chemical modifications on materials. There is incredible opportunity and potential in using click chemistry to design and build materials with any desired properties.

Chapter 4

ADDITIVE MANUFACTURING OF MULTIFUNCTIONAL METAL OXIDES VIA IN-SITU COMBUSTION SYNTHESIS

Chapter Abstract

The previous two chapters explored how surface chemistry and click-chemistry based monomer synthesis can be accessible approaches for the additive manufacturing of architected functional polymer structures. In the following chapters, we turn our attention to functional *non-polymeric* materials. We discuss how reframing the polymer structures that we fabricate as reaction vessels — where we print a "chemical reactor" that contains all the necessary reagents that react *in situ* to produce the desired material — will allow us to adapt the field of materials chemistry to additive manufacturing.

This chapter will focus on the additive manufacturing of multifunctional *binary* metal oxide ceramics with sub-micron features. We demonstrate the combination of *in situ* combustion synthesis and two-photon lithography, in a novel technique called Photopolymer Complex Synthesis, to fabricate architected piezoelectric zinc oxide structures with sub-micron features.

This chapter has been adapted with permission from:

1. Yee*, D. W., Lifson*, M. L., Edwards, B. W. & Greer, J. R. Additive Manufacturing of 3D-Architected Multifunctional Metal Oxides. *Advanced Materials* **31,** 1901345. doi:https://doi.org/10.1002/adma.201901345 (2019).

Contributions: participated in the conception of the project, developed the polymer chemistry, fabricated the structures, performed some of the material characterizations, and wrote the manuscript.

4.1 Vat Photopolymerization of Multifunctional Metal Oxides

Multifunctional metal oxide ceramics are of significant technological importance in modern society today. These materials exhibit a variety of functional properties, such as superconductivity [230], ferroelectricity [231], ferromagnetism [232], and biocompatibility [233]. As a result, they have found application in almost every scientific and engineering field, ranging from catalysis [234], implantable biomedical devices [235, 236], to large-scale energy generation [237], and storage [238]. But an ongoing challenge in the use of these materials is that, like all ceramics, they are difficult to process and shape. Unlike their metal or polymer counterparts, manufacturing processes like melt casting and machining cannot be easily applied to ceramics due to their high melting points and hardness [239]. To circumvent that, ceramic components are often processed from a ceramic slurry instead. These slurries can be shaped into a green body, and then fired at high temperatures to give the final ceramic part [240]. However, the nature of some of these techniques, like injection molding or slip casting, still imposes a geometrical limitation on the fabricated parts, precluding the formation of arbitrarily complex geometries [57, 240].

The emergence of additive manufacturing (AM) has enabled the fabrication of three-dimensional (3D) metal oxides with almost arbitrary geometries [57]. The ability to combine both architecture and functionality has been a boon for the materials community — new experimental devices that utilize architected metal oxides have demonstrated either significant improvements in performances [129, 241] or previously impossible functionalities [242, 243].

As described briefly at the end of Chapter 1, ceramic materials can be fabricated with vat photopolymerization (VP) either through a slurry approach or an inorganic-organic photoresin approach[1].

4.1.1 Slurry Approach

In the slurry approach, fine metal oxide particles are dispersed in a photosensitive liquid binder. This photosensitive slurry is then shaped with an appropriate VP technique to form the green body — photopolymerization of the liquid binder traps the metal oxide particles within the polymer structure. The green body is then subjected to a high temperature thermal treatment to remove the polymer binder and sinter the metal oxide particles together to form the final metal oxide structure [244,

[1] I encourage the reader to refer to [57] for more information on ceramic AM techniques.

245] (Fig. 4.1).

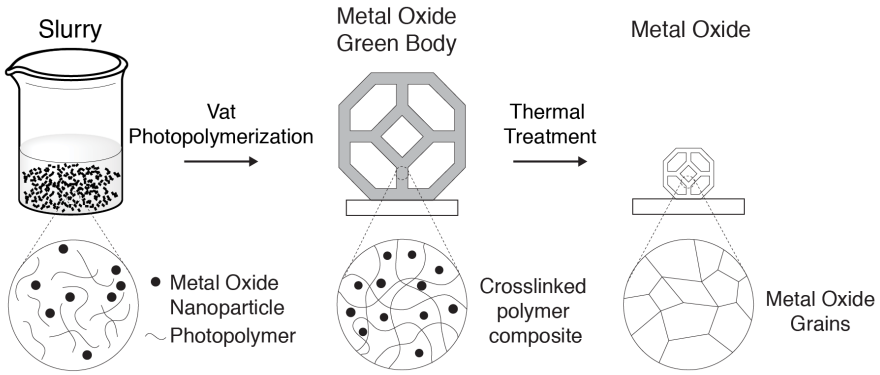

Figure 4.1: Schematic of slurry approach to fabricating metal oxide ceramics with vat photopolymerization. Note the formation of a nanoparticle composite in the green body.

The advantages of this approach are its accessibility and versatility. As long as the metal oxide can be obtained in powder form, the photosensitive slurry can be produced, and the structure fabricated [244]. However, the high volume fraction of particles needed often results in a host of different problems: agglomeration of particles leads to inhomogeneity within the structures. The high viscosities of the slurries make fabrication challenging [57]. The particles also scatter light, reducing the resolution acheivable and affecting dimensional accuracy [246].

4.1.2 Inorganic-Organic Photoresin Approach

An alternative approach that circumvents these issues is to use inorganic-organic photoresins instead[2]. These homogeneous photoresins often contain polymers that have metal heteroatoms in their backbones and photopolymerizable organic side/end groups. In this case, the polymer is both the binder and metal oxide precursor at the same time. The precursors are also incorporated into the fabricated structure on a molecular level. Similar to the slurry approach, a high temperature treatment is then used to burn off the organic components and leave the inorganic structure behind [129, 247, 248] (Fig. 4.2).

These homogeneous photoresins often have lower viscosities, and also do not have issues with light-scattering, allowing them to achieve higher resolutions. The drawbacks to this approach are that it is limited in the compositions of the oxides attainable [249]. Furthermore, these photoresins are often not commercially

[2]While often referred to as pre-ceramic polymers in the literature, the term inorganic-organic photoresins was chosen here as pre-ceramic polymers are sometimes assumed to be silicon based.

available, and sometimes require a complex multistep synthesis.

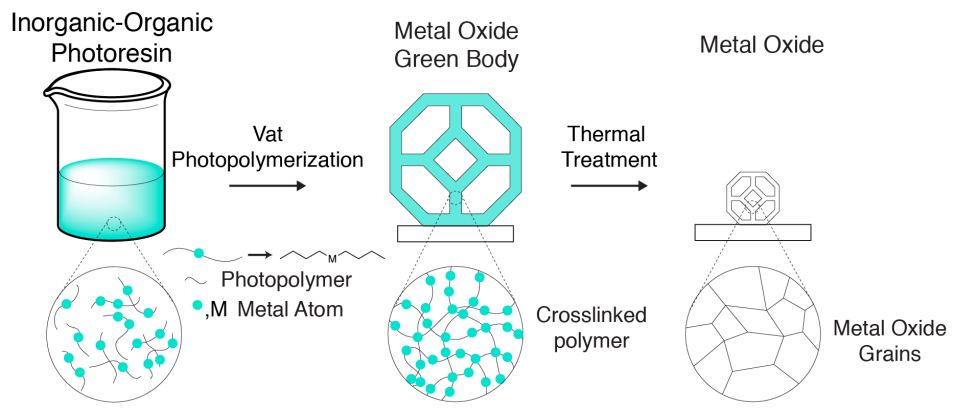

Figure 4.2: Schematic of inorganic-organic photoresin approach to fabricating metal oxide ceramics with vat photopolymerization.

In this chapter, we explore the combination of solution combustion synthesis and vat photopolymerization as a facile and accessible approach to fabricating metal oxide structures. We achieve this via the use of a homogeneous aqueous metal-nitrate containing photoresin that later undergoes combustion synthesis to form the metal oxide *in situ*. As a proof of concept, we demonstrate the fabrication of architected zinc oxide (ZnO) structures with sub-micron features, and electromechanical properties.

More generally, this chapter highlights how we can adapt solution-based materials synthesis to vat photopolymerization by treating the as-printed green bodies as "chemical reactors". By incorporating the necessary reagents in the polymer *system*, we can then initiate the reaction to generate the desired material *in situ*.

4.2 Concept of Architected "Chemical Reactors"

At a fundamental level, the main idea behind both the slurry and inorganic-organic photoresin approach is the incorporation of a metal oxide precursor in a polymer system that undergoes a reaction to give the final metal oxide material. In short, one can view the as-fabricated green bodies as "chemical reactors". From this point of view, the slurry approach is essentially a thermal decomposition of the polymer binder and the sintering of the metal oxide particles [250]. The inorganic-organic photoresins undergo a much more complicated set of reactions, which generally involves the loss of hydrocarbons and hydrogen and the formation of metal-oxygen bonds. The reaction is closer to a sol-gel metal oxide synthesis, as the polymer

precursors are actually hybrid sol-gel networks [251, 252].

With this "chemical reactor" framework in mind, we can start to approach the fabrication of metal oxides from a material synthesis perspective and exploit the extensive reactions already developed in the materials chemistry field. The goal is to now design a photoresin that can utilize one of these reactions to initiate the *in situ* generation of a material.

It is important to highlight that this concept is not entirely new: the use of active fillers that transform during the ceramization process of pre-ceramic polymers is based on the same concept [253, 254]. Some recent studies have also started to explore this idea — Shukrun et al. formulated a photoresin that slowly underwent sol-gel polycondensation after photopolymerization [255]; Chiappone et al. incorporated sol-gel precursors into a photoresin that reacted to form nanoparticles *in situ* on exposure to acid vapors [256]; and Zhang et al. precipitated perovskite nanoparticles within an organogel [257] — but the fabrication of a homogeneous metal oxide has yet to be realized.

4.3 Solution Combustion Synthesis

Solution combustion synthesis (SCS), in particular, is a promising class of reactions for use with VP as it can be used to synthesize a variety of metal oxide nanomaterials[3]. In brief, it involves the mixing of metal nitrates and water-soluble organic compounds in water to form a homogeneous solution, which is then heated to initiate a self-sustaining redox exothermic (combustion) reaction to form a metal oxide [258]. Metal nitrates are used as they are strong oxidizers, have high solubilities in water, have low decomposition temperatures, and leave behind little residue after combustion [258, 259]. The organic compounds serve as fuel during the reaction, and also as a complexing agent with the metal ions to prevent them from precipitating out as water is removed [260]. Some of the commonly used fuels are urea, glycine, and citric acid [258]. Polymers like poly(ethylene glycol), poly(vinyl alcohol), and poly(acrylic acid) have also been demonstrated to be suitable fuels, in a similar combustion technique called Polymer Complex Solution [261, 262]. An example of a SHS reaction between nickel nitrate hexahydrate and glycine is given below:

[3]I strongly encourage the reader to refer to [258] for an in-depth review on this subject.

$$Ni(NO_3)_2 \cdot 6H_2O + nC_2H_5NO_2 + \frac{9n-10}{4}O_2 = NiO + \frac{n+2}{2}N_2 + 2nCO_2 + \frac{12+5n}{2}H_2O \quad (4.1)$$

Where n is the number of moles of fuel (glycine) added for each mole of nickel nitrate. The reaction mechanism behind SCS is not well understood, and is further complicated by the fact that it is highly system dependent. But it has been suggested that the products from the decomposition of the nitrates react exothermically with the organic fuel to initiate the reaction. This exothermic reaction results in a self-accelerating reaction as the increase in temperature leads to an increase in reaction rate. A high temperature is rapidly reached, resulting in the combustion of the system to form metal oxides [258]. This is clear from the time-temperature plot of a combustion synthesis reaction, as exemplified by Fig. 4.3 for a iron nitrate-glycine SCS.

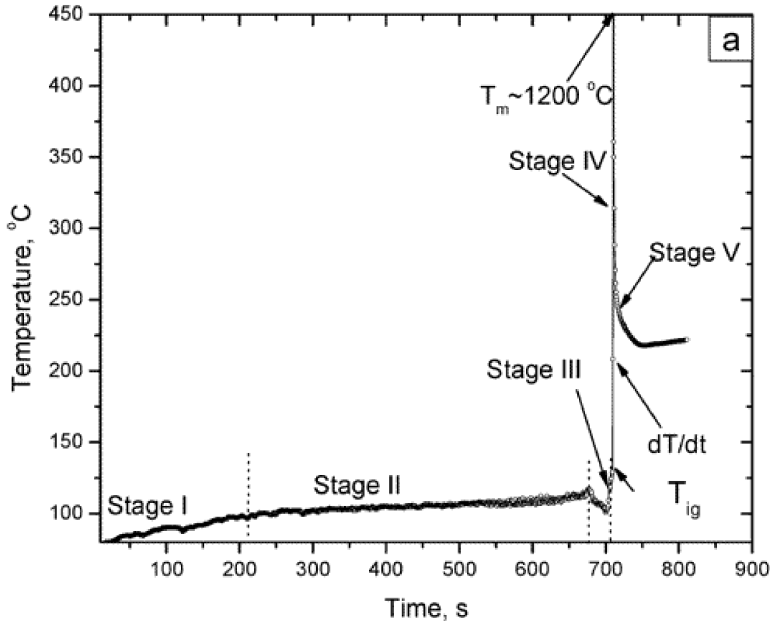

Figure 4.3: Time-temperature history of iron oxide combustion synthesis using iron nitrate and glycine. At the ignition temperature T_{ig}, SCS occurs as the temperature increases rapidly. Reprinted with permission from Deshpande et al. [263]. Copyright (2004) American Chemical Society.

One of the main advantages of SCS is that the reagents are mixed in aqueous solutions at the molecular level, which prevents any issues with inhomogeneity. The

reagents are also easily accessible and the reaction simple to set up. Furthermore, below the nitrate decomposition temperature, the reactive solution is also stable for a long time, without any precipitation of the reagents [258]. Taken together, these make SCS promising for use with VP.

4.4 Photoresin Design for Solution Combustion Synthesis

In order to initiate SCS in a vat photopolymerized structure, we need to design the photoresin to have the following: metal nitrate, fuel, photopolymerizable binder, and photoinitiator. More importantly, they all need to be soluble in water.

The requirement for water solubility is similar to that of hydrogel fabrication, and as a result, we designed an aqueous photoresin based on poly(ethylene glycol) diacrylate (PEGda). Since polymers can also be used as fuels [261], the telechelic PEGda macromonomers act as both the fuel and the binder — allowing us to achieve both SCS and spatial polymerization with VP. The inclusion of an appropriate metal nitrate then completes the photoresin. It is important to emphasize that at a fundamental level, the concept behind this approach is still the inclusion of a metal precursor that undergoes a reaction to form a metal oxide. However, unlike the slurry and inorganic-organic approaches that use metal oxide nanoparticles and metal atoms respectively as their precursors, here, we use metal ions (Fig. 4.4).

We coined this process "Photopolymer Complex Synthesis", a portmanteau of photopolymerization, polymer complex solution, and solution combustion synthesis — the three fields from which this methodology draws.

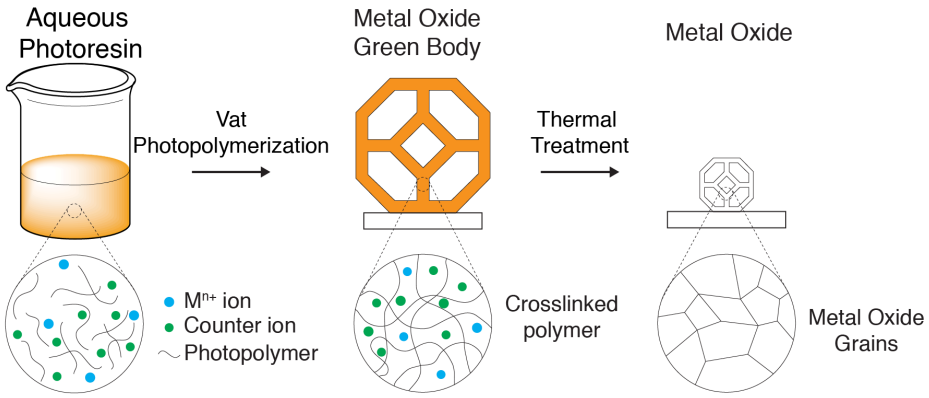

Figure 4.4: Schematic of photopolymer complex synthesis approach to fabricating metal oxide ceramics with vat photopolymerization.

This process combines the beneficial aspects of the existing slurry and inorganic-organic approaches: the wide variety of metal nitrates available allows

for a large composition window, and the homogeneity and low viscosity of the aqueous photoresin minimizes light scattering, improving the resolutions achievable.

4.5 Photopolymer Complex Synthesis of Zinc Oxide

As a demonstration of this process, we decided to use a zinc-nitrate containing photoresin with two-photon lithography (TPL) to produce zinc oxide (ZnO) architected structures with sub-micron features. This is depicted schematically in Fig. 4.5.

We chose ZnO as a model material because it has a suite of useful properties, such as a direct band gap and piezoelectricity [264]. Recent work in the field has also shown that architecting a piezoelectic material allows for the tuning of its electromechanical response [265]. As ZnO is commonly used in microelectromechanical systems (MEMS) devices, there is immense potential in architecting it at the micron scale to achieve something similar. However, previous attempts to do so at this scale, through templating [266, 267], coatings [268, 269], or the inclusion of ZnO nanowires [270], have been unable to fabricate monolithic topologically defined ZnO architectures.

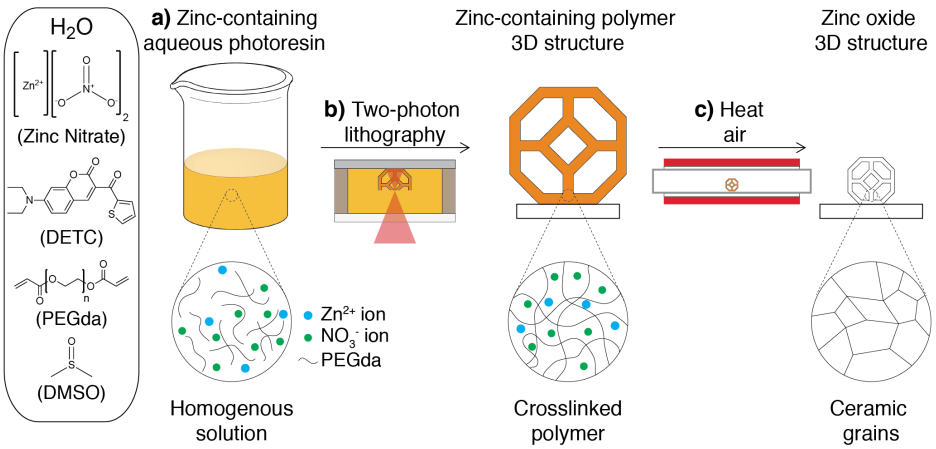

Figure 4.5: Photopolymer Complex Synthesis approach for two-photon lithography of ZnO. **a**. A zinc-nitrate containing aqueous photoresin is prepared by mixing zinc nitrate, water, PEGda, DETC, and DMSO to create a homogeneous pale orange solution. **b**. TPL is used to selectively pattern the zinc-nitrate containing photoresin into the designed 3D architecture. **c**. Calcination in air produces a zinc oxide replica of this 3D structure with isotropic linear shrinkage.

4.5.1 Proof of Concept Experiments

We first wanted to verify that these aqueous zinc photoresins could a) produce zinc oxide and b) do so via combustion synthesis. These can be determined via X-ray

diffraction (XRD) and thermogravimetric analysis (TGA) respectively. However, TPL is unable to fabricate samples that are large enough for characterization with those two techniques. To conduct these proof of concept experiments, we fabricated large samples via casting into a mold, followed by UV curing instead. Two casting resins were prepared, one with zinc nitrate, and a control without.

4.5.1.1 Casting Photoresins Formulation

Aqueous Zinc Photoresin for Casting

We first dissolved 5 g of zinc nitrate hexahydrate (98%, Sigma-Aldrich) in 1 mL of deionized water to give a 3.6 mL solution. To this zinc nitrate solution, 2.67 mL of poly(ethylene glycol) diacrylate M_n = 575 (PEGda, Sigma-Aldrich) was added and mixed until a homogeneous colorless transparent solution was obtained. In a separate vial, 23 mg of lithium phenyl-2,4,6-trimethylbenzoylphosphinate (LAP, >95%, Sigma-Aldrich) was dissolved in 1 mL of deionized water to give a colorless transparent solution. 2 mL of the zinc nitrate/PEGda solution was then mixed with 200 μL of the LAP solution to give a colorless transparent solution.

Control Photoresin for Casting

The control casting resin used pure deionized water instead of the zinc nitrate solution: 3.6 mL of deionized water was added to 2.67 mL of PEGda to give a clear solution. 200 μL of the LAP solution prepared above was then added to 2 mL of the water/PEGda solution and mixed until a homogenous colorless transparent solution was formed.

Curing of Casting Photoresins

1.5 mL of the casting photoresin was poured into a polydimethylsiloxane circular mold 4 cm in diameter and then cured with a UV curing lamp (350–380 nm, 36W) (MelodySusie DR 301C) for 15 min to give the cast polymer. Gelation occurred within two minutes. The remaining time under UV was for post-curing. Both cast polymers were transparent and showed no signs of phase separation or precipitation.

4.5.1.2 Thermogravimetric Analysis of Cast Polymers

Both the zinc polymer and control polymer were then subjected to TGA to determine their thermal degradation profiles. TGA was performed on a STA 6000 (PerkinElmer) from 30 to 900 °C at a heating rate of 5 °C/min under air with a flow

rate of 20 mL/min. <100 mg of each polymer was used for the analysis. Fig. 4.6 shows the TGA curves of both cast polymers.

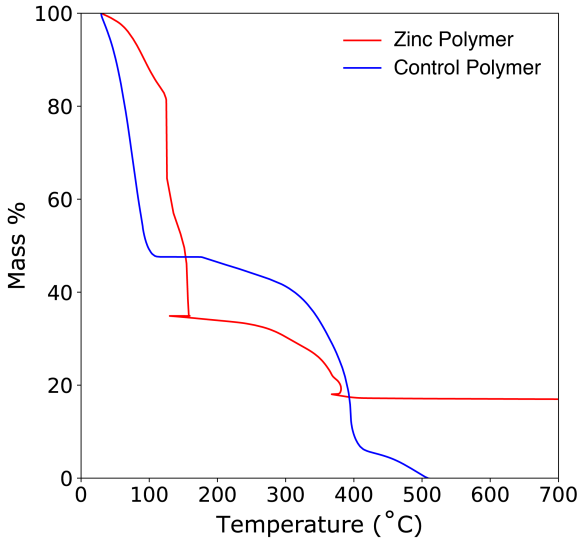

Figure 4.6: Representative thermogravimetric analysis curves of the zinc polymer and its control. A rapid mass loss from 115 – 150 °C can be observed with the zinc polymer, which is absent in the control. The large mass loss in the control polymer on heating to 100 °C is due to the loss of water from the polymer. The control exhibits complete mass loss above 500°C, whereas a finite mass remains with the zinc polymer.

The TGA curve of the zinc polymer showed 3 distinct stages of mass loss. At the first stage between 30 - 115 °C, 16 wt% of mass loss was observed. This likely corresponds to the mass loss associated with the evaporation of water. From 115 – 150 °C, a rapid mass loss of approximately 50% was observed, which is characteristic of a combustion reaction between the nitrates and PEGda. Above 150 °C, a slow decomposition corresponding to a mass loss of 16% was observed, indicating the elimination of any residual organic material left behind from incomplete combustion. Beyond 400 °C, no further mass change was observed.

In contrast, the control polymer showed a completely different thermal behavior. From 30 – 100 °C, a large mass loss of ≈ 50 wt% was observed. This was due to the loss of water from the polymer. No change in mass was observed from 100 – 170 °C as the PEG was stable in that temperature range. The polymer then underwent a gradual mass loss of ≈ 40 wt% of the initial mass on further heating to 400 °C. Complete degradation was observed past 500 °C.

From the TGA curves, it was clear that the zinc polymer underwent a combustion reaction, indicating that the photoresin developed could successfully undergo a post-

polymerization SCS reaction. In addition, the results also showed that at 500 °C, the temperature was sufficiently high for the complete reaction of the zinc polymer, and for the removal of all other organics.

4.5.1.3 X-Ray Diffraction of Calcined Cast Polymers

XRD was used to determine the phase of the calcined polymers. The zinc polymer precursor and the control were first calcined in a furnace (MTI OTF-1500X) at ambient pressure in air at 0.5 °C/min to 500 °C and then cooled back to room temperature at 2 °C/min. The resulting materials were an off-white brittle ceramic (zinc polymer precursor) and gray ash (control polymer), which is consistent with both ZnO and carbon residue respectively. As expected, the samples also shrank significantly. XRD was then performed on a Bruker D2 Phaser equipped with a Cu source and a LyneEye detector. The spectra was collected at 30 kV and 10 mA. Fig. 4.7 shows the XRD spectra of both calcined cast polymers.

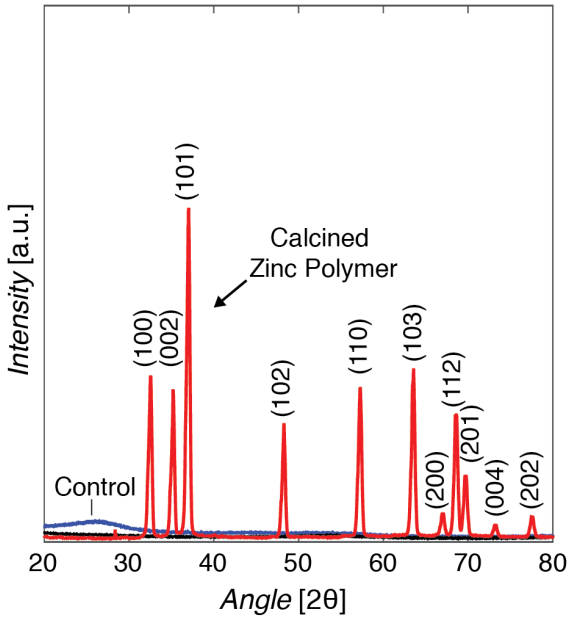

Figure 4.7: XRD spectra of calcined cast polymers. The spectra of the calcined zinc and control polymers are shown in red and blue respectively.

The XRD spectrum from the calcined zinc polymer had sharp diffraction peaks that were in good agreement with those of ZnO (JCPDS card no. 36-1451), and also did not contain any discernible impurities, such as zinc carbonate. In contrast, the calcined control polymer exhibited a single low angle broad peak in its spectrum, which was likely due to amorphous carbon.

Taken together, the proof of concept experiments revealed that the aqueous zinc photoresin developed could be used to fabricate materials that could undergo a post-polymerization SCS reaction to form ZnO.

4.5.2 Two-Photon Lithography of Aqueous Zinc Photoresins

A new photoresin compatible with TPL was first prepared: a zinc nitrate solution was prepared by dissolving 5 g of zinc nitrate hexahydrate in 1 mL of deionized water. To this zinc nitrate solution, 2.67 mL of PEGda was added and mixed until a homogeneous colorless transparent solution was obtained. In a separate vial, 6.2 mg of the two-photon initiator 7-diethylamino-3-thenoylcoumarin (DETC, Exciton) was dissolved in 465 μL of dimethyl sulfoxide (DMSO, Sigma-Aldrich) to give a yellow solution. 500 μL of the zinc nitrate/PEGda solution was then mixed with 50 μL of the DETC solution to give a pale orange solution.

The composition of the resin was ≈51 wt% zinc nitrate hexahydrate and 0.08 wt% DETC. These compositions were determined using an iterative approach where the goal was to maximize the amount of zinc nitrate hexahydrate and DETC in the resin, while still maintaining homogeneity and long-term stability of the photoresin. Increasing the zinc nitrate mass loading would decrease shrinkage upon calcination, and increasing DETC would improve the printing speed. However, higher amounts of zinc nitrate would often result in the precipitation of the DETC photoiniator over time, likely due to the increased ionic strength of the solution.

TPL was performed using a commercially available system (Photonic Professional GT, Nanoscribe GmbH) using a Zeiss Plan-Apochromat 63×/1.4 Oil DIC objective. Rastering of the laser was achieved via a set of galvo mirrors and piezoelectric actuators. The TPL setup is as follows. The aqueous zinc photoresin is first drop cast onto a glass substrate 30 mm in diameter and 0.17 mm thick. A silicon chip 1 cm x 1 cm (W) is placed over the drop, using Kapton tape of ≈100 μm in thickness as a spacer (Fig. 4.8). The structures were then written on the silicon chip via TPL.

4.5.2.1 Two-Photon Lithography Fabrication Parameters

To determine the fabrication parameters for TPL, a parameter sweep was first conducted. Pillars approximately 9 μm in diameter and 10 μm tall were written with varying photon doses, at a z-layer spacing and hatching distance of 150 nm. The laser power was varied from 5 – 50 mW, in steps of 5 mW, and the laser raster speed was varied from 1 – 10 mm/s. Fig. 4.9 shows a scanning electron

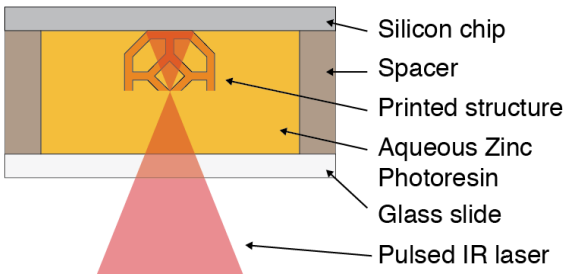

Figure 4.8: Schematic of the TPL setup. The aqueous zinc photoresin is sandwiched between a glass slide and a silicon chip, using Kapton tape as a spacer. The structures are written on the silicon chip using TPL.

microscope (SEM) image of the results of the parameter sweep. The images were obtained using a FEI Versa 3D Dual Beam. A low accelerating voltage of 2kV was used to minimize charging.

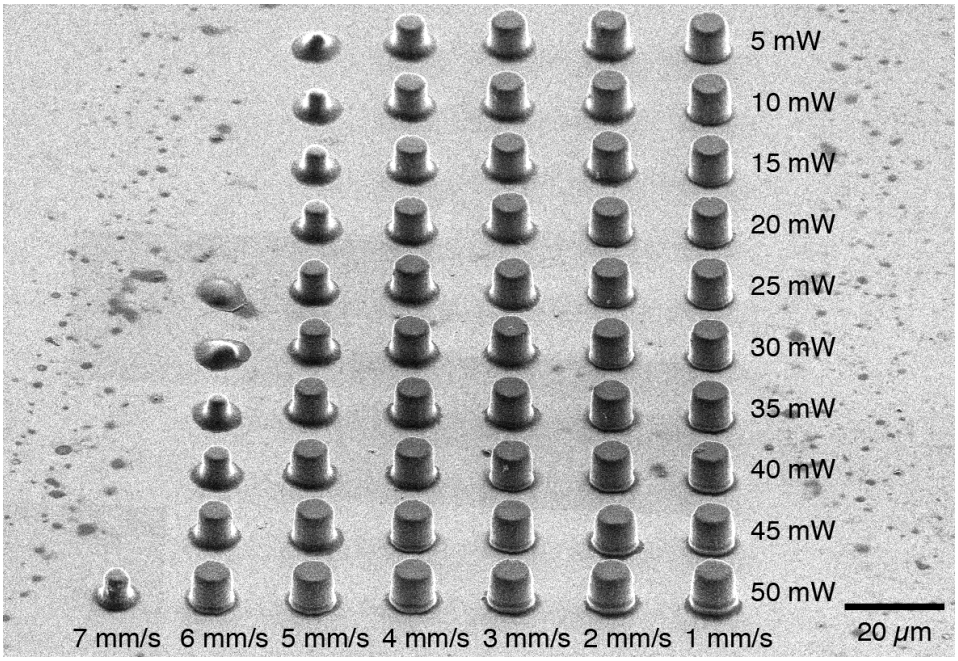

Figure 4.9: Schematic of the TPL setup. The aqueous zinc photoresin is sandwiched between a glass slide and a silicon chip, using Kapton tape as a spacer. The structures are written on the silicon chip using TPL.

As seen, a wide range of power and scan speed combinations can be used in the two-photon lithography process, due to the small z-layer spacing and hatching distances used. At the extreme ends of the power spectrum, structures were fully formed at a raster speed of 1 mm/s with a laser power of 5 mW and at 6 mm/s with a laser power of 50 mW. Regardless of power, no structures could be seen when used in conjunction with raster speeds above 6 mm/s. The parameters of 50 mW and 1

mm/s were chosen for the TPL process, as that was likely to result in the highest degree of polymer crosslinking, and consequently structures with the best structural integrity.

4.6 Architected ZnO Structures

Structures of increasing complexity were then fabricated using TPL: from cylindrical pillars to individual unit cells to microlattices. The fabricated structures were developed in water for five minutes, and then calcined at 500 °C. The temperature profile used for calcination was identical to that described earlier for the cast polymers. Fig. 4.10 shows the SEM images of the structures before and after calcination.

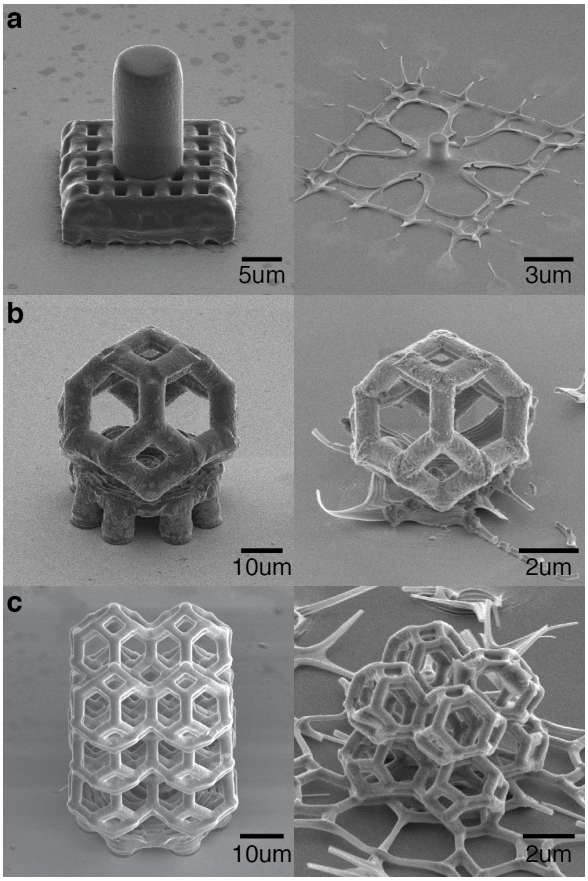

Figure 4.10: SEM images of **a**. a cylindrical pillar, **b**. a tetrakaidecahedron unit cell, and **c**. a microlattice of tetrakaidecahedrons made via TPL of the aqueous zinc photoresin before (left) and after (right) calcination. The linear dimensions of all structures were reduced by 87 ± 2%.

As seen, the as-printed zinc polymer structures exhibited smooth features and uniform beams. Each structure was also fabricated on top of a support structure.

This was to prevent the structures from breaking due to the interfacial stresses generated during shrinkage. Structures that were fabricated directly on the substrate did not survive the calcination process. The support geometry is not unique and can be as simple as a pedestal (Fig. 4.10b) or as complicated as a layer of tetrakaidecahedron unit cells (Fig. 4.10c).

After calcination, the ZnO structures exhibited self-similar architectures as their polymeric predecessors, albeit with linear shrinkages of ≈87 ± 2 %. The linear shrinkages were determined by:

$$LinearShrinkage = \left(1 - \frac{L_{final}}{L_{initial}}\right) \times 100 \tag{4.2}$$

where $L_{initial}$ and L_{final} were the lengths of the unit cell before and after calcination respectively. The structures also had smooth surfaces, with no visible cracks or macro-pores. For the most part, the supports were destroyed after calcination, but as seen in Fig. 4.10c, a substantial amount of material can still remain. Thus, while any support geometry can be used, there is likely an optimal design that will result in less residual material. Alternatively, the supports could be fabricated with another photoresin that will degrade completely at the calcination temperature.

4.6.1 Shrinkage Analysis

The substantial shrinkages observed bear further investigation as they could be exploited to fabricate structures with higher resolutions than what can be achieved with TPL alone. For example, in Fig. 4.10cm, features sizes on the order of 250 nm were obtained after shrinkage. We found that the linear shrinkage observed depended on the initial concentration of zinc nitrate in the resin *and* on the development time of the printed structures in water.

The shrinkage of the structures can be theoretically determined by a simple analytical model that assumes the following: a) each mole of Zn^{2+} is converted into a mole of ZnO, b) the calcined structures is pure ZnO, and c) the calcined structures have self-similar architectures as their polymer predecessors, and only exhibit changes in dimensions. As would be expected, the theoretical shrinkage is solely dependent on the initial concentration of zinc in the polymer. Thus, for a particular volume of polymer, $V_{polymer}$, the corresponding volume of the calcined ZnO, V_{ZnO} is given by:

$$V_{ZnO} = \frac{m_{ZN,polymer}}{Mw_{ZN}} \cdot \frac{Mw_{ZnO}}{\rho_{ZnO}} \tag{4.3}$$

where $m_{ZN,polymer}$ is the mass of zinc nitrate hexahydrate in the polymer, Mw_{ZN} and Mw_{ZnO} the molecular weight of zinc nitrate hexahydrate and ZnO respectively, and ρ_{ZnO} is the density of ZnO. The linear shrinkage can then be determined by:

$$\begin{aligned} TheoreticalLinearShrinkage &= \left(1 - \sqrt[3]{\frac{V_{ZnO}}{V_{polymer}}}\right) \times 100 \\ &= \left(1 - \sqrt[3]{\frac{m_{ZN,polymer} \cdot Mw_{ZnO}}{Mw_{ZN} \cdot \rho_{ZnO} \cdot V_{polymer}}}\right) \times 100 \end{aligned} \tag{4.4}$$

In this work, the aqueous zinc TPL photoresin contained 0.4 g of zinc nitrate hexahydrate in 550 μL of photoresin. The molecular weight of ZnO and zinc nitrate hexahydrate were taken to be 81.38 g/mol and 297.49 g/mol respectively. The density of bulk ZnO was taken to be 5.61 g/cm^3. Using the shrinkage equation derived above (Equation 4.4), the theoretical shrinkage was determined to be 67%.

The discrepancy between the theoretical shrinkage of 67% and the observed shrinkage of 87% was hypothesized to be due to the development process. During the development process, the zinc ions are able to leach out of the polymer and diffuse into the water, which reduces the amount of zinc nitrate left in the polymer (Fig. 4.12). As a result, a smaller volume of ZnO is left after calcination.

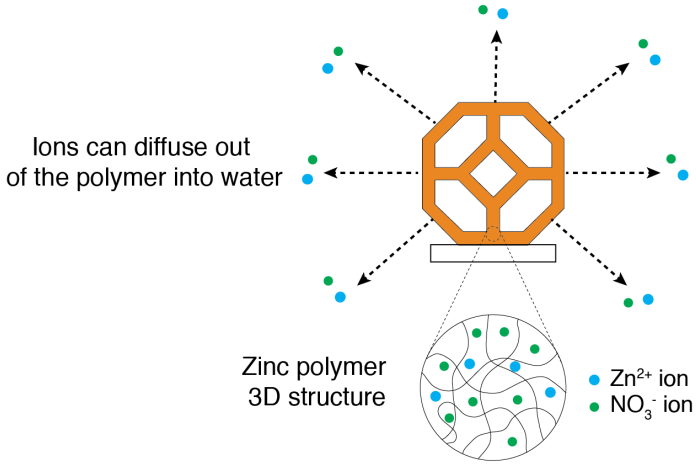

Figure 4.11: Schematic of the zinc ions leaching out of the polymer during the development process. This reduces the amount of zinc in the polymer, causing a larger shrinkage after calcination.

To quantify the dependence of development time on the final linear shrinkage observed after calcination, pillars with heights of 15 μm and diameters of 9.5 μm

were printed using two-photon lithography and then developed in water for varying amounts of time, followed by calcination at 500 °C. The diameters and heights of the calcined pillars were then compared against the as-printed pillars and their linear shrinkage determined via Equation 4.2, with $L_{initial}$ and L_{final} being the relevant dimensions before and after calcination. Fig. 4.12 shows the linear shrinkages observed in both the axial and radial dimensions as a function of development time in water.

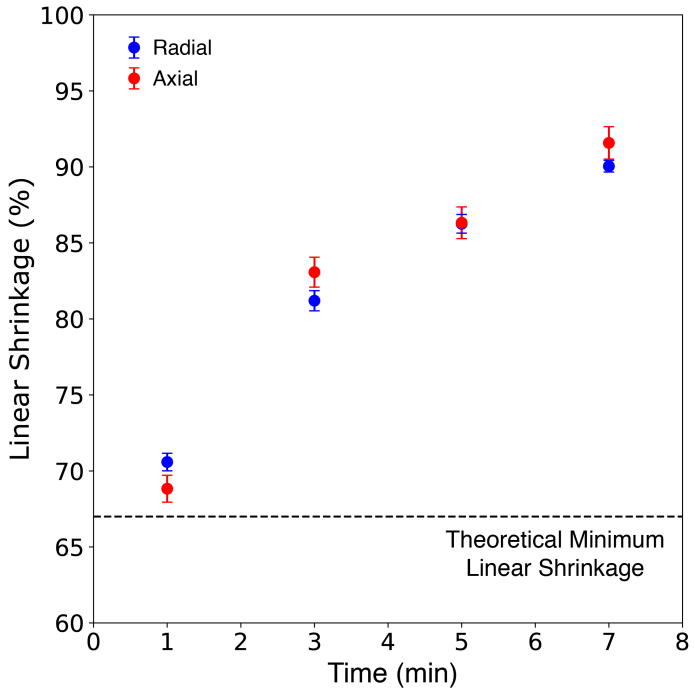

Figure 4.12: The dependence of linear shrinkage on development time in water. A larger shrinkage was observed with an increase in development time. Comparison of the radial and axial shrinkages showed that there was no significant anisotropy in the observed shrinkages. Each data point was the average of three pillars (n=3), and the error bars shown are the standard deviation.

The linear shrinkages were found to increase with development time, lending credence to our hypothesis of ion leaching. Furthermore, the linear shrinkages after one minute of development were in close agreement with those predicted using the analytical model described above. One minute was the minimum amount of time needed for development of the resin. Analysis of the radial and axial shrinkages also indicated the shrinkages to be isotropic, with the absolute difference between the two shrinkage measurements being <2%.

This method of tuning the linear shrinkage via leaching of zinc ions effectively provides another mechanism for refining the resolution of the structures fabricated

using this technique.

4.7 Characterization of ZnO Structures

The ZnO structures were further characterized using energy-dispersive X-ray spectroscopy (EDS) and transmission electron microscopy (TEM).

4.7.1 Energy-dispersive X-ray Spectroscopy

EDS was performed on the ZnO structures to determine their composition. The EDS data were generated in a Zeiss 1550VP FESEM equipped with an Oxford X-Max SDD EDS system. The applied voltage was 15 kV. Fig. 4.13 shows the results from the EDS analysis.

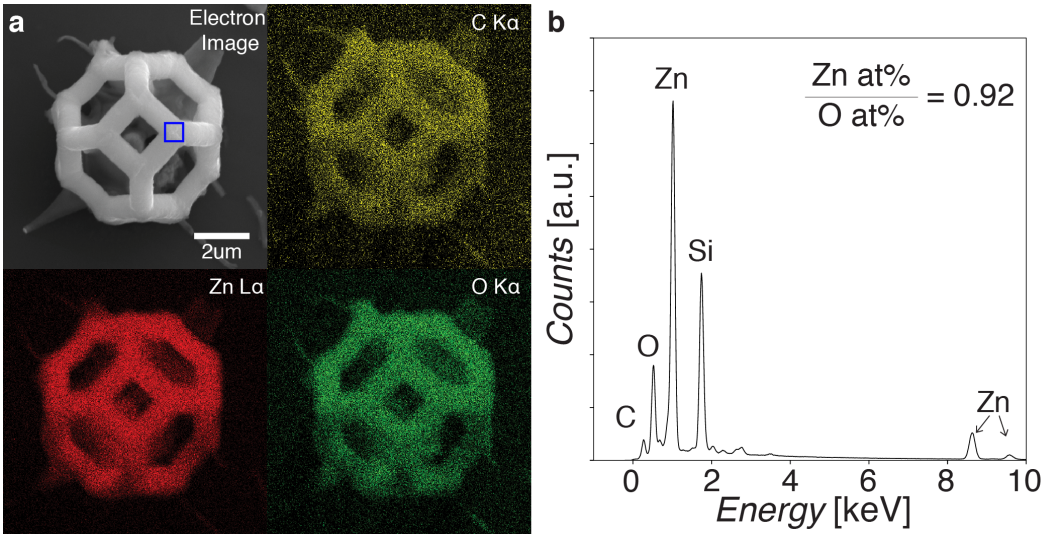

Figure 4.13: EDS characterization of ZnO Structures. **a**. Zinc, carbon, and oxygen elemental maps of the ZnO structure. **b**. EDS spectrum obtained from the top beam of the structure, as highlighted by the blue box in the electron image of **a**.

The EDS elemental maps in Fig. 4.13a showed that there was a homogeneous distribution of zinc, oxygen, and carbon throughout the structure, with no apparent segregation into individual element-rich phases. The amounts of Zn and O, after excluding silicon and carbon, were 45.0 and 48.9 at% respectively, resulting in a Zn to O ratio of 0.92 (Fig. 4.13b). The silicon detected was due to the silicon substrate that the structures were fabricated on. The composition should be treated as an approximation due to the inaccuracies associated with measuring light elements using EDS. Carbon was excluded from our analysis due to the unknown contributions of the carbon signal from both the structure and the substrate. Possible sources of C on the substrate include combustion residue and SEM chamber deposits.

The EDS analysis of the structures and the XRD spectra from the cast polymers both point to the calcined structures being predominantly ZnO, with some residual carbon from incomplete combustion.

4.7.2 Transmission Electron Microscopy

TEM was also performed on the ZnO structures to determine their phase and grain size. A cross-section of a beam from a ZnO tetrakaidecahedron unit cell was removed using a focused ion beam (FIB) lift-out method, and then imaged in an FEI Tecnai F30 TEM at 300 kV. Fig. 4.14 shows the results from the TEM analysis.

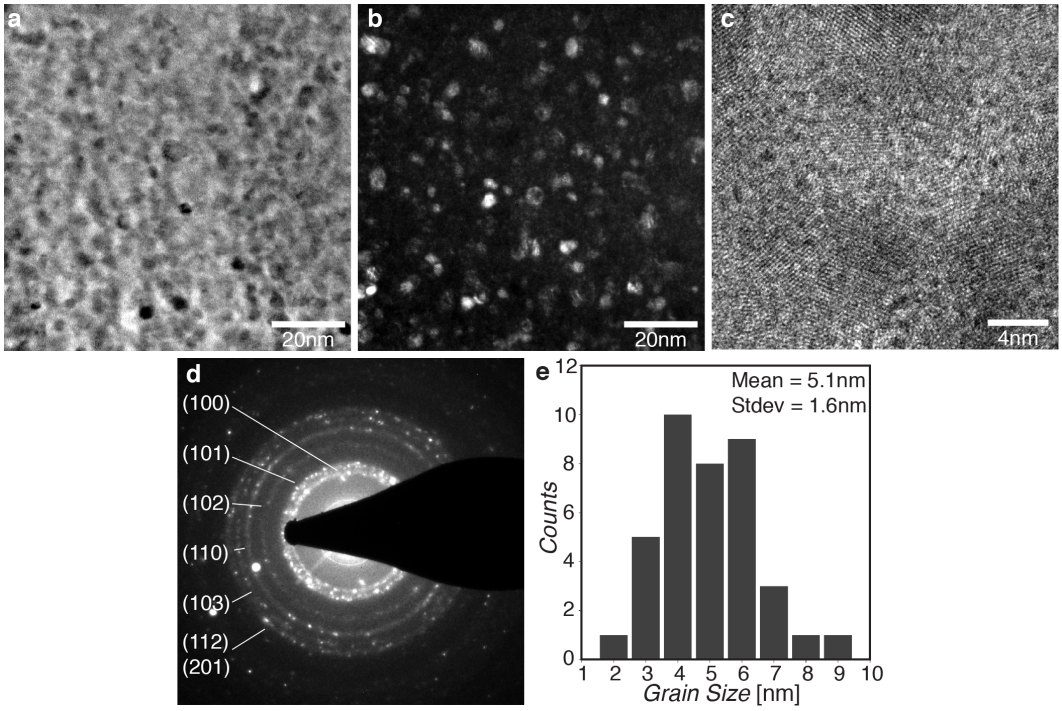

Figure 4.14: TEM analysis of a ZnO structure. **a**. Bright field, **b**. dark field, **c**. high-resolution TEM images, and **d**. a TEM diffraction pattern taken from a cross-section of a ZnO structure show the nanocrystalline nature of the material. **e**. Histogram of grain sizes measured from the dark field TEM image revealed that they were 5.1 ± 1.6 nm in diameter (N = 40).

The bright field, dark field, and high-resolution TEM images (Fig. 4.14a-c) clearly show that the calcined ZnO was fully dense and nanocrystalline. The average grain size, as determined from the dark field image, was determined to be 5.1 ± 1.6 nm in diameter (N = 40) (Fig. 4.14d). The selected area electron diffraction (SAED) pattern obtained also contained characteristic rings, whose spacing corresponded to the labeled crystallographic orientations of polycrystalline ZnO. The outermost ring was labeled (112)/(201) because the spacing of these two orientations was so close

that it was not possible to distinguish between them experimentally. The two large diffraction spots in the lower left quadrant of the diffraction pattern were likely a result of electron beam overlap with the underlying silicon substrate.

The three independent characterization techniques of XRD, EDS, and TEM strongly suggest that calcination of the zinc polymer structures resulted in their conversion to monolithic polycrystalline ZnO.

4.8 Electromechanical Properties of Architected ZnO Structures

To demonstrate the potential of these architected ZnO microstructures as electromechanical device elements, we measured their electromechanical response using a custom-built experimental setup. The setup measures the open circuit voltage (OCV) of the structures during compression by using a modified *in situ* nanomechanical instrument (InSEM from Nanomechanics, Inc.) inside an SEM chamber (FEI Quanta 200F) (Fig. 4.15). (See Lifson's Ph.D thesis for more details on this setup [271].)

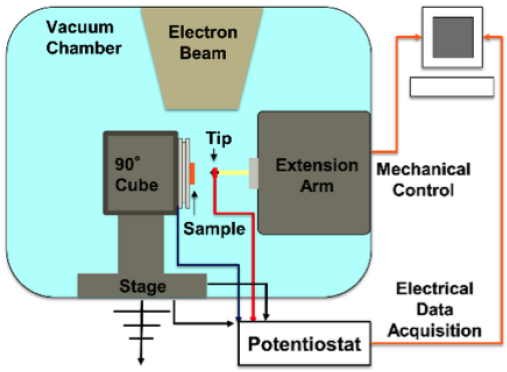

Figure 4.15: Schematic of the electromechanical measurement experimental setup. The sample is placed on an aluminum stub, mounted at 90°, in an SEM chamber equipped with a nanoindenter arm. A potentiostat is connected to measure the open circuit voltage between the grounded stage and the indenter tip during the experiment.

We measured the open circuit voltage (OCV) response of a tetrakaidecahedron ZnO structure and a similar control structure made of the zinc polymer during *in situ* compression. To compare the response between the two materials, the size and design of both structures had to be as similar as possible. This was challenging to achieve due to the large shrinkages experienced by the ZnO structures. This was further complicated by the fact that the compression tip was only $\approx$5 μm across, constraining the size of the structure allowed. While it was relatively easy

to fabricate fully resolved ZnO structures ≈ 5 μm in size by accounting for and exploiting the large shrinkages that occurred, the equivalent polymer structures had poorly resolved features due to the inability of TPL alone to reach the resolutions needed. However, as a test of *an* electromechanical response, the poorly resolved polymer structure was still sufficient.

Fig. 4.16 shows the OCV measurements of the polymer structure after ≈ 350 nm of compression. As would be expected from an amorphous polymer, compression of the structure did not result in any electrical response.

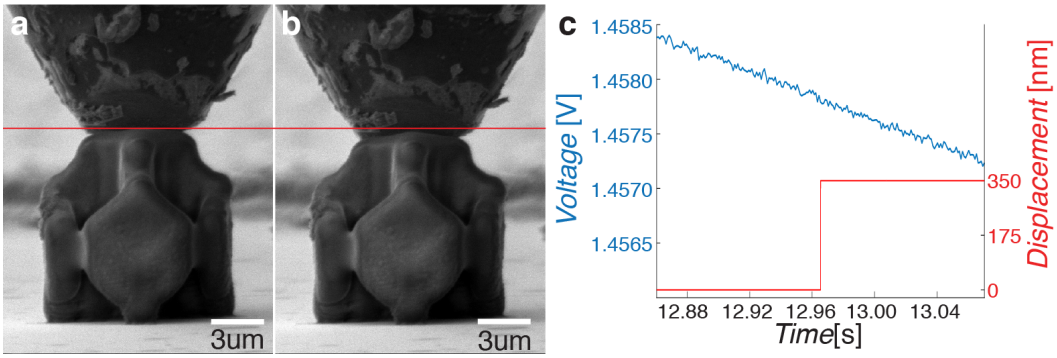

Figure 4.16: Electromechanical response of an architected zinc polymer structure. SEM images during a representative *in situ* experiment **a**. before and **b**. after ≈ 350 nm of compression. The red line serves as a guide to the eye. **c**. The OCV data shows no significant deviation from the baseline during the experiment.

The linear decrease in OCV observed over time was the background signal, and could be attributed to the experimental setup: the applied compression was determined by image analysis before and after each incremental displacement of the nanoindenter tip. The beam was turned off during the displacement of the tip. The constant imaging likely resulted in the build up of charge in the non-conductive structures, which then dissipated through the complex circuit over time. Much like a discharging capacitor, the long term OCV response decays exponentially [271], but due to the short time frames involved with each compression, the decay appears linear.

In contrast, compression of an architected ZnO structure showed a distinct voltage drop at the time of compression (Fig. 4.17). The difference between the two tests clearly proves that the ZnO structures have electromechanical properties. Furthermore, the OCV measurements did not short upon contact with the ZnO structures, which indicates that the residual carbon in the structures (Fig. 4.13) did not form an electrically conductive pathway.

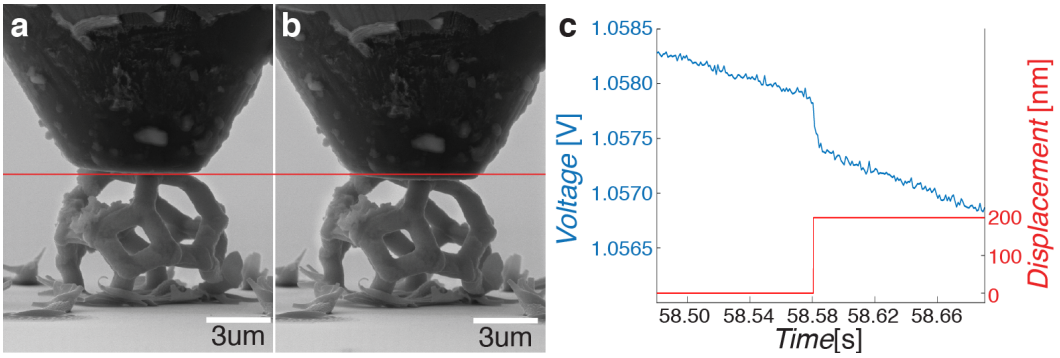

Figure 4.17: Electromechanical response of an architected ZnO structure. SEM images during a representative *in situ* experiment **a**. before and **b**. after ≈ 200 nm of compression. The red line serves as a guide to the eye. **c**. The OCV data shows a distinct drop of 0.52 mV at the time of compression.

It is important to emphasize that these tests were designed to determine if the structures could exhibit *an* electromechanical response. The electromechanical experimental setup is currently unable to precisely quantify the OCV response of the structure — the value of the voltage drop observed in Fig. 4.17 represents the voltage drop as measured using *this* system, and not the voltage response of the material itself. There are significant ongoing efforts to calibrate and validate the system for quantitative measurements.

The impact of grain size on the electromechanical response of the ZnO structures is also part of an ongoing investigation. The results from the TEM analysis (Fig. 4.14) clearly show that the fabricated materials are polycrystalline, so it was surprising that we were still able to exhibit an electromechanical response. One hypothesis is that because the structures are so small, there are insufficient grains for the dipole moments to completely cancel each other out, resulting in a small net dipole moment. A systematic study where the grain sizes are varied while keeping the overall structure size constant is currently underway.

4.9 Mechanical Properties of Architected ZnO Structures

To determine if these architected ZnO structures could withstand repeated loading, we performed cyclic compression experiments on these ZnO structures. These mechanical experiments were conducted using a separate commercial *in situ* setup as the custom-built electromechanical setup was unable to precisely control the displacement rate of the nanoindenter tip. The structures were compressed using a 15 μm diamond flat punch (Synton-MDP Ltd.) affixed to a nanoindenter (InSEM from Nanomechanics Inc.) installed in an SEM chamber (FEI Quanta 200F). A

displacement rate of 8 nm/s was used for the experiments.

Fig. 4.18 shows the results of the cyclic compression experiments on an individual ZnO tetrakaidecahedron unit cell.

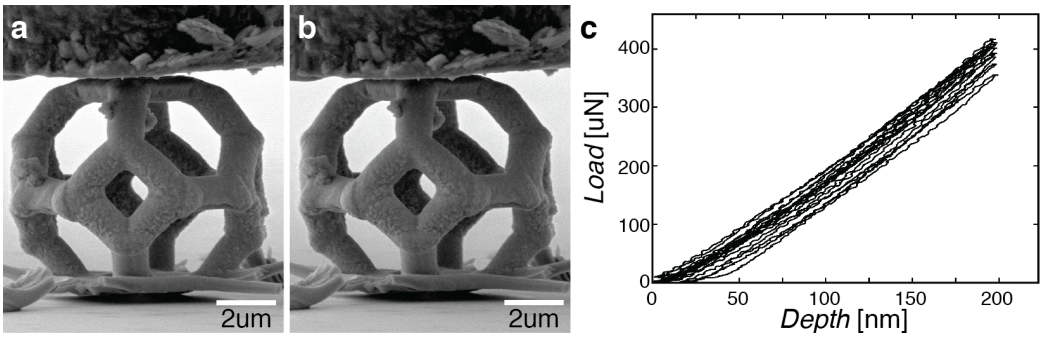

Figure 4.18: Cyclic compression experiments on ZnO structure. SEM images of the ZnO structure **a**. before and **b**. after 9 cycles of uniaxial compression of 200 nm. **c**. Load-displacement curves of the structure during cyclic loading.

The structure displayed no signs of catastrophic or localized failure even after 9 cycles of uniaxial compression of 200 nm. The load-displacement curves during cyclic loading showed no significant deviation from elastic behavior, with the displacement shifts observed likely due to drift during the experiment. Analysis of the load-displacement curves showed that the loading and unloading stiffness of the *structure* were 2.37 ± 0.15 kN/m and 2.52 ± 0.13 kN/m respectively. The stiffness values did not exhibit any discernible trends over the 9 cycles. The compressive strain to failure for these structures was determined to be ≈ 3.5 %. which was expected since ZnO is a brittle ceramic.

The results from the compression experiments indicate that these structures are able to withstand repeated loading. Although not experimentally shown, from the results so far, it is reasonable to expect an electromechanical response with each compression. These architected ZnO structures thus have the potential to be used as electromechanical device elements.

4.10 Summary and Outlook

In this chapter, we developed a new technique for the fabrication of 3D architected metal oxide structures using vat photopolymerization. This technique, called Photopolymer Complex Synthesis, utilizes a post-polymerization solution combustion synthesis reaction to convert a metal nitrate containing polymer into a metal oxide. As a demonstration of this technique, we used it with two-photon lithography to fabricate 3D architected ZnO structures with sub-micron features.

Using characterization techniques such as XRD, EDS, TGA, and TEM, we show that these structures were composed of monolithic polycrystalline ZnO. *In situ* compressions of these architected ZnO structures using a custom-build electromechanical setup also indicated that these structures had electromechanical capabilities.

The ability to fabricate architected piezoelectric structures at these scales is a significant step forward from the current state of the art, and could enable new 3D MEMS devices. More generally, photopolymer complex synthesis is a facile and accessible route to fabricating metal oxide structures. The potential versatility in the technique in fabricating other kinds of 3D multifunctional metal oxides has direct implications in a variety of fields, from chemical catalysis to energy storage, and could enable the production of previously impossible smart devices.

However, before we can get there, we need to develop a better understanding of this technique. The mechanism of metal oxide formation, the impact of resin formulation on microstructure, amongst others, are all important questions that need to be addressed. From a photoresin development perspective, there is also immense potential in exploring other kinds of metal salts, like acetates or chlorides, and binders, like acrylamide or acrylic acid, as they could lead to very interesting materials.

Finally, the work in this chapter highlights the utility of approaching materials development in additive manufacturing from a chemical reaction point of view. By printing "chemical reactors" — materials that contain all the necessary reagents for a subsequent reaction — we will be able to tap into the vast array of reactions developed by the materials chemistry community to expand the library of materials compatible with additive manufacturing.

Chapter 5

PHOTOPOLYMER COMPLEX SYNTHESIS OF ARCHITECTED COMPLEX METAL OXIDE CATHODES

Chapter Abstract

In the previous chapter, we explored a new technique called photopolymer complex synthesis, and how it could be used with two-photon lithograpy to fabricate multifunctional *binary* metal oxides at the micron/sub-micron scales.

This chapter seeks to expand on this technique by fabricating *complex* metal oxides at larger scales. We demonstrate this with the fabrication of lithium cobalt oxide using a digital light processing printer. We discuss the impact of photoresin formulation on material microstructure and highlight its use as a 3D architected lithium-ion battery cathode.

This chapter has been adapted from:

1. Yee*, D. W., Citrin*, M. A., Taylor, Z. W., Saccone, M. A., Victoria, T. & Greer, J. R. Aqueous Salt Solutions As a Platform for Additive Manufacturing of Architected Complex Metal Oxides. *In Preparation* (2020).

Contributions: participated in the conception of the project, developed the polymer chemistry, fabricated the structures, performed the material characterizations, and wrote the manuscript.

5.1 Complex Metal Oxides via Photopolymer Complex Synthesis

Complex metal oxides are oxides that contain two or more different cations. These cations often have different oxidation states, ionic radii, and coordination numbers, which result in the formation of significantly more complex crystal structures compared to those of simple binary oxides. The diversity and complexity of these structures are responsible for some of the multifunctional properties that these materials can exhibit [272]. For example, perovskites oxides have the chemical formula ABO_3, with A and B being different cations, and their layered structure gives rise to its dielectric, optical, and piezoelectric properties, amongst others [273].

As discussed in the previous chapter, there is considerable interest in architecting these metal oxide materials via additive manufacturing. In particular, vat photopolymerization (VP) of these materials has garnered significant attention due to the high resolutions and throughput achievable [57, 100, 274]. However, the increased complexity in the elemental composition of these complex metal oxides often presents an additional challenge for the slurry and inorganic-organic photoresins VP approaches that are commonly used.

With the slurry method, fabrication of these materials is relatively straightforward if the complex metal oxides can be readily obtained as powders [275–277]. However, when this is not the case, a combination of different powders has to be used instead (Fig. 5.1a). The powders are mixed such that the overall stoichiometry of the elements results in that of the desired complex metal oxide [278–280]. The formation of the final material is thus dependent on a solid state reaction, which requires high temperatures, and can often result in compositional inhomogeneity [281].

The inorganic-organic approach runs into a similar issue — polymers/monomers with the appropriate metal heteroatoms need to be combined with the right stoichiometry to reach the desired composition of the complex metal oxide (Fig. 5.1b). These metal inorganic-organic compounds can be difficult to synthesize/obtain and might have issues with stability. There are only a few examples of this described in the literature, all of which have focused on fabricating glasses [248, 249], but the concept of mixing metal containing monomers/polymers still stands.

Photopolymer complex synthesis (PCS) presents itself as a facile and accessible approach to fabricating complex metal oxides. As discussed in the previous chapter, PCS utilizes an aqueous photoresin, that contains dissolved metal nitrates, with

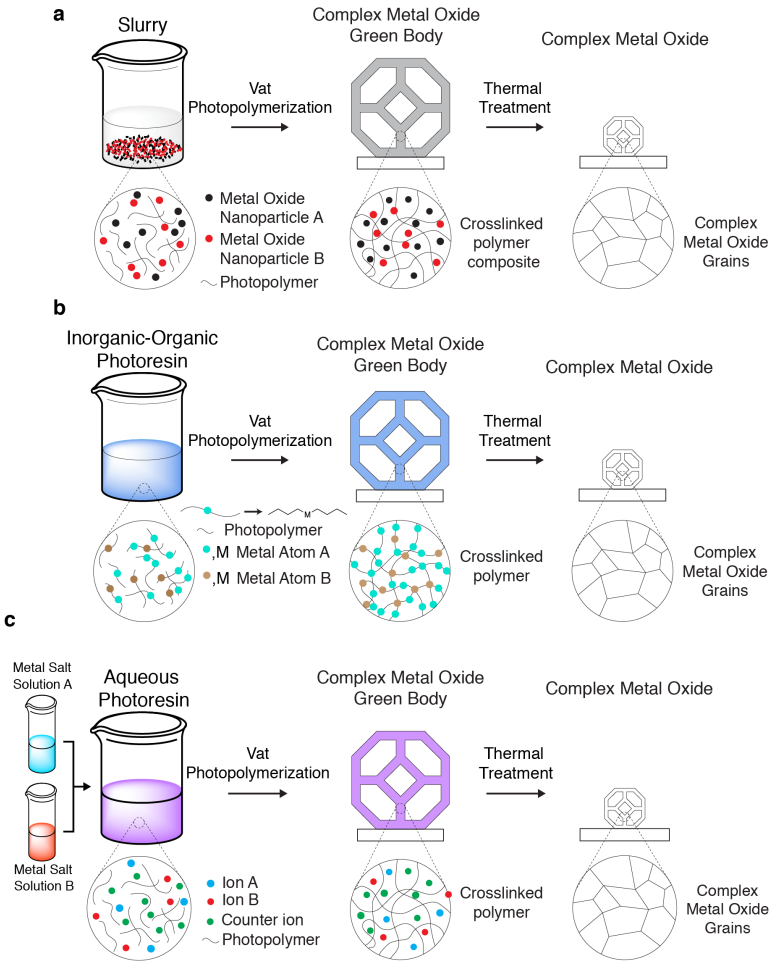

Figure 5.1: Schematic of **a**. slurry approach, **b**. inorganic-organic photoresin approach, and **c**. photopolymer complex synthesis for fabricating complex metal oxides with vat photopolymerization. The schematic shown in **a** is for when the complex metal oxide cannot be directly obtained in powder form.

vat photopolymerization to fabricate metal nitrate containing polymer structures. Calcination of these structures then initiates a solution combustion synthesis reaction for the *in situ* formation of the metal oxide.

The use of aqueous metal salt solutions as precursors provides a unique opportunity to fabricate complex metal oxides as the identity and stoichiometry of the precursors can be precisely and simply controlled. The metal salts just need to be dissolved in the desired ratios to prepare the precursor solution (Fig. 5.1c). Furthermore, the use of solutions means that the metal cations are mixed at the molecular level, preventing any issues with inhomogeneity [258].

In this chapter, we will explore the use of PCS in fabricating architected complex

metal oxides. We demonstrate this with the fabrication of lithium cobalt oxide (LCO), and highlight how 3D architected LCO can be used to potentially improve the performance of lithium-ion batteries (LIBs).

5.2 Architected Complex Metal Oxides for Lithium-Ion Battery Cathodes

The lithium-ion battery (LIB) is currently the most successful rechargeable battery today. Despite being in use for over three decades[1], there is still significant research activity in the field — most of which is focused on improving the performance of LIBs to meet the increasingly demanding energy storage needs of society [282].

In brief, a LIB consists of a cathode, anode, electrolyte, separator, and two current collectors. Lithium ions are stored within the cathode and the anode. During discharging, the lithium ions are extracted from the anode and travel through the separator to the cathode via the electrolyte, while the electrons reach the cathode via an external circuit. Charging of the LIB reverses this process (Fig. 5.2a).

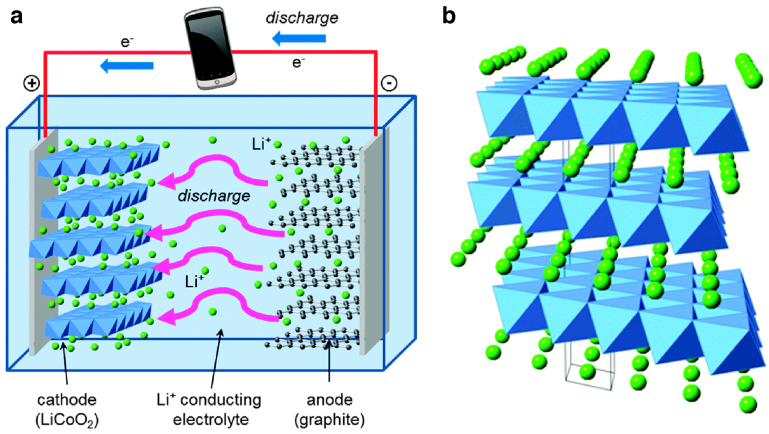

Figure 5.2: a. Schematic diagram of a lithium ion battery. During discharging, lithium ions flow from the anode to the cathode through the electrolyte, while electrons flow via the external circuit and generate power. The separator is not shown. **b**. Representative crystal structure for layered lithium cobalt oxide. Lithium is shown in green, and CoO_6 octahedra in blue. The black lines highlight one unit cell. Images reproduced from [283] - Published by the Royal Society of Chemistry, and is under the Creative Commons Attribution 3.0 Unported License.

The cathode material is often a lithium transition metal oxide, of which the most commonly used one is lithium cobalt oxide ($LiCoO_2$, LCO), which has an α-$NaFeO_2$ type crystal structure (Fig. 5.2b) [282]. The anode is typically graphite. As the capacity of the LIB is fundamentally linked to the amount of lithium ions that the

[1]And winning the Nobel Prize in Chemistry in 2019 along the way.

electrodes can host, most of the research in the community has been focused on discovering new materials that are able to host more lithium ions [284].

A complementary approach to improving the performance of LIBs without changing the underlying materials chemistry is to optimize the design of the battery. This has the potential to allow us to use known materials that already have higher capacities, but are incompatible with the current conventional LIB designs. For example, pure lithium is an ideal anode material [285]. However, the formation of lithium dendrites during charging can cause a short-circuit if the dendrites penetrate through the separator and come into contact with the cathode (Fig. 5.3). This is especially concerning with the use of liquid electrolytes, which are typically flammable and could lead to an explosion [286, 287].

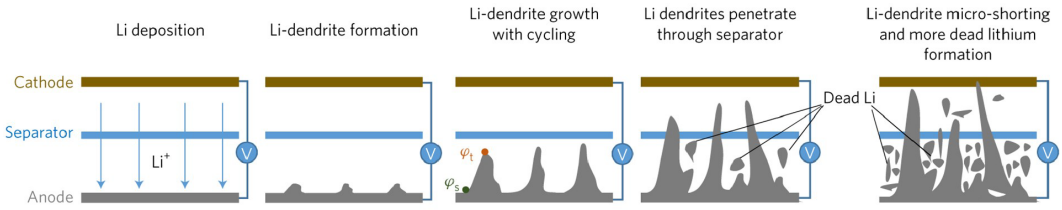

Figure 5.3: Schematic of LIB short-circuit via lithium dendrite formation from using a lithium anode. Reproduced with permission from Liu et al. [287] Copyright (2017) Springer Nature: Nature Energy.

The use of a solid electrolyte (SE) can address this by suppressing the penetration of the lithium dendrites. However, some of the most promising SEs are oxide ceramics which are extremely brittle [288]. This becomes a challenge when it comes to integration into conventional LIB "jelly-roll" designs, where the anodes and cathodes are thin slurry films wound around a central post (Fig. 5.4). The brittle SEs would likely fracture in this configuration [289].

The reason why LIBs have converged on this jelly-roll design is that it allows for large energy densities while maintaining thin electrode layers. Thin film electrodes suffer from low energy densities due to their low mass, but have exception power densities due to the reduced transport lengths for lithium ions and electrons. Increasing the thickness of the electrodes would increase the energy density but at loss of power density [291] (Fig. 5.5). The jelly-roll design thus circumvents this and allows for an increase in electrode masses without increasing the film thickness.

Over the past decade, there has been a growing interest in using 3D architected electrodes to replace this jelly-roll design [292]. By using architecture, tall electrodes

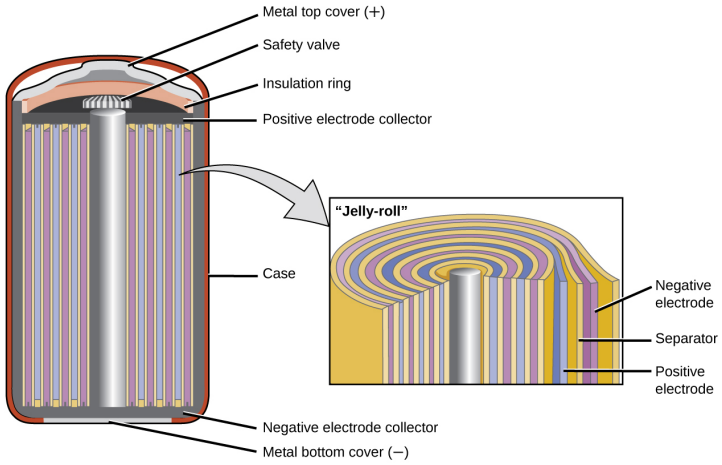

Figure 5.4: Schematic of "jelly-roll" LIB design. Reproduced from [290] under the Creative Commons Attribution 4.0 International License.

with thin feature sizes can be fabricated, effectively increasing the mass loading while still maintaining the short lithium ion and electron transport lengths (Fig. 5.5).

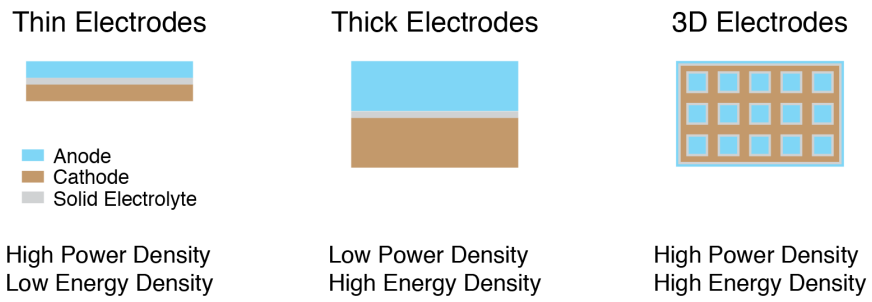

Figure 5.5: Schematic of LIB design with (left) thin electrodes, (center) thick electrodes, and (right) 3D electrodes.

Additive manufacturing (AM) is a promising route to creating these 3D electrodes and has been explored extensively in recent years. However, almost every demonstration of it so far has revolved around the extrusion of nanoparticle inks [293–295], which places an inherent limitation on the resolutions and geometries possible. Vat photopolymerization techniques offer better resolutions and are able to access more complex geometries, but have struggled with fabricating these non-polymeric electrode materials.

5.3 Photopolymer Complex Synthesis of Lithium Cobalt Oxide

PCS presents itself as a suitable approach to fabricating these complex metal oxide LIB cathode materials. To demonstrate this, we used PCS to fabricate architected

LCO structures with digital light processing (DLP) printing. We chose LCO as a candidate material because of its well-understood electrochemical properties and its common use as a LIB cathode material [296].

5.3.1 Li/Co Photoresin Preparation

The fabrication of complex metal oxides with DLP printing has several implications for the preparation of the photoresin. First, unlike the binary oxide photoresin demonstrated in the previous chapter, the amount of each metal nitrate used here affects both the final composition of the oxide and the amount of shrinkage observed. In addition, the use of DLP, a one-photon absorption photopolymerization process, means that we will need to use a UV-absorbing dye as well. This is to control the depth of photopolymerization during UV exposure.

Since we are now working with multiple different salts, it is easier to use stock solutions so that the desired stoichiometric ratios can be easily achieved. Thus, to prepare the Li/Co photoresins, 2.67 molar stock solutions of lithium nitrate (ReagentPlus, Sigma-Aldrich) and cobalt(II) nitrate hexahydrate (≥ 98 %, Sigma-Aldrich) were first prepared with deionized water, and then mixed together in a 1:1 volume ratio to give the metal precursor solution. 2.67 molar solutions were used as it was close to the solubility limit for the cobalt solution.

The metal precursors were then mixed with poly(ethylene glycol) diacrylate M_n = 575 (PEGda, Sigma-Aldrich) at a prescribed volume ratio to form a maroon solution. Tartrazine (TZ, ≥ 85 %, Sigma-Aldrich), a UV-absorbing dye, and lithium phenyl-2,4,6-trimethylbenzoylphosphinate (LAP, ≥ 95 %, Sigma-Aldrich), a photoinitiator, were then dissolved in water (10 vol % of the metal nitrate/PEGda solution) to give a bright yellow solution. The amount of LAP and tartrazine were fixed at 2.5 mg and 0.5 mg per mL of metal nitrate/PEGda. The photoactive solution was then added to the metal nitrate/PEGda solution to yield a homogeneous orange solution (Fig. 5.6).

The amount of photoinitiator and UV-absorbing dye were decided using an iterative approach where the goal was to maximize the print speed and z-layer resolution of the photoresin. The prepared resins had viscosities similar to that of water, and were used directly after mixing. The resins were observed to be stable for upwards of six months.

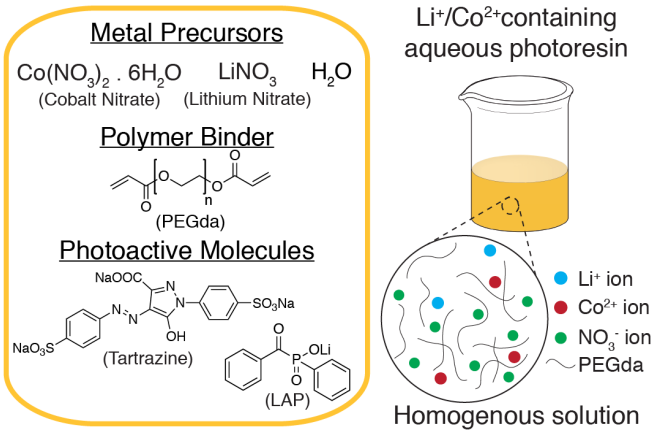

Figure 5.6: Li/Co Photoresin formulation.

5.3.2 Proof of Concept Experiments

We first wanted to verify that these Li/Co photoresins could produce LCO. We prepared a photoresin using the procedure above with 60 vol% of PEGda. The tartrazine was also omitted to allow for more efficient UV curing. 1.5 mL of the casting photoresin was then poured into a polydimethylsiloxane circular mold 4 cm in diameter and cured with a UV curing lamp (405 nm, 60 W, Peopoly) for 10 minutes to give the cast polymer. The cast polymer was transparent and showed no signs of phase separation or precipitation.

The cast polymer was then calcined in a vacuum furnace (MTI OTF-1500X) in a quartz tube (1m in length, 92mm inner diameter) to give a brittle black material. The temperature profile was as follows: a ramp to 700 °C at 1 °C/min. The sample was held at 700 °C for 3 hours, before cooling to room temperature at 2 °/min. 700 °C was chosen as the maximum temperature because previous work on the combustion synthesis of LCO showed that it resulted in high specific discharge capacities [297].

The calcined polymer was pulverized between two glass slides and then investigated with X-ray diffraction (XRD). XRD (PANalytical X'Pert Pro) data was collected at 45 kV and 40 mA using a Cu source. The XRD spectrum of the calcined polymer is shown in Fig. 5.7 below.

The XRD spectrum from the calcined Li/Co cast polymer had sharp diffraction peaks that were in good agreement with that of LCO (ICSD #51182). It is unclear if there were any other impurities in the material due to the strong fluorescence of cobalt with Cu kα X-rays. This strong background signal could have masked the signals from any non-cobalt phases.

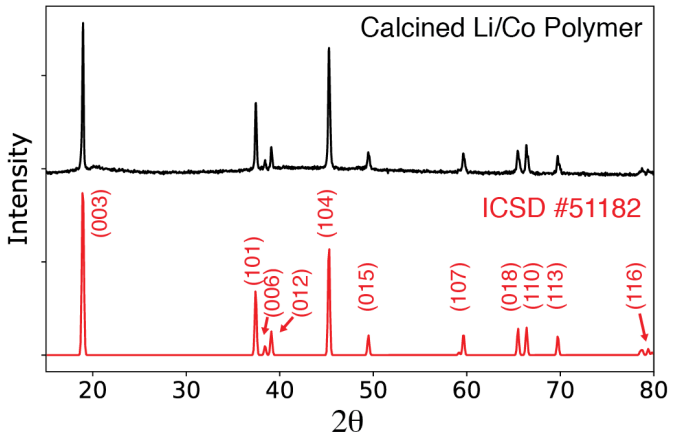

Figure 5.7: XRD spectra of calcined cast Li/Co polymer and LCO reference.

5.3.3 Digital Light Processing Printing of Li/Co Photoresin

A commercial DLP printer, the Autodesk Ember, was used to directly fabricate 3D Li/Co hydrogel cubic lattices from the Li/Co photoresins. Cubic lattices with unit cell length of 850 μm and beam thicknesses of approximately 150 μm were designed. The unit cells were arranged in a circular array to best fit the area of the coin cell that would be used for subsequent electrochemical testing (Fig. 5.8a). The design can be broken down into two separate pattern slices (Fig. 5.8b), and it was found that Slice B typically needed approximately twice the UV exposure of Slice A for the structure to be fabricated properly. This was suspected to be due to the fragility of these small features, resulting in them needing additional cross-linking to survive the fabrication process.

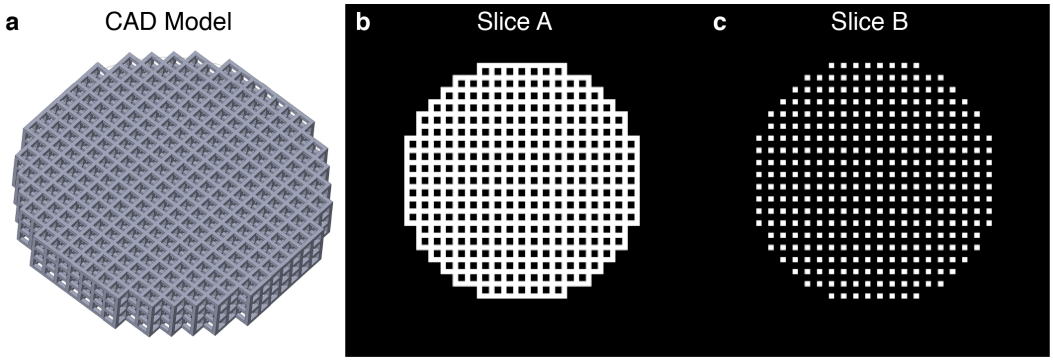

Figure 5.8: **a**. Computer-aided design model of cubic lattices. **b, c**. The two different slice patterns that make up the model.

The fabricated structures were not developed in any solvent to prevent ion-leaching from occurring. The excess photoresin was removed using compressed air. The size

of the printed lattices were approximately 16 mm in diameter and 3 mm thick. Cubic lattices were chosen as they exemplified a design that could be easily fabricated with DLP printing, but were challenging with other manufacturing techniques. The simultaneous formation of an entire layer allows for the fabrication of even 90° overhangs, allowing for the fabrication of other complex geometries.

The use of this resin with DLP presented a few complications that were not observed with two-photon lithography. The exposure parameters for these lattices varied with the amount of PEGda in the photoresin (more on this below), with the exposure needed increasing as the concentration of PEGda decreased. The increased exposure can lead to unwanted polymerization beyond the plane of exposure, resulting in defects in the fabrication (Fig. 5.9a). Optimizing the ratio of photoinitiator to UV-absorbing dye helps to improve the resolutions achievable (Fig. 5.9b).

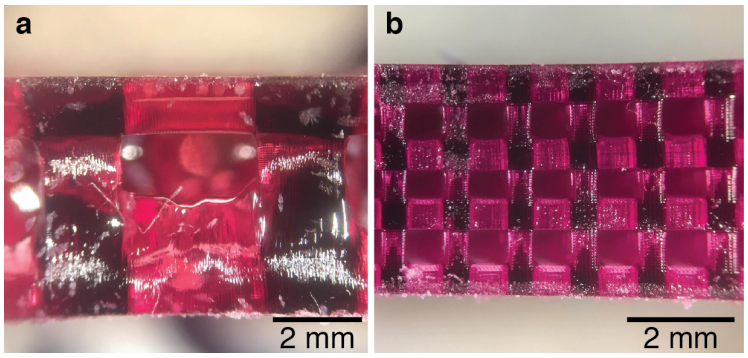

Figure 5.9: **a**. Poor print resolution due to imbalances in photoinitiator to UV-absorbing dye ratio. **b**. Significantly improved print resolutions with optimized ratio. These were made with a different UV-absorbing dye, hence the non-orange color, but the point still stands.

An additional complication is that due to the setup of the DLP printer, the resin is exposed to the atmosphere during fabrication. This results in the evaporation of water over time, leading to a gradual increase in the concentration of all the reagents. The rate of evaporation is also not strictly linear since the viscosity of the photoresin increases with the concentration of PEGda. The implication of this is that the exposure parameters change over time, with the amount of exposure needed decreasing as a function of time. The amount of shrinkage experienced after calcination will also decrease since there will be less shrinkage due to water loss.

To allow us to make the assumption that the fabricated Li/Co hydrogels had the same composition as that of the as-prepared photoresin, we used each photoresin

for a maximum of three hours. The change in photoresin properties as a function of evaporation time is still a subject of ongoing investigation.

5.4 Architected LCO Structures

The Li/Co hydrogels lattices were calcined at 700 °C to obtain the corresponding black LCO cubic lattices (Fig. 5.10). The temperature was ramped up to 500 °C at 0.25 °C/min, then to 700 °C at 2 °C/min, held at 700 °C for 3 hours, and then cooled at 2 °C/min to room temperature, all at a reduced air pressure of 20 Torr. The reduced pressure was achieved by flowing compressed air into the tube at a flow rate of 250 standard cubic centimeters per minute (SCCM) while a pump evacuated the tube. The reduced pressure and slow ramps were used to impede the combustion reaction and minimize the rate of outgassing volatiles. Lattices that were calcined under atmospheric conditions either fragmented or experienced significant warping during the process.

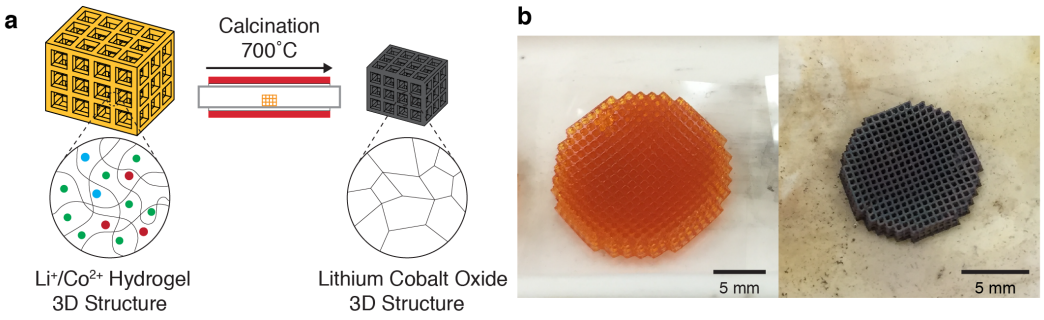

Figure 5.10: Architected LCO cubic lattices **a**. Schematic of the calcination process. **b**. Representative images of Li/Co polymer lattice (left) and LCO lattice (right).

The calcined lattices had self-similar architectures as their hydrogel precursors, but experienced a substantial amount of shrinkage and mass loss. As discussed in the previous chapter, the extent of shrinkage and mass loss is dependent on the ratio of metal salt to binder used. However, what is less immediately obvious is that the extent of porosity is also heavily dependent on the amount of polymer in the system. Since porosity is likely detrimental to the performance of the material, it is worth investigating this in more detail.

5.4.1 Cross-sectional Analysis of Porosity within LCO Structures

The general equation for the combustion synthesis of LCO with PEGda ($C_{26}H_{46}O_{13}$) can be represented by the following equation:

$$LiNO_3 + Co(NO_3)_2 \cdot 6H_2O + n_{PEGda}C_{26}H_{46}O_{13} + (31n_{PEGda} - 3.5)O_2 \\ = LiCoO_2 + (23n_{PEGda} + 6)H_2O + 1.5N_2 + 26n_{PEGda}CO_2 \quad (5.1)$$

where n_{PEGda} is the mol ratio of PEGda to $Co(NO_3)_2 \cdot 6\ H_2O$. In this simplified model, it is assumed that the only decomposition products are H_2O, N_2, and CO_2. However, it still shows that for every mole of LCO formed, (49 n_{PEGda} + 7.5) moles of gas are evolved. The significant amount of gas evolved results in internal porosity within the material [298], as we shall see below as well.

To determine the impact of n_{PEGda} on the microstructure of the lattices, we used photoresins with different volume ratios of metal salt solutions to PEGda, corresponding to $n_{PEGda} \approx$ 2.2, 1.0, 0.5, and 0.4. The precise compositions of the photoresins are shown in Table 5.1.

Name	**n_{PEGda}**	**Li soln (mL)**	**Co soln (mL)**	**PEGda (mL)**	**LAP (mg)**	**TZ (mg)**	**Water (mL)**
I	2.2	20.0	20.0	60.0	250	50	10.0
II	1.0	30.0	30.0	40.0	250	50	10.0
III	0.5	37.5	37.5	25	250	50	10.0
IV	0.4	40.0	40.0	20.0	250	50	10.0

Table 5.1: Composition of Li/Co photoresins with different values of n_{PEGda}.

The theoretical amount of gas evolved as a function of n_{PEGda}, as determined via Equation 5.1 for these four different photoresins compositions, is shown in Fig. 5.11 below.

Lattices made from photoresin I and II exhibited a significant amount of cracks on their surfaces, as would be expected from the relatively large amount of gases evolved. At lower n_{PEGda} values (Photoresin III and IV), little to no cracking was observed on the surfaces of the lattices. These cracks could be clearly seen from the scanning electron microscope (SEM) images taken of the surface of the lattices (Fig. 5.12a, b) The images were taken using an FEI Versa 3D DualBeam at an accelerating voltage of 10 kV.

The periodic "diamond" arrays observed on all the lattices were due to the pixel pattern of the DLP printer [299]. Further analysis of the surface features indicated

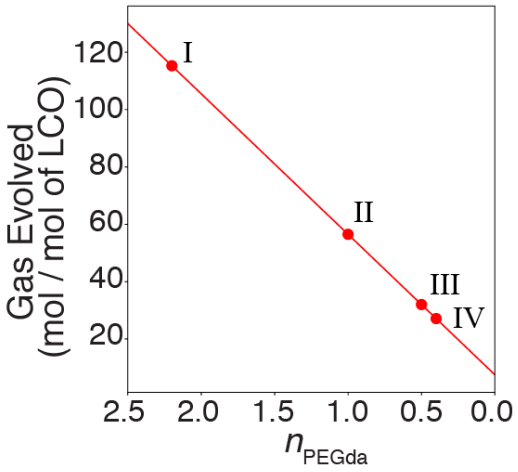

Figure 5.11: Theoretical amount of gas evolved per mole of LCO formed as a function of n_{PEGda}, as determined via Equation 5.1.

that they were comprised of partially sintered faceted particles approximately 153 ± 88 nm in size (mean ± standard deviation, n = 72) (Fig. 5.12c, d).

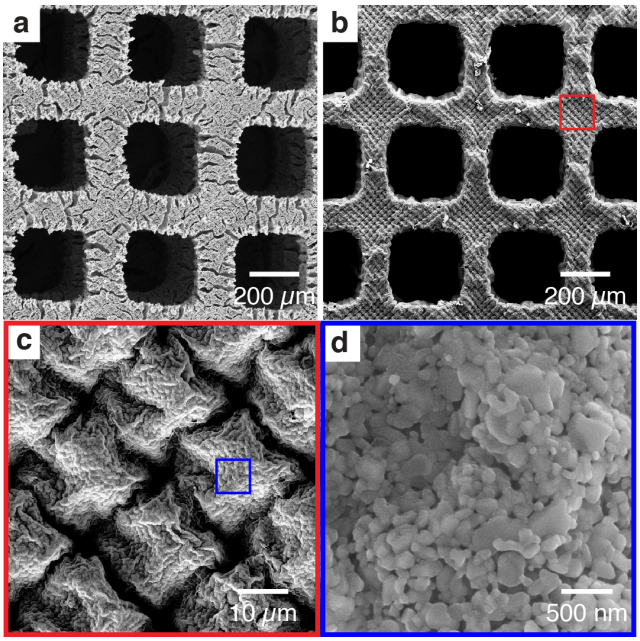

Figure 5.12: Surface microstructure of LCO lattices made from **a**. photoresin I, II and **b**. photoresin III, IV. **c**. Zoomed-in microstructure of the red region outlined in **b**. **d**. Zoomed-in microstructure of the blue region outlined in **c**.

To determine the level of porosity within the structure, a gallium focused ion beam (FIB) (FEI Versa 3D DualBeam) was used to make cross-sections of the nodes of the lattice. Since large cross-sections had to be made, FIB milling was conducted

at an accelerating voltage of 30 kV and a current of 65 nA, followed by cleaning at 16 kV and 42 nA.

Large pores at least 80 μm in size were found in the lattices made from the n_{PEGda} $\approx$ 2.2 photoresins (Fig. 5.13a), which were then replaced with large cracks $\approx$ 10 μm wide as n_{PEGda} decreased to 1.0 (Fig. 5.13b). As n_{PEGda} decreased further, the number of large cracks decreased qualitatively, with the largest cracks having crack widths $\approx$ 5 μm wide (Fig. 5.13c, d). These results indicated that photoresin formulations with lower n_{PEGda} resulted in better quality LCO structures. Attempts were made to reduce the n_{PEGda} value further, but it was challenging to fabricate self-supporting structures with such low binder contents.

Based on the FIB cross-section analysis, we decided to focus on the $n_{PEGda} \approx 0.4$ photoresins. In addition to the one described in Table 5.1, we formulated another photoresin with $n_{PEGda} \approx 0.4$, but with 5 mol% excess Li precursor. This was done to compensate for the volatilization of lithium during the combustion process [300, 301]. Cross-sections of these nodes revealed a similar microstructure (Fig. 5.13e) to its stoichiometric counterparts, with the presence of micropores and sub-micron pores. For ease of reference, structures made from the stoichiometric $n_{PEGda} \approx 0.4$ photoresin are labeled as LCO-s, while those made from $n_{PEGda} \approx 0.4$ with excess lithium are labeled as LCO-e.

It is also worth noting that this level of porosity was not observed in the zinc oxide structures in the previous chapter. This was likely due to the small sizes of the structures fabricated using two-photon lithography, which reduced the diffusion distances for the gases evolved during combustion to escape.

5.4.2 Estimated Porosity in $n_{PEGda} \approx 0.4$ Structures

The LCO-s and LCO-e lattices were observed to have the densest microstructures, having no large pores and the smallest cracks. However, the presence of micropores was still observed in the cross-sections and surface microstructures (Fig. 5.12, 5.13).

We can estimate the porosity within the structures by comparing the theoretical shrinkages and mass losses with the experimentally determined values. The theoretical shrinkage can be determined using a simple model, similar to what was described in the previous chapter, by assuming: a) each mole of Li^+ and Co^{2+} ions in the Li/Co hydrogel is combined to form a mole of LCO; b) the calcined structures are pure LCO; and c) the calcined structures have self-similar architectures as their polymer predecessors, only exhibiting changes in dimension.

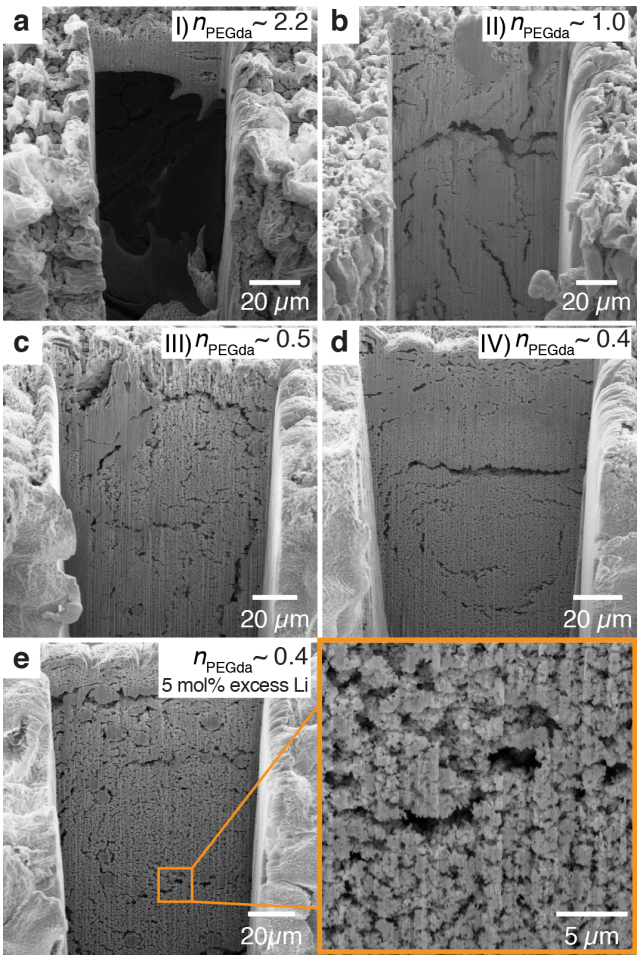

Figure 5.13: FIB cross-sections of LCO lattices made from photoresins with **a**. $n_{PEGda} \approx 2.2$, **b**. $n_{PEGda} \approx 1.0$, **c**. $n_{PEGda} \approx 0.5$, **d**. $n_{PEGda} \approx 0.4$, and **e**. $n_{PEGda} \approx 0.4$ with 5 mol% excess Li. Cracks, micropores and sub-micron pores were observed in the microstructures.

Thus, for a particular volume of polymer, $V_{polymer}$, the shrinkage experienced to obtain the volume of calcined LCO, V_{LCO}, can be given as[2]:

$$\begin{aligned} TheoreticalLinearShrinkage &= \left(1 - \sqrt[3]{\frac{V_{LCO}}{V_{polymer}}}\right) \times 100 \\ &= \left(1 - \sqrt[3]{\frac{m_{CN,polymer} \cdot Mw_{LCO}}{Mw_{CN} \cdot \rho_{LCO} \cdot V_{polymer}}}\right) \times 100 \end{aligned} \tag{5.2}$$

where $m_{CN,polymer}$ is the mass of cobalt nitrate hexahydrate in the polymer, Mw_{CN} and Mw_{LCO} the molecular weight of cobalt nitrate hexahydrate and LCO

[2]See Chapter 4, Section 1.6.1 of this thesis for more details.

respectively, and ρ_{LCO} the density of LCO. The theoretical mass loss can also be determined by making similar assumptions, and can be approximated by:

$$MassLoss = \left(1 - \frac{m_{CN,polymer} \cdot Mw_{LCO}}{Mw_{CN} \cdot m_{polymer}}\right) \times 100 \tag{5.3}$$

where $m_{polymer}$ is the mass of the polymer structure. The $n_{PEGda} \approx 0.4$ photoresins contained 31.1 g of cobalt nitrate hexahydrate in 110 mL of photoresin, the total mass of which was 131.1 g. The molecular weight of LCO and cobalt nitrate hexahydrate were taken to be 97.87 g/mol and 291.3 g/mol respectively. The density of bulk LCO was taken to be 5.05 g/cm^3. Using the equations above, the theoretical shrinkage and mass loss were determined to be 73.4% and 92.0% respectively.

The experimental shrinkage and mass loss of the LCO structures were found to be 43.8% and 92.2% respectively. While the experimentally determined mass loss closely matched that of the theoretically evaluated value, the shrinkage values were significantly different. This discrepancy between the theoretical and experimental shrinkage is attributed to the porosity in the material.

One approach to estimating the porosity is to compare the measured mass of the lattice to the expected mass of the lattice based on the volume of the structure. The calcined lattices had, on average, beam thicknesses of 100 μm and a unit cell length of 500 μm. Using a CAD model to construct a lattice with the same number of unit cells but with these dimensions, we obtain a lattice of volume 13.54 mm^3. Taking the density of LCO as 5.05 mg/mm^3, we obtain a theoretical mass of 68.4 mg. However, the average mass of the calcined lattices was 29.9 mg. Taking the ratio of the difference in masses to the mass expected based on the volume of the structure, we obtain an estimated microstructure porosity of 56.3 %.

Another approach is to compare the actual linear shrinkage to the theoretical shrinkage. By finding the difference between the expected size of the lattice (26.5% of the original diameter) to the actual size of the lattice (56.3% of the original diameter), we can estimate the porosity to be 52.9%, which is consistent with the value from the mass approach. The difference between the values obtained by the two methods is likely due to the fact that the lattices are not perfectly periodic or smooth, which will influence the accuracy of the computed volume of the lattice.

The microscale porosity of the cross-section of the lattice (Fig. 5.13e) was also determined via SEM image analysis. Using ImageJ, we determined the porosity

in that cross-section image to be approximately 31%. The discrepancy between this number and the calculated porosity of ≈ 55% was due to the presence of cracks and/or large pores throughout the structure. Furthermore, the accuracy of the ImageJ analysis is influenced by the choice of the threshold brightness value that is used to distinguish between a grain and a pore. Given that the cross-sections are imaged at an angle, with shadowing effects due to the surrounding materials, the brightness of the cross-section is not constant throughout the height of the cross-section image. Consequently, the brightness threshold value is not constant throughout the field of view.

The porosity of ≈ 55% is significant and is responsible for the poor mechanical strength of these lattices. The porosity can potentially be decreased by: a) using even lower values of n_{PEGda}, b) higher concentrations of metal salts, and c) the use of a post-calcination sintering step to densify the material. Changing the underlying chemistry to move towards a more controlled reaction is another approach that is currently being explored, and will be addressed in the next chapter.

5.5 Characterization of LCO Structures

The LCO-s and LCO-e lattices were further characterized using XRD and energy-dispersive X-ray spectroscopy (EDS).

5.5.1 X-ray Diffraction

The LCO-s and LCO-e lattices were each pulverized between two glass slides to obtain a fine powder, and then subjected to XRD. Similar to the proof of concept experiments, the XRD spectra from the pulverized lattices showed peaks that were consistent with the hexagonal α-$NaFeO_2$ layered structure expected of LCO (Fig. 5.14).

From the peak positions, we determined the c/a ratio for both LCO-s and LCO-e materials to be 4.98, which is close to the 4.99 value expected for compositionally stoichiometric LCO ($LiCoO_2$) [302]. The ratio was used to account for any systematic peak shifts that could occur from the instrument or the experimental setup. It is also important to emphasize again that due to the fluorescence from cobalt, it is difficult to ascertain if there were any other non-cobalt based impurities in the material. The peaks from these phases (if any) would be masked by the large background signal.

A common metric used to estimate the degree of cation mixing within the layers

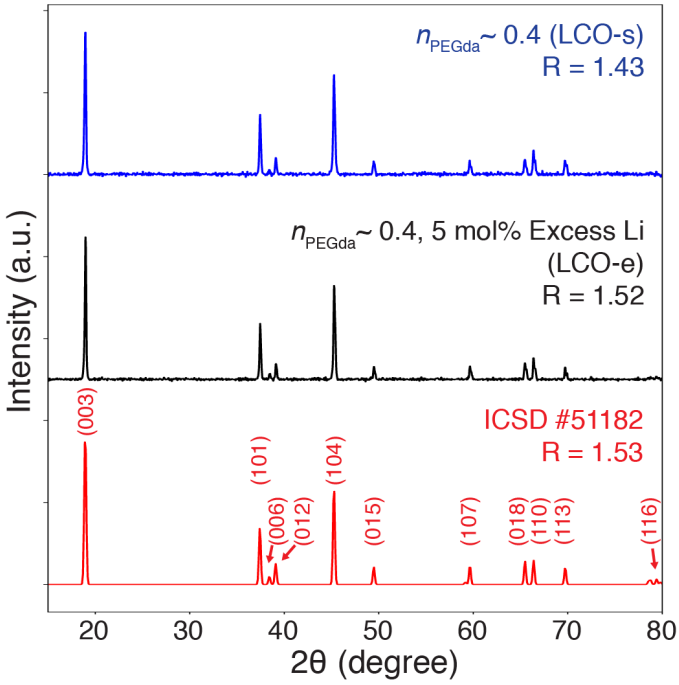

Figure 5.14: XRD spectra of LCO-s and LCO-e lattices. Both showed peaks consistent with a standard for LCO.

is the peak intensity ratio, R, between $I_{(003)}$ and $I_{(104)}$. The higher the value of R above 1.2, the better the cation ordering within the material [303, 304]. The R values for the LCO-s and LCO-e materials were determined to be 1.42 and 1.52 respectively, signalling that the cations in both structures were well ordered. The larger R value for LCO-e was likely due to the improved compositional accuracy from the compensation of lithium loss during combustion.

5.5.2 Energy-dispersive X-ray Spectroscopy

Given the higher value of R for the LCO-e material, further tests were only done with the LCO-e lattices. EDS was then used to determine the composition of the lattice, the results of which are shown in Fig. 5.15 below. EDS data was collected using a Zeiss 1550 VP FESEM equipped with an Oxford X-Max SDD EDS system. The applied voltage was 10kV.

EDS elemental mapping of the LCO-e lattices showed a homogeneous distribution of cobalt and oxygen throughout the structure (Fig. 5.15a). Lithium was not detected due to limitations with the detector used in the setup. The combined at% of impurities was 7.5 at%, assuming an equivalent percentage of lithium and cobalt (Fig. 5.15b). A considerable amount of the impurities was carbon (6.4%), which was

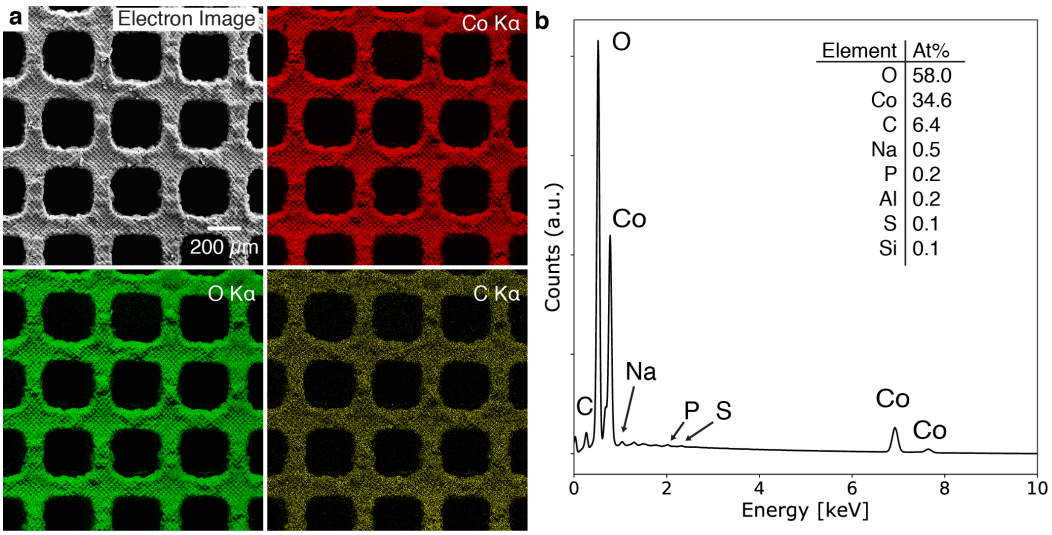

Figure 5.15: EDS analysis of LCO-e lattices. **a**. Elemental maps of cobalt, oxygen and carbon. **b**. EDS spectrum highlighting the composition of the material.

likely due to the incomplete combustion of the PEGda during the synthesis. Sulfur, phosphorous, and sodium were also uniformly distributed throughout the structure, and were attributed to residue from the UV-absorbing dye and the photoinitiator (Fig. 5.6). Aluminium and silicon were only found in small patches, and were likely due to contaminants from the quartz tube or during the transfer process.

Interestingly, the ratio between oxygen and cobalt, based on the at% of the elements determined via EDS, was 1.68, which is significantly less than the 2.00 expected from compositionally stoichiometric LCO. Although quantification of light elements in EDS is relatively inaccurate, with the amounts varying by a few at%, this discrepancy is still significant. We suspect that the calcination of LCO at the reduced pressure of 20 Torr resulted in oxygen-deficient LCO, although it is currently unclear if this is the case. Efforts are currently underway to investigate the relationship between calcination conditions and the material composition.

It is worth noting that previous work in the literature has suggested that XRD is unable to detect this oxygen deficiency since the material still exhibits the same long-range order as its stoichiometric counterparts [305]. Techniques such as inductively coupled plasma - optical emission spectrometry (ICP-OES), X-ray photoelectron spectroscopy (XPS), and Raman spectroscopy will need to be used as well to provide a more comprehensive understanding of the synthesized material.

5.6 Electrochemical Performance of Architected LCO Cathodes

To demonstrate the potential of these architected LCO-e lattices as LIB cathodes, we performed both cyclic voltammetry (CV) and electrochemical cycling on these LCO-e materials.

5.6.1 Cyclic Voltammetry on LCO-e Slurry Electrodes

CV was first used to electrochemically characterize the material, by determining the characteristic voltages where electrochemical reactions occurred. This would be reflected as peaks in current at those voltages. The procedure for preparing the slurry electrode coin cell is as follows:

LCO-e lattices were crushed by vortexing them in a vial with isopropanol (Sigma-Aldrich) and zirconia ball-mill balls for 2 hours. The slurry was then dried at 60 °C for 2 hours and then at 100 °C under vacuum for 18 hours. The electrode slurry was then prepared with the following composition in N-methyl-2-pyrrolidone (NMP, anhydrous, 99.5 %, Sigma-Aldrich): 80 wt% LCO powder, 10 wt% Timical Super C65 carbon black (MTI Corporation), and 10 wt% polyvinylidene fluoride (PVDF, Mw $\approx$ 534 kDa, Sigma-Aldrich). The slurry was vortexed again in a vial with zirconia ball-mill balls for 5 hours, and then cast onto an aluminium foil using a film applicator blade, before being dried at 50 °C for 12 hours. Electrode discs, 11.1 mm in diameter, were then punched out of the foil and then dried for at 100 °C for 18 hours under vacuum. The slurry electrodes were then tested in CR2032 coin cells that were assembled in an argon-filled glovebox — 30 μL of a lithium hexafluorophosphate solution (1M $LiPF_6$ in ethylene carbonate (EC) and diethyl carbonate (DEC) 1:1 volume ratio, Selectilyte LP 40, BASF) was used as the electrolyte. Li foil (Sigma-Aldrich) was used as the counter electrode with a 25 μm thick polypropylene separator. CV was performed using a BioLogic BCS-805 battery cycler scanning between 3 V and 4.2 V at a scan rate of 5 μV/s.

A representative cyclic voltammogram showing the first cycle scan for the LCO-e slurry electrode is shown in Fig. 5.16 below.

The CV of the first cycle showed three pairs of redox peaks that closely matched that found in the literature for stoichiometric LCO. The first major pair of peaks at 3.948 and 3.886 V was observed for the anodic (Li extraction) and cathodic (Li insertion) scans respectively, corresponding to the first order phase transition between two hexagonal phases. The two smaller pairs observed at 4.077 / 4.064V and 4.181 / 4.160V correspond to an order / disorder transition of Li ions with a distortion to a

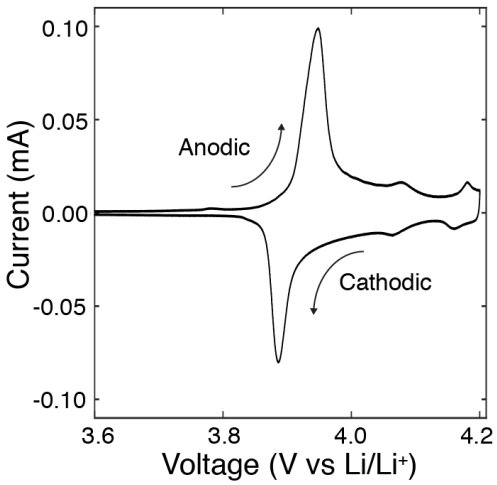

Figure 5.16: Cyclic voltammogram showing a representative first cycle scan of the LCO-e slurry electrodes conducted at a scan rate of 5 μV/s.

monoclinic phase [306, 307].

The results from the CV scans further confirmed the identity of the synthesized material as LCO, and also indicated that it was electrochemically active.

5.6.2 Electrochemical Cycling of Architected LCO Cathodes

Coin cells with LCO-e lattices as cathodes were then prepared and subjected to electrochemical cycling. The procedure for preparing the coin cells is as follows:

A conductive adhesive was first prepared by mixing 75 wt% conductive Timical Super C65 carbon black and 25 wt% PVDF binder in NMP. 1.28 mL of NMP was used for every 100mg of the carbon black/PVDF mixture. The solution was vortexed in a vial with zirconia ball-mill balls for 24 hours. The mixture was drop-casted onto a 0.2mm thick stainless steel spacer and the droplet thinned to 0.5mm thickness using a film applicator blade. The LCO lattice was then carefully placed into the middle of the adhesive and the whole stack was dried at 35°C for 4 hours. A polypropylene ring 0.18 mm thick with inner and outer diameters of 11 mm and 15.9 mm, respectively, was placed around the LCO structure to support the stress of the coin cell spring. Cells were then assembled in an argon-filled glovebox using a lithium foil as the counter electrode, and Selectilyte LP 40 as the electrolyte. 400 μL of electrolyte was added into the cell cavity prior to the addition of the lithium foil, although some electrolyte spilled out of the cell during crimping. A schematic of the coin cell stack is shown in Fig. 5.17 below.

The coin cells were analyzed by a Neware BTS4000 cycler and were cycled

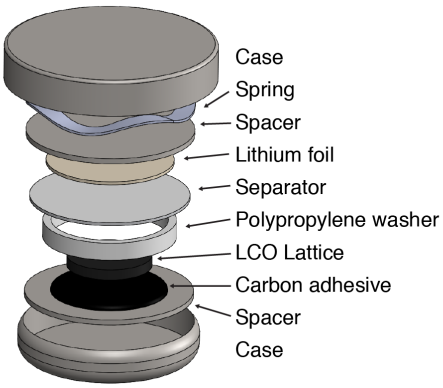

Figure 5.17: Schematic of the coin cell stack with LCO-e lattice as the cathode.

galvanostatically between 3.0 and 4.2 V at C/40 for two cycles, then at 5 cycles each at C/20, C/10, C/5, 2C/5, 1C, and 2C. Following these, the cells were cycled for 100 cycles at C/10. A rate of 1C corresponds to a discharge or charge in 1 hour based on the maximum practical capacity of LCO (155 mAh/g [308]), 2C corresponds to a 30 minutes discharge or charge half-cycle, etc.

The specific discharge capacities and Coulombic efficiencies (CE) for three separate coin cells (LCO-e1, LCOe2, LCO-e3), each with a mass loading of 50 mg/cm^2, are shown in Fig. 5.18 below.

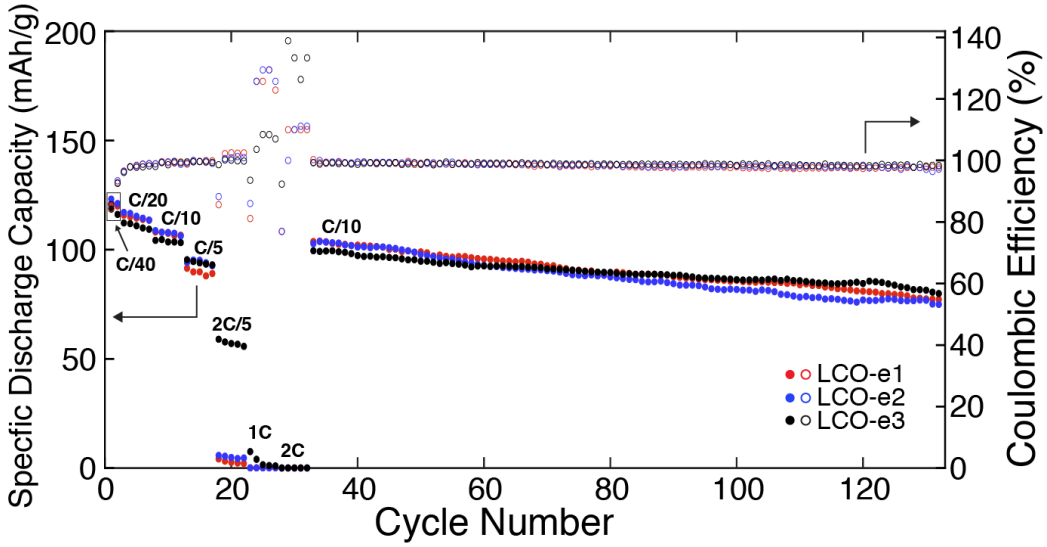

Figure 5.18: Electrochemical cycling of three nominally identical LCO lattices, LCO-e1 (red circles), LCO-e2 (blue circles), and LCO-e3 (black circles), between 3.0 and 4.2 V at different C-rates. The specific discharge capacities and Coulombic efficiencies are shown for the 132 cycles tested.

The average first cycle specific discharge capacity at C/40 was 121 mAh/g, which was slightly lower compared to similar materials in the literature [302]. The decreased capacity was possibly due to parts of the lattice breaking and becoming electrically isolated during the coin cell fabrication. The Ohmic impedance across the electrode is also relatively large because of the height of the electrode and the lack of a conductive additive.

The capacity also decreased as the C rate increased. At C/20, C/10, C/5, 2C/5, and 1C, the average first cycle specific discharge capacities were 115, 107, 94, 23, and 2.6 mAh/g respectively. The lattices did not show any capacity at 2C. The CE at 2C/5, 1C, and 2C deviated significantly from 100% due to the near zero capacities at those C rates. The steady decrease in capacity at higher C-rates were likely due to the increase in polarization and ohmic drop [309].

Of the three samples, LCO-e3 (black circles) exhibited a much higher specific discharge capacity at 2C/5. It is still unclear why this is the case, but it is suspected that it could be due to the sample-to-sample variation in the adherence of the lattice to the current collector, with LCO-e3 being better adhered. More cells are currently being tested to provide more data on this.

Extended cycling at C/10 showed a linear capacity decay of $\approx 0.24\%$ per cycle, resulting in a capacity retention of 76% after 100 cycles. The average CE for the final 100 cycles was determined to be $98.5 \pm 0.5\%$. The decrease in capacity over time was likely due to the gradual degradation of the lattice, causing parts of it to become disconnected and no longer active. Other more typical battery degradation mechanisms like electrolyte decomposition or structural changes in the LCO could also have played a part in it. Nevertheless, the results clearly indicate that, even after 100 cycles, these 3D architected lattices were still electrochemically active and could function as LIB cathodes.

5.7 Summary and Outlook

In summary, we show that photopolymer complex synthesis is a unique and facile platform for the digital fabrication of 3D architected multifunctional complex metal oxides. The homogeneity and compositional versatility of these aqueous metal salt photoresins address some of the limitations faced by the current state-of-the-art slurry and organic-inorganic resin approaches, as highlighted in our facile fabrication of LCO cubic lattices. The impact of photoresin formulation on the resulting microstructure of the LCO structures was also explored, which provided some

insight into how these materials can be optimized. The demonstration of these architected materials as 3D LIB cathodes also highlighted the potential of this platform in enabling the production of previously impossible devices to address issues facing society today.

There is significant room for exploration with this technique: on the LIB material front, more advanced cathode materials like lithium nickel cobalt aluminium oxide (NCA, $LiNi_{0.8}Co_{0.15}Al_{0.05}O_2$) and lithium nickel manganese cobalt oxide (NMC, $LiNi_{0.33}Mn_{0.33}Co_{0.33}O_2$) which have higher specific capacities and are also more environmentally friendly are currently under investigation. Solid oxide electrolytes like lithium lanthanum zirconate (LLZO, $Li_7La_3Zr_2O_{12}$) can also potentially be made. Material aside, the geometries of the structures can also be optimized to improve the energy density and power density of the electrodes. This ability to tune the electrochemical properties of both the cathode and solid electrolyte could be a significant step forward in the realization of a 3D solid-state battery.

While we have made some progress on understanding the impact of binder content and microstructure, there is still more room for development. Preliminary work on the fabrication of NMC with $n_{PEGda} \approx 0.4$ showed the presence of large pores $\approx$ 100 μm in size within the material, which contradicts the findings for LCO. The amount of gas evolved during combustion is clearly not the only factor in determining porosity. It is likely that the thermodynamics of the reaction and the energy released during combustion also play a significant role in this. The combustion process also warrants further investigation — the impact of photoresin formulation on the extent of combustion, the influence of calcination parameters (ramp rate, atmosphere, stages) on the microstructure are all important studies that will provide a better understanding of the mechanism behind the technique developed in this work.

That notwithstanding, the ability to fabricate architected metal oxides at both the micro- and macro-scales is a significant step towards expanding the library of materials that is compatible with additive manufacturing. Moreover, the accessibility of this technique will allow researchers from a broad spectrum of backgrounds to start exploring this field and will enable further studies on the design and application of 3D multifunctional materials.

Chapter 6

EXPANDING PHOTOPOLYMER COMPLEX SYNTHESIS: MULTIMATERIAL AND METAL FABRICATION

Chapter Abstract

In the previous two chapters, we explored how photopolymer complex synthesis (PCS) could be used to fabricate multifunctional metal oxides at both the micro- and macro-scales.

This chapter seeks to discuss how this technique can be further developed and expanded to encompass a broader range of materials. We briefly highlight how PCS could be modified to fabricate architected metal structures via reduction of metal oxides. We also briefly explore how multimaterial fabrication can be achieved by exploiting the capacities of these hydrogels to swell solvents.

This chapter has been adapted from:

1. Yee, D. W., Saccone, M. A. & Greer, J. R. Additive Manufacturing of Metals via Photopolymer Complex Synthesis. *In Preparation* (2020).

Contributions: participated in the conception of the project, developed polymer chemistry, fabricated and characterized the samples.

1. Yee, D. W., Lifson, M. L., Citrin, M. A. & Greer, J. R. 3D Printing of Metal Containing Structures. *U.S. Patent Application No. 16/577,253* (September 20, 2019).

Contributions: participated in the conception of the project, developed polymer chemistry, fabricated and characterized the samples, and wrote the application.

6.1 Expanding Photopolymer Complex Synthesis

Over the course of this thesis, we have explored different approaches to developing functional materials for vat photopolymerization (VP), specifically for polymers and ceramics. It thus seems natural to dedicate a chapter to looking at the other classes of materials — metals and composites — and discuss how photopolymer complex synthesis (PCS) can easily be extended to fabricate them. Unfortunately, due to the COVID19 situation at the time of this writing, the initial planned study could not be completed, and this chapter will serve as a demonstration of the *potential* of PCS in fabricating these classes of materials instead.

6.2 Vat Photopolymerization of Metals

Metal additive manufacturing (AM) is one of the fastest growing segments of the AM industry, with some estimating that the market for metal AM will approach $11 billion by 2024 [310]. Industrial giants such as General Electric [311], Ford Motor Company [312], and Boeing [313] have all started to incorporate metal AM into their manufacturing processes, and it seems likely that many more companies will start to follow suit as the cost of the technology decreases.

Currently, metal AM is mostly achieved via powder bed fusion (PBF), directed energy deposition (DED), or binder jetting processes [314], with powder bed fusion technologies being the most predominant [315]. Metal fabrication with VP is relatively uncommon, with few demonstrations in the literature, although commercial metal photoresins have been developed. In general, metal VP can be achieved through one of the following ways: the use of metal powders in a photosensitive slurry (Admatec BV, Tethon 3D), inorganic-organic photoresins [129], and laser-induced photoreduction [316, 317]. The former two approaches are similar to that used in ceramic VP, with the difference being the use of an inert atmosphere during the debinding and/or sintering step. As the name implies, laser-induced photoreduction revolves around the use of a pulsed femtosecond laser to initiate photochemical reduction of a photosensitive metal salt solution [318].

Similar to ceramic VP, the number of metals that have been demonstrated with VP is quite low, and there is thus significant interest in developing metals and alloys that are compatible with VP processes.

6.3 Photopolymer Complex Synthesis of Metals

The ability for solution combustion synthesis to synthesize metal oxides should, in theory, also allow for the synthesis of metals, via an additional reduction step from

metal oxide to metal. This has been demonstrated in the literature, for both pure metals and alloys [319, 320], and has been achieved through the use of reductive gases, such as ammonia (NH_3) and hydrogen (H_2), and/or through carbothermal reduction [258]. Often, by using an appropriate fuel, with an excess fuel to oxidant ratio, the metals can be synthesized in a single step via the *in situ* generation of the appropriate reducing agent.

With that in mind, photopolymer complex synthesis is thus well poised to fabricate metals via the direct reduction of metal oxides as well. However, with our current understanding of the process, where we are working with as little fuel/polymer as possible to minimize porosity, the reduction reaction has to be done as an additional post-processing step.

6.3.1 Redesigning the PCS Process — Swelling of Salt Solutions

Copper was our first candidate material as it is one of the most highly sought after materials for metal AM. Its high thermal and electronic conductivities have the potential to allow for the design of novel thermal management systems and microelectronic devices. However, the high thermal conductivity [321] and reflectivity [322] of copper has made it challenging to fabricate with laser-based PBF and DED processes.

We first formulated an aqueous photoresin based on copper(II) nitrate hemi(pentahydrate) (98%, Sigma-Aldrich): a 2 molar copper solution was mixed with poly(ethylene glycol) diacrylate (PEGda, M_w = 575, Sigma-Aldrich), such that the mol ratio of PEGda to copper salt was 0.4. Lithium phenyl-2,4,6,-trimethylbenzoylphosphinate (LAP, ≥ 95%, Sigma-Aldrich) of varying amounts was then dissolved in water and added to the copper/PEGda solution. The LAP solution used was 10 vol% that of the copper/PEGda solution.

However, attempts to cure this copper photoresin were unsuccessful, even with increased amounts of LAP (up to 5 wt%) and prolong UV exposure times (up to 30 minutes for a thin film). This was likely due to the fact that copper(II) ions have been shown to inhibit polymerization [323, 324][1].

Since the key idea behind PCS is the conversion of a metal salt solution within the polymer, we reasoned that it did not matter when the salt solution was introduced into the system. Thus, to circumvent this issue of copper-inhibition, we redesigned the PCS process to *swell in* the copper salt solution instead of polymerizing *with* it

[1]Not to be confused with atom transfer radical polymerization processes.

(Fig. 6.1). By fabricating "blank" polymer structures that are then immersed in a salt solution to swell in the relevant salts, metal salt containing polymer structures can be similarly achieved.

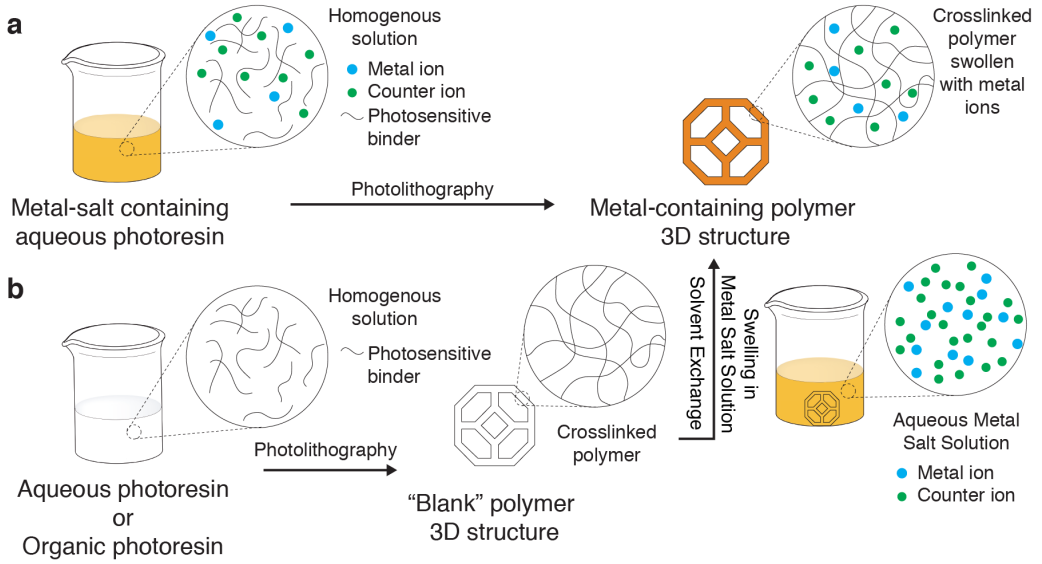

Figure 6.1: Schematic of swell-in process for photopolymer complex synthesis. **a**. PCS process with metal salt solution *in* the photoresin. **b**. PCS process where the metal salt is *swelled into* the "blank" polymer.

We decided to conduct the initial proof of concept experiments by using the Li/Co hydrogel structures developed in the previous chapter, and leaching out all the metal nitrates in them to obtain the "blank" hydrogels.

6.3.2 Proof of Concept Experiments — Copper Fabrication

In brief, the Li/Co hydrogel structures used were ≈ 80 vol% of a lithium nitrate and cobalt nitrate hexahydrate solution (50/50 vol%), and ≈ 20 vol% poly(ethylene glycol) diacrylate (PEGda, M_w = 575, Sigma-Aldrich). Lithium phenyl-2,4,6-trimethylbenzoylphosphinate (≥ 95%, Sigma-Aldrich) and tartrazine (≥ 85%, Sigma-Aldrich) were used as the photoinitiator and UV-absorbing dye respectively[2].

The Li/Co hydrogels were first soaked in water for 2 hours. The resulting pink solution was then decanted and the process repeated. The solution remained colorless at the end of the second soak. The now "blank" hydrogel was then soaked in 20 mL of 200 mg/mL copper(II) nitrate hemi(pentahydrate) solution for 4 hours.

[2]See Chapter 5, Table 5.1, Resin IV for more details.

The resulting green hydrogel structure (Fig. 6.2a) was then calcined (MTI OTF-1500X) at a reduced pressure of 20 Torr. The reduced pressure was achieved by flowing compressed air into the quartz tube (1 m in length, 92 mm inner diameter) at a flow rate of 250 standard cubiccentimeters per minute (SCCM) while a vacuum pump evacuated the tube. The temperature profile used was as follows: 1 °C/min to 100 °C, followed by 0.25 °C/min to 500 °, and then 2 °C/min to 700 °C. The structures were held at 700 °C for 3 hours before cooling at 2 °C/min to room temperature.

The calcined structures were black, which is consistent with the color of copper(II) oxide (CuO) (Fig. 6.2b). The structures were then reduced in forming gas (95% nitrogen (N_2), 5% hydrogen (H_2)) at 900 °C. The temperature profile was as follows: 3 °C/min to 900 °C, followed by a hold at 900 °C for 6 hours, before cooling at 3 °C/min to room temperature. The resulting structure was reflective and had the characteristic color of copper (Fig. 6.2c). A linear shrinkage of ≈ 75% was observed going from swollen hydrogel to the final reduced structure.

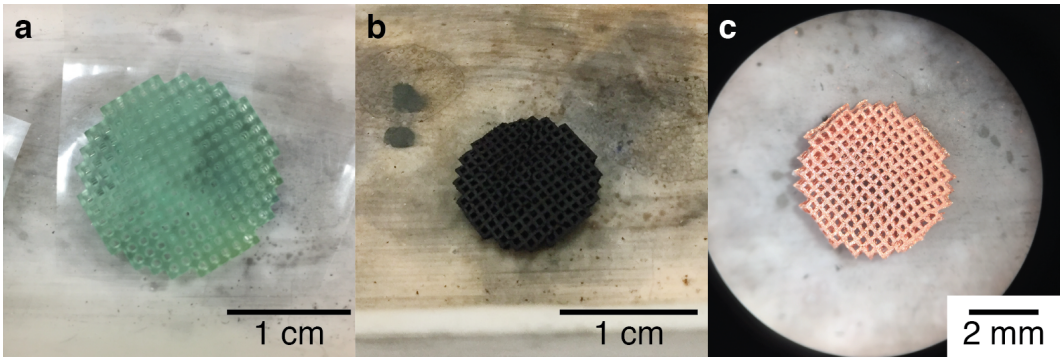

Figure 6.2: a. Hydrogel cubic lattices swollen with copper(II) nitrate hemi(pentahydrate). The "blank" hydrogels were originally Li/Co hydrogels that had their metal salts leached out in solution. **b**. Calcined structures that had the characteristic color of copper(II) oxide. **c**. Reduced structures that were a metallic sheen and the characteristic color of copper.

6.3.2.1 Characterization of Structures after Reduction

Scanning electron microscope (SEM) images of the structure after reduction are shown in Fig. 6.3 below. The SEM images were taken in a Zeiss 1550VP FESEM equipped with an Oxford X-Max SDD EDS system.

The SEM images revealed the presence of numerous cracks and pores throughout the structure, with the underlying microstructure being comprised of grains approximately 5 - 20 μm in size. Large precipitates were also observed on the

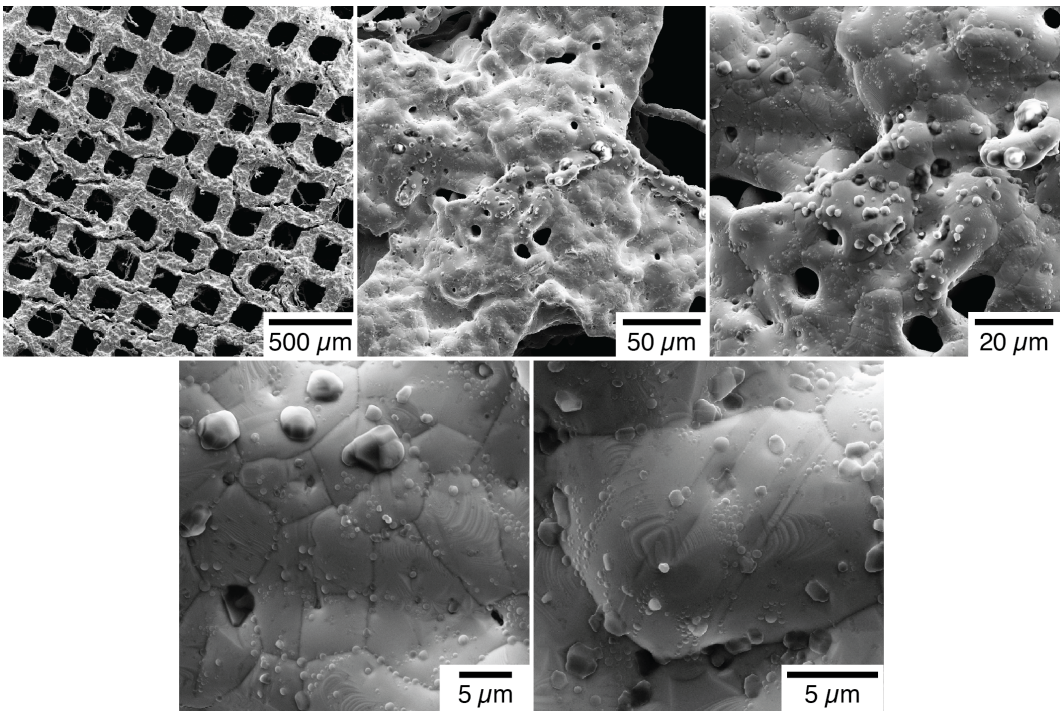

Figure 6.3: SEM images of the proof-of-concept structures after reduction in forming gas. Cracks, pores, and precipitates could be seen in the microstructure. Possible annealing twins were also observed.

surface, with smaller ones dispersed along the grain boundaries of the microstructure. What appears to be annealing twins were also observed on some grains, which was especially promising since that is characteristic of copper.

Energy-dispersive X-ray spectroscopy (EDS) was then conducted on the structures to determine its composition. The EDS data was collected on the same Zeiss SEM as described above. Fig. 6.4 shows the results from the EDS analysis.

It is clear that the grains were predominantly copper (88.0 at%) with carbon (6.6 at%) and oxygen (4.2 at%) as the majority impurity elements. While the equilibrium solid solubility of carbon in copper at room temperature is practically zero [325], it is unclear if we cooled the copper structure slow enough to allow for phase equilibrium. Furthermore, supersaturated alloys of copper with 10 at% of carbon have been reported in the literature [326], so it is currently difficult to determine how much of the carbon detected was from surface/chamber contamination or from some form of alloying.

The precipitates on the surface of the grains and on the grain boundaries were likely some form of phosphate (PO_4^{3-}) since the ratio of O (76.4 at%) to P (16.8 at%) was

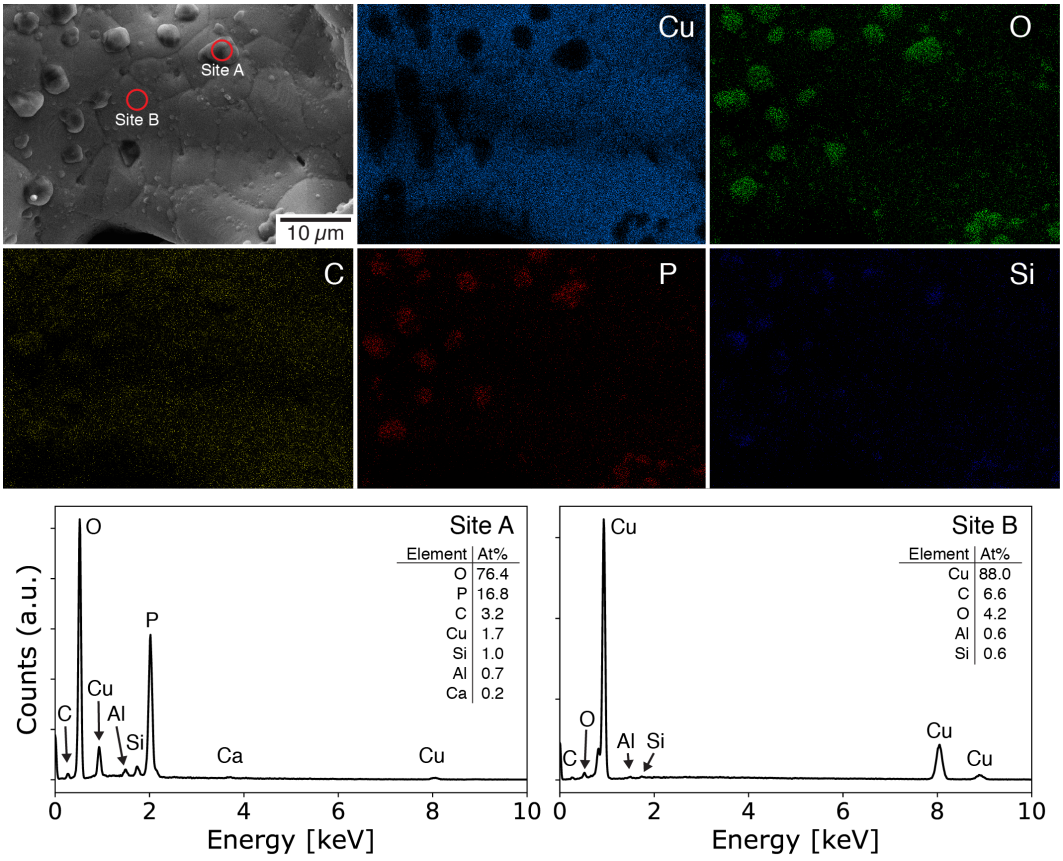

Figure 6.4: EDS elemental maps of the structures after reduction in forming gas. Composition analysis of the grains and precipitates revealed that the grains were predominantly copper and the precipitates likely a type of phosphate.

$\approx$ 4.5. These phosphates likely stemmed from the residual phosphorous after the decomposition of the LAP photoinitiator. The Si, Al, and Ca could have been from the quartz tube and/or during the handling process.

Following EDS, the structures were compressed into a flat disc and then subjected to X-ray diffraction (XRD). XRD (PANalytical X'Pert Pro) data was collected at 45 kV and 40 mA using a Cu source. The XRD spectrum of the reduced structure is shown in Fig. 6.5 below. The spectrum from the flattened structure showed sharp peaks that were consistent with that given by the reference copper spectrum (ICSD #43493), indicating that the constituent material of the structures was indeed copper. Interestingly, the phosphates were not observed in the XRD spectrum — it is possible that during the flattening process, some of the surface precipitates got dislodged or embedded into the copper matrix.

Nevertheless, the results from the SEM, EDS, and XRD characterization

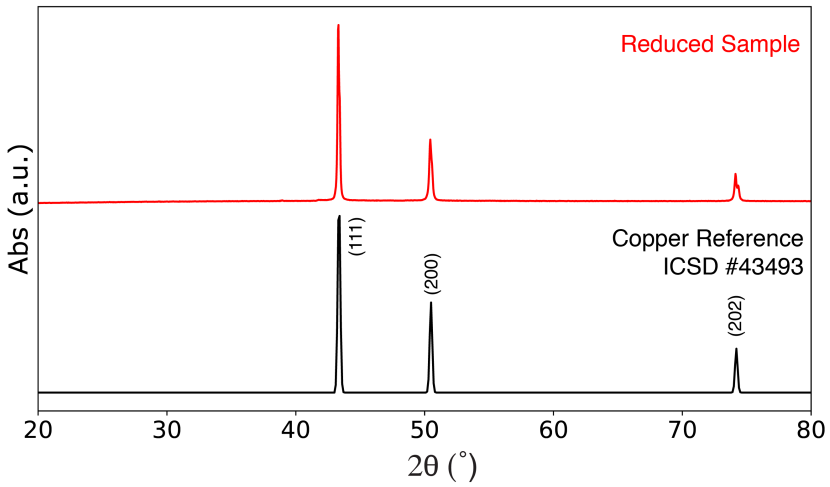

Figure 6.5: XRD spectrum of the reduced sample (red), and that of a copper reference ICSD #43493 (black).

experiments indicate that the proposed methodology of swelling in copper salts could be used to make metallic copper structures.

6.3.3 "Blank" Organogel Photoresin Formulation

The presence of phosphate precipitates on the copper microstructure led us to rethink how we approached the fabrication of these "blank" hydrogels. The requirement for water solubility meant that we were constrained to using organic salts for our photoinitiators and UV-absorbing dyes, which would likely lead to the inevitable formation of these precipitates. To circumvent that, much like how we did a metal salt exchange with the Li/Co hydrogels in the proof-of-concept experiments, we reasoned that we could form the "blank" hydrogel via a solvent exchange from an organogel instead. Furthermore, by using organic solvents with low vapor pressures, we could also address one of the issues with the use of aqueous photoresins — the evaporation of water over time.

N,N-Dimethylformamide (DMF) was the organic solvent of choice to synthesize the organogel due to its high miscibility with water, and its low vapor pressure ($\approx$ 6 times lower than water at 20 °C). Its ability to solvate a wide variety of compounds also meant that a much larger pool of photoinitiators and UV-absorbing dyes could now be used. We sought to use compounds that only contained carbon, nitrogen, and oxygen, so that we could minimize any residue after calcination. As a starting point, we formulated the following photoresin for use with digital light processing (DLP) printing:

63.75 mL of DMF (anhydrous, 99.8%, Sigma-Aldrich) was added to 11.25 mL of poly(ethylene glycol) diacrylate (PEGda, M_w = 575, Sigma-Aldrich). In a separate vial, 555 mg of Irgacure 379 (Ciba), 377 mg of Michler's ketone (98%, Sigma-Aldrich), and 10 mg of Sudan I (≥ 95%, Sigma-Aldrich) were dissolved in 7.5 mL of DMF. The photoactive solution was then added to the PEGda solution to yield the yellowish-brown organogel photoresin. This resin was termed the "85/15 Organogel", since it was ≈ 85vol% DMF.

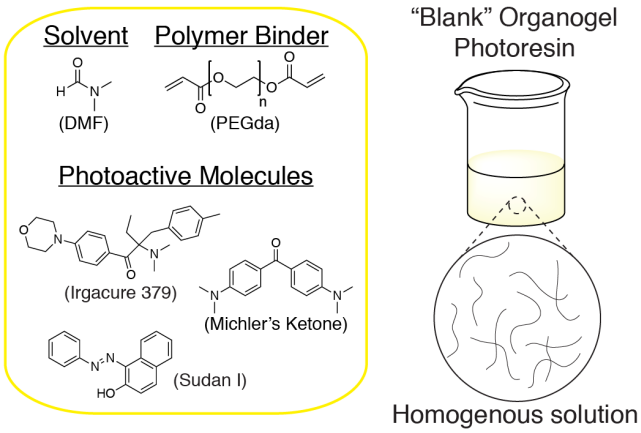

Figure 6.6: "Blank" organogel photoresin formulation.

Since most visible light photoinitiators are phosphine oxide derivatives, we used a combination of Michler's ketone (a photosensitizer) with Irgacure 379 to improve photoinitiation at 405 nm, the wavelength used with our DLP printer.

6.3.4 Architected "Blank" Hydrogels from Organogels

The "blank" photoresins were then used with a DLP printer (Autodesk Ember) to fabricate octet or cubic lattices of varying sizes. The fabricated structures were washed with DMF, and then soaked in DMF at 70 °C for 120 minutes. The DMF was decanted and the process repeated again. The purpose of this was to leach out as much of the unreacted photoactive molecules from the structures before the solvent exchange with water. When this step was omitted and the structures directly immersed in water, the water-insoluble Irgacure 379, Michler's Ketone, and Sudan I would precipitate within the structure. Following the DMF soak, the structures were then soaked in water at 70 °C for 120 minutes. When this was complete, the water was decanted and the process repeated again. At the end of the water soak, the structures were translucent and assumed to be hydrogels. Fig. 6.7 shows some images of the various architected hydrogels fabricated.

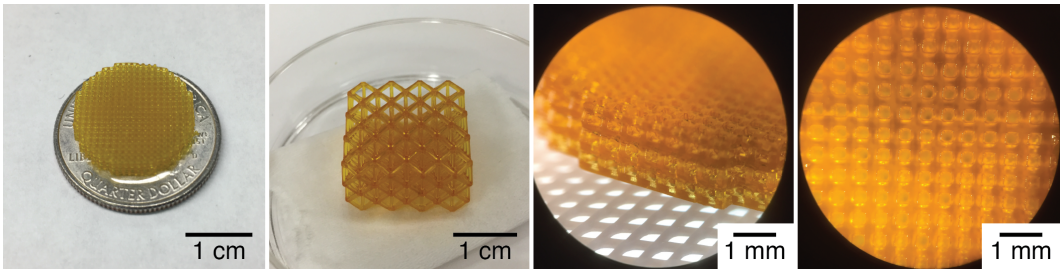

Figure 6.7: Images of architected "blank" hydrogels obtained from solvent exchange of "blank" organogels. The different images highlight the versatility of DLP printing in fabricating structures of varying geometries and sizes.

6.3.5 Swelling of Copper Nitrate

Copper(II) nitrate hemi(pentahydrate) solutions with concentrations ranging from 1 - 5 molar were first prepared. The hydrogels were then soaked in the copper solution for 12 hours at either room temperature or at 70 °C. The structures turned a dark shade of green after the soaking step, which is consistent with the blue copper solution and the yellow-brown hydrogel. Unfortunately, due to the COVID19 situation at the time of this writing, we were only able to perform the subsequent post-processing steps on a select few swollen structures. The data presented from here onwards thus represents only a fraction of the study. Fig. 6.8 shows some images of the structures after the swelling process.

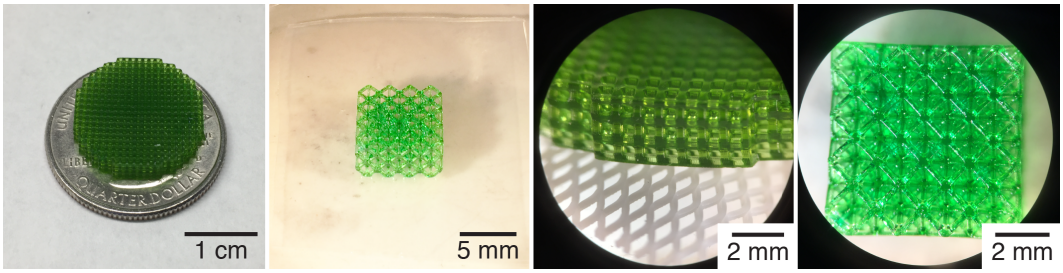

Figure 6.8: Images of architected hydrogels swollen with copper nitrate. The structures turned a characteristic dark green after the swelling process. The difference in color between the structures in the top row is due to the lighting.

6.3.6 Calcination of Swollen Copper Hydrogels

The swollen structures were then calcined at a reduced pressure of 8 Torr. The reduced pressure was achieved by flowing compressed air into the quartz tube (1 m in length, 92 mm inner diameter) at a flow rate of 50 standard cubic centimeters per minute (SCCM) while a vacuum pump evacuated the tube. The temperature profile was as follows: 0.25 °C/min to 500 °C, followed by 1 °C/min to 700 °C, and then a

5 hour hold at 700 ° before cooling at 1 °C/min to room temperature. The calcined structures (Fig. 6.9) were black, which is consistent with the color of copper(II) oxide (CuO).

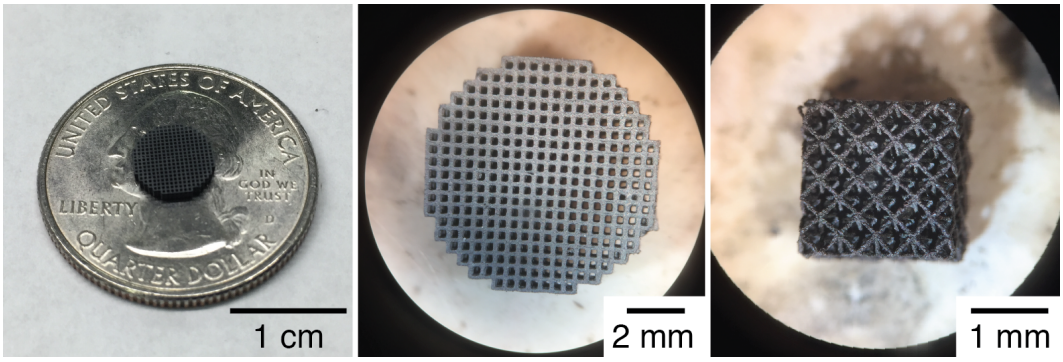

Figure 6.9: Images of architected copper(II) oxide structures. The difference in color between the structures is due to the lighting.

As expected, the amount of shrinkage and mass loss experienced was dependent on the molarity of the copper solution the hydrogels swelled in, although more samples are needed to better quantify this. Interestingly, it was observed that structures swelled in copper solutions with higher molarities (4 and 5M) became significantly cracked after calcination. Fig. 6.10 below shows the surface and cross-section of a CuO cubic lattice that had been swollen in 4M copper solution at room temperature for 12 hours. Large cracks could be seen running through the nodes, and cross-sections obtained via focused-ion beam (FIB) milling (FEI Versa 3D DualBeam, 30 kV accelerating voltage, 65 nA current) also showed large pores in the middle of the nodes.

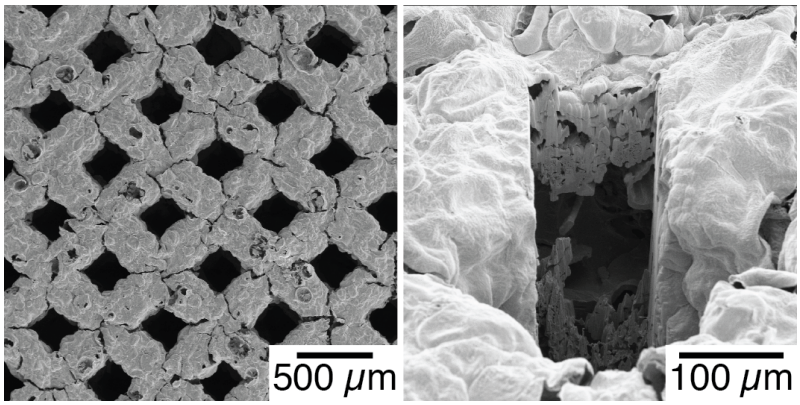

Figure 6.10: SEM images of the surface (left) and cross-section (right) of the calcined structures obtained from structures swollen in 4M copper solution at room temperature.

It is currently unclear what the influence of copper nitrate concentration used for swelling has on the resulting microstructure. Further work on evaluating the combustion behavior of these swollen polymers, and determining the degree of swelling, will provide more insight into the microstructure formation.

6.3.7 Architected Copper Structures

The remaining calcined structures that were swollen in 1 - 3M copper nitrate solutions were then reduced in forming gas (95% N_2, 5% H_2) at a reduced pressure of $\approx$ 14 Torr. This was achieved by flowing forming gas at a flow rate of 100 SCCM while a vacuum pump evacuated the tube. The temperature profile was as follows: 3 °C/min to 900 °C, followed by a hold at 900 °C for 3 hours, before cooling at 3 °C/min to room temperature. The reduced copper structures are shown in Fig. 6.11.

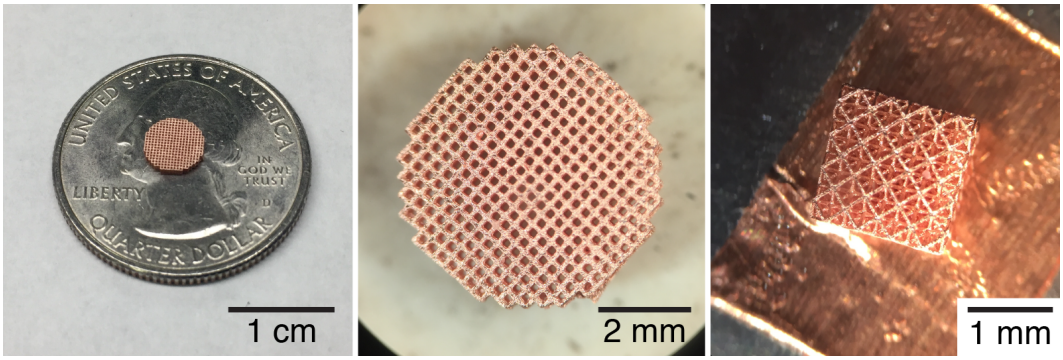

Figure 6.11: Images of architected copper structures.

As expected, the structures after reduction had the metallic sheen and characteristic color expected of copper. To evaluate the quality of the material fabricated, we used a FIB to obtain cross-sections of the nodes. The cross-sections from two different structures: one in a 1 M copper solution at 70 °C, and another in a 2 M copper solution at 70 °C as well, are shown in Fig. 6.12 below.

The 1M structure only had a few pores in its microstructure, whereas the 2M structure had large pores ($\geq$ 10 μm) dispersed throughout its cross-section. Between the cross-sections from the 1M, 2M, and 4M structures, it might appear that swelling in lower concentrations of copper results in a denser microstructure. However, with only three structures samples, it is difficult to draw any meaningful conclusions from the data. Nevertheless, the 1M structure highlights the fact that, unlike the metal oxide structures in the previous chapter, it is possible to fabricate metallic structures that

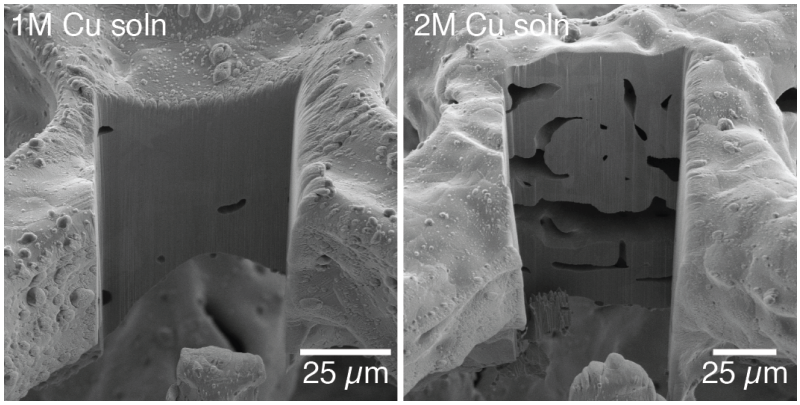

Figure 6.12: Cross-section images of copper structures that were swollen in 1M (left) and 2M (right) copper nitrate solutions at 70 °C for 12 hours.

have very little porosity. The lower melting points of metals make it significantly easier to reach a higher homologous temperature for sintering and grain growth.

6.3.8 Architected Alloys

With the demonstration of the fabrication of pure metal, we sought to investigate if we could also fabricate alloys using this swell-in approach. Similar to how we fabricated complex metal oxides, we hypothesized that swelling the "blank" hydrogel in a solution that contained multiple different metal cations could be used to fabricate alloys. A challenge we anticipated would be the differences in diffusion rates between the various metal cations. This would result in the formation of alloys that had compositions that differed from those of the salt solutions.

To test this hypothesis, we prepared a 50/50 vol% solution of 2.5 molar copper nitrate hemi(pentahydrate) and 2.5 molar nickel nitrate hexahydrate (99.999%, Sigma-Aldrich) to determine if we could fabricate a 50-50 cupronickel alloy. A "blank" octet hydrogel structure was immersed into the solution at 70 °C for 12 hours, and then calcined and reduced using the same procedure outlined above for the copper structures (Fig. 6.13).

After the calcination and reduction treatments, the structure turned a reflective silver, which was characteristic of cupronickel alloys. We then performed EDS on the structures to determine their composition (Fig. 6.14). The results from the EDS elemental maps indicated that copper and nickel were homogeneously distributed throughout the structure. Oxygen was also detected throughout the structure, indicating either incomplete reduction or the presence of an oxygen-containing phase. As anticipated, the atomic percentages of copper and nickel were

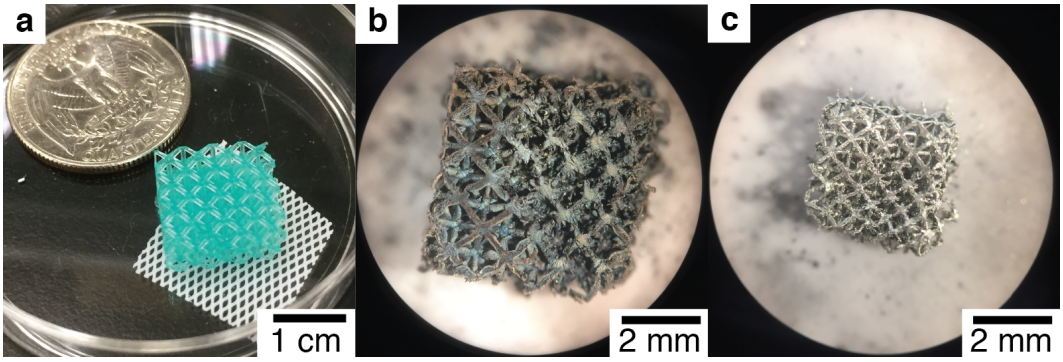

Figure 6.13: Fabrication of the cupronickle structure. **a**. Structure after swelling in the 50/50 vol% solution of copper nitrate and nickel nitrate. **b**. Calcination resulted in a silvery-grey brittle material. The structure was damaged at this step during handling, which resulted in the broken beams seen on half the structure. **c**. Reduction of the structure resulted in a reflective silver material.

not equivalent, with ≈ 30% more copper than nickel. Considering that the size of the six-coordinated aquo complex for Cu^{2+} and Ni^{2+} was 73 and 69 pm respectively [327], this implied that the rate of diffusion was not completely dependent on just the size of the aquo metal complex. PEG has been shown to be able to complex with metal ions [328], so it is more likely that the coordination geometry/affinity of the metal cations with the PEG is the cause for this large deviation in stoichiometry.

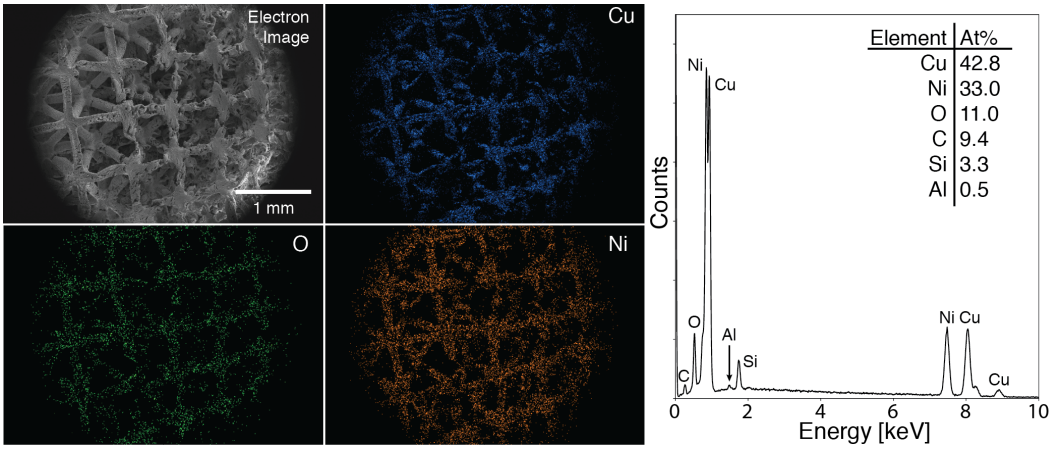

Figure 6.14: EDS elemental maps of the cupronickel structure showed the homogeneous distribution of copper and nickel. Composition analysis showed that there was 30% more copper than nickel.

Closer inspection of the microstructure revealed that the material was comprised of large grains approximately 10 - 30 μm in size. Precipitates up to 2 μm in size were found to be dispersed throughout the surface of the structure. Twins could also be observed on certain grains in the microstructure (Fig. 6.15).

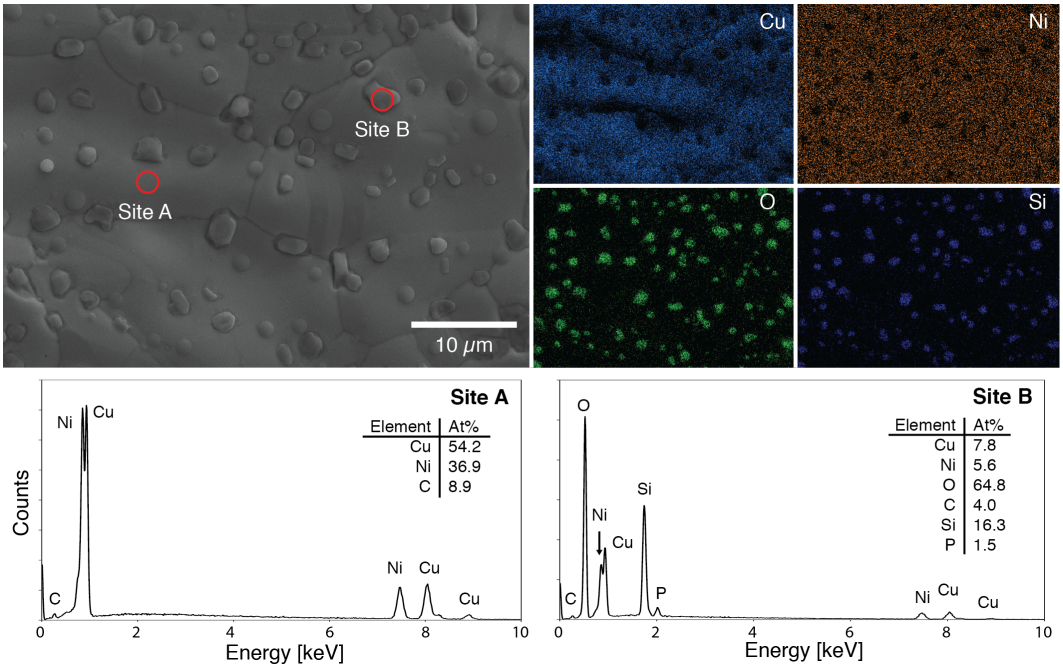

Figure 6.15: EDS analysis of the microstructure of the cupronickel structure. The elemental maps indicated that the grains were predominantly copper and nickel, with carbon as its only impurity. On the other hand, the precipitates had little copper and nickel, but had a high percentage of oxygen and silicon.

EDS analysis of the microstructure indicated that the grains were predominantly copper (52.2 at%) and nickel (36.9 at%), with carbon as the only impurity (8.9 at%). Considering the fact that the solubility of carbon in cupronickel alloys is generally < 1 at% at room temperature [329], the large amount of carbon detected could have been due to surface adventitious carbon. In contrast, the precipitates had a large amount of silicon (16.3 at%) and oxygen (64.8 at%), with little copper (7.8 at%) and nickel (5.6 at%). It was thus likely that the precipitates were a type of silicate, possibly an orthosilicate (SiO_4^{4-}) since the ratio of oxygen to silicon was ≈ 4. The source of the silicon impurity was suspected to be from the quartz tube used, as shown in the literature for other types of high temperature syntheses [330, 331].

Although more materials characterization needs to be conducted to further validate the composition and phase of the material, the EDS results still suggest that the constituent material of the structure was indeed a cupronickel alloy.

6.3.9 Future Direction for Metal Fabrication

In terms of pure metals, we have not only shown the process for copper fabrication in this chapter, but we have also explored other metals like iron, nickel, and cobalt. In

theory, any metal oxide that can be reduced by hydrogen can be fabricated using this technique. For the metal oxides that cannot be reduced by hydrogen, the polymer chemistry and heat treatment conditions could be tuned to allow for residue carbon in the structure to effect carbothermal reduction. However, a potential complication in doing so would be the formation of carbides during the high temperature treatment.

A more comprehensive understanding of the swelling process still needs to be developed — the amount and type of polymer and metal salt and the thermal treatment profiles all play a significant role in influencing the resulting metal microstructure and need to be systematically investigated.

The possibility of fabricating alloys opens up even more avenues of exploration. It would be interesting to investigate how the concentrations of the various metal salts in the solution could be used to influence their diffusion rates by changing their concentration gradients. The use of polymers that have increased affinity for certain metal cations also presents itself as an opportunity to make materials with spatially varying compositions. All these could potentially allow for finer control over the resulting alloy composition.

That much said, it has to be acknowledged that as more elements are involved, the possibility of the formation of undesired phases increases as we explore a larger composition space. Understanding how to limit the residues from the organic phases will be key to addressing these phases, as well as, improving the process to allow for different atmospheres, cooling rates, etc.

Nevertheless, the use of photopolymer complex synthesis to fabricate metals from a hydrogel precursor is a significant advancement in the field, and has the potential of making the process of metal additive manufacturing accessible to the greater scientific community.

6.4 Multimaterial Fabrication

Most of the work explored in the thesis so far has focused on developing new techniques for the fabrication of functional single phase[3] materials for additive manufacturing. However, in the greater AM community, there is also considerable interest in multimaterial fabrication. The ability to precisely control the orientation and topology of *two or more* different phases within a single material has significant potential, and has been touted as the next frontier in AM as it could bring us closer to the complexities that we see in natural systems.

Multimaterial AM has largely been explored using material extrusion or material jetting processes, as it is relatively simple to use multiple nozzles or quickly switch between different material feedstocks in these family of processes [75, 116, 278, 332, 333]. This is much more challenging to achieve with vat photopolymerization as the nature of the process requires the structures to be fabricated *within* the material feedstock (photoresin) rather than *from* the feedstock.

Demonstrations of multimaterial VP have thus largely revolved around the use of orthogonal photo-crosslinking systems. For example, both Dolinski et al. and Schwartz and Boydston showed that with judicious choice of photoactive molecules, a photoresin system could be formulated that produced distinctly different polymer networks using different wavelengths of light [334, 335]. Another approach has been to engineer a system where the photoresin could be exchanged during the printing process. For example, Kowsari et al. designed a system that utilized small drops of photoresin for fabrication, which was then removed via an air jet [336]. Mayer et al. developed a microfluidic system that was used to flow different photoresins into a chamber for VP [337]. However, all these multimaterial VP demonstrations have focused on polymeric materials, although they could in theory be extended to non-polymeric materials as well by using the slurries or inorganic-organic photoresins described throughout the course of this thesis.

In the last portion of this chapter, we will briefly demonstrate how photopolymer complex synthesis can be used for multimaterial ceramic fabrication, and also discuss how it could be extended towards metal-ceramic composite materials as well.

[3] If you discount the presence of undesired precipitates on the metal and metal oxide structures.

6.4.1 Multimaterial Photopolymer Complex Synthesis

The concept behind multimaterial PCS is to simply introduce the desired metal cation(s) into selected areas of the "blank" hydrogel structures. On calcination, the different metal ions are converted into their corresponding metal oxides, resulting in a structure with spatially varying composition. This approach is unique in that the composition is decided post-fabrication — the "blank" hydrogel is simply a platform on which the final material is built from. The metal ions are introduced in solution form, and can involve either dropping the appropriate metal salt solution onto certain areas of the "blank" structure or directly immersing selected areas of the "blank" structure into the metal salt solution (Fig. 6.16).

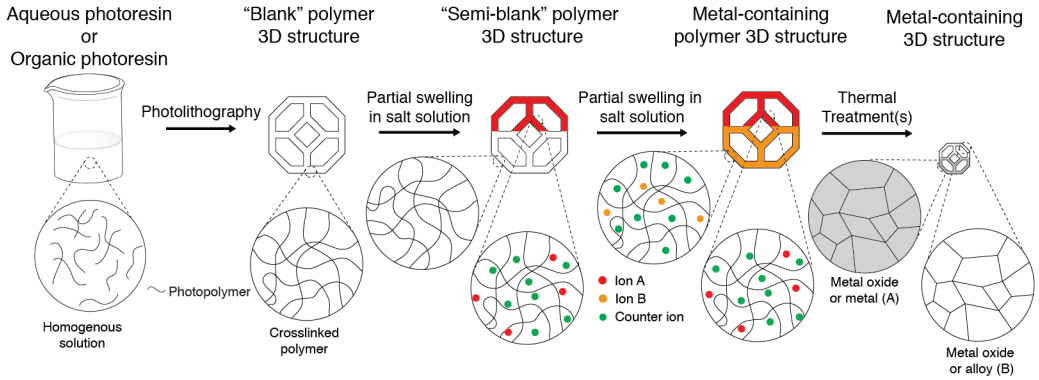

Figure 6.16: Schematic of multimaterial PCS fabrication from a "blank" hydrogel. The desired metal cation(s) are introduced into selected areas of the structure. Calcination of the structure then results in a structure with spatially varying composition.

Another approach is to first fabricate a metal ion containing hydrogel structure using conventional PCS. The hydrogel is then selectively immersed in water to leach out the metal cations in those sections to form a "semi-blank" structure. That "blank" section is then re-immersed in another metal salt solution to introduce the desired metal cations there (Fig. 6.17). The reason to utilize this approach is if the multimaterial structure includes a complex oxide/alloy, since it is challenging to diffuse in their constituent metal ions in the right stoichiometry.

6.4.2 Proof-of-Concept Experiment

As a proof of concept, we took one of the Li/Co hydrogel structures that we made in the previous chapter, partially submerged it in water to leach out the metal cations in that section, and then re-immersed that "blank" section into a 200 mg/mL solution of iron (III) nitrate nonahydrate ($\geq$ 98%, Sigma-Aldrich). Fig. 6.18 shows the structure at each step of the process. The leach time in water was kept short at 30 minutes at

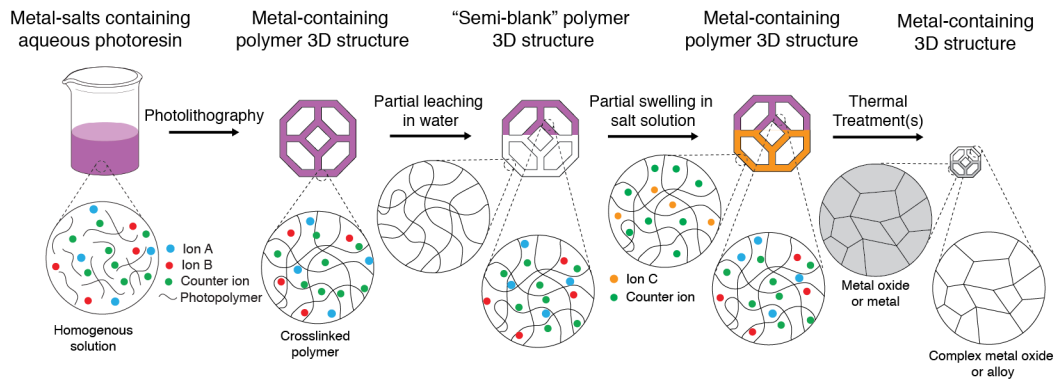

Figure 6.17: Schematic of multimaterial PCS fabrication using a "leach-and-swell" approach. A metal-ion containing hydrogel structure is first fabricated, and then partially immersed in water to leach out the metal cations from those sections. The "blank" sections are then re-immersed in a different metal salt solution to swell in the new metal cations. Calcination of the structure then gives the multimaterial structure.

room temperature, since it was unclear how much of the ions in the un-immersed sections would diffuse through the beams and leach into solution. Even with these short leaching times, it can be clearly seen that there is a pink gradient throughout the structure, indicating that some of the cobalt ions were still able to diffuse through the beams and into the water. Immersion of the "semi-blank" structure into the iron nitrate solution then resulted in a hybrid hydrogel that was half brown and half pink. As seen in Fig. 6.18e, the structure was no longer uniform in shape due to the difference in the amount of metal salts in each section.

The hybrid structure was then calcined in air at 700 °C at a reduced pressure of 20 Torr. The reduced pressure was achieved by flowing compressed air into the quartz tube (1 m in length, 92 mm inner diameter) at a flow rate of 250 SCCM while a vacuum pump evacuated the tube. The temperature profile was as follows: 0.25 °C/min to 500 °C, followed by 1 °C/min to 700 °C, and then a 5 hour hold at 700 °C before cooling at 1 °C/min to room temperature. The calcined structures (Fig. 6.19) were half brown and half black, which corresponded to the color of iron oxide and lithium cobalt oxide respectively.

As seen, an uneven amount of shrinkage was observed in the structure. This was attributed to the unequal amount of metal salts on each side of the "interface", which resulted in different degrees of shrinkage after calcination. It is thus important to control the diffusion of metal ions across the interface while swelling in the right amount of metal ions into the "blank" sections, such that the shrinkages are matched. The bowing out of the structure at the "interface" was likely due to this asymmetrical

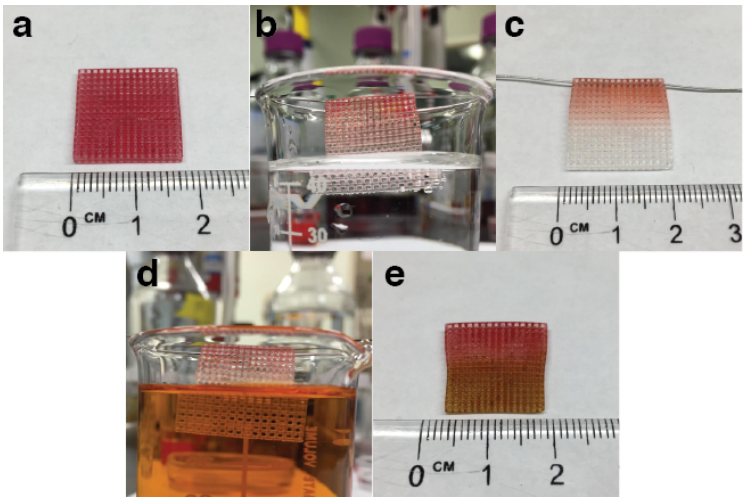

Figure 6.18: Multimaterial PCS "leach-and-swell" approach. **a**. A Li/Co hydrogel structure, as described in the previous chapter, was used as the starting hydrogel. An older generation of photoresin was used, hence the pink color instead of the orange. **b**. The hydrogel is partially submerged in water to leach out the metal ions in those sections. **c**. Image of the "semi-blank" structure. **d**. Immersion of the "blank" regions into the iron nitrate solution. **d**. Image of the hydrogel with spatially different metal cations.

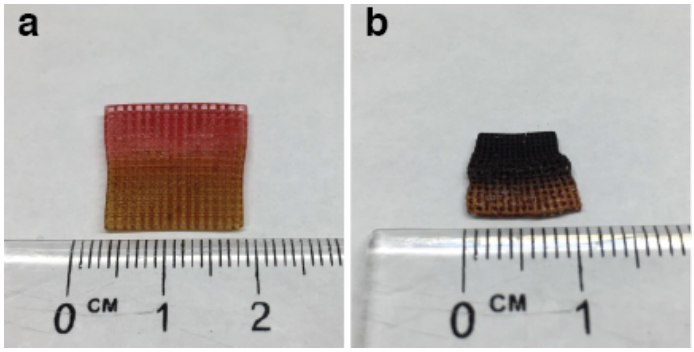

Figure 6.19: Multimaterial structures **a**. before and **b**. after calcination. The iron nitrate section turned brown, while the lithium nitrate and cobalt nitrate section turned black.

shrinkage, causing the structure to warp during the conversion process.

EDS was then used to determine the composition of the structure on both sides of the "interface" (Fig. 6.20). It was found that the interface region, i.e. the region that contained both cobalt and iron, was approximately 5 mm in size, which constituted almost half the structure. Due to the size of the interface region, the EDS elemental map shown was a composite image built from many different areas of the structure. Away from this interface region, either iron or cobalt could be detected on each side, but not both. The interface was also heavily cracked, which was to be expected since a non-uniform amount of metal salts was present in that region. Significant

stresses would thus be generated in those areas due to the non-uniform shrinkages experienced.

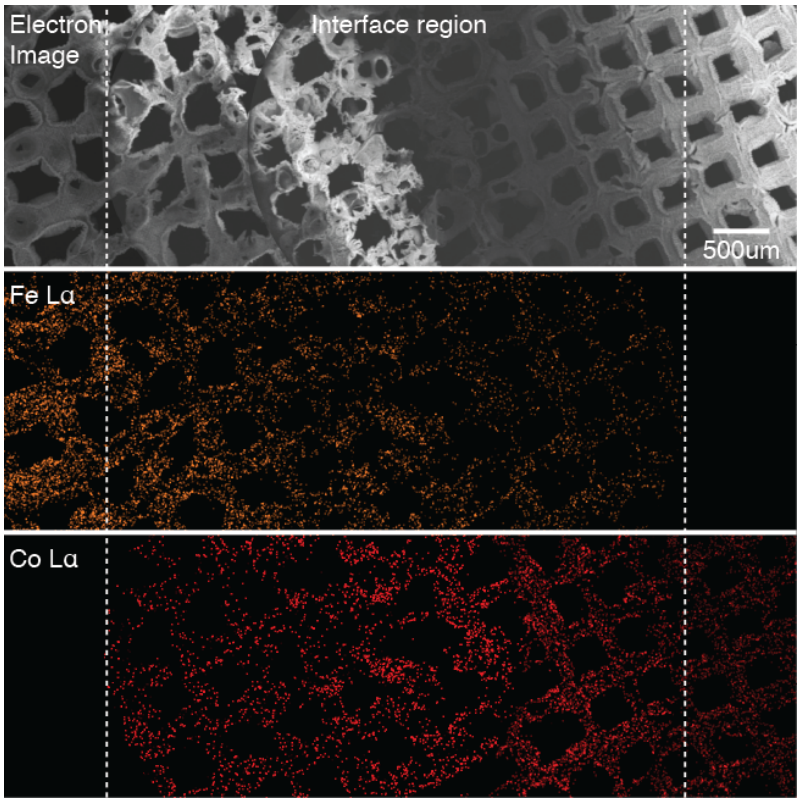

Figure 6.20: EDS elemental maps of the multimaterial structure fabricated indicated that the interface region was approximately 5 mm in size. Away from the interface, either cobalt or iron could be detected on each side, but not both.

Although the interface region was a lot larger than expected, the proof-of-concept experiment showed that it was possible to fabricate multimaterial structures via the proposed "leach-and-swell" method. More generally, spatial control of the metal ions could be used to fabricate multimaterial structures.

6.4.3 Future Direction for Multimaterial Fabrication

Although we had planned to explore this area further, due to the COVID19 situation at the time of this writing, we were only able to fabricate one structure. There are thus various aspects of the work that are incomplete and warrant significant investigation. One of the biggest questions that need to be addressed is how to mitigate the unwanted diffusion of metal ions across the interface. A systematical study needs to be conducted to establish the rates of diffusion of the metal ions in and out of the structures, so as to determine the optimal time for the leaching and swelling processes.

An organic solvent that is immiscible with the metal salt solution could also be used to better control the leaching process. By placing the structure at the interface of these immiscible liquids, it might be possible to impede the diffusion of metal ions across the interface. This method would not stop the ions from diffusing through the beams, but when combined with the diffusion study, could help to further minimize the size of the transition zone.

The use of a polymer system that could spatially undergo further crosslinking after fabrication is another approach that could be taken. By forming regions of higher or lower crosslink density, we might be able to have more control over the extent of metal ion diffusion through these areas.

Aside from making multimaterial metal oxide structures, the proposed methods could also theoretically be used to make multimaterial metal structures as well. As discussed earlier, this just requires the multimaterial metal oxide structures to be thermally treated in a reducing atmosphere. An interesting direction to take would be to fabricate a structure with a combination of metal oxides that are both able *and* unable to be reduced by forming gas. In this way, it might be possible to make metal-metal oxide composite structures as only the areas of the structures that are reducible with forming gas will be reduced to metal, leaving the rest as metal oxide.

6.5 Summary and Outlook

In this chapter, we briefly demonstrate and discuss how photopolymer complex synthesis can be expanded to encompass both metal and multimaterial/composite fabrication. Metals can be fabricated by simply treating the metal oxide structures in a reducing atmosphere, and multimaterial/composites can be made by spatial control of the metal ions in the structure. We also demonstrate a new approach to fabricating these metal-ion containing structures via swelling in of the desired metal salts into "blank" hydrogel structures. This swelling in approach is unique amongst other AM fabrication in that the structure is fabricated first, with the material being decided after. There is thus a lot of potential in using these "blank" systems as a versatile platform for other materials synthesis reactions.

While there are still many aspects of the syntheses that remain to be understood, we believe that the ability to access such a wide range of materials with one facile technique has notable implications for the general scientific community, and will enable the fabrication and application of 3D functional materials for new emerging technologies.

More generally, we hope that the demonstrations of photopolymer complex synthesis over the past three chapters in fabricating multiple classes of material have elucidated the immense potential of architected "chemical reactors" in expanding the library of materials that are compatible with additive manufacturing.

Chapter 7

THESIS SUMMARY & OUTLOOK

7.1 Summary

The goal of this thesis was to explore how we could expand the library of functional materials that were compatible with vat photopolymerization. Particular focus was placed on developing methodologies that were accessible to the general scientific community.

For polymeric materials, we first showed that surface coatings could be used as a facile method for imbuing functionality onto an otherwise inert substrate. The advantage of this approach is that it allows us to take advantage of all the commercially available photoresins that have been highly engineered for printability, resolution, and mechanical properties. In this way, we retain the desired bulk properties of the substrate material while introducing new functionalities. We demonstrated how this approach could be used to fabricate an inexpensive architected genomic DNA coated device for the reduction of off-target toxicity in chemotherapy. These DNA coatings were stable, and were able to sequester doxorubicin, a commonly used chemotherapeutic agent, from solution. More generally, we highlight the potential of additive manufacturing in situations where control and direction of fluid flow is necessary, and also the concept of drug capture for the mitigation of off-target toxicity in medicine.

Aside from surface chemistry, we also showed how click chemistry, specifically the thiol-Michael addition, could be used in the synthesis of functional acrylates for vat photopolymerization. We demonstrated the compatibility of the thiol-Michael reaction with a wide variety of functional groups, and used the synthesized monomers with two-photon lithography to fabricate functional micro-architected polymeric materials. The work highlights the utility and accessibility of click chemistry in allowing material scientists to venture into the organic synthesis arena for the chemical modifications of materials.

We also explored how polymers could be used to fabricate ceramics and metals. By reframing the polymer structures that we fabricate as "chemical reactors", we can start to design polymer systems that contain reagents that can undergo a reaction to synthesize the desired materials *in situ*. To illustrate this, we developed

a technique called photopolymer complex synthesis that combines solution combustion synthesis with vat photopolymerization. We achieve this via the fabrication of metal nitrate containing hydrogels which are then thermally treated in air to induce combustion synthesis, leaving behind a metal oxide ceramic structure. We demonstrated the capabilities of photopolymer complex synthesis by fabricating zinc oxide architectures with sub-micron features using two-photon lithography. These zinc oxide 3D structures also exhibit electromechanical properties, which is promising for the development of 3D devices.

Building on the initial success of photopolymer complex synthesis in fabricating simple metal oxides at the micron scale, we explored the use of the technique in producing architected complex metal oxides at the centimeter scale. This was achieved by simply using the appropriate combination of metal salt solutions to formulate the photoresin. We demonstrated the fabrication of lithium cobalt oxide cubic lattices, and showed that they could be used as lithium-ion battery cathodes.

Finally, we showed that photopolymer complex synthesis could be expanded to also fabricate metal and multimaterial 3D architectures. We achieved this via the use of "blank" hydrogel structures which we then swell in with the appropriate precursor solution. This approach is unique in that the material is decided after the structure is fabricated, which makes this a powerful platform for the fabrication of a wide range of materials. We highlight this in the fabrication of structures made from copper, a cupronickel alloy, and a multimaterial of iron oxide and lithium cobalt oxide.

At the start of the thesis, we posed the following three questions: How can we synthesize functional polymers in an accessible way? How can we fabricate advanced ceramics with simple reagents? And can we use vat photopolymerization as an inexpensive alternative for metal additive manufacturing? Over the course of this thesis, I hope that we have addressed these by showing that surface chemistry and click-chemistry are accessible methods for obtaining functional polymeric materials; and that photopolymer complex synthesis is an accessible and inexpensive approach to fabricating advanced ceramics and metals.

Taken together, we hope that this work highlights the potential of architected functional materials, and more importantly, is a step towards the democratization of the fabrication of advanced functional materials. Additive manufacturing has immense potential, not just for industry, but also for society. And the only way we can realize it is when everyone, from the hobbyist to the research scientist, has access to the same materials as everyone else.

7.2 Outlook

We have only scratched the surface of what we can achieve with additive manufacturing. Advancements in fabrication processes, like the use of a continuous liquid interface and volumetric printing, have already started to reposition vat photopolymerization as an industrial manufacturing process. It is only a matter of time before it joins the ranks of established industrial processes, like injection molding or investment casting. We have also started to see the power of a "citizen supply chain", no more so than in the COVID19 situation of 2020, where ordinary citizens used their additive manufacturing systems to produce personal protective equipment for healthcare workers. Their collective efforts might have saved thousands of lives in that crisis. It will be extremely interesting to see how this distributed manufacturing will play out for industry and society in the future.

There is untold potential of additive manufacturing, but one thing that is certain is that it will be limited by either our imagination or by our materials[1]. As materials scientists, our role in this is to develop and understand the materials that can be used with them. And there is so much more for us to explore! In this section, I will briefly highlight a few of the many directions of research that I am personally interested in.

7.2.1 Architected Chemical Reactors

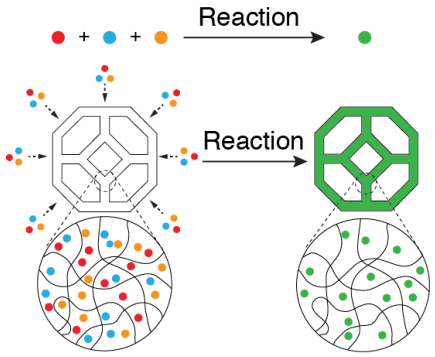

Figure 7.1: Schematic of the concept of architected "chemical reactors". Inclusion of the appropriate precursors that can react to form the desired material *in situ*.

The entire field of materials chemistry could be adapted to additive manufacturing the moment we start to think of our structures as "chemical reactors" (Fig. 7.1). I believe that this will be key to significantly expanding the library of materials

[1]Probably both.

compatible with additive manufacturing using one simple platform. While this process will work well for fabricating composite materials [256, 257] or materials that are highly stable against heat. It will be challenging for materials that are heat sensitive. The big issues that needs to be resolved are how to remove the polymer binder and how to fuse the *in situ* generated materials together, both of which are typically simultaneously achieved via thermal treatments. Addressing these will be crucial in advancing this paradigm of material synthesis for additive manufacturing.

7.2.2 Supramolecular Chemistry

Supramolecular chemistry is the study of chemical interactions that are non-covalent in nature, including hydrogen bonding, pi-pi interactions, electrostatic interactions, etc [338]. This has led to the emergence of phenomena like molecular self-assembly [339], molecular recognition [340], host-guest chemistry [341], and mechanically-interlocked molecules [342]. Materials that incorporate these supramolecular moieties have been found to exhibit self-healing capabilities (Fig. 7.2), elastomeric properties, stimuli-responsiveness, etc [128, 343], so there is a lot of potential in utilizing these functional materials with additive manufacturing. But more importantly, supramolecular chemistry is the foundation of life — the folding of proteins, the transport of metal ions through cell membranes, and enzyme activity all originate from supramolecular interactions [338]. Architecting materials with supramolecular functionalities would thus put us closer to approximating the natural materials that we see today, and will be a step towards truly biomimetic materials with both form and function.

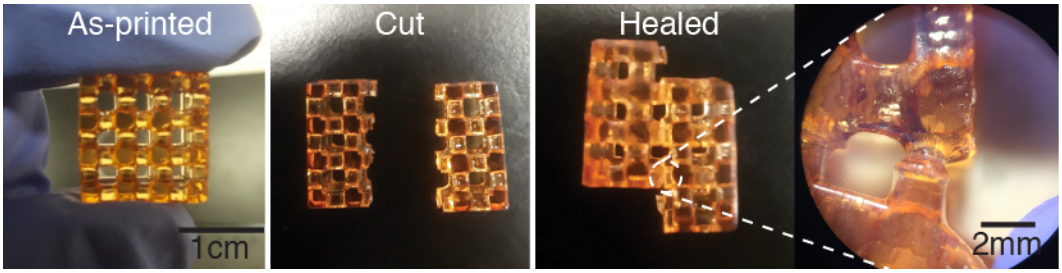

Figure 7.2: An architected metallo-polyelectrolyte complex polymer fabricated using digital light processing printing. These materials demonstrate self-healing capabilities. Unpublished work by Yee, D. W., Taylor, Z. W. & Greer, J. R.

7.2.3 Additive Manufacturing of Self-Assembling Hierarchical Materials

Hierarchical materials have been sought after by materials scientists for decades due to the emergent properties that can arise from the interactions between structural

features over multiple length-scales. Additive manufacturing has been useful as a means of replicating some levels of hierarchy [332], but has struggled to span the entire length-scale of hierarchical organization. I believe that the fields of self-assembly and polymer network topology can bridge this gap in scales and create more intricate superstructures — additive manufacturing for architecting the material at the micron scale and above, and self-assembly/control of the polymer network topology for sub-micron features (Fig. 7.3). It will be challenging to design materials that can undergo controlled and tunable self-assembly during or after the fabrication process, but the possibilities are endless if we can achieve it. The combination of additive manufacturing and self-assembly could lead to truly hierarchical materials where we have absolute control over each level of hierarchy.

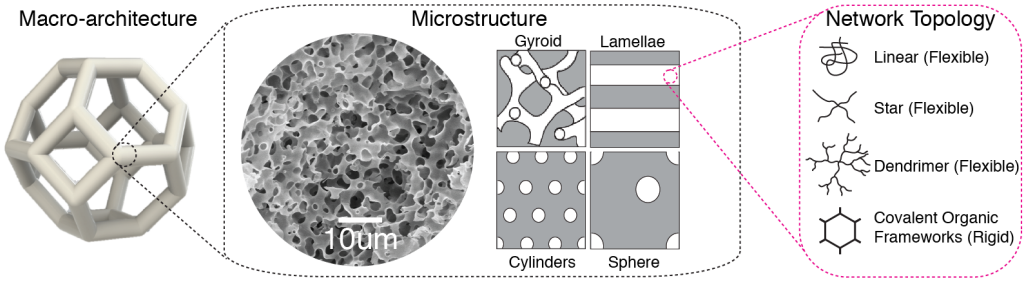

Figure 7.3: Additive manufacturing of self-assembling hierarchical materials. Schematic of possible levels of hierarchical control, through the use of additive manufacturing, self-assembly, and control over the polymer network topology.

At the end of the day, materials science is not just about developing new materials. It is a means to an end, and I am excited to see how we can apply these architected functional materials to solve real-world problems today. There is still so much left for us material scientists to do, so let's go exploring!

REFERENCES

1. Center, N. R. *Materials and Man's Needs: Materials Science and Engineering; Supplementary Report* doi:https://doi.org/10.17226/10436 (The National Academies Press, 1974).

2. Basu, J., Basu, J. K. & Bhattacharyya, T. K. The evolution of graphene-based electronic devices. *International Journal of Smart and Nano Materials* **1,** 201–223. doi:https://doi.org/10.1080/19475411.2010.510856 (2010).

3. Fahrenholtz, W. G., Wuchina, E. J., Lee, W. E. & Zhou, Y. *Ultra-high temperature ceramics: materials for extreme environment applications* doi:https://doi.org/10.1002/9781118700853 (John Wiley & Sons, 2014).

4. Damtoft, J. S., Lukasik, J., Herfort, D., Sorrentino, D. & Gartner, E. M. Sustainable development and climate change initiatives. *Cement and concrete research* **38,** 115–127. doi:https://doi.org/10.1016/j.cemconres.2007.09.008 (2008).

5. Ding, M., Flaig, R. W., Jiang, H.-L. & Yaghi, O. M. Carbon capture and conversion using metal–organic frameworks and MOF-based materials. *Chemical Society Reviews* **48,** 2783–2828. doi:https://doi.org/10.1039/C8CS00829A (2019).

6. Chapman, L. Transport and climate change: a review. *Journal of transport geography* **15,** 354–367. doi:https://doi.org/10.1016/j.jtrangeo.2006.11.008 (2007).

7. Arunachalam, V. & Fleischer, E. The global energy landscape and materials innovation. *MRS bulletin* **33,** 264–288. doi:https://doi.org/10.1557/mrs2008.61 (2008).

8. Ding, X., Duan, S., Ding, X., Liu, R. & Xu, F.-J. Versatile antibacterial materials: an emerging arsenal for combatting bacterial pathogens. *Advanced Functional Materials* **28,** 1802140. doi:https://doi.org/10.1002/adfm.201802140 (2018).

9. Bush, K. *et al.* Tackling antibiotic resistance. *Nature Reviews Microbiology* **9,** 894–896. doi:https://doi.org/10.1038/nrmicro2693 (2011).

10. Hillie, T. & Hlophe, M. Nanotechnology and the challenge of clean water. *Nature nanotechnology* **2,** 663. doi:https://doi.org/10.1038/nnano.2007.350 (2007).

11. Sattler, M. L. in *Greenhouse Gases* (IntechOpen, 2016). doi:https://doi.org/10.5772/62254.

12. Jain, A. *et al.* Commentary: The Materials Project: A materials genome approach to accelerating materials innovation. *Apl Materials* **1,** 011002. doi:https://doi.org/10.1063/1.4812323 (2013).

13. Butler, K. T., Davies, D. W., Cartwright, H., Isayev, O. & Walsh, A. Machine learning for molecular and materials science. *Nature* **559,** 547–555. doi:https://doi.org/10.1038/s41586-018-0337-2 (2018).

14. Valdevit, L., Bertoldi, K., Guest, J. & Spadaccini, C. Architected Materials: Synthesis, Characterization, Modeling, And Optimal Design. *Journal of Materials Research* **33,** 241–246. doi:https://doi.org/10.1557/jmr.2018.18 (2018).

15. Ashby, M. Designing architectured materials. *Scripta Materialia* **68,** 4–7. doi:https://doi.org/10.1016/j.scriptamat.2012.04.033 (2013).

16. Meza, L. R. *et al.* Resilient 3D hierarchical architected metamaterials. *Proceedings of the National Academy of Sciences* **112,** 11502–11507. doi:https://doi.org/10.1073/pnas.1509120112 (2015).

17. Sundaram, M. M. & Ananthasuresh, G. Gustave Eiffel and his optimal structures. *Resonance* **14,** 849. doi:https://doi.org/10.1007/s12045-009-0081-x (2009).

18. Osanov, M. & Guest, J. K. Topology optimization for architected materials design. *Annual Review of Materials Research* **46,** 211–233. doi:https://doi.org/10.1146/annurev-matsci-070115-031826 (2016).

19. Chen, P.-Y., McKittrick, J. & Meyers, M. A. Biological materials: functional adaptations and bioinspired designs. *Progress in Materials Science* **57,** 1492–1704. doi:https://doi.org/10.1016/j.pmatsci.2012.03.001 (2012).

20. Luo, S. & Greer, J. R. Bio-Mimicked Silica Architectures Capture Geometry, Microstructure, and Mechanical Properties of Marine Diatoms. *Advanced Engineering Materials* **20,** 1800301. doi:https://doi.org/10.1002/adem.201800301 (2018).

21. Sun, J. & Bhushan, B. Hierarchical structure and mechanical properties of nacre: a review. *Rsc Advances* **2,** 7617–7632. doi:https://doi.org/10.1039/C2RA20218B (2012).

22. Wegst, U. G., Bai, H., Saiz, E., Tomsia, A. P. & Ritchie, R. O. Bioinspired structural materials. *Nature materials* **14,** 23–36. doi:https://doi.org/10.1038/nmat4089 (2015).

23. Autumn, K. *et al.* Evidence for van der Waals adhesion in gecko setae. *Proceedings of the National Academy of Sciences* **99,** 12252–12256. doi:https://doi.org/10.1073/pnas.192252799 (2002).

24. Autumn, K. *et al.* Adhesive force of a single gecko foot-hair. *Nature* **405,** 681–685. doi:https://doi.org/10.1038/35015073 (2000).

25. Dean, B. & Bhushan, B. Shark-skin surfaces for fluid-drag reduction in turbulent flow: a review. *Philosophical Transactions of the Royal Society A: Mathematical, Physical and Engineering Sciences* **368,** 4775–4806. doi:https://doi.org/10.1098/rsta.2010.0201 (2010).

26. Srinivasarao, M. Nano-optics in the biological world: beetles, butterflies, birds, and moths. *Chemical reviews* **99,** 1935–1962. doi:https://doi.org/10.1021/cr970080y (1999).

27. Burg, S. L. & Parnell, A. J. Self-assembling structural colour in nature. *Journal of Physics: Condensed Matter* **30,** 413001. doi:https://doi.org/10.1088/1361-648X/aadc95 (2018).

28. Libonati, F. & Buehler, M. J. Advanced structural materials by bioinspiration. *Advanced Engineering Materials* **19,** 1600787. doi:https://doi.org/10.1002/adem.201600787 (2017).

29. Thavapalan, S. *The Meaning of Color in Ancient Mesopotamia* doi:https://doi.org/10.1163/9789004415416 (Brill, 2019).

30. Mallick, P. K. *Fiber-reinforced composites: materials, manufacturing, and design* doi:https://doi.org/10.1201/9781420005981 (CRC press, 2007).

31. Gibson, L. J. & Ashby, M. F. *Cellular Solids: Structure and Properties* 2nd ed. doi:10.1017/CBO9781139878326 (Cambridge University Press, 1997).

32. Ashby, M. The properties of foams and lattices. *Philosophical Transactions of the Royal Society A: Mathematical, Physical and Engineering Sciences* **364,** 15–30. doi:https://doi.org/10.1098/rsta.2005.1678 (2006).

33. Jin, F.-L., Zhao, M., Park, M. & Park, S.-J. Recent Trends of Foaming in Polymer Processing: A Review. *Polymers* **11,** 953. doi:https://doi.org/10.3390/polym11060953 (2019).

34. Banhart, J. Light-metal foams—History of innovation and technological challenges. *Advanced Engineering Materials* **15,** 82–111. doi:https://doi.org/10.1002/adem.201200217 (2013).

35. Colombo, P. Conventional and novel processing methods for cellular ceramics. *Philosophical Transactions of the Royal Society A: Mathematical, Physical and Engineering Sciences* **364,** 109–124. doi:https://doi.org/10.1098/rsta.2005.1683 (2006).

36. Brothers, A. H. & Dunand, D. C. Ductile bulk metallic glass foams. *Advanced Materials* **17,** 484–486. doi:https://doi.org/10.1002/adma.200400897 (2005).

37. Baino, F., Fiorilli, S. & Vitale-Brovarone, C. Bioactive glass-based materials with hierarchical porosity for medical applications: review of recent advances. *Acta biomaterialia* **42,** 18–32. doi:https://doi.org/10.1016/j.actbio.2016.06.033 (2016).

38. Duarte, I. & Ferreira, J. M. Composite and nanocomposite metal foams. *Materials* **9,** 79. doi:https://doi.org/10.3390/ma9020079 (2016).

39. Kausar, A. Polyurethane composite foams in high-performance applications: A review. *Polymer-Plastics Technology and Engineering* **57,** 346–369. doi:https://doi.org/10.1080/03602559.2017.1329433 (2018).

40. Gómez-Rojo, R., Alameda, L., Rodrıguez, Á., Calderón, V. & Gutiérrez-González, S. Characterization of polyurethane foam waste for reuse in eco-efficient building materials. *Polymers* **11,** 359. doi:https://doi.org/10.3390/polym11020359 (2019).

41. Deshpande, V., Ashby, M. & Fleck, N. Foam topology: bending versus stretching dominated architectures. *Acta materialia* **49,** 1035–1040. doi:https://doi.org/10.1016/S1359-6454(00)00379-7 (2001).

42. Groβ, J., Schlief, T. & Fricke, J. Ultrasonic evaluation of elastic properties of silica aerogels. *Materials Science and Engineering: A* **168,** 235–238. doi:https://doi.org/10.1016/0921-5093(93)90733-U (1993).

43. Liu, Z., Chuah, C. & Scanlon, M. Compressive elastic modulus and its relationship to the structure of a hydrated starch foam. *Acta Materialia* **51,** 365–371. doi:https://doi.org/10.1016/S1359-6454(02)00400-7 (2003).

44. Celzard, A., Zhao, W., Pizzi, A. & Fierro, V. Mechanical properties of tannin-based rigid foams undergoing compression. *Materials Science and Engineering: A* **527,** 4438–4446. doi:https://doi.org/10.1016/j.msea.2010.03.091 (2010).

45. Meza, L. R. *et al.* Reexamining the mechanical property space of three-dimensional lattice architectures. *Acta Materialia* **140,** 424–432. doi:https://doi.org/10.1016/j.actamat.2017.08.052 (2017).

46. Schaedler, T. A. *et al.* Ultralight metallic microlattices. *Science* **334,** 962–965. doi:https://doi.org/10.1126/science.1211649 (2011).

47. Zhao, X. *et al.* Templating methods for preparation of porous structures. *Journal of Materials Chemistry* **16,** 637–648. doi:https://doi.org/10.1039/B513060C (2006).

48. Lehmhus, D., Vesenjak, M., Schampheleire, S. & Fiedler, T. From Stochastic Foam to Designed Structure: Balancing Cost and Performance of Cellular Metals. *Materials* **10,** 922. ISSN: 1996-1944. doi:http://doi.org/10.3390/ma10080922 (2017).

49. Fujita, T. Hierarchical nanoporous metals as a path toward the ultimate three-dimensional functionality. *Science and Technology of Advanced Materials* **18,** 724–740. doi:https://doi.org/10.1080/14686996.2017.1377047 (2017).

50. Qi, Z. & Weissmüller, J. Hierarchical nested-network nanostructure by dealloying. *Acs Nano* **7,** 5948–5954. doi:https://doi.org/10.1021/nn4021345 (2013).

51. Zhou, N., Bates, F. S. & Lodge, T. P. Mesoporous membrane templated by a polymeric bicontinuous microemulsion. *Nano letters* **6,** 2354–2357. doi:https://doi.org/10.1021/nl061765t (2006).

52. Stein, A., Wright, G., Yager, K. G., Doerk, G. S. & Black, C. T. Selective directed self-assembly of coexisting morphologies using block copolymer blends. *Nature communications* **7,** 1–7. doi:https://doi.org/10.1038/ncomms12366 (2016).

53. Huang, Y., Leu, M. C., Mazumder, J. & Donmez, A. Additive manufacturing: current state, future potential, gaps and needs, and recommendations. *Journal of Manufacturing Science and Engineering* **137.** doi:https://doi.org/10.1115/1.4028725 (2015).

54. Gibson, I., Rosen, D. W., Stucker, B., *et al. Additive manufacturing technologies* doi:https://doi.org/10.1007/978-1-4419-1120-9 (Springer, 2014).

55. Wohlers, T. & Garnett, T. History of additive manufacturing; Wohlers Associates. *INC: Fort Collins, CO, USA,* 34 (2014).

56. Kodama, H. Automatic method for fabricating a three-dimensional plastic model with photo-hardening polymer. *Review of scientific instruments* **52,** 1770–1773. doi:https://doi.org/10.1063/1.1136492 (1981).

57. Chen, Z. *et al.* 3D printing of ceramics: A review. *Journal of the European Ceramic Society* **39,** 661–687. doi:https://doi.org/10.1016/j.jeurceramsoc.2018.11.013 (2019).

58. Frazier, W. E. Metal additive manufacturing: a review. *Journal of Materials Engineering and Performance* **23,** 1917–1928. doi:https://doi.org/10.1007/s11665-014-0958-z (2014).

59. Ligon, S. C., Liska, R., Stampfl, J., Gurr, M. & Mülhaupt, R. Polymers for 3D printing and customized additive manufacturing. *Chemical reviews* **117,** 10212–10290. doi:https://doi.org/10.1021/acs.chemrev.7b00074 (2017).

60. Fowlkes, J. D. *et al.* Simulation-guided 3D nanomanufacturing via focused electron beam induced deposition. *ACS nano* **10,** 6163–6172. doi:https://doi.org/10.1021/acsnano.6b02108 (2016).

61. Of Maine, T. U. *UMaine Composites Center receives three Guinness World Records related to largest 3D printer* https://umaine.edu/news/blog/2019/10/10/umaine-composites-center-receives-three-guinness-world-records-related-to-largest-3d-printer/ (2020).

62. Attaran, M. The rise of 3-D printing: The advantages of additive manufacturing over traditional manufacturing. *Business Horizons* **60,** 677–688. doi:https://doi.org/10.1016/j.bushor.2017.05.011 (2017).

63. Ford, S. & Minshall, T. Invited review article: Where and how 3D printing is used in teaching and education. *Additive Manufacturing* **25,** 131–150. doi:https://doi.org/10.1016/j.addma.2018.10.028 (2019).

64. Tofail, S. A. *et al.* Additive manufacturing: scientific and technological challenges, market uptake and opportunities. *Materials today* **21,** 22–37. doi:https://doi.org/10.1016/j.mattod.2017.07.001 (2018).

65. Maric, J., Rodhain, F. & Barlette, Y. Frugal innovations and 3D printing: insights from the field. *Journal of Innovation Economics Management,* 57–76. doi:https://doi.org/10.3917/jie.021.0057 (2016).

66. Administration, U. S. F. D̃. *FAQs on 3D Printing of Medical Devices, Accessories, Components, and Parts During the COVID-19 Pandemic* https://www.fda.gov/medical-devices/3d-printing-medical-devices/faqs-3d-printing-medical-devices-accessories-components-and-parts-during-covid-19-pandemic (2020).

67. Astm, I. ASTM52900-15 Standard Terminology for Additive Manufacturing—General Principles—Terminology. *ASTM International, West Conshohocken, PA* **3,** 5. doi:https://doi.org/10.1520/ISOASTM52900-15 (2015).

68. Gokuldoss, P. K., Kolla, S. & Eckert, J. Additive manufacturing processes: Selective laser melting, electron beam melting and binder jetting—Selection guidelines. *Materials* **10,** 672. doi:https://doi.org/10.3390/ma10060672 (2017).

69. Ko, S. H., Chung, J., Hotz, N., Nam, K. H. & Grigoropoulos, C. P. Metal nanoparticle direct inkjet printing for low-temperature 3D micro metal structure fabrication. *Journal of Micromechanics and Microengineering* **20,** 125010. doi:https://doi.org/10.1088/0960-1317/20/12/125010 (2010).

70. Graf, D. *et al.* Influence of Al2O3 nanoparticle addition on a UV cured polyacrylate for 3D inkjet printing. *Polymers* **11,** 633. doi:https://doi.org/10.3390/polym11040633 (2019).

71. Lee, T.-M. *et al. 3D metal microstructure fabrication using a molten metal DoD inkjet system* in *TRANSDUCERS 2007-2007 International Solid-State Sensors, Actuators and Microsystems Conference* (2007), 1637–1640. doi:https://doi.org/10.1109/SENSOR.2007.4300463.

72. Bader, C. *et al.* Making data matter: Voxel printing for the digital fabrication of data across scales and domains. *Science advances* **4,** eaas8652. doi:https://doi.org/10.1126/sciadv.aas8652 (2018).

73. Gonzalez-Gutierrez, J. *et al.* Additive manufacturing of metallic and ceramic components by the material extrusion of highly-filled polymers: A review and future perspectives. *Materials* **11,** 840. doi:https://doi.org/10.3390/ma11050840 (2018).

74. Lewis, J. A. & Gratson, G. M. Direct writing in three dimensions. *Materials today* **7,** 32–39. doi:https://doi.org/10.1016/S1369-7021(04)00344-X (2004).

75. Skylar-Scott, M. A., Mueller, J., Visser, C. W. & Lewis, J. A. Voxelated soft matter via multimaterial multinozzle 3D printing. *Nature* **575,** 330–335. doi:https://doi.org/10.1038/s41586-019-1736-8 (2019).

76. Magdassi, S. & Kamyshny, A. *Nanomaterials for 2D and 3D Printing* doi:https://doi.org/10.1002/9783527685790 (John Wiley & Sons, 2017).

77. Lee, J.-Y., An, J. & Chua, C. K. Fundamentals and applications of 3D printing for novel materials. *Applied Materials Today* **7,** 120–133. doi:https://doi.org/10.1016/j.apmt.2017.02.004 (2017).

78. Odian, G. *Principles of polymerization* doi:https://doi.org/10.1002/047147875X (John Wiley & Sons, 2004).

79. Lee, T. Y., Roper, T. M., Jönsson, E. S., Guymon, C. & Hoyle, C. Influence of hydrogen bonding on photopolymerization rate of hydroxyalkyl acrylates. *Macromolecules* **37,** 3659–3665. doi:https://doi.org/10.1021/ma0305277 (2004).

80. Belon, C., Allonas, X., Croutxé-Barghorn, C. & Lalevée, J. Overcoming the oxygen inhibition in the photopolymerization of acrylates: A study of the beneficial effect of triphenylphosphine. *Journal of Polymer Science Part A: Polymer Chemistry* **48,** 2462–2469. doi:https://doi.org/10.1002/pola.24017 (2010).

81. Pfeifer, C. S., Wilson, N. D., Shelton, Z. R. & Stansbury, J. W. Delayed gelation through chain-transfer reactions: mechanism for stress reduction in methacrylate networks. *Polymer* **52,** 3295–3303. doi:10.1016/j.polymer.2011.05.034 (2011).

82. Burdick, J. A., Lovestead, T. M. & Anseth, K. S. Kinetic chain lengths in highly cross-linked networks formed by the photoinitiated polymerization of divinyl monomers: A gel permeation chromatography investigation. *Biomacromolecules* **4,** 149–156. doi:https://doi.org/10.1021/bm025677o (2003).

83. Bowman, C. N. & Kloxin, C. J. Toward an enhanced understanding and implementation of photopolymerization reactions. *AIChE Journal* **54,** 2775–2795. doi:https://doi.org/10.1002/aic.11678 (2008).

84. Flory, P. J. Molecular size distribution in three dimensional polymers. I. Gelation1. *Journal of the American Chemical Society* **63,** 3083–3090. doi:https://doi.org/10.1021/ja01856a061 (1941).

85. Karalekas, D. & Aggelopoulos, A. Study of shrinkage strains in a stereolithography cured acrylic photopolymer resin. *Journal of materials processing technology* **136,** 146–150. doi:https://doi.org/10.1016/S0924-0136(03)00028-1 (2003).

86. Pynaert, R., Buguet, J., Croutxe-Barghorn, C., Moireau, P. & Allonas, X. Effect of reactive oxygen species on the kinetics of free radical photopolymerization. *Polymer Chemistry* **4,** 2475–2479. doi:https://doi.org/10.1039/C3PY21163K (2013).

87. Yogesh, P., Richa, P., Chandrashekhar, N. & Karunakaran, K. in *Advances in Additive Manufacturing and Joining* 179–187 (Springer, 2020). doi:https://doi.org/10.1007/978-981-32-9433-2_15.

88. Wang, J.-C., Ruilova, M. & Lin, Y.-H. *The development of an active separation method for bottom-up stereolithography system* in *2017 IEEE/SICE International Symposium on System Integration (SII)* (2017), 108–114. doi:https://doi.org/10.1109/SII.2017.8279197.

89. Liravi, F., Das, S. & Zhou, C. Separation force analysis and prediction based on cohesive element model for constrained-surface Stereolithography processes. *Computer-Aided Design* **69,** 134–142. doi:https://doi.org/10.1016/j.cad.2015.05.002 (2015).

90. Pan, Y., Zhou, C. & Chen, Y. A fast mask projection stereolithography process for fabricating digital models in minutes. *Journal of Manufacturing Science and Engineering* **134.** doi:https://doi.org/10.1115/1.4007465 (2012).

91. Dendukuri, D., Pregibon, D. C., Collins, J., Hatton, T. A. & Doyle, P. S. Continuous-flow lithography for high-throughput microparticle synthesis. *Nature materials* **5,** 365–369. doi:https://doi.org/10.1038/nmat1617 (2006).

92. Naik, D. L. & Kiran, R. On anisotropy, strain rate and size effects in vat photopolymerization based specimens. *Additive Manufacturing* **23,** 181–196. doi:https://doi.org/10.1016/j.addma.2018.08.021 (2018).

93. Quintana, R., Choi, J.-W., Puebla, K. & Wicker, R. Effects of build orientation on tensile strength for stereolithography-manufactured ASTM D-638 type I specimens. *The International Journal of Advanced Manufacturing Technology* **46,** 201–215. doi:https://doi.org/10.1007/s00170-009-2066-z (2010).

94. Bertsch, A., Jézéquel, J. & André, J. Study of the spatial resolution of a new 3D microfabrication process: the microstereophotolithography using a dynamic mask-generator technique. *Journal of Photochemistry and Photobiology A: Chemistry* **107,** 275–281. doi:https://doi.org/10.1016/S1010-6030(96)04585-6 (1997).

95. Sun, C., Fang, N., Wu, D. & Zhang, X. Projection micro-stereolithography using digital micro-mirror dynamic mask. *Sensors and Actuators A: Physical* **121,** 113–120. doi:https://doi.org/10.1016/j.sna.2004.12.011 (2005).

96. Monzón, M., Ortega, Z., Hernández, A., Paz, R. & Ortega, F. Anisotropy of photopolymer parts made by digital light processing. *Materials* **10,** 64. doi:https://doi.org/10.3390/ma10010064 (2017).

97. Tumbleston, J. R. *et al.* Continuous liquid interface production of 3D objects. *Science* **347,** 1349–1352. doi:https://doi.org/10.1126/science.aaa2397 (2015).

98. Janusziewicz, R., Tumbleston, J. R., Quintanilla, A. L., Mecham, S. J. & DeSimone, J. M. Layerless fabrication with continuous liquid interface production. *Proceedings of the National Academy of Sciences* **113,** 11703–11708. doi:https://doi.org/10.1073/pnas.1605271113 (2016).

99. Media, F. *3D-Printing Unicorn Carbon Gets A High-Powered CEO In Ellen Kullman, Formerly Of DuPont, As Its Founding CEO Moves Aside* https://www.forbes.com/sites/amyfeldman/2019/11/21/founding-ceo-of-3d-printing-unicorn-carbon-steps-down-in-favor-of-ex-dupont-ceo-ellen-kullman/#2a4615957cb5 (2020).

100. Walker, D. A., Hedrick, J. L. & Mirkin, C. A. Rapid, large-volume, thermally controlled 3D printing using a mobile liquid interface. *Science* **366,** 360–364. doi:https://doi.org/10.1126/science.aax1562 (2019).

101. Baldacchini, T. *Three-dimensional microfabrication using two-photon polymerization: fundamentals, technology, and applications* doi:https://doi.org/10.1016/C2014-0-01016-7 (William Andrew, 2015).

102. LaFratta, C. N., Fourkas, J. T., Baldacchini, T. & Farrer, R. A. Multiphoton fabrication. *Angewandte Chemie International Edition* **46,** 6238–6258. doi:https://doi.org/10.1002/anie.200603995 (2007).

103. Hahn, V., Mayer, F., Thiel, M. & Wegener, M. 3-D Laser Nanoprinting. *Optics and Photonics News* **30,** 28–35. doi:https://doi.org/10.1364/OPN.30.10.000028 (2019).

104. Kelly, B. E. *et al.* Volumetric additive manufacturing via tomographic reconstruction. *Science* **363,** 1075–1079. doi:https://doi.org/10.1126/science.aau7114 (2019).

105. Loterie, D., Delrot, P. & Moser, C. High-resolution tomographic volumetric additive manufacturing. *Nature communications* **11,** 1–6. doi:https://doi.org/10.1038/s41467-020-14630-4 (2020).

106. Shusteff, M. *et al.* One-step volumetric additive manufacturing of complex polymer structures. *Science advances* **3,** eaao5496. doi:https://doi.org/10.1126/sciadv.aao5496 (2017).

107. Crook, C. *et al.* Plate-nanolattices at the theoretical limit of stiffness and strength. *Nature communications* **11,** 1–11. doi:https://doi.org/10.1038/s41467-020-15434-2 (2020).

108. Portela, C. M. *et al.* Extreme mechanical resilience of self-assembled nanolabyrinthine materials. *Proceedings of the National Academy of Sciences* **117,** 5686–5693. doi:https://doi.org/10.1073/pnas.1916817117 (2020).

109. Guell Izard, A., Bauer, J., Crook, C., Turlo, V. & Valdevit, L. Ultrahigh Energy Absorption Multifunctional Spinodal Nanoarchitectures. *Small* **15,** 1903834. doi:https://doi.org/10.1002/smll.201903834 (2019).

110. Mateos, A. J., Huang, W., Zhang, Y.-W. & Greer, J. R. Discrete-continuum duality of architected materials: failure, flaws, and fracture. *Advanced Functional Materials* **29,** 1806772. doi:https://doi.org/10.1002/adfm.201806772 (2019).

111. Brodnik, N. R. *Fracture and Toughening of Brittle Structures with Designed Anisotropy* PhD thesis (California Institute of Technology, 2020).

112. Frenzel, T., Kadic, M. & Wegener, M. Three-dimensional mechanical metamaterials with a twist. *Science* **358,** 1072–1074. doi:https://doi.org/10.1126/science.aao4640 (2017).

113. Shaw, L. A. *et al.* Computationally efficient design of directionally compliant metamaterials. *Nature communications* **10,** 1–13. doi:https://doi.org/10.1038/s41467-018-08049-1 (2019).

114. Saxena, K. K., Das, R. & Calius, E. P. Three decades of auxetics research- materials with negative Poisson's ratio: a review. *Advanced Engineering Materials* **18,** 1847–1870. doi:https://doi.org/10.1002/adem.201600053 (2016).

115. Frenzel, T., Findeisen, C., Kadic, M., Gumbsch, P. & Wegener, M. Tailored buckling microlattices as reusable light-weight shock absorbers. *Advanced Materials* **28,** 5865–5870. doi:https://doi.org/10.1002/adma.201600610 (2016).

116. Al-Ketan, O., Soliman, A., AlQubaisi, A. M. & Abu Al-Rub, R. K. Nature-Inspired Lightweight Cellular Co-Continuous Composites with Architected Periodic Gyroidal Structures. *Advanced Engineering Materials* **20,** 1700549. doi:https://doi.org/10.1002/adem.201700549 (2018).

117. Al-Ketan, O., Al-Rub, R. K. A. & Rowshan, R. Mechanical properties of a new type of architected interpenetrating phase composite materials. *Advanced Materials Technologies* **2,** 1600235. doi:https://doi.org/10.1002/admt.201600235 (2017).

118. Chernow, V., Alaeian, H., Dionne, J. & Greer, J. Polymer lattices as mechanically tunable 3-dimensional photonic crystals operating in the infrared. *Applied Physics Letters* **107,** 101905. doi:https://doi.org/10.1063/1.4930819 (2015).

119. Peng, S. *et al.* Three-dimensional single gyroid photonic crystals with a mid-infrared bandgap. *ACS Photonics* **3,** 1131–1137. doi:https://doi.org/10.1021/acsphotonics.6b00293 (2016).

120. Liu, Y. *et al.* Structural color three-dimensional printing by shrinking photonic crystals. *Nature communications* **10,** 1–8. doi:https://doi.org/10.1038/s41467-019-12360-w (2019).

121. Chernow, V. F. *Design, Fabrication, and Characterization of 3D Nanolattice Photonic Crystals for Bandgap and Refractive Index Engineering* PhD thesis (California Institute of Technology, 2018).

122. Chartrain, N. A., Williams, C. B. & Whittington, A. R. A review on fabricating tissue scaffolds using vat photopolymerization. *Acta biomaterialia* **74,** 90–111. doi:https://doi.org/10.1016/j.actbio.2018.05.010 (2018).

123. Ferlin, K. M., Prendergast, M. E., Miller, M. L., Kaplan, D. S. & Fisher, J. P. Influence of 3D printed porous architecture on mesenchymal stem cell enrichment and differentiation. *Acta biomaterialia* **32,** 161–169. doi:https://doi.org/10.1016/j.actbio.2016.01.007 (2016).

124. Moussi, K., Bukhamsin, A., Hidalgo, T. & Kosel, J. Biocompatible 3D Printed Microneedles for Transdermal, Intradermal, and Percutaneous Applications. *Advanced Engineering Materials* **22,** 1901358. doi:https://doi.org/10.1002/adem.201901358 (2020).

125. Zhu, W. *et al.* 3D-printed artificial microfish. *Advanced materials* **27,** 4411–4417. doi:https://doi.org/10.1002/adma.201501372 (2015).

126. Bagheri, A. & Jin, J. Photopolymerization in 3D printing. *ACS Applied Polymer Materials* **1,** 593–611. doi:https://doi.org/10.1021/acsapm.8b00165 (2019).

127. Appuhamillage, G. A. *et al.* 110th Anniversary: Vat Photopolymerization-Based Additive Manufacturing: Current Trends and Future Directions in Materials Design. *Industrial & Engineering Chemistry Research* **58,** 15109–15118. doi:https://doi.org/10.1021/acs.iecr.9b02679 (2019).

128. Wilts, E. M. *et al.* Vat photopolymerization of charged monomers: 3D printing with supramolecular interactions. *Polymer Chemistry* **10,** 1442–1451. doi:https://doi.org/10.1039/C8PY01792A (2019).

129. Vyatskikh, A., Kudo, A., Delalande, S. & Greer, J. R. Additive manufacturing of polymer-derived titania for one-step solar water purification. *Materials Today Communications* **15,** 288–293. doi:https://doi.org/10.1016/j.mtcomm.2018.02.010 (2018).

130. Nic, M. & Znamenacek, J. IUPAC. Compendium of Chemical Terminology 2nd ed.(the "Gold Book"). *International Union of Pure and Applied Chemistry* **1670.** doi:https://doi.org/10.1351/goldbook (2005).

131. Nadgorny, M. & Ameli, A. Functional polymers and nanocomposites for 3D printing of smart structures and devices. *ACS applied materials & interfaces* **10,** 17489–17507. doi:https://doi.org/10.1021/acsami.8b01786 (2018).

132. Odent, J. *et al.* Highly elastic, transparent, and conductive 3D-printed ionic composite hydrogels. *Advanced Functional Materials* **27,** 1701807. doi:https://doi.org/10.1002/adfm.201701807 (2017).

133. Wu, Y. *et al.* Fabrication of conductive polyaniline hydrogel using porogen leaching and projection microstereolithography. *Journal of materials chemistry B* **3,** 5352–5360. doi:https://doi.org/10.1039/C5TB00629E (2015).

134. Cullen, A. T. & Price, A. D. Digital light processing for the fabrication of 3D intrinsically conductive polymer structures. *Synthetic Metals* **235,** 34–41. doi:https://doi.org/10.1016/j.synthmet.2017.11.003 (2018).

135. Kurselis, K., Kiyan, R., Bagratashvili, V. N., Popov, V. K. & Chichkov, B. N. 3D fabrication of all-polymer conductive microstructures by two photon polymerization. *Optics express* **21,** 31029–31035. doi:https://doi.org/10.1364/OE.21.031029 (2013).

136. Löwa, N. *et al.* 3D-printing of novel magnetic composites based on magnetic nanoparticles and photopolymers. *Journal of Magnetism and Magnetic Materials* **469,** 456–460. doi:https://doi.org/10.1016/j.jmmm.2018.08.073 (2019).

137. Lu, L., Guo, P. & Pan, Y. Magnetic-field-assisted projection stereolithography for three-dimensional printing of smart structures. *Journal of Manufacturing Science and Engineering* **139.** doi:https://doi.org/10.1115/1.4035964 (2017).

138. Aduba Jr, D. C. *et al.* Vat photopolymerization 3D printing of acid-cleavable PEG-methacrylate networks for biomaterial applications. *Materials Today Communications* **19,** 204–211. doi:https://doi.org/10.1016/j.mtcomm.2019.01.003 (2019).

139. Walker, J. M. *et al.* Effect of chemical and physical properties on the in vitro degradation of 3D printed high resolution poly (propylene fumarate) scaffolds. *Biomacromolecules* **18,** 1419–1425. doi:https://doi.org/10.1021/acs.biomac.7b00146 (2017).

140. Smith, P. T. *et al.* Additive Manufacturing of Bovine Serum Albumin-based Hydrogels and Bioplastics. *Biomacromolecules.* doi:https://doi.org/10.1021/acs.biomac.9b01236 (2019).

141. Tayalia, P., Mendonca, C. R., Baldacchini, T., Mooney, D. J. & Mazur, E. 3D cell-migration studies using two-photon engineered polymer scaffolds. *Advanced materials* **20,** 4494–4498. doi:https://doi.org/10.1002/adma.200801319 (2008).

142. Chan, V., Zorlutuna, P., Jeong, J. H., Kong, H. & Bashir, R. Three-dimensional photopatterning of hydrogels using stereolithography for long-term cell encapsulation. *Lab on a Chip* **10,** 2062–2070. doi:https://doi.org/10.1039/C004285D (2010).

143. Lu, Y. *et al.* Microstereolithography and characterization of poly (propylene fumarate)-based drug-loaded microneedle arrays. *Biofabrication* **7,** 045001. doi:https://doi.org/10.1088/1758-5090/7/4/045001 (2015).

144. Economidou, S. N., Lamprou, D. A. & Douroumis, D. 3D printing applications for transdermal drug delivery. *International journal of pharmaceutics* **544,** 415–424. doi:https://doi.org/10.1016/j.ijpharm.2018.01.031 (2018).

145. Bloomquist, C. J. *et al.* Controlling release from 3D printed medical devices using CLIP and drug-loaded liquid resins. *Journal of controlled release* **278,** 9–23. doi:https://doi.org/10.1016/j.jconrel.2018.03.026 (2018).

146. Mishra, A. K. *et al.* Autonomic perspiration in 3D-printed hydrogel actuators. *Science Robotics* **5.** doi:10.1126/scirobotics.aaz3918 (2020).

147. Cao, B., Boechler, N. & Boydston, A. J. Additive manufacturing with a flex activated mechanophore for nondestructive assessment of mechanochemical reactivity in complex object geometries. *Polymer* **152,** 4–8. doi:https://doi.org/10.1016/j.polymer.2018.05.038 (2018).

148. Garcia, C. *et al.* Smart pH-responsive antimicrobial hydrogel scaffolds prepared by additive manufacturing. *ACS Applied Bio Materials* **1,** 1337–1347. doi:https://doi.org/10.1021/acsabm.8b00297 (2018).

149. Han, D. *et al.* Soft robotic manipulation and locomotion with a 3D printed electroactive hydrogel. *ACS applied materials & interfaces* **10,** 17512–17518. doi:https://doi.org/10.1021/acsami.8b04250 (2018).

150. Wales, D. J. *et al.* 3D-printable photochromic molecular materials for reversible information storage. *Advanced Materials* **30,** 1800159. doi:https://doi.org/10.1002/adma.201800159 (2018).

151. Shafranek, R. T. *et al.* Stimuli-responsive materials in additive manufacturing. *Progress in Polymer Science.* doi:https://doi.org/10.1016/j.progpolymsci.2019.03.002 (2019).

152. Medellin, A. *et al.* Vat Photopolymerization 3D Printing of Nanocomposites: A Literature Review. *Journal of Micro and Nano-Manufacturing* **7.** doi:https://doi.org/10.1115/1.4044288 (2019).

153. Wang, X. *et al.* i3DP, a robust 3D printing approach enabling genetic post-printing surface modification. *Chemical Communications* **49,** 10064–10066. doi:https://doi.org/10.1039/C3CC45817B (2013).

154. Luan, B., Yeung, M., Wells, W. & Liu, X. Chemical surface preparation for metallization of stereolithography polymers. *Applied surface science* **156,** 26–38. doi:https://doi.org/10.1016/S0169-4332(99)00339-6 (2000).

155. Hong, J. M. *et al.* Enhancement of bone regeneration through facile surface functionalization of solid freeform fabrication-based three-dimensional scaffolds using mussel adhesive proteins. *Acta Biomaterialia* **8,** 2578–2586. doi:https://doi.org/10.1016/j.actbio.2012.03.041 (2012).

156. Kao, C.-T. *et al.* Poly (dopamine) coating of 3D printed poly (lactic acid) scaffolds for bone tissue engineering. *Materials Science and Engineering: C* **56,** 165–173. doi:https://doi.org/10.1016/j.msec.2015.06.028 (2015).

157. Richter, B. *et al.* Three-Dimensional Microscaffolds Exhibiting Spatially Resolved Surface Chemistry. *Advanced Materials* **25,** 6117–6122. doi:https://doi.org/10.1002/adma.201302678 (2013).

158. Weems, A. C., Delle Chiaie, K. R., Yee, R. & Dove, A. P. Selective Reactivity of Myrcene for Vat Photopolymerization 3D Printing and Postfabrication Surface Modification. *Biomacromolecules* **21,** 163–170. doi:https://doi.org/10.1021/acs.biomac.9b01125 (2019).

159. Nishimura, S.-n. *et al.* Photocleavable Peptide–Poly (2-hydroxyethyl methacrylate) Hybrid Graft Copolymer via Postpolymerization Modification by Click Chemistry To Modulate the Cell Affinities of 2D and 3D Materials. *ACS applied materials & interfaces* **11,** 24577–24587. doi:https://doi.org/10.1021/acsami.9b06807 (2019).

160. Guo, Q., Cai, X., Wang, X. & Yang, J. "Paintable" 3D printed structures via a post-ATRP process with antimicrobial function for biomedical applications. *Journal of Materials Chemistry B* **1,** 6644–6649. doi:https://doi.org/10.1039/C3TB21415J (2013).

161. Li, S., Xu, Y., Yu, J. & Becker, M. L. Enhanced osteogenic activity of poly (ester urea) scaffolds using facile post-3D printing peptide functionalization strategies. *Biomaterials* **141,** 176–187. doi:https://doi.org/10.1016/j.biomaterials.2017.06.038 (2017).

162. Society, A. C. Global Cancer Facts & Figures 4th Edition. doi:https://doi.org/10.1021/acsami.9b06807 (2018).

163. Yeh, E. T. & Bickford, C. L. Cardiovascular complications of cancer therapy: incidence, pathogenesis, diagnosis, and management. *Journal of the American College of Cardiology* **53,** 2231–2247. doi:https://doi.org/10.1016/j.jacc.2009.02.050 (2009).

164. Cleeland, C. S. *et al.* Reducing the toxicity of cancer therapy: recognizing needs, taking action. *Nature reviews Clinical oncology* **9,** 471. doi:https://doi.org/10.1038/nrclinonc.2012.99 (2012).

165. Porrata, L. & Adjei, A. The pharmacologic basis of high dose chemotherapy with haematopoietic stem cell support for solid tumours. *British journal of cancer* **85,** 484–489. doi:https://doi.org/10.1054/bjoc.2001.1970 (2001).

166. Kroschinsky, F. *et al.* New drugs, new toxicities: severe side effects of modern targeted and immunotherapy of cancer and their management. *Critical Care* **21,** 89. doi:https://doi.org/10.1186/s13054-017-1678-1 (2017).

167. Siddiqui, M. & Rajkumar, S. V. *The high cost of cancer drugs and what we can do about it* in *Mayo Clinic Proceedings* **87** (2012), 935–943. doi:https://doi.org/10.1016/j.mayocp.2012.07.007.

168. Organization, W. H. *et al.* Technical report: pricing of cancer medicines and its impacts: a comprehensive technical report for the World Health Assembly Resolution 70.12: operative paragraph 2.9 on pricing approaches and their impacts on availability and affordability of medicines for the prevention and treatment of cancer (2018).

169. Yousuf Zafar, S. Financial toxicity of cancer care: it's time to intervene. *Journal of the National Cancer Institute* **108,** djv370. doi:https://doi.org/10.1093/jnci/djv370 (2016).

170. Rammohan, A. *et al.* Embolization of liver tumors: Past, present and future. *World journal of radiology* **4,** 405. doi:https://doi.org/10.4329/wjr.v4.i9.405 (2012).

171. Llovet, J. M. *et al.* Arterial embolisation or chemoembolisation versus symptomatic treatment in patients with unresectable hepatocellular carcinoma: a randomised controlled trial. *The Lancet* **359,** 1734–1739. doi:https://doi.org/10.1016/S0140-6736(02)08649-X (2002).

172. Hwu, W.-J. *et al.* A clinical-pharmacological evaluation of percutaneous isolated hepatic infusion of doxorubicin in patients with unresectable liver tumors. *Oncology Research Featuring Preclinical and Clinical Cancer Therapeutics* **11,** 529–537 (1999).

173. Patel, A. S. *et al.* Development and validation of endovascular chemotherapy filter device for removing high-dose doxorubicin: preclinical study. *Journal of medical devices* **8.** doi:https://doi.org/10.1115/1.4027444 (2014).

174. Oh, H. J. *et al.* 3D Printed Absorber for Capturing Chemotherapy Drugs before They Spread through the Body. *ACS central science* **5,** 419–427. doi:https://doi.org/10.1021/acscentsci.8b00700 (2019).

175. Chen, X. C. *et al.* Block copolymer membranes for efficient capture of a chemotherapy drug. *ACS macro letters* **5,** 936–941. doi:https://doi.org/10.1021/acsmacrolett.6b00459 (2016).

176. Yee, C. *et al.* Endovascular Ion Exchange Chemofiltration Device Reduces Off-Target Doxorubicin Exposure in a Hepatic Intra-arterial Chemotherapy Model. *Radiology: Imaging Cancer* **1,** e190009. doi:https://doi.org/10.1148/rycan.2019190009 (2019).

177. Yu, J. *Development of filter device to limit systemic toxicity from doxorubicin chemotherapy: DNA ChemoFilter* PhD thesis (University of California, San Francisco, 2015).

178. Aboian, M. S. *et al.* In vitro clearance of doxorubicin with a DNA-based filtration device designed for intravascular use with intra-arterial chemotherapy. *Biomedical microdevices* **18,** 98. doi:https://doi.org/10.1007/s10544-016-0124-5 (2016).

179. Blumenfeld, C. M. *et al.* Drug capture materials based on genomic DNA-functionalized magnetic nanoparticles. *Nature communications* **9,** 1–7. doi:https://doi.org/10.1038/s41467-018-05305-2 (2018).

180. Maani, N. *CFD MODELING IN DESIGN AND EVALUATION OF AN ENDOVASCULAR CHEMOFILTER DEVICE* PhD thesis (Purdue University Graduate School, 2019).

181. Maani, N., Hetts, S. W. & Rayz, V. L. A two-scale approach for CFD modeling of endovascular Chemofilter device. *Biomechanics and modeling in mechanobiology* **17,** 1811–1820. doi:https://doi.org/10.1007/s10237-018-1058-z (2018).

182. Maani, N., Diorio, T. C., Hetts, S. W. & Rayz, V. L. Computational modeling of drug transport and mixing in the chemofilter device: enhancing the removal of chemotherapeutics from circulation. *Biomechanics and Modeling in Mechanobiology,* 1–13. doi:https://doi.org/10.1007/s10237-020-01313-8 (2020).

183. Rahman, A. M., Yusuf, S. W. & Ewer, M. S. Anthracycline-induced cardiotoxicity and the cardiac-sparing effect of liposomal formulation. *International journal of nanomedicine* **2,** 567 (2007).

184. Gnapareddy, B. *et al.* Chemical and physical characteristics of doxorubicin hydrochloride drug-doped salmon DNA thin films. *Scientific reports* **5,** 12722. doi:https://doi.org/10.1038/srep12722 (2015).

185. Mookadam, F. *et al.* Effect of positional changes on inferior vena cava size. *European Journal of Echocardiography* **12,** 322–325. doi:https://doi.org/10.1093/ejechocard/jer018 (2011).

186. Dizdaroglu, M. & Jaruga, P. Mechanisms of free radical-induced damage to DNA. *Free radical research* **46,** 382–419. doi:https://doi.org/10.3109/10715762.2011.653969 (2012).

187. Devor, E. J., Behlke, M. A., *et al.* Strategies for attaching oligonucleotides to solid supports. *IDT DNA Rep,* 1–24 (2005).

188. Liu, X., Diao, H. & Nishi, N. Applied chemistry of natural DNA. *Chemical Society Reviews* **37,** 2745–2757. doi:https://doi.org/10.1039/b801433g (2008).

189. Gates, K. S. An overview of chemical processes that damage cellular DNA: spontaneous hydrolysis, alkylation, and reactions with radicals. *Chemical research in toxicology* **22,** 1747–1760. doi:https://doi.org/10.1021/tx900242k (2009).

190. Aucamp, J., Bronkhorst, A. J., Badenhorst, C. P. & Pretorius, P. J. The diverse origins of circulating cell-free DNA in the human body: a critical re-evaluation of the literature. *Biological Reviews* **93,** 1649–1683. doi:https://doi.org/10.1111/brv.12413 (2018).

191. Spisák, S. *et al.* Complete genes may pass from food to human blood. *PLoS One* **8,** e69805. doi:https://doi.org/10.1371/journal.pone.0069805 (2013).

192. Glenting, J. & Wessels, S. Ensuring safety of DNA vaccines. *Microbial cell factories* **4,** 26. doi:https://doi.org/10.1186/1475-2859-4-26 (2005).

193. Yamada, M. *et al.* Preparation and characterization of DNA films induced by UV irradiation. *Chemistry–A European Journal* **8,** 1407–1412. doi:https://doi.org/10.1002/1521-3765(20020315)8:6<1407::AID-CHEM1407>3.0.CO;2-L (2002).

194. Nazari, Z. E. & Gurevich, L. Molecular Combing of DNA: Methods and Applications. *Journal of Self-assembly and Molecular Electronics (same)* **1,** 125–148. doi:https://doi.org/10.13052/same2245-4551.116 (2013).

195. Bensimon, A. *et al.* Alignment and sensitive detection of DNA by a moving interface. *Science* **265,** 2096–2098. doi:https://doi.org/10.1126/science.7522347 (1994).

196. Jewell, C. M. & Lynn, D. M. Surface-mediated delivery of DNA: cationic polymers take charge. *Current opinion in colloid & interface science* **13,** 395–402. doi:https://doi.org/10.1016/j.cocis.2008.03.005 (2008).

197. Nakagawa, T. *et al.* Fabrication of amino silane-coated microchip for DNA extraction from whole blood. *Journal of Biotechnology* **116,** 105–111. doi:https://doi.org/10.1016/j.jbiotec.2004.08.018 (2005).

198. Nakagawa, T. *et al.* Capture and release of DNA using aminosilane-modified bacterial magnetic particles for automated detection system of single nucleotide polymorphisms. *Biotechnology and bioengineering* **94,** 862–868. doi:https://doi.org/10.1002/bit.20904 (2006).

199. Farrer, R. A. *et al.* Selective functionalization of 3-D polymer microstructures. *Journal of the American Chemical Society* **128,** 1796–1797. doi:https://doi.org/10.1021/ja0583620 (2006).

200. Laucirica, G., Marmisollé, W. A. & Azzaroni, O. Dangerous liaisons: anion-induced protonation in phosphate–polyamine interactions and their implications for the charge states of biologically relevant surfaces. *Physical Chemistry Chemical Physics* **19,** 8612–8620. doi:https://doi.org/10.1039/C6CP08793K (2017).

201. Kustanovich, A., Schwartz, R., Peretz, T. & Grinshpun, A. Life and death of circulating cell-free DNA. *Cancer biology & therapy* **20,** 1057–1067. doi:https://doi.org/10.1080/15384047.2019.1598759 (2019).

202. Cheung, B. C., Sun, T. H., Leenhouts, J. M. & Cullis, P. R. Loading of doxorubicin into liposomes by forming Mn2+-drug complexes. *Biochimica et Biophysica Acta (BBA)-Biomembranes* **1414,** 205–216. doi:https://doi.org/10.1016/S0005-2736(98)00168-0 (1998).

203. Abraham, S. A. *et al.* Formation of transition metal–doxorubicin complexes inside liposomes. *Biochimica et Biophysica Acta (BBA)-Biomembranes* **1565,** 41–54. doi:https://doi.org/10.1016/S0005-2736(02)00507-2 (2002).

204. Kaushik, D. & Bansal, G. Four new degradation products of doxorubicin: An application of forced degradation study and hyphenated chromatographic techniques. *Journal of pharmaceutical analysis* **5,** 285–295. doi:https://doi.org/10.1016/j.jpha.2015.05.003 (2015).

205. Malinauskas, M., Farsari, M., Piskarskas, A. & Juodkazis, S. Ultrafast laser nanostructuring of photopolymers: A decade of advances. *Physics Reports* **533,** 1–31. doi:https://doi.org/10.1016/j.physrep.2013.07.005 (2013).

206. Hippler, M. *et al.* 3D scaffolds to study basic cell biology. *Advanced Materials* **31,** 1808110. doi:https://doi.org/10.1002/adma.201808110 (2019).

207. Lemma, E. D., Spagnolo, B., De Vittorio, M. & Pisanello, F. Studying cell mechanobiology in 3D: the two-photon lithography approach. *Trends in biotechnology* **37,** 358–372. doi:https://doi.org/10.1016/j.tibtech.2018.09.008 (2019).

208. Barner-Kowollik, C. *et al.* 3D laser micro-and nanoprinting: challenges for chemistry. *Angewandte Chemie International Edition* **56,** 15828–15845. doi:https://doi.org/10.1002/anie.201704695 (2017).

209. Xing, J.-F., Zheng, M.-L. & Duan, X.-M. Two-photon polymerization microfabrication of hydrogels: an advanced 3D printing technology for tissue engineering and drug delivery. *Chemical Society Reviews* **44,** 5031–5039. doi:10.1039/C5CS00278H (2015).

210. Peters, C. *et al.* Superparamagnetic Twist-Type Actuators with Shape-Independent Magnetic Properties and Surface Functionalization for Advanced Biomedical Applications. *Advanced Functional Materials* **24,** 5269–5276. doi:https://doi.org/10.1002/adfm.201400596 (2014).

211. Krini, R. *et al.* Photosensitive Functionalized Surface-Modified Quantum Dots for Polymeric Structures via Two-Photon-Initiated Polymerization Technique. *Macromolecular rapid communications* **36,** 1108–1114. doi:https://doi.org/10.1002/marc.201500045 (2015).

212. Ushiba, S., Shoji, S., Masui, K., Kono, J. & Kawata, S. Direct laser writing of 3D architectures of aligned carbon nanotubes. *Advanced Materials* **26,** 5653–5657. doi:https://doi.org/10.1002/adma.201400783 (2014).

213. Sun, Z.-B. *et al.* Multicolor polymer nanocomposites: in situ synthesis and fabrication of 3D microstructures. *Advanced materials* **20,** 914–919. doi:https://doi.org/10.1002/adma.200702035 (2008).

214. Claus, T. K. *et al.* Simultaneous dual encoding of three-dimensional structures by light-induced modular ligation. *Angewandte Chemie International Edition* **55,** 3817–3822. doi:https://doi.org/10.1002/anie.201509937 (2016).

215. Gräfe, D. *et al.* It's in the Fine Print: Erasable Three-Dimensional Laser-Printed Micro-and Nanostructures. *Angewandte Chemie International Edition.* doi:https://doi.org/10.1002/anie.201910634 (2019).

216. Gomez, L. P. C. *et al.* Rapid Prototyping of Chemical Microsensors Based on Molecularly Imprinted Polymers Synthesized by Two-Photon Stereolithography. *Advanced Materials* **28,** 5931–5937. doi:https://doi.org/10.1002/adma.201600218 (2016).

217. Tudor, A. *et al.* Fabrication of soft, stimulus-responsive structures with submicron resolution via two-photon polymerization of poly (ionic liquid) s. *Materials Today* **21,** 807–816. doi:https://doi.org/10.1016/j.mattod.2018.07.017 (2018).

218. Kolb, H. C., Finn, M. & Sharpless, K. B. Click chemistry: diverse chemical function from a few good reactions. *Angewandte Chemie International Edition* **40,** 2004–2021. doi:https://doi.org/10.1002/1521-3773(20010601)40:11<2004::AID-ANIE2004>3.0.CO;2-5 (2001).

219. Liang, L. & Astruc, D. The copper (I)-catalyzed alkyne-azide cycloaddition (CuAAC)"click" reaction and its applications. An overview. *Coordination Chemistry Reviews* **255,** 2933–2945. doi:https://doi.org/10.1016/j.ccr.2011.06.028 (2011).

220. Wang, S. *et al.* Strain-promoted azide-alkyne cycloaddition "click" as a conjugation tool for building topological polymers. *Polymer* **55,** 4812–4819. doi:https://doi.org/10.1016/j.polymer.2014.08.003 (2014).

221. Dong, J., Krasnova, L., Finn, M. & Sharpless, K. B. Sulfur (VI) fluoride exchange (SuFEx): another good reaction for click chemistry. *Angewandte Chemie International Edition* **53,** 9430–9448. doi:https://doi.org/10.1002/anie.201309399 (2014).

222. Hoyle, C. E. & Bowman, C. N. Thiol–ene click chemistry. *Angewandte Chemie International Edition* **49,** 1540–1573. doi:https://doi.org/10.1002/anie.200903924 (2010).

223. Xi, W., Scott, T. F., Kloxin, C. J. & Bowman, C. N. Click chemistry in materials science. *Advanced Functional Materials* **24,** 2572–2590. doi:https://doi.org/10.1002/adfm.201302847 (2014).

224. Nair, D. P. *et al.* The thiol-Michael addition click reaction: a powerful and widely used tool in materials chemistry. *Chemistry of Materials* **26,** 724–744. doi:https://doi.org/10.1021/cm402180t (2014).

225. Schmidt, C. & Scherzer, T. Monitoring of the shrinkage during the photopolymerization of acrylates using hyphenated photorheometry/near-infrared spectroscopy. *Journal of Polymer Science Part B: Polymer Physics* **53,** 729–739. doi:https://doi.org/10.1002/polb.23694 (2015).

226. Quick, A. S. *et al.* Preparation of reactive three-dimensional microstructures via direct laser writing and thiol-ene chemistry. *Macromolecular rapid communications* **34,** 335–340. doi:https://doi.org/10.1002/marc.201200796 (2013).

227. Zhang, W., Yu, Z., Chen, Z. & Li, M. Preparation of super-hydrophobic Cu/Ni coating with micro-nano hierarchical structure. *Materials Letters* **67,** 327–330. doi:https://doi.org/10.1016/j.matlet.2011.09.114 (2012).

228. Noel, S., Liberelle, B., Robitaille, L. & De Crescenzo, G. Quantification of primary amine groups available for subsequent biofunctionalization of polymer surfaces. *Bioconjugate chemistry* **22,** 1690–1699. doi:https://doi.org/10.1021/bc200259c (2011).

229. Ovsianikov, A., Li, Z., Torgersen, J., Stampfl, J. & Liska, R. Selective functionalization of 3D matrices via multiphoton grafting and subsequent click chemistry. *Advanced Functional Materials* **22,** 3429–3433. doi:https://doi.org/10.1002/adfm.201200419 (2012).

230. Yan, M. F., Rhodes, W. W. & Gallagher, P. K. Dopant effects on the superconductivity of YBa2Cu3O7 ceramics. *Journal of applied physics* **63,** 821–828. doi:https://doi.org/10.1063/1.340075 (1988).

231. Bowen, C., Kim, H., Weaver, P. & Dunn, S. Piezoelectric and ferroelectric materials and structures for energy harvesting applications. *Energy & Environmental Science* **7,** 25–44. doi:https://doi.org/10.1039/C3EE42454E (2014).

232. Rao, C. N. R. Transition metal oxides. *Annual Review of Physical Chemistry* **40,** 291–326. doi:https://doi.org/10.1146/annurev.pc.40.100189.001451 (1989).

233. Ryu, H.-S. *et al.* Magnesia-doped HA/β-TCP ceramics and evaluation of their biocompatibility. *Biomaterials* **25,** 393–401. doi:https://doi.org/10.1016/S0142-9612(03)00538-6 (2004).

234. Gawande, M. B., Pandey, R. K. & Jayaram, R. V. Role of mixed metal oxides in catalysis science—versatile applications in organic synthesis. *Catalysis Science & Technology* **2,** 1113–1125. doi:https://doi.org/10.1039/C2CY00490A (2012).

235. Chen, Y.-W., Moussi, J., Drury, J. L. & Wataha, J. C. Zirconia in biomedical applications. *Expert review of medical devices* **13,** 945–963. doi:https://doi.org/10.1080/17434440.2016.1230017 (2016).

236. Andreescu, S., Ornatska, M., Erlichman, J. S., Estevez, A. & Leiter, J. in *Fine particles in medicine and pharmacy* 57–100 (Springer, 2012). doi:https://doi.org/10.1007/978-1-4614-0379-1_3.

237. Li, Z. *et al.* Scalable fabrication of perovskite solar cells. *Nature Reviews Materials* **3,** 1–20. doi:https://doi.org/10.1038/natrevmats.2018.17 (2018).

238. Arteaga, J., Zareipour, H. & Thangadurai, V. Overview of lithium-ion grid-scale energy storage systems. *Current Sustainable/Renewable Energy Reports* **4,** 197–208. doi:https://doi.org/10.1007/s40518-017-0086-0 (2017).

239. Rahaman, M. N. *Ceramic processing and sintering* doi:https://doi.org/10.1201/9781315274126 (CRC press, 2003).

240. Richerson, D. W. *Modern ceramic engineering: properties, processing, and use in design* doi:https://doi.org/10.1201/b18952 (CRC press, 2005).

241. Li, W. *et al.* Direct imprinting of scalable, high-performance woodpile electrodes for three-dimensional lithium-ion nanobatteries. *ACS applied materials & interfaces* **10,** 5447–5454. doi:https://doi.org/10.1021/acsami.7b14649 (2018).

242. Zhang, L. *et al.* Pseudo-ductile fracture of 3D printed alumina triply periodic minimal surface structures. *Journal of the European Ceramic Society* **40,** 408–416. doi:https://doi.org/10.1016/j.jeurceramsoc.2019.09.048 (2020).

243. Kern, C., Schuster, V., Kadic, M. & Wegener, M. Experiments on the parallel Hall effect in three-dimensional metamaterials. *Physical Review Applied* **7,** 044001. doi:https://doi.org/10.1103/PhysRevApplied.7.044001 (2017).

244. Griffith, M. L. & Halloran, J. W. Freeform fabrication of ceramics via stereolithography. *Journal of the American Ceramic Society* **79,** 2601–2608. doi:https://doi.org/10.1111/j.1151-2916.1996.tb09022.x (1996).

245. Zocca, A., Colombo, P., Gomes, C. M. & Günster, J. Additive manufacturing of ceramics: issues, potentialities, and opportunities. *Journal of the American Ceramic Society* **98,** 1983–2001. doi:https://doi.org/10.1111/jace.13700 (2015).

246. Gentry, S. P. & Halloran, J. W. Depth and width of cured lines in photopolymerizable ceramic suspensions. *Journal of the European Ceramic Society* **33,** 1981–1988. doi:https://doi.org/10.1016/j.jeurceramsoc.2013.02.033 (2013).

247. Colombo, P., Mera, G., Riedel, R. & Soraru, G. D. Polymer-derived ceramics: 40 years of research and innovation in advanced ceramics. *Journal of the American Ceramic Society* **93,** 1805–1837. doi:https://doi.org/10.1111/j.1551-2916.2010.03876.x (2010).

248. Gailevičius, D. *et al.* Additive-manufacturing of 3D glass-ceramics down to nanoscale resolution. *Nanoscale Horizons* **4,** 647–651. doi:https://doi.org/10.1039/C8NH00293B (2019).

249. Moore, D. G., Barbera, L., Masania, K. & Studart, A. R. Three-dimensional printing of multicomponent glasses using phase-separating resins. *Nature Materials* **19,** 212–217. doi:https://doi.org/10.1038/s41563-019-0525-y (2020).

250. Böhnlein-Mauß, J. *et al.* The function of polymers in the tape casting of alumina. *Advanced Materials* **4,** 73–81. doi:https://doi.org/10.1002/adma.19920040203 (1992).

251. Schottner, G. Hybrid sol- gel-derived polymers: applications of multifunctional materials. *Chemistry of materials* **13,** 3422–3435. doi:https://doi.org/10.1021/cm011060m (2001).

252. Schubert, U., Hüsing, N. & Lorenz, A. Hybrid inorganic-organic materials by sol-gel processing of organofunctional metal alkoxides. *Chemistry of materials* **7,** 2010–2027. doi:https://doi.org/10.1021/cm00059a007 (1995).

253. Greil, P. Active-filler-controlled pyrolysis of preceramic polymers. *Journal of the American Ceramic Society* **78,** 835–848. doi:https://doi.org/10.1111/j.1151-2916.1995.tb08404.x (1995).

254. Colombo, P., Bernardo, E. & Parcianello, G. Multifunctional advanced ceramics from preceramic polymers and nano-sized active fillers. *Journal of the European Ceramic Society* **33,** 453–469. doi:https://doi.org/10.1016/j.jeurceramsoc.2012.10.006 (2013).

255. Shukrun, E., Cooperstein, I. & Magdassi, S. 3D-Printed Organic–Ceramic Complex Hybrid Structures with High Silica Content. *Advanced Science* **5,** 1800061. doi:https://doi.org/10.1002/advs.201800061 (2018).

256. Chiappone, A. *et al.* 3D printed PEG-based hybrid nanocomposites obtained by sol–gel technique. *ACS applied materials & interfaces* **8,** 5627–5633. doi:https://doi.org/10.1021/acsami.5b12578 (2016).

257. Zhang, Y. *et al.* Homogeneous Freestanding Luminescent Perovskite Organogel with Superior Water Stability. *Advanced Materials* **31,** 1902928. doi:https://doi.org/10.1002/adma.201902928 (2019).

258. Varma, A., Mukasyan, A. S., Rogachev, A. S. & Manukyan, K. V. Solution combustion synthesis of nanoscale materials. *Chemical reviews* **116,** 14493–14586. doi:https://doi.org/10.1021/acs.chemrev.6b00279 (2016).

259. Yuvaraj, S., Fan-Yuan, L., Tsong-Huei, C. & Chuin-Tih, Y. Thermal decomposition of metal nitrates in air and hydrogen environments. *The Journal of Physical Chemistry B* **107,** 1044–1047. doi:https://doi.org/10.1021/jp026961c (2003).

260. Wen, W. & Wu, J.-M. Nanomaterials via solution combustion synthesis: a step nearer to controllability. *RSC Advances* **4,** 58090–58100. doi:https://doi.org/10.1039/C4RA10145F (2014).

261. Kakihana, M. & Yoshimura, M. Synthesis and characteristics of complex multicomponent oxides prepared by polymer complex method. *Bulletin of the Chemical Society of Japan* **72,** 1427–1443. doi:https://doi.org/10.1246/bcsj.72.1427 (1999).

262. Krsmanović, R. M., Antić, Ž., Nikolić, M. G., Mitrić, M. & Dramićanin, M. D. Preparation of Y2O3: Eu3+ nanopowders via polymer complex solution method and luminescence properties of the sintered ceramics. *Ceramics International* **37,** 525–531. doi:https://doi.org/10.1016/j.ceramint.2010.09.040 (2011).

263. Deshpande, K., Mukasyan, A. & Varma, A. Direct synthesis of iron oxide nanopowders by the combustion approach: reaction mechanism and properties. *Chemistry of materials* **16,** 4896–4904. doi:https://doi.org/10.1021/cm040061m (2004).

264. Tynell, T. & Karppinen, M. Atomic layer deposition of ZnO: a review. *Semiconductor Science and Technology* **29,** 043001. doi:https://doi.org/10.1088/0268-1242/29/4/043001 (2014).

265. Cui, H. *et al.* Three-dimensional printing of piezoelectric materials with designed anisotropy and directional response. *Nature materials* **18,** 234–241. doi:https://doi.org/10.1038/s41563-018-0268-1 (2019).

266. Liu, Z. *et al.* Synthesis and cathodoluminescence properties of porous wood (fir)-templated zinc oxide. *Ceramics international* **34,** 69–74. doi:https://doi.org/10.1016/j.ceramint.2006.08.006 (2008).

267. Araki, S. *et al.* Fabrication of nanoshell-based 3d periodic structures by templating process using solution-derived Zno. *Nanoscale research letters* **12,** 1–9. doi:https://doi.org/10.1186/s11671-017-2186-6 (2017).

268. Bagal, A. *et al.* Large-area nanolattice film with enhanced modulus, hardness, and energy dissipation. *Scientific reports* **7,** 1–9. doi:https://doi.org/10.1038/s41598-017-09521-6 (2017).

269. Giakoumaki, A. N. *et al.* 3D micro-structured arrays of ZnO nanorods. *Scientific reports* **7,** 1–9. doi:https://doi.org/10.1038/s41598-017-02231-z (2017).

270. Fonseca, R. D. *et al.* Fabrication of zinc oxide nanowires/polymer composites by two-photon polymerization. *Journal of Polymer Science Part B: Polymer Physics* **52,** 333–337. doi:https://doi.org/10.1002/polb.23418 (2014).

271. Lifson, M. L. *Electromechanical Properties of 3D Multifunctional Nano-Architected Materials* PhD thesis (California Institute of Technology, 2019). doi:https://doi.org/10.7907/D0AD-4T88.

272. Ishihara, T. *Perovskite oxide for solid oxide fuel cells* doi:https://doi.org/10.1007/978-0-387-77708-5 (Springer Science & Business Media, 2009).

273. Bhalla, A., Guo, R. & Roy, R. The perovskite structure—a review of its role in ceramic science and technology. *Materials Research Innovations* **4,** 3–26. doi:https://doi.org/10.1007/s100190000062 (2000).

274. Vyatskikh, A., Ng, R. C., Edwards, B., Briggs, R. M. & Greer, J. R. Additive Manufacturing of High Refractive Index, Nano-architected Titanium Dioxide for 3D Dielectric Photonic Crystals. *Nano Letters.* doi:https://doi.org/10.1021/cm011060m (2020).

275. Wei, L. *et al.* A novel fabrication of yttria-stabilized-zirconia dense electrolyte for solid oxide fuel cells by 3D printing technique. *International Journal of Hydrogen Energy* **44,** 6182–6191. doi:https://doi.org/10.1016/j.ijhydene.2019.01.071 (2019).

276. Tesavibul, P. *et al.* Biocompatibility of hydroxyapatite scaffolds processed by lithography-based additive manufacturing. *Bio-medical materials and engineering* **26,** 31–38. doi:https://doi.org/10.3233/BME-151549 (2015).

277. Song, X. *et al.* Piezoelectric component fabrication using projection-based stereolithography of barium titanate ceramic suspensions. *Rapid Prototyping Journal.* doi:https://doi.org/10.1108/RPJ-11-2015-0162 (2017).

278. Zhang, G., Carloni, D. & Wu, Y. 3D printing of transparent YAG ceramics using copolymer-assisted slurry. *Ceramics International.* doi:https://doi.org/10.1016/j.ceramint.2020.03.247 (2020).

279. Wei, X. *et al.* Fabrication of YBa2Cu3O7- x (YBCO) superconductor bulk structures by extrusion freeforming. *Ceramics International* **42,** 15836–15842. doi:https://doi.org/10.1016/j.ceramint.2016.07.052 (2016).

280. McOwen, D. W. *et al.* 3D-printing electrolytes for solid-state batteries. *Advanced Materials* **30,** 1707132. doi:https://doi.org/10.1002/adma.201707132 (2018).

281. Stein, A., Keller, S. W. & Mallouk, T. E. Turning down the heat: Design and mechanism in solid-state synthesis. *Science* **259,** 1558–1564. doi:https://doi.org/10.1126/science.259.5101.1558 (1993).

282. Chakraborty, A. *et al.* Layered Cathode Materials for Lithium-Ion Batteries: Review of Computational Studies on LiNi1-x-yCoxMnyO2 and LiNi1-x-yCoxAlyO2. *Chemistry of Materials.* doi:https://doi.org/10.1021/acs.chemmater.9b04066 (2020).

283. Islam, M. S. & Fisher, C. A. Lithium and sodium battery cathode materials: computational insights into voltage, diffusion and nanostructural properties. *Chemical Society Reviews* **43,** 185–204. doi:https://doi.org/10.1039/C3CS60199D (2014).

284. Eftekhari, A. Lithium-ion batteries with high rate capabilities. *ACS Sustainable Chemistry & Engineering* **5,** 2799–2816. doi:https://doi.org/10.1021/acssuschemeng.7b00046 (2017).

285. Lu, J., Chen, Z., Pan, F., Cui, Y. & Amine, K. High-performance anode materials for rechargeable lithium-ion batteries. *Electrochemical Energy Reviews* **1,** 35–53. doi:https://doi.org/10.1007/s41918-018-0001-4 (2018).

286. Hess, S., Wohlfahrt-Mehrens, M. & Wachtler, M. Flammability of Li-ion battery electrolytes: flash point and self-extinguishing time measurements. *Journal of The Electrochemical Society* **162,** A3084–A3097. doi:https://doi.org/10.1149/2.0121502jes (2015).

287. Liu, Y. *et al.* Making Li-metal electrodes rechargeable by controlling the dendrite growth direction. *Nature Energy* **2,** 1–10. doi:https://doi.org/10.1038/nenergy.2017.83 (2017).

288. Janek, J. & Zeier, W. G. A solid future for battery development. *Nature Energy* **1,** 1–4. doi:https://doi.org/10.1038/nenergy.2016.141 (2016).

289. Roberts, M. *et al.* 3D lithium ion batteries—from fundamentals to fabrication. *Journal of Materials Chemistry* **21,** 9876–9890. doi:https://doi.org/10.1039/C0JM04396F (2011).

290. CNX, O. *OpenStax, Chemistry* http://cnx.org/contents/85abf193-2bd2-4908-8563-90b8a7ac8df6@9.311 (2016).

291. Kuang, Y., Chen, C., Kirsch, D. & Hu, L. Thick Electrode Batteries: Principles, Opportunities, and Challenges. *Advanced Energy Materials* **9,** 1901457. doi:https://doi.org/10.1002/aenm.201901457 (2019).

292. Sun, H. *et al.* Hierarchical 3D electrodes for electrochemical energy storage. *Nature Reviews Materials* **4,** 45–60. doi:https://doi.org/10.1038/s41578-018-0069-9 (2019).

293. Zhang, F. *et al.* 3D printing technologies for electrochemical energy storage. *Nano Energy* **40,** 418–431. doi:https://doi.org/10.1016/j.nanoen.2017.08.037 (2017).

294. Yang, Y. *et al.* Overview on the applications of three-dimensional printing for rechargeable lithium-ion batteries. *Applied Energy* **257,** 114002. doi:https://doi.org/10.1016/j.apenergy.2019.114002 (2020).

295. Chang, P., Mei, H., Zhou, S., Dassios, K. G. & Cheng, L. 3D printed electrochemical energy storage devices. *Journal of materials chemistry A* **7,** 4230–4258. doi:https://doi.org/10.1039/C8TA11860D (2019).

296. Nitta, N., Wu, F., Lee, J. T. & Yushin, G. Li-ion battery materials: present and future. *Materials today* **18,** 252–264. doi:https://doi.org/10.1016/j.mattod.2014.10.040 (2015).

297. Santiago, E., Andrade, A., Paiva-Santos, C. & Bulhoes, L. Structural and electrochemical properties of LiCoO2 prepared by combustion synthesis. *Solid State Ionics* **158,** 91–102. doi:https://doi.org/10.1016/S0167-2738(02)00765-8 (2003).

298. Vakifahmetoglu, C., Zeydanli, D. & Colombo, P. Porous polymer derived ceramics. *Materials Science and Engineering: R: Reports* **106,** 1–30. doi:https://doi.org/10.1016/j.mser.2016.05.001 (2016).

299. Gong, H., Beauchamp, M., Perry, S., Woolley, A. T. & Nordin, G. P. Optical approach to resin formulation for 3D printed microfluidics. *RSC advances* **5,** 106621–106632. doi:https://doi.org/10.1039/C5RA23855B (2015).

300. Li, H. *et al.* Glucose-assisted combustion synthesis of Li 1.2 Ni 0.13 Co 0.13 Mn 0.54 O 2 cathode materials with superior electrochemical performance for lithium-ion batteries. *RSC Advances* **6,** 79050–79057. doi:https://doi.org/10.1039/C6RA15639H (2016).

301. Sathiya, M., Prakash, A. S., Ramesha, K. & Shukla, A. K. Nitrate-melt synthesized HT-LiCoO2 as a superior cathode-material for lithium-ion batteries. *Materials* **2,** 857–868. doi:https://doi.org/10.3390/ma2030857 (2009).

302. Zhuravlev, V. *et al.* Solution Combustion Synthesis of Lithium Cobalt Oxide–Cathode Material for Lithium-Ion Batteries. *Int. J. Electrochem. Sci* **14,** 2965–2983. doi:https://doi.org/10.20964/2019.03.79 (2019).

303. Ohzuku, T., Ueda, A., Nagayama, M., Iwakoshi, Y. & Komori, H. Comparative study of LiCoO2, LiNi12Co12O2 and LiNiO2 for 4 volt secondary lithium cells. *Electrochimica Acta* **38,** 1159–1167. doi:https://doi.org/10.1016/0013-4686(93)80046-3 (1993).

304. Aziz, N. A. A., Abdullah, T. K. & Mohamad, A. A. Synthesis of LiCoO 2 via sol-gel method for aqueous rechargeable lithium batteries. *Ionics* **24,** 403–412. doi:https://doi.org/10.1007/s11581-017-2225-4 (2018).

305. Dai, T. *et al.* Synergy of Lithium, Cobalt, and Oxygen Vacancies in Lithium Cobalt Oxide for Airborne Benzene Oxidation: A Concept of Reusing Electronic Wastes for Air Pollutant Removal. *ACS Sustainable Chemistry & Engineering* **7,** 5072–5081. doi:https://doi.org/10.1021/acssuschemeng.8b05894 (2019).

306. Shin, H.-C. & Pyun, S.-I. Investigation of lithium transport through lithium cobalt dioxide thin film sputter-deposited by analysis of cyclic voltammogram. *Electrochimica acta* **46,** 2477–2485. doi:https://doi.org/10.1016/S0013-4686(01)00457-1 (2001).

307. Courtney, I. A. & Dahn, J. Electrochemical and in situ X-ray diffraction studies of the reaction of lithium with tin oxide composites. *Journal of the Electrochemical Society* **144,** 2045. doi:https://doi.org/10.1149/1.1837740 (1997).

308. Linden, D. & Reddy, T. B. *Handbook of Batteries* (McGraw-Hill, 1995).

309. Citrin, M. A. *Nanomechanical Properties of Electrodeposited Li and Fabrication of 3D Architected Cathodes for Li-Based Batteries* PhD thesis (California Institute of Technology, 2020).

310. Network, 3. P. M. *Additive Manufacturing with Metal Powders Market to Top $11B by 2024* https://www.3dprintingmedia.network/additive-manufacturing-with-metal-powders/ (2020).

311. *GE Aviation invests in widespread rollout of GE Additive Arcam EBM technology to support GE9X blade production* https://www.ge.com/additive/press-releases/ge-aviation-invests-widespread-rollout-ge-additive-arcam-ebm-technology-support-ge9x (2020).

312. *Ford Develops 3D-Printed Locking Wheel Nuts to Thwart Thieves* https://media.ford.com/content/fordmedia/img/me/en/news/2020/02/05/ford-develops-3d-printed-locking-wheel-nuts-to-help-keep-thieves.html (2020).

313. *3D Printing Done Right* https://www.boeing.com/features/innovation-quarterly/nov2017/feature-thought-leadership-3d-printing.page (2020).

314. Herzog, D., Seyda, V., Wycisk, E. & Emmelmann, C. Additive manufacturing of metals. *Acta Materialia* **117,** 371–392. doi:https://doi.org/10.1016/j.actamat.2016.07.019 (2016).

315. Bartlett, J. L. & Li, X. An overview of residual stresses in metal powder bed fusion. *Additive Manufacturing*. doi:https://doi.org/10.1016/j.addma.2019.02.020 (2019).

316. Arakane, S., Mizoshiri, M. & Hata, S. Direct patterning of Cu microstructures using femtosecond laser-induced CuO nanoparticle reduction. *Japanese Journal of Applied Physics* **54,** 06FP07. doi:https://doi.org/10.7567/JJAP.54.06FP07 (2015).

317. Ishikawa, A. & Tanaka, T. Two-Photon Fabrication of Three-Dimensional Metallic Nanostructures for Plasmonic Metamaterials. *Journal of Laser Micro/Nanoengineering* **7.** doi:https://doi.org/10.2961/jlnm.2012.01.0002 (2012).

318. Hirt, L., Reiser, A., Spolenak, R. & Zambelli, T. Additive manufacturing of metal structures at the micrometer scale. *Advanced Materials* **29,** 1604211. doi:https://doi.org/10.1002/adma.201604211 (2017).

319. Jiang, Y., Yang, S., Hua, Z. & Huang, H. Sol–gel autocombustion synthesis of metals and metal alloys. *Angewandte Chemie International Edition* **48,** 8529–8531. doi:https://doi.org/10.1002/anie.200903444 (2009).

320. Liu, Y. *et al.* Solution combustion synthesis of nanocrystalline Fe–50% Ni alloy powder. *Powder technology* **267,** 68–73. doi:https://doi.org/10.1016/j.powtec.2014.07.003 (2014).

321. Tran, T. Q. *et al.* 3D Printing of Highly Pure Copper. *Metals* **9,** 756. doi:https://doi.org/10.3390/met9070756 (2019).

322. Lodes, M. A., Guschlbauer, R. & Körner, C. Process development for the manufacturing of 99.94% pure copper via selective electron beam melting. *Materials Letters* **143,** 298–301. doi:https://doi.org/10.1016/j.matlet.2014.12.105 (2015).

323. Evstratova, S. *et al.* Copper (II) nitrate complex with acrylamide: synthesis and crystal structure. *Russian Journal of Coordination Chemistry* **27,** 735–737. doi:https://doi.org/10.1023/A:1012362511561 (2001).

324. Abramov, L., Zilberman, Y. N. & Ivanova, V. Effect of copper and iron salts on the radical polymerization of acrylamide in water. *Polymer Science USSR* **31,** 1573–1578. doi:https://doi.org/10.1016/0032-3950(89)90501-7 (1989).

325. López, G. & Mittemeijer, E. The solubility of C in solid Cu. *Scripta Materialia* **51,** 1–5. doi:https://doi.org/10.1016/j.scriptamat.2004.03.028 (2004).

326. Marques, M., Correia, J. & Conde, O. Carbon solubility in nanostructured copper. *Scripta materialia* **50,** 963–967. doi:https://doi.org/10.1016/j.scriptamat.2004.01.016 (2004).

327. Shannon, R. D. Revised effective ionic radii and systematic studies of interatomic distances in halides and chalcogenides. *Acta crystallographica section A: crystal physics, diffraction, theoretical and general crystallography* **32,** 751–767. doi:https://doi.org/10.1107/S0567739476001551 (1976).

328. Sari, N., Kahraman, E., Sari, B. r. & Özgün, A. n. Synthesis of Some Polymer-Metal Complexes and Elucidation of their Structures. *Journal of Macromolecular Science Part A: Pure and Applied Chemistry* **43,** 1227–1235. doi:https://doi.org/10.1080/10601320600737484 (2006).

329. Anderson, J. R. *Solubility of carbon in molten copper-manganese and copper-nickel alloys* PhD thesis (Massachusetts Institute of Technology, 1946).

330. Gomez-Martinez, A., Márquez, F. & Morant, C. A new approach of the synthesis of SiO2 nanowires by using bulk copper foils as catalyst. *Applied Surface Science* **387,** 1072–1079. doi:https://doi.org/10.1016/j.apsusc.2016.06.115 (2016).

331. Al-Kamiyani, S. & Mohiuddin, T. Improved control in elimination of white impurities on graphene by chemical vapor deposition (CVD). *AIP Advances* **8,** 125325. doi:https://doi.org/10.1063/1.5051693 (2018).

332. Gu, G. X., Takaffoli, M. & Buehler, M. J. Hierarchically enhanced impact resistance of bioinspired composites. *Advanced Materials* **29,** 1700060. doi:https://doi.org/10.1002/adma.201700060 (2017).

333. Liu, W. *et al.* Rapid continuous multimaterial extrusion bioprinting. *Advanced materials* **29,** 1604630. doi:https://doi.org/10.1002/adma.201604630 (2017).

334. Dolinski, N. D. *et al.* Solution Mask Liquid Lithography (SMaLL) for One-Step, Multimaterial 3D Printing. *Advanced Materials* **30,** 1800364. doi:https://doi.org/10.1002/adma.201800364 (2018).

335. Schwartz, J. & Boydston, A. J. Multimaterial actinic spatial control 3D and 4D printing. *Nature communications* **10,** 1–10. doi:https://doi.org/10.1038/s41467-019-08639-7 (2019).

336. Kowsari, K., Akbari, S., Wang, D., Fang, N. X. & Ge, Q. High-efficiency high-resolution multimaterial fabrication for digital light processing-based three-dimensional printing. *3D Printing and Additive Manufacturing* **5,** 185–193. doi:https://doi.org/10.1089/3dp.2018.0004 (2018).

337. Mayer, F. *et al.* Multimaterial 3D laser microprinting using an integrated microfluidic system. *Science advances* **5,** eaau9160. doi:https://doi.org/10.1126/sciadv.aau9160 (2019).

338. Steed, J. W. & Atwood, J. L. *Supramolecular chemistry* doi:https://doi.org/10.1002/9780470740880 (John Wiley & Sons, 2013).

339. Zhang, J. *et al.* Self-assembling nanocomposite tectons. *Journal of the American Chemical Society* **138,** 16228–16231. doi:https://doi.org/10.1021/jacs.6b11052 (2016).

340. Lehn, J.-M. Perspectives in supramolecular chemistry—from molecular recognition towards molecular information processing and self-organization. *Angewandte Chemie International Edition in English* **29,** 1304–1319. doi:https://doi.org/10.1002/anie.199013041 (1990).

341. Cram, D. J. & Cram, J. M. Host-guest chemistry. *Science* **183,** 803–809 (1974).

342. Stoddart, J. F. Mechanically interlocked molecules (MIMs)—Molecular shuttles, switches, and machines (Nobel Lecture). *Angewandte Chemie International Edition* **56,** 11094–11125. doi:https://doi.org/10.1002/anie.201703216 (2017).

343. Pekkanen, A. M., Mondschein, R. J., Williams, C. B. & Long, T. E. 3D printing polymers with supramolecular functionality for biological applications. *Biomacromolecules* **18,** 2669–2687. doi:https://doi.org/10.1021/acs.biomac.7b00671 (2017).